

SUPERMASSIVE BLACK HOLE ACTIVITY IN THE COSMIC EVOLUTION
SURVEY

by

Jonathan Russell Trump

A Dissertation Submitted to the Faculty of the
DEPARTMENT OF ASTRONOMY
In Partial Fulfillment of the Requirements
For the Degree of
DOCTOR OF PHILOSOPHY
In the Graduate College
THE UNIVERSITY OF ARIZONA

2 0 1 0

THE UNIVERSITY OF ARIZONA
GRADUATE COLLEGE

As members of the Dissertation Committee, we certify that we have read the dissertation prepared by Jonathan Russell Trump entitled Supermassive Black Hole Activity in the Cosmic Evolution Survey and recommend that it be accepted as fulfilling the dissertation requirement for the Degree of Doctor of Philosophy.

Christopher D. Impey Date: 16 April 2010

Romeel Davé Date: 16 April 2010

Richard F. Green Date: 16 April 2010

Dennis Zaritsky Date: 16 April 2010

Final approval and acceptance of this dissertation is contingent upon the candidate's submission of the final copies of the dissertation to the Graduate College.

I hereby certify that I have read this dissertation prepared under my direction and recommend that it be accepted as fulfilling the dissertation requirement.

Dissertation Director: Christopher D. Impey Date: 16 April 2010

STATEMENT BY AUTHOR

This dissertation has been submitted in partial fulfillment of requirements for an advanced degree at The University of Arizona and is deposited in the University Library to be made available to borrowers under rules of the Library.

Brief quotations from this dissertation are allowable without special permission, provided that accurate acknowledgment of source is made. Requests for permission for extended quotation from or reproduction of this manuscript in whole or in part may be granted by the head of the major department or the Dean of the Graduate College when in his or her judgment the proposed use of the material is in the interests of scholarship. In all other instances, however, permission must be obtained from the author.

SIGNED: Jonathan Russell Trump

ACKNOWLEDGMENTS

I leaned on and learned from a lot of people on the way to my Ph.D., and I'd like to use this space to formally thank them.

First, I'd like to thank my parents. I was always lucky to come from a supportive family which highly valued education and encouraged me to succeed. I never lacked for educational opportunities, with my parents offering everything from financial support for academic competitions in high school and college to an always-interested ear throughout my pursuits. I thank them most for their patience: I've been in school for 22 straight years, and I think my parents showed a tremendous amount of faith in me to remain so supportive throughout the myriad missteps and dead-ends in such a long path. I'm simply a better human being from their influence, and for that, I am truly thankful.

I'd also like to thank all the teachers and mentors of my "formative" years, when I didn't know starlight from satellites and quasars were just another twinkle in the sky. I owe a great deal to Mr. Moyer, who taught me that everyone has a great talent just waiting to be recognized (and he was somehow able to recognize this in 10-year-olds). I want to thank Mr. Dietrich, who really set me on the path of my first true research projects and taught me about the pride and success that comes from hard work. I'd especially like to thank my uncle, the late Frank Schweingruber, whose contagious enthusiasm led me to love the physics of the universe. I still vividly recall the boundless enthusiasm of my Uncle Frank as he mentored me in designing my senior project in high school: a double-slit experiment demonstrating the wave-particle duality of light.

I want to thank my professors at Penn State, especially those who taught me what it is to be an astronomer. Jane Charlton and Caryl Gronwall gave me much-needed advice when it came to choosing a graduate school, and with Niel Brandt, Mike Eracleous, Chris Palma, Larry Ramsey, and Steinn Sigurdsson showed an enthusiasm for astronomy that I can only hope to match. I also want to thank my undergraduate advisor Don Schneider and Gordon Richards (at the time, Don's postdoc). They gave me a comfortable introduction to the large survey AGN science that I eventually pursued for my thesis (and will continue for as a postdoc). And they were also bold enough to hand a significant project to a fresh-faced student with a lot to learn: with their help, my undergraduate research resulted in a widely cited published paper. Making your student's research well-known is surely the greatest gift than an advisor can give.

It's also important to me to recognize those friends who encouraged me in my education and research, and made academic life much easier. I'll start with Amy and Andrew, two of my oldest friends, because it's friends like these that help you realize it's perfectly natural to love science. I'd like to thank my study partners and fellow stargazers in college: Shoe, Kimbo, Bragg, Sloan, and Danimal; Nate, Nate, and Seltzer; Rick, Eric, Adam, and Dave. Joe and Megan certainly showed

me that it's far easier to learn with partners like them by your side. Brooklyn, Ben Opp, Jerry, Brandon, Iva, Maggie, the Stephs, James, Suz, Coley, and Boz all made Tucson an easy place to live and work. The Steward Mug Club was the ultimate blessing, because with Brandon, Nopey, and my heterolifemate Aleks as both best friends and my colleagues, the frustrations of graduate school are no more distressing than an empty 25-oz mug. And special thanks go to my brother Ben, who's always been a far better listener than I, and showed it constantly through my trials even as our lives led us so far apart. I want to thank my partner, Lindsay, for her patience and support through the inevitable stresses of a thesis.

Ultimately, this thesis is the product of collaboration with many colleagues. Nick Scoville made the Cosmic Evolution Survey an easy place for a graduate student to succeed, always ensuring that I was comfortable and had a large suite of scientific real estate to explore. Martin Elvis was consistently my go-to pundit when I needed a quasar expert, and originally suggested several of the research paths pursued in this work. I'd like to thank Pat McCarthy for teaching me how to observe, and the staffs at the Magellan and MMT telescopes for making my observations painless. (I should also thank the Chilean weather, with only one night lost over 20 nights of observing.) Knud Jahnke, Anton Koekemoer, Marcella Brusa, Andrea Comastri, Francesca Civano, Patrick Shopbell, and Mara Salvato also helped with guidance and countless discussions. I want to thank Yoshi Taniguchi, Tohru Nagao, and their students at Ehime University for making Matsuyama, Japan like a second home to me while I worked there on research visits. My research was also reliant on financial support from an ARCS fellowship, a NSF/JSPS summer fellowship, NSF/DDEP grant #0943995, NSF grant #NNX08AJ28G, and NASA grant HST-GO-09822.

I owe a great deal to my graduate advisor, Chris Impey. I first began this research after Chris sent an email to all students in the department explaining that he needed someone to go observing in Chile. A trip to South America sounded pretty good to me, and five and a half years later I've been observing in Chile four times, plus three trips to Japan, two to China, and an observing run in Hawaii. All this because Chris encouraged me to write ambitious proposals, and then had the patience to help mold them into success. And whenever Chris felt he lacked the expertise on an issue, he made sure to send me to a conference full of experts. Chris was patient, but also knew how to push me when I needed that extra motivation. I hope that some day I can give my students all that Chris has given me in my graduate career.

Thanks also go to Sandy Faber, David Koo, and Raja Guhathakurta... because it's far easier to write and defend a thesis when you have an excellent postdoc job waiting for you in Santa Cruz.

DEDICATION

For Frank Schweingruber, who taught me that the universe is a beautiful and fascinating subject of study.

TABLE OF CONTENTS

LIST OF FIGURES	9
LIST OF TABLES	11
ABSTRACT	12
CHAPTER 1 INTRODUCTION	14
CHAPTER 2 THE COSMOS AGN SPECTROSCOPIC SURVEY: XMM COUN-	
TERPARTS	20
2.1 Chapter Introduction	20
2.2 Observations	25
2.2.1 XMM-Newton	25
2.2.2 Magellan/IMACS	26
2.2.3 MMT/Hectospec	36
2.2.4 SDSS	40
2.3 Spectral Analysis	40
2.3.1 AGN Classification	41
2.3.2 AGN, Starbursts, and Quiescent Galaxies	90
2.4 Completeness	95
2.4.1 X-ray Flux Limit	96
2.4.2 Optical Flux Limit	96
2.4.3 Redshift-Dependent Completeness	98
2.4.4 Characterizing the Low-Confidence Targets	103
2.5 Discussion	106
2.5.1 Demographics	106
2.5.2 Obscured to Unobscured AGN Ratio	109
2.6 Conclusions and Future Projects	114
CHAPTER 3 OBSERVATIONAL LIMITS ON TYPE 1 AGN ACCRETION RATE	
IN COSMOS	116
3.1 Chapter Introduction	116
3.2 Observational Data	119
3.2.1 Sample	119
3.2.2 Spectral Fitting	120
3.3 Estimated Black Hole Masses	122
3.3.1 Error	137
3.3.2 Completeness	140
3.4 Discussion	143
3.5 Summary	147

TABLE OF CONTENTS — *Continued*

CHAPTER 4	THE NATURE OF OPTICALLY DULL ACTIVE GALACTIC NUCLEI IN COSMOS	148
4.1	Chapter Introduction	148
4.2	Observations	151
4.2.1	X-ray Selection	151
4.2.2	Spectroscopy	152
4.2.3	Optical and Infrared Photometry	153
4.2.4	Host Morphologies	157
4.2.5	Completeness	157
4.3	Multiwavelength Properties	158
4.3.1	Optical Fitting: Host and AGN Components	163
4.3.2	X-ray to Optical Ratio	170
4.3.3	Infrared Color: Dust Properties	172
4.3.4	X-ray Column Density	174
4.3.5	Host Galaxy Properties	176
4.4	Discussion	181
4.4.1	The Case for Dilution	182
4.4.2	The Case for Radiatively Inefficient Accretion	183
4.5	Accretion Properties	184
4.6	Chapter Summary	188
CHAPTER 5	ACCRETION RATE AND THE PHYSICAL NATURE OF ACTIVE GALAXIES	189
5.1	Chapter Introduction	189
5.2	Observational Data	193
5.3	Characterizing AGN Specific Accretion Rate	211
5.3.1	Intrinsic Luminosity Estimates	211
5.3.2	Black Hole Mass Estimates	215
5.3.3	Error Budget	218
5.4	The Physical Effects of Specific Accretion Rate	220
5.4.1	The Role of Obscuration	223
5.4.2	Physics of the Accretion Disk	228
5.4.3	Accretion Rate and Outflows	231
5.4.4	Accretion Rate and the IR “Torus”	233
5.5	A Simple Model for Unifying AGNs by Specific Accretion Rate	236
5.6	Predictions and Future Observational Tests	238
CHAPTER 6	CONCLUSIONS, PREDICTIONS, AND FUTURE OBSERVATIONS .	240
REFERENCES	243

LIST OF FIGURES

1.1	The multiwavelength detection limits of COSMOS with example AGN SEDs	18
2.1	X-ray depth and survey size for X-ray surveys, with flux limits of COSMOS X-ray sources.	24
2.2	X-ray sensitivity maps in COSMOS	27
2.3	Maps of spectroscopic observations in COSMOS	29
2.4	COSMOS Magellan/IMACS spectra with broad emission lines	33
2.5	COSMOS Magellan/IMACS spectra without broad emission lines . .	34
2.6	Observed wavelengths of broad emission lines with redshift.	38
2.7	Comparison of Magellan/IMACS and MMT/Hectospec spectra	39
2.8	Spectroscopic redshift templates	42
2.9	X-ray luminosity distribution for COSMOS AGNs.	92
2.10	X-ray flux and optical magnitude for COSMOS AGNs.	93
2.11	S/N and optical magnitude for COSMOS AGNs	97
2.12	Redshift completeness with type and optical magnitude	99
2.13	Redshift completeness with redshift for broad-line AGNs	102
2.14	Redshift distributions of COSMOS AGNs	104
2.15	Photometric redshifts for objects without high-confidence spectroscopic redshifts	107
2.16	Absolute magnitude of AGNs with redshift	108
2.17	The obscured/unobscured AGN ratio	111
3.1	Fits and line profiles for three broad-line AGNs	123
3.2	Black hole mass with optical luminosity and redshift for COSMOS Type 1 AGNs	139
3.3	Comparison of luminosity estimates from this work and those from VLT/VIMOS spectra	141
3.4	Broad emission line FWHM with S/N for observed and simulated Type 1 AGNs	142
3.5	Eddington ratio (accretion rate) with black hole mass, optical luminosity, and redshift for COSMOS Type 1 AGNs	144
4.1	[OII] and $H\beta$ emission line luminosities for optically dull and Type 2 AGNs	154
4.2	Fits to the optical photometry of optically dull AGNs	167
4.3	Optical photometry and fits for a highly variable optically dull AGN .	169
4.4	X-ray flux and optical magnitudes of optically dull AGNs	171
4.5	Spitzer/IRAC Infrared colors of optically dull AGNs	173
4.6	X-ray column density and infrared color for optically dull AGNs . . .	175

LIST OF FIGURES — *Continued*

4.7	HST/ACS images of optically dull AGNs and their host galaxies . . .	177
4.8	Axis ratio (host inclination) with redshift for optically dull AGNs . .	178
4.9	Composite spectrum for RIAF-candidate optically dull AGNs	185
4.10	Radio fluxes and optical magnitudes of optically dull AGNs	187
5.1	Spectral energy distributions with accretion disk plus X-ray power-law fits	216
5.2	Distribution of accretion rates for broad-line, narrow-line, and lineless AGNs	221
5.3	Accretion rate with the disk/X-ray luminosity ratio, disk peak temperature, and X-ray power-law slope	222
5.4	Accretion rate with disk/X-ray luminosity ratio, disk temperature, and X-ray slope for unabsorbed ($N_H < 10^{22} \text{ cm}^{-2}$) AGNs	225
5.5	Column density with X-ray power-law slope	227
5.6	Accretion rate with radio-loudness (radio/disk luminosity ratio) . . .	232
5.7	Accretion rate with $1 < \lambda < 10\mu$ infrared power-law slope	234
5.8	Schematic model demonstrating the physical differences between AGN at high and low accretion rates	237

LIST OF TABLES

2.1	Observation Log of the IMACS Spectroscopy in COSMOS	30
2.2	COSMOS XMM Optical Spectroscopy Catalog	45
2.3	Targeting and Redshift Yields	94
3.1	COSMOS Type 1 AGN Black Hole Mass Catalog	124
4.1	COSMOS Optical and Infrared Photometry	156
4.2	Optically Dull AGN Properties	160
5.1	COSMOS Multiwavelength Data	195
5.2	Catalog of AGN accretion rates	197

ABSTRACT

I investigate active supermassive black holes, also called active galactic nuclei (AGNs). My tool for this work is the Cosmic Evolution Survey (COSMOS), a deep multiwavelength survey over 2 deg^2 of the sky. I describe the COSMOS AGN optical spectroscopy campaign, and present the largest AGN sample to date with full multiwavelength (radio, IR, optical, UV and X-ray) spectral energy distributions. Studying the COSMOS AGN sample reveals a unified model for supermassive black hole activity based on accretion rate, as shown by the following main results. (1) Classically “obscured” (Type 2) AGNs are more prevalent at higher redshifts and lower luminosities, suggesting that these objects accrete through low-level stochastic disk feeding by their hosts. (2) The presence of broad emission lines in an AGN requires a minimum accretion rate ($L/L_{Edd} > 0.01$). Broad-line (Type 1) AGNs in COSMOS span a large range of accretion rates ($0.01 < L/L_{Edd} < 1$), in contrast to results from previous, shallower surveys, and broad-line AGNs become more optically luminous as accretion rate increases. (3) Lineless, “optically dull” AGNs have very different SEDs than broad-line and narrow-line AGNs, with comparatively brighter X-ray emission, redder optical continua, no infrared hot dust, and stronger radio emission. While up to 2/3 of optically dull AGNs may be “normal” AGNs diluted by extranuclear host galaxy light, at least 1/3 are best described as unobscured, intrinsically weak AGNs. (4) At low accretion rates, material accreting onto an AGN changes from a thin disk to an advection-dominated flow near the black hole, resulting in very different observed properties: the broad-line region disappears, radio jets become more important, and the hot dust signature changes. In contrast to previous unification models, observations indicate that most of the narrow-line and lineless AGNs in COSMOS are best described as weakly accreting

AGNs. We conclude by noting a few predictions and observational tests to further investigate our model of AGN unification by accretion rate.

CHAPTER 1

INTRODUCTION

Supermassive black holes (SMBHs) have only been known to exist for about 50 years (Schmidt, 1963; Salpeter, 1964; Lynden-Bell, 1969), and until the last decade they were thought to be an exotic phenomenon. Recently, however, astronomers have realized that SMBHs are ubiquitous in the centers of all known massive galaxies. Our own Milky Way contains a SMBH known as Sag A*, with a mass of 3 million solar masses (Schodel et al., 2002; Ghez et al., 2003). Essentially all massive galaxies have one or more episodes of the AGN phase (Soltan, 1982; Magorrian et al., 1998; Marconi et al., 2004), presumably including our own Milky Way. The activity of smaller, less luminous AGNs peaks more recently than more luminous AGNs (Ueda et al., 2003; Brandt & Hasinger, 2005; Bongiorno et al., 2007), in an analogous fashion to the early build-up of the largest galaxies, and this phenomenon is known as “downsizing.” Any prescription of galaxy evolution requires an understanding of SMBH growth through the AGN phase.

As AGNs have been detected and studied over the past ~ 50 years, it has been recognized that they exhibit wildly different properties but can be grouped into a few general categories. Type 1 AGNs or quasars are generally unobscured and exhibit broad emission lines superimposed on a blue power-law continuum in their optical/UV spectra (e.g., Vanden Berk et al., 2001). They are the most luminous persistent sources in the sky (Nicastro & Elvis, 2000) and have high accretion rates (Kollmeier et al., 2006). Type 2 AGNs, on the other hand, have narrow emission lines (especially by forbidden transitions) in their optical spectra, and their optical continua are usually overwhelmed by their host galaxy (e.g. Zakamska et al., 2003). The related class of “optically dull” AGNs have no optical emission lines in their

spectra, despite having the bright X-ray emission of an AGN. X-ray spectra can also be used to classify AGNs by their inferred X-ray column density N_H . In general, optically dull (lineless) and Type 2 (narrow-line) AGNs are typically more X-ray obscured (i.e., have a higher column density N_H) than Type 1 (broad-line) AGNs, although X-ray and optical classifications differ for $\sim 20\%$ of objects (Trouille et al., 2009).

Historically, Type 2 and optically dull AGNs have been described as obscured versions of Type 1 AGNs, with the broad emission line region hidden behind obscuring gas and dust (Krolik & Begelman, 1988) while the narrow lines remain visible. The best evidence for this scenario is the observation that some Type 2 AGNs have a “hidden” BLR, revealed by deep spectropolarimetry (Antonucci, 1993). Other authors, however, have suggested that many “obscured” AGNs might instead be intrinsically weak, with the broad emission line region disappearing at low accretion rates (Nicastro, 2000; Bianchi et al., 2008). Local low-luminosity AGNs tend to have very different spectral energy distributions (SEDs) than luminous Type 1 AGNs (Ho, 2008), and low fueling rates might alter the SED of a Type 2 AGN in the same way as obscuration (Hopkins et al., 2009). The degeneracy between fueling rate and obscuration as a driver of AGN type remains an open question in the study of SMBH growth.

The observations linking AGN growth with their host galaxies suggests that AGNs exert feedback on their host, regulating star formation and the growth of the galaxy as the SMBH grows (Silva et al., 1998; Di Matteo, Springel, & Hernquist, 2005; Chartas et al., 2007). Downsizing and the episodic nature of AGN activity suggest that host galaxies regulate the fueling and growth of their SMBHs in turn (Hopkins et al., 2005; Babic et al., 2007; Younger et al., 2008). Several recent theoretical models attempt to explain these dual feedback processes with a

paradigm linking SMBH fueling and activity to star formation and gas feeding in the host. High mass AGNs are thought to be powered by major mergers (Hopkins et al., 2006), while lower mass and weaker AGNs may be fueled by minor mergers (Taniguchi, 1999) or stochastic disk accretion (Hopkins & Hernquist, 2006). Many of the details in the interplay between AGN activity and galaxy evolution remain in dispute: some authors suggest that star formation is quenched when the AGN reaches its most active phase (Hopkins et al., 2005; Croton et al., 2006; Bundy et al., 2008), while others suggest that AGN activity and star formation peak at the same time (Silverman et al., 2009; Shi et al., 2009). In addition, some authors have found evidence for evolution in the $M_{BH} - M_*$ relation ((e.g., Peng et al., 2006; Woo et al., 2008; Jahnke et al., 2009; Merloni et al., 2010). Such studies would indicate that SMBH-host connection changes significantly with redshift, although they are contaminated by observational biases (lauer et al., 2007) and rely on black hole masses which have systematic uncertainties of at least 0.4 dex (Krolik, 2001). Understanding evolution in the connection between SMBH properties (like mass, SED shape, and accretion rate) and host galaxy properties (like star formation, host mass, and environment), requires a large sample of AGNs and host galaxies over a large range in redshift and from a large area of the sky.

The Cosmic Evolution Survey (COSMOS, Scoville et al., 2007) provides just such a sample. COSMOS was initiated with HST imaging and motivated by the study of galaxy evolution and morphology, but its deep multiwavelength photometry make it ideal for studying AGNs. Figure 1.1 shows the detection limits of COSMOS with SEDs for a bright (10^{46} erg s $^{-1}$) and faint (4×10^{44} erg s $^{-1}$) unobscured Type 1 AGN and the heavily obscured AGN Arp 220, all shifted out to $z = 1.5$. It is immediately clear that AGNs, whether obscured or unobscured, emit over a large range of wavelengths, and a wide range of multiwavelength photometry is necessary

to fully characterize the SED. In the past, the largest AGN surveys have used optical selection, which is heavily contaminated by starlight and misses obscured or weakly accreting AGNs. X-ray surveys are generally the most efficient way to select AGNs, as they have the least contamination and find AGN sky densities 10-20 times higher than optical surveys (Brandt & Hasinger, 2005, e.g.). This work uses a large sample of X-ray selected AGNs with multiwavelength photometry from COSMOS.

The thesis is structured as follows. In Chapter 2, I present the details of the COSMOS AGN spectroscopy campaign, detailing the classification, redshifts, and selection effects. Chapter 2 also presents the basic demographics of the full sample, including intriguing results on the ratio of classically “obscured” (narrow-line and lineless) AGNs to broad-line (Type 1) AGNs which suggest that host galaxies preferentially fuel Type 2 AGNs at lower accretion rates. Chapter 2 focuses on the Type 1 AGNs, using the virial scaling relations to estimate black hole masses and estimating accretion rates using the COSMOS multiwavelength data. I show that Type 1 AGNs range in accretion rate over 2 orders of magnitude, but are limited by a minimum accretion rate of $L/L_{Edd} > 0.01$. In Chapter 4 I focus on a very different type of object, “optically dull” AGNs. These objects are so named because they have the bright X-ray emission characteristic of an AGN but are optically under-luminous. I show that optically dull AGNs are unobscured, have nuclear optical continua which are bluer than their hosts but redder than typical AGNs, lack a hot dusty torus, and are radio-loud, additionally showing that at least 1/3 of these AGNs have physically different accretion flows than their bright Type 1 AGN counterparts. The nature of AGN accretion is further discussed in Chapter 5, where I calculate accurate accretion rates for the full COSMOS sample of broad-line, narrow-line, and lineless AGNs. I show that most of the narrow-line and lineless AGNs in COSMOS are unobscured and have low accretion rates, while lacking the IR hot dust signature and

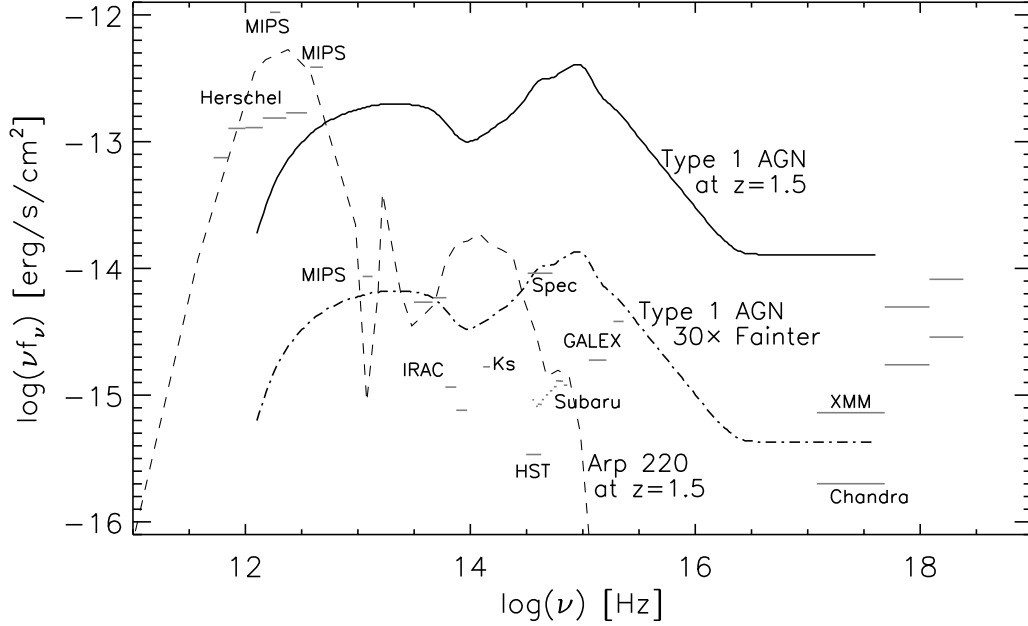


Figure 1.1 The 5σ detection limits across the electromagnetic spectrum for COSMOS are shown as gray lines, and the solid curve is a mean Type 1 SED from Richards et al. (2006) with $L_{3000\text{\AA}} = 10^{46} \text{ erg s}^{-1}$ scaled at $z = 1.5$. The dot-dashed line, a factor of thirty lower, represents a luminosity detected by the COSMOS Magellan/IMACS spectroscopy (described in Chapter 2). The dashed line is the model fit of Silva et al. (1998) to Arp 220, a well-studied local ULIRG and obscured AGN, also scaled to $z = 1.5$. In this energy per unit bandwidth plot, higher regions are the largest contributors to the bolometric luminosity. The Herschel limits represent a future GTO program, and all other data have been observed and reduced (and are used in this thesis).

being more radio-loud than broad-line AGNs which have uniformly high accretion rates. These observations are neatly explained by a unified model for AGNs where low accretion rates result in physically different accretion flows, where low accretion rates cause a region of optically thin and geometrically thick advection-dominated accretion to develop at inner radii of the classical optically thick and geometrically thin accretion disk. I conclude in Chapter 6 with predictions of this model for AGN unification by accretion rate and a few ideas for future observations.

CHAPTER 2

THE COSMOS AGN SPECTROSCOPIC SURVEY: XMM COUNTERPARTS

We present optical spectroscopy for an X-ray and optical flux-limited sample of 677 XMM-Newton selected targets covering the 2 deg^2 COSMOS field, with a yield of 485 high-confidence redshifts. The majority of the spectra were obtained over three seasons (2005-2007) with the IMACS instrument on the Magellan (Baade) telescope. We also include in the sample previously published Sloan Digital Sky Survey spectra and supplemental observations with MMT/Hectospec. We detail the observations and classification analyses. The survey is 90% complete to flux limits of $f_{0.5-10\text{keV}} > 8 \times 10^{-16} \text{ erg cm}^{-2} \text{ s}^{-1}$ and $i_{\text{AB}}^+ < 22$, where over 90% of targets have high-confidence redshifts. Making simple corrections for incompleteness due to redshift and spectral type allows for a description of the complete population to $i_{\text{AB}}^+ < 23$. The corrected sample includes 57% broad emission line (Type 1, unobscured) AGN at $0.13 < z < 4.26$, 25% narrow emission line (Type 2, obscured) AGN at $0.07 < z < 1.29$, and 18% absorption line (host-dominated, obscured) AGN at $0 < z < 1.22$ (excluding the stars that made up 4% of the X-ray targets). We show that the survey's limits in X-ray and optical flux include nearly all X-ray AGN (defined by $L_{0.5-10\text{keV}} > 3 \times 10^{42} \text{ erg s}^{-1}$) to $z < 1$, of both optically obscured and unobscured types. We find statistically significant evidence that the obscured to unobscured AGN ratio at $z < 1$ increases with redshift and decreases with luminosity.

2.1 Chapter Introduction

Active Galactic Nuclei (AGN) are the brightest persistent extragalactic sources in the sky across nearly all of the electromagnetic spectrum. Only in the relatively

narrow range of infrared (IR) through ultraviolet (UV) wavelengths are AGN often outshone by stellar emission. Here the central engines can be dimmed by obscuring dust and gas while starlight, either direct or absorbed and re-emitted by dust, peaks. Historically, the largest AGN surveys have been based on optical selection (e.g. BQS, Schmidt & Green, 1983; LBQS, Hewett, Foltz, & Chaffee, 1995; HES, Wisotzki et al., 2000; 2dF, Croom et al., 2001; SDSS, Schneider et al., 2007). Yet in both the local and distant universe, obscured AGN are generally thought to outnumber their unobscured counterparts (e.g. Maiolino & Rieke, 1995; Gilli et al., 2001; Steffen et al., 2004; Barger et al., 2005; Martinez-Sansigre et al., 2005; Daddi et al., 2007; Treister, Krolik & Dullemond, 2008), indicating that optical surveys probably miss the majority of AGN. A more complete census of AGN must use their X-ray, mid-infrared, and radio emission, where obscuration and host contamination are minimized. X-ray and mid-IR selected surveys do in fact reveal a far greater space density of AGN than optical selection: for example, the *Chandra* deep fields reveal AGN sky densities 10-20 times higher than those of optically selected surveys to the same limiting optical magnitudes (Bauer et al., 2004; Risaliti & Elvis, 2004; Brandt & Hasinger, 2005). However, most X-ray and mid-IR surveys either have significantly smaller areas and numbers of AGN or are wide-area but substantially shallower than optical surveys (e.g. Schwobe et al., 2000; Lonsdale et al., 2003). Here we present a deep spectroscopic survey of AGN both without the biases of optical selection and over a relatively large field.

The Cosmic Evolution Survey (COSMOS, Scoville et al., 2007)¹ is built upon an HST Treasury project to fully image a 2 deg² equatorial field. The 590 orbits of HST ACS *i*-band observations have been supplemented by observations at wavelengths from radio to X-ray, including deep VLA, Spitzer, CFHT, Subaru (6 broad bands and

¹The COSMOS website is <http://cosmos.astro.caltech.edu/>.

14 narrow bands), GALEX, XMM-Newton, and Chandra data. Here we present a complete spectroscopic survey of XMM-selected AGN in the COSMOS field. Most (601) targets have spectra taken with the IMACS spectrograph (Bigelow et al., 1998) on the Magellan telescope, including 282 spectra previously published by (Trump et al., 2007). An additional 76 X-ray targets were excluded from IMACS observations because they already had SDSS spectra. For 134 of the targets with IMACS coverage, we additionally acquired spectra with the Hectospec spectrograph (Fabricant et al., 2005) on the MMT telescope as ancillary data with extended blue coverage. In total, we were able to target 52% (677/1310) of the available $i_{\text{AB}}^+ < 23.5$ X-ray targets, resulting in 485 high-confidence redshifts. The relevant observing strategies and configurations are described in detail in §2. We were 90% complete in assigning high-confidence redshifts to all spectral types at $i_{\text{AB}}^+ < 22$, with decreasing confidence, dependent on both redshift and spectral type, at fainter magnitudes. The IMACS spectroscopy campaign additionally targeted AGN candidates selected by their radio (VLA, 605 targets) and IR (Spitzer/IRAC, 236 targets) emission, but these objects are not included in this study and will be presented in future work.

We place this work in the context of other large X-ray AGN surveys in Figure 2.1, where the left panel compares the X-ray depth, areal coverage, and number of sources for various X-ray AGN surveys. The right panel of Figure 2.1 shows our flux limits with the customary “AGN locus” (Maccacaro et al., 1988). The depth of XMM-Newton in COSMOS most closely resembles the AEGIS (Davis et al., 2007) survey, with roughly the same number of X-ray targets in both despite their slight differences in area and X-ray depth. There exists no purely optical survey to the depth of our spectroscopy ($i_{\text{AB}}^+ < 23.5$) with this number of spectroscopic redshifts. The AGN spectroscopic campaign presented here is significantly deeper than large optical surveys like the 2dF Quasar Redshift Survey (2dF, Croom et al., 2001) and

the Sloan Digital Sky Survey (SDSS, Schneider et al., 2007). In particular, we present targets ~ 60 times fainter than the main SDSS spectroscopy ($g < 19.1$), and ~ 20 times fainter than the deepest SDSS spectroscopy ($g < 20.2$) for quasars, and our spectroscopy reaches a (arbitrary) quasar/Seyfert boundary of $M_i = -23$ at $z \sim 3$. Surveys like the VIMOS Very Deep Survey (VVDS, Gavignaud et al., 2006) may reach similarly faint magnitudes ($i \lesssim 24$ in VVDS) but have far fewer AGN (130 in VVDS). We additionally note that the Magellan AGN sample will eventually be augmented by ~ 300 X-ray AGN from the faint zCOSMOS survey of galaxy redshifts with VLT/VIMOS (Lilly et al., 2007).

We discuss the analysis of the spectra in §3, including the methods for classifying the AGN and determining redshifts. In §4 we characterize the completeness of the survey and discuss the populations of different AGN types. We use the sample to understand the X-ray AGN population in §5, and we discuss future projects using this dataset in §6. We adopt a cosmology consistent with WMAP results (Spergel et al., 2003) of $h = 0.70$, $\Omega_M = 0.3$, $\Omega_\Lambda = 0.7$.

Throughout the paper we use “unobscured” to describe Type 1 AGN with broad emission lines and “obscured” to describe X-ray AGN where the host galaxy light dominates the optical continuum. Thus we use “obscured AGN” to describe both spectroscopically-defined Type 2 AGN (with narrow emission lines, classified as “nl” or “nla” in the catalog) and XBONGs (X-ray bright, optically normal galaxies, classified as “a” in the catalog, see also Comastri et al., 2002; Rigby et al., 2006; Civano et al., 2007). It is important to note that our designation as “obscured” does not necessarily describe the physical reason for the faint optical nuclear emission: the AGN might simply be under-luminous in the optical instead of being hidden by obscuring material. Indeed, many Type 2 AGN appear to be unobscured in the X-rays (Szokoly et al., 2004), while broad absorption line (BAL) Type 1 AGN are

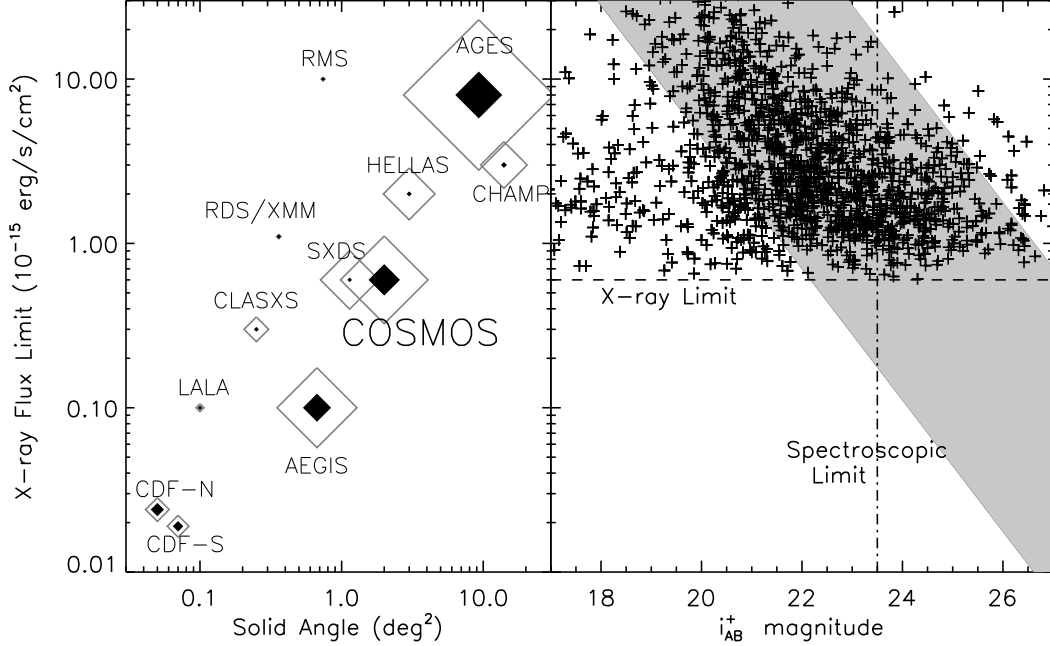


Figure 2.1 The X-ray depth and survey size of various deep X-ray AGN surveys, along with the X-ray and optical flux for targets in COSMOS. At left, symbol sizes indicate each survey’s number of X-ray point sources: open indicate all sources, and filled indicate those with optical spectroscopy. References for the surveys are as follows: AEGIS (Davis et al., 2007), AGES (Brand et al., 2006), CDF-N (Alexander et al., 2003; Barger et al., 2003), CDF-S (Luo et al., 2008), CHAMP (Kim et al., 2004; Green et al., 2004), CLASXS (Yang et al., 2004), HELLAS2XMM (Fiore et al., 2003; Cocchia et al., 2007), LALA (Wang et al., 2004), RDS/XMM (Lehmann et al., 2001), RMS (Hasinger et al., 2005), and SXDS (Ueda et al., 2008). At right, the crosses represent all XMM point sources from Brusa et al. (2010) and the gray shaded area represents the “AGN locus” of $-1 < \log(f_X/f_O) < 1$ (Maccacaro et al., 1988). The COSMOS Chandra data (not presented here) go four times deeper in the central 0.8 deg 2 , doubling the number of COSMOS point sources.

typically X-ray obscured (Brandt, Laor, & Wills, 2000; Gallagher et al., 2006). We also note that even our “obscured” AGN types have moderate X-ray luminosity and we are not sensitive to heavily X-ray obscured (e.g., Compton-thick, $N_H \gtrsim 1 \times 10^{24} \text{ cm}^{-2}$) AGN which are too faint for our XMM-Newton observations.

2.2 Observations

2.2.1 XMM-Newton

The COSMOS field has been observed with XMM-*Newton* for a total of ~ 1.55 Ms at the homogeneous vignetting-corrected depth of ~ 50 ks (Hasinger et al., 2007; Cappelluti et al., 2007, 2009). The final catalog includes 1887 point-like sources detected in at least one of the soft (0.5-2 keV), hard (2-10 keV) or ultra-hard (5-10 keV) bands down to limiting fluxes of 5×10^{-16} , 3.3×10^{-15} , and $5 \times 10^{-15} \text{ erg cm}^{-2} \text{ s}^{-1}$, respectively (see Cappelluti et al., 2007, 2009, for more details). The detection threshold corresponds to a probability $< 4.5 \times 10^{-5}$ that a source is instead a background fluctuation. The XMM fluxes have been computed converting the count-rate into flux assuming a spectral index $\Gamma = 2.0$ and Galactic column density $N_H = 2.5 \times 10^{20} \text{ cm}^2$ for 0.5-2 keV and $\Gamma = 1.7$ and Galactic column density $N_H = 2.5 \times 10^{20} \text{ cm}^2$ for 2-10 keV. Following Brusa et al. (2010), we exclude 24 sources which are a blend of two *Chandra* sources and 26 faint XMM sources coincident with diffuse emission (Finoguenov et al., 2007). We impose a brighter flux limit than the full catalog because the XMM-*Newton* observations were not complete until the 3rd season (2007) of spectroscopic observing. Figure 2.2 shows the X-ray sensitivity for each of the three seasons of IMACS, revealing that the first two seasons (2005-2006) suffer from slightly shallower X-ray catalogs. The sample we use is limited to flux limits of the 50% XMM coverage area, which has only 186 few sources than from the limits of the entire XMM coverage. The sample includes 1651 X-ray sources

detected at fluxes larger than 1×10^{-15} cgs, 6×10^{-15} cgs, 1×10^{-14} cgs, in the 0.5-2 keV, 2-10 keV or 5-10 keV bands, respectively, as presented by Brusa et al. (2010).

Brusa et al. (2010) associated the X-ray point sources with optical counterparts using the likelihood ratio technique to match to the optical, near-infrared (K-band) and mid-infrared (IRAC) photometric catalogs (Capak et al., 2007). The images for the XMM-COSMOS subsample additionally covered by *Chandra* observations were matched to the Chandra/ACIS images by visual inspection (Elvis et al., 2009; Puccetti et al., 2009). We use the COSMOS *Chandra* observations for reliability checks only, since it covers only the central 0.8 deg^2 and is still undergoing basic analyses.

Of the 1651 sources in the XMM-COSMOS catalog described above, 1465 sources have an unique/secure optical counterpart from the multiwavelength analysis with a probability of misidentification of $< 1\%$. For an additional 175 sources, there is a second optical source with a comparable probability to be the correct counterpart. Because the alternate counterpart shows comparable optical to IR properties (and comparable photometric redshifts, Salvato et al., 2009) to the primary counterpart, the primary counterpart can be considered statistically representative of the true counterpart for these 175 X-ray sources, and we include the primary counterparts in the target sample. Eleven sources (outside the Chandra area) remain unidentified because they had no optical or infrared counterparts (i.e., their optical/infrared counterparts were fainter than our photometry). We designated the 1310 optical counterparts with $i_{AB}^+ \leq 23.5$ (from the CFHT) as the X-ray selected targets for the spectroscopic survey.

2.2.2 Magellan/IMACS

The bulk of the spectroscopic data comes from observations with the Inamori Magellan Areal Camera and Spectrograph (IMACS, Bigelow et al., 1998) on the 6.5 m

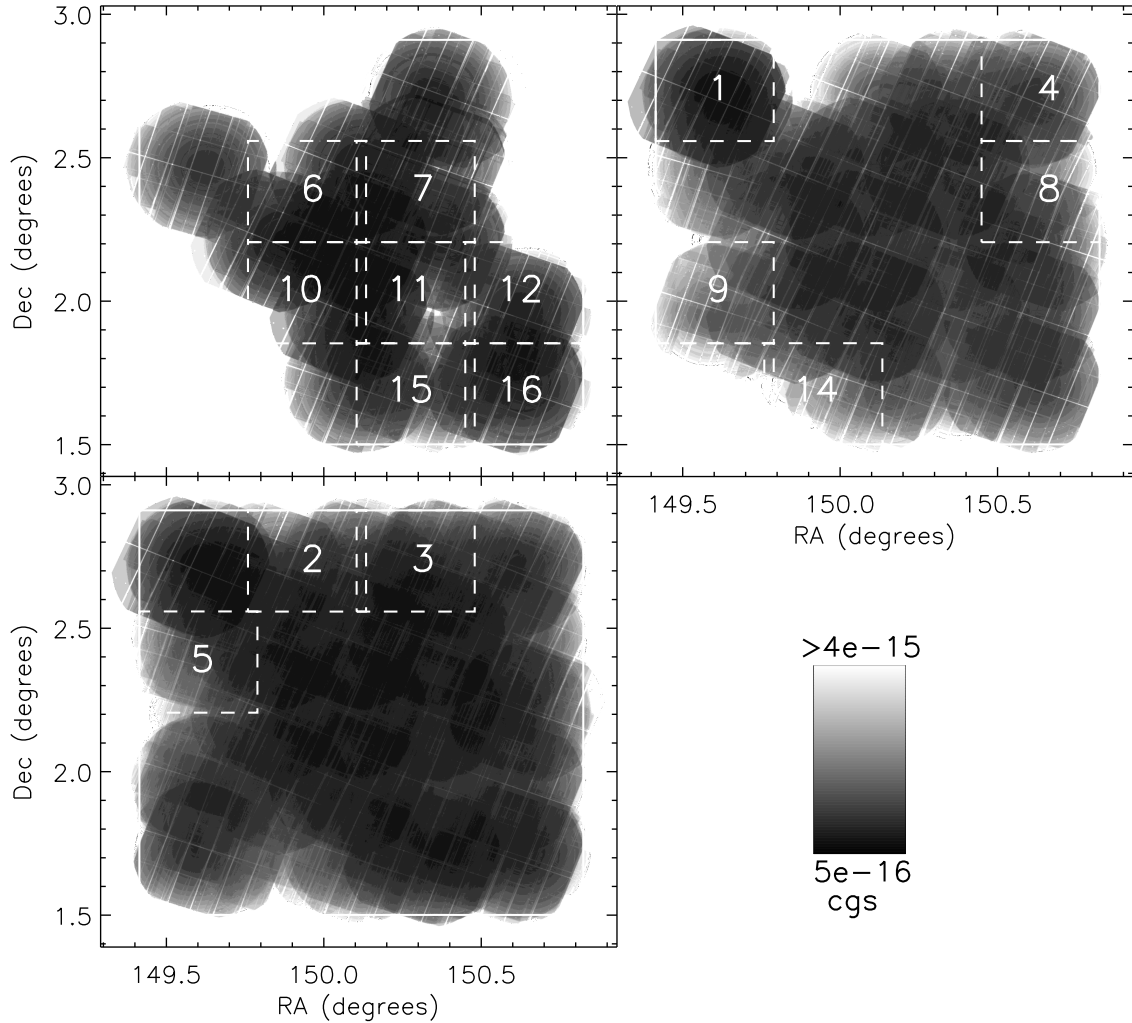


Figure 2.2 Maps of X-ray sensitivity for each of the three years of IMACS observing. The top left panel shows the XMM depth and IMACS pointings for the first year, the top right shows the second year cumulative depth and pointings, and the lower left shows the third year cumulative depth and pointings. Since the XMM observations were ongoing during the spectroscopy campaign, we chose each year's IMACS pointings from the regions of greatest XMM uniformity and depth lacking previous spectroscopic observations.

Magellan/Baade telescope. The IMACS field of view is $22'30'' \times 21'10''$ (with only 10% vignetting at the extreme chip edge), requiring 16 tiled pointings to fully observe the entire 2 deg^2 COSMOS field as shown in Figure 2.3. We observed these 16 pointings over the course of 26 nights (18 clear) through three years, as detailed in Table 2.1. The total exposure time for each pointing is 4-6 hours (shown in Table 2.1 and Figure 2.3). Henceforth we refer to each pointing by its number in Table 2.1 and Figure 2.3. We were able to simultaneously observe 200-400 spectra per mask: generally ~ 40 of these were the X-ray targets described here (shown in the last column of Table 2.1), and the additional slits were ancillary targets to be described in future work. We were generally able to target $\sim 50\%$ of the available $i_{\text{AB}}^+ \leq 23.5$ X-ray targets in each tiled IMACS field, or 601/1310 X-ray targets over the 2 deg^2 .

All IMACS spectra were obtained over the wavelength range of 5600-9200 Å, with the Moon below the horizon and a mean airmass of 1.3. We used the 200 l/mm grism in the first year and a 150 l/mm grism designed and constructed for COSMOS in the second and third years. The lower-resolution 150 l/mm grism had a resolution element of 10 Å. Since all observed broad line AGN had line widths $> 1500 \text{ km s}^{-1}$ and all observed narrow line AGN had line widths $< 1000 \text{ km s}^{-1}$, the resolution of the grism was sufficient to distinguish broad and narrow line AGN. The gain in S/N from 200 l/mm to 150 l/mm was only marginal, but the 150 l/mm grism allowed for a maximum of 400 slits per mask, $\sim 35\%$ more than the maximum 300 slits per mask for the 200 l/mm grism. The slits were $11'' \times 1''$ (55×5 pixels), though only $5''.4 \times 1''$ of the slit was cut, so that an extra adjacent $5''.6$ was reserved as an “uncut region” to accommodate “nod-and-shuffle” observing (see below). We attempted to observe each mask for 5 or more hours, which achieves high completeness of AGN redshifts at $i_{\text{AB}}^+ \simeq 23$, although as Figure 2.3 shows this was not always achieved. We estimate the impact of the nonuniform spectroscopic depth on the sample’s completeness in

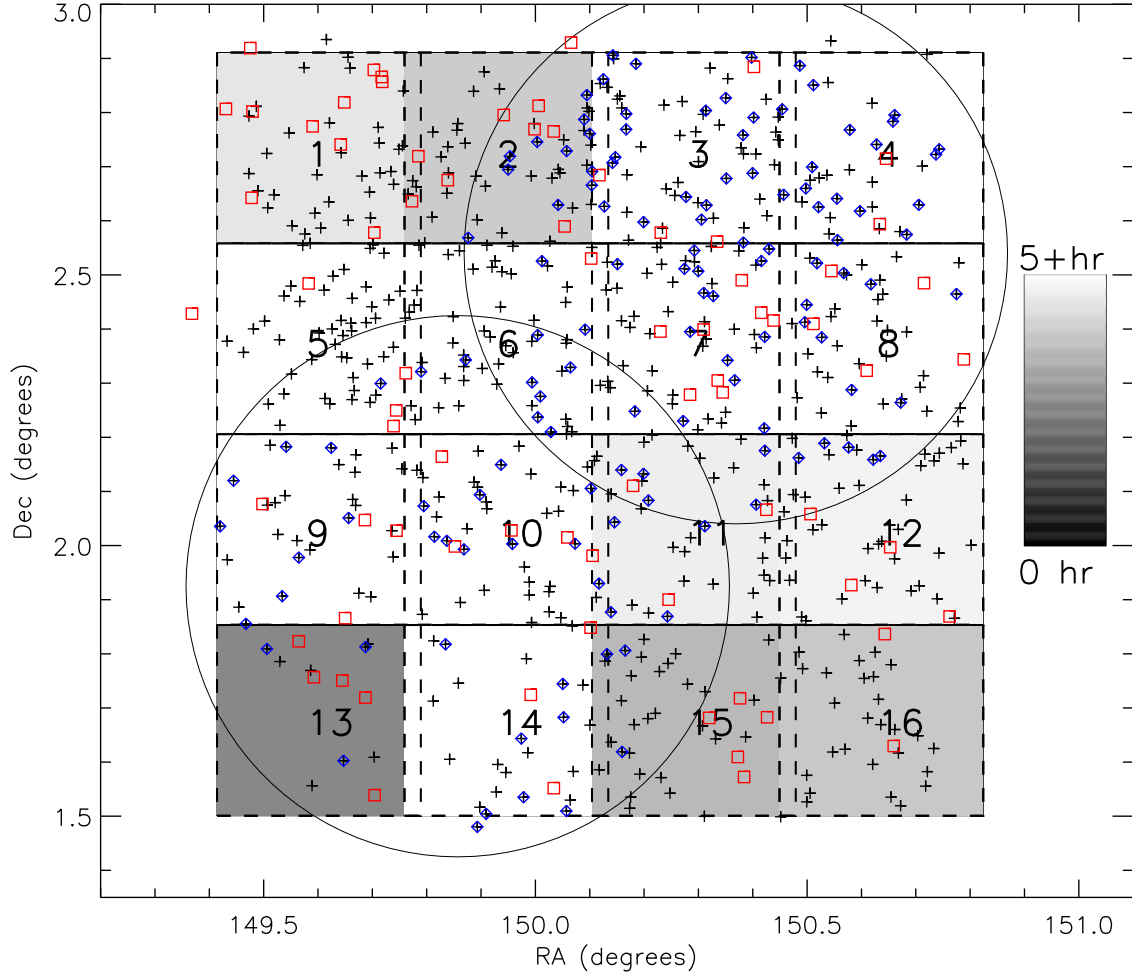


Figure 2.3 Spectroscopic observations of the 2 deg² COSMOS area. X-ray targets with IMACS spectra are shown as crosses, those with MMT spectra are diamonds, and those with SDSS spectra are squares. The 16 tiled IMACS pointings are shown as boxes of 22'30" \times 21'10" and are shaded according to their exposure time. The two 1-deg diameter MMT pointings are shown as circles. COSMOS also includes deeper Chandra coverage, not used here, over the field's central square degree (fields 6, 7, 10, and 11, with portions of the other 8 fields).

Table 2.1. Observation Log of the IMACS Spectroscopy in COSMOS

IMACS Field	Center (J2000)		Observation Year	Exposure (hours)	Number of Spectra
	RA	Dec			
1	09:58:24	02:42:34	2006	4.52	33
2	09:59:48	02:42:30	2007	4.00	46
3	10:01:06	02:42:38	2006,2007 ^a	6.00	75
4	10:02:33	02:42:34	2006	5.33	37
5	09:58:26	02:21:25	2006,2007 ^a	6.00	56
6	09:59:47	02:21:25	2005	6.90	43
7	10:01:10	02:21:25	2005	6.03	48
8	10:02:36	02:21:29	2006	5.10	42
9	09:58:25	02:00:13	2006	5.03	27
10	09:59:47	02:00:17	2005	6.64	35
11	10:01:10	02:00:17	2005	4.67	39
12	10:02:37	02:02:05	2005	4.77	37
13	09:58:24	01:39:08	2006	2.67	7
14	09:59:47	01:39:08	2006	5.33	23
15	10:01:10	01:39:08	2005	3.63	25
16	10:02:33	01:39:08	2005	3.93	28

^aFields 3 and 5 were observed for one hour in 2006 and five hours in 2007, for six total hours of exposure.

§4.1.

We observed using the “nod-and-shuffle” technique, which allowed for sky subtraction and fringe removal in the red up to an order of magnitude more precisely than conventional methods. The general principles of nod-and-shuffle are described by Glazebrook & Bland-Hawthorn (2001), and our approach is detailed in Appendix 1 of Abraham et al. (2004). Briefly, we began observing with the target objects offset from the vertical center of the cut region, $1/3$ of the way from the bottom to the top (that is, $1''8$ from the bottom slit edge, and $3''6$ from the top edge of the cut region and the cut/uncut boundary). After 60 seconds we closed the shutter, noded the telescope by $1''8$ (9 pixels) along the slit, and shuffled the charge to the reserved uncut region. The object was then observed for 60 seconds in the new position, $2/3$ of the way from the bottom to the top of the cut region ($3''6$ from the bottom and $1''8$ from the top). We then closed the shutter, noded back to the original position, and shuffled the charge back onto the cut region on the mask. This cycle was repeated (typically 15-20 times) with the net result that the sky and object had been observed for equal amounts of time on identical pixels on the CCD. Nod-and-shuffle worked well while the seeing was $\lesssim 1''$, which was true for all observations.

To extract and sky-subtract individual 2D linear IMACS spectra, we used the publicly available Carnegie Observatories System for MultiObject Spectroscopy (with coincidentally the acronym “COSMOS,” written by A. Oemler, K. Clardy, D. Kelson, and G. Walth and publicly available at <http://www.ociw.edu/Code/cosmos>). We combined the two nod positions in the nod-and-shuffle data, then co-added the individual 2D exposures of each pointing while rejecting cosmic rays as 4.5σ outliers from the mean of the individual exposures. Wavelength calibration was performed using an He/Ne/Ar arc lamp exposure in each slit. The 2D spectra were extracted to 1D flux-calibrated spectra using our own IDL software, adapted from the `ispec2d`

package (Moustakas & Kennicutt, 2006). While flux calibration used only a single standard star at the center of the IMACS detector, we estimate by eye that vignetting has $< 10\%$ effect on the spectral shape or throughput across the field, in agreement with the predictions of the IMACS manual.

IMACS spectra can be contaminated or compromised in several ways, including 0th and 2nd order lines from other spectra, bad pixels and columns, chip gaps, poorly machined slits, and cosmic rays missed during co-adding. To eliminate these artifacts, we generated bad pixel masks for all 1D spectra by visual inspection of the calibrated 1D and 2D data. The nod-and-shuffle 2D data were especially useful for artifact rejection: any feature appearing in only one of the two nod positions is clearly an artifact. Pixels designated as bad in the mask were ignored in all subsequent analyses.

We show 10 examples of IMACS spectra in Figures 2.4 and 2.5. These spectra are representative of the targets in the survey. Each of these spectra are smoothed by the 5-pixel resolution element. We discuss each object below, with the spectral classification, confidences, and redshift algorithms detailed in §3. Briefly, $z_{\text{conf}} = 3, 4$ refer to high confidence and $z_{\text{conf}} = 1, 2$ are lower confidence guesses (but see also §3.1 for the subtleties in confidence assignment). All spectra are publicly available on the COSMOS IRSA server (<http://irsa.ipac.caltech.edu/data/COSMOS/>).

1. COSMOS J095909.53+021916.5, $i_{\text{AB}}^+ = 20.05$, $z = 0.38$, $z_{\text{conf}} = 4$: This is a low redshift Type 1 Seyfert. The emission lines are bright and easily identified.
2. COSMOS J095752.17+015120.1, $i_{\text{AB}}^+ = 21.00$, $z = 4.17$, $z_{\text{conf}} = 4$: This is a high redshift Type 1 quasar. $\text{Ly}\alpha$ is especially prominent along other broad emission features, and so this redshift is very reliable.
3. COSMOS J095836.69+022049.0, $i_{\text{AB}}^+ = 23.04$, $z = 1.19$, $z_{\text{conf}} = 4$: We classify

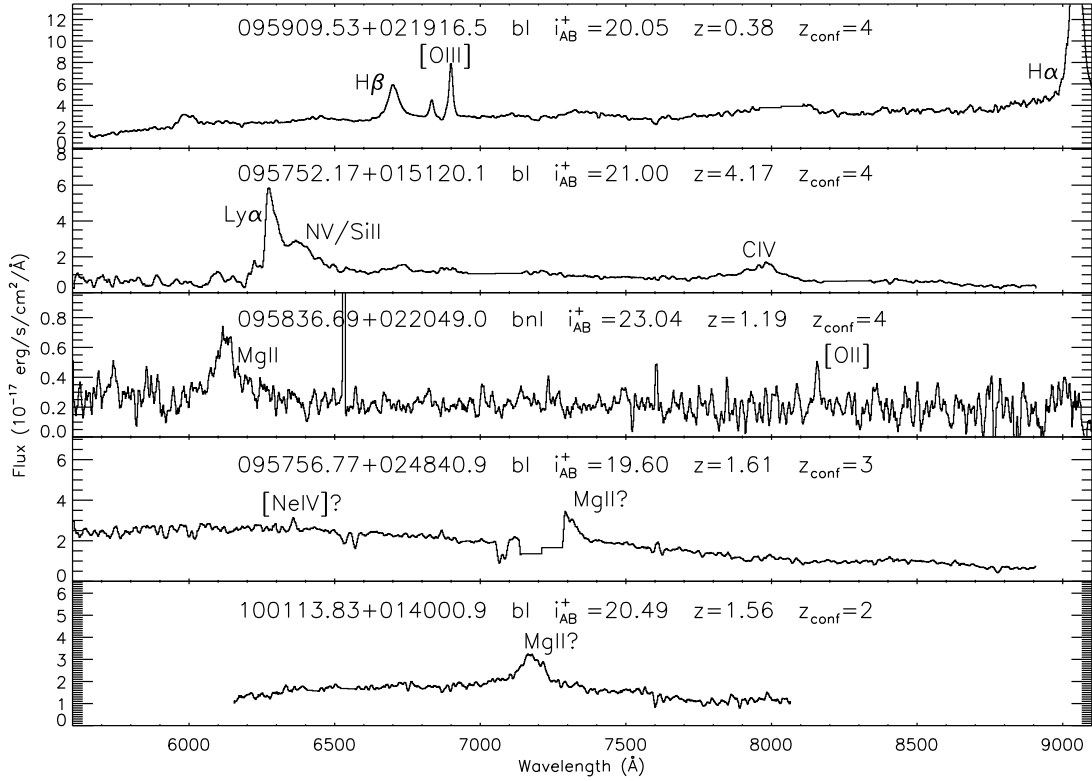


Figure 2.4 Five examples of IMACS spectra with broad emission lines. The dominant line species are labeled in each spectrum and bad pixels are omitted. The first two objects are Type 1 AGN (“bl”) with the highest redshift confidences, the third is a high-confidence AGN with both narrow and broad emission (“bnl”), and the bottom two are Type 1 AGN (“bl”) with uncertain redshifts. We discuss these objects in §2.2.

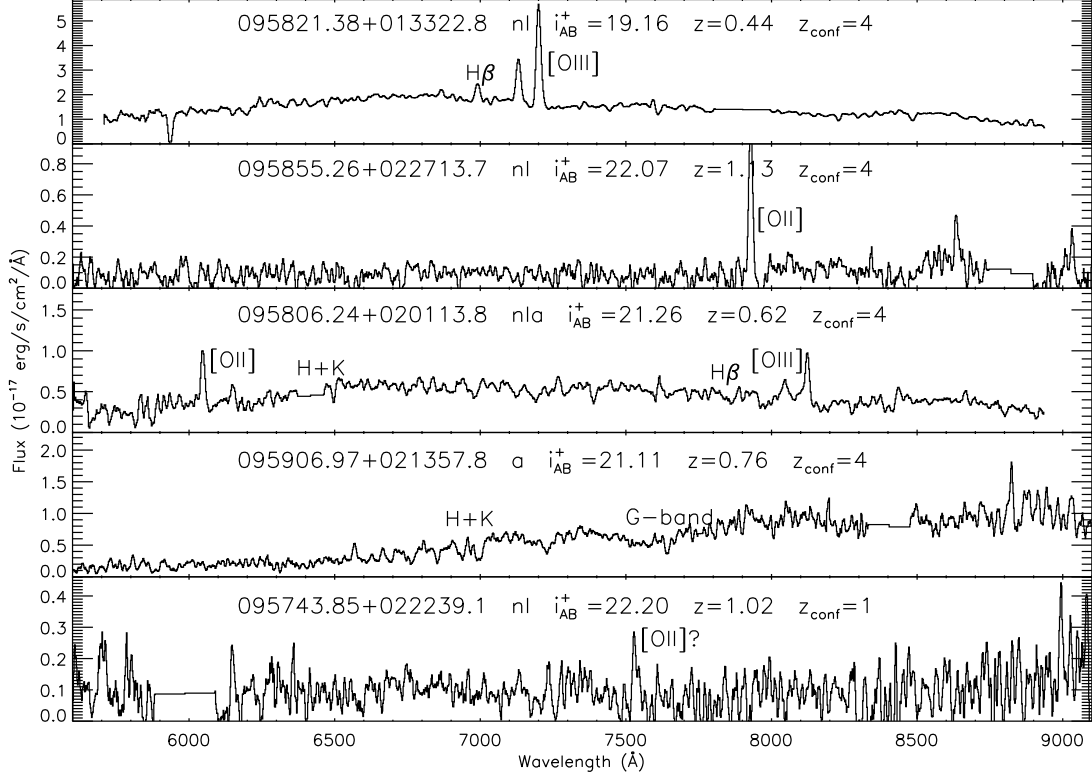


Figure 2.5 Five more examples of IMACS spectra, including four targets with narrow emission lines and one absorption line galaxy. The prominent absorption and emission features are labeled. The third target is a hybrid “nIa” object with both narrow emission and absorption lines. The first four objects have the highest redshift confidence, while the bottom target has an extremely uncertain redshift, calculated from a single emission line which may be solely due to noise. The first is a starburst galaxy by its X-ray emission, while the second, third, and fourth spectra are all AGN which meet both of the X-ray criteria of §3.2. We discuss these objects in §2.2.

this target as a hybrid “bnl” object with both broad and narrow emission lines. The narrow [O II] line is evident above the noise and strong broad Mg II is also present.

4. COSMOS J095756.77+024840.9, $i_{\text{AB}}^+ = 19.60$, $z = 1.61$, $z_{\text{conf}} = 3$: In this spectrum, a broad emission line is cut off by a detector chip gap. Identifying the broad feature as Mg II and the minor narrow emission line at $\sim 6375 \text{ \AA}$ as [N IV] yields a good redshift, but we assign only $z_{\text{conf}} = 3$ because of the uncertainty from the chip gap position.
5. COSMOS J100113.83+014000.9, $i_{\text{AB}}^+ = 20.49$, $z = 1.56$, $z_{\text{conf}} = 2$: The blue end of this spectrum lies on a chip gap, and much of the red end is corrupted by second order features from another bright spectrum on the mask. Only one broad emission line is present, and so while the target is clearly a Type 1 AGN, the line could be either C III] or Mg II. The redshift solution is degenerate and we assign only $z_{\text{conf}} = 2$.
6. COSMOS J095821.38+013322.8, $i_{\text{AB}}^+ = 19.16$, $z = 0.44$, $z_{\text{conf}} = 4$: This spectrum contains several bright emission lines, and is clearly identified as a “nl” class object. This object has $L_{0.5-10 \text{ keV}} < 3 \times 10^{42}$ and $-2 \leq \log f_X/f_O \leq -1$, and it is probably a starburst galaxy (see §3.2 for our distinction between AGN and starbursts).
7. COSMOS J095855.26+022713.7, $i_{\text{AB}}^+ = 22.07$, $z = 1.13$, $z_{\text{conf}} = 4$: This narrow emission line spectrum is faint, but the [O II] emission feature has a strong signal above the noisy continuum. We assign this spectrum $z_{\text{conf}} = 4$ because there is no other plausible redshift solution for a single bright narrow emission line. The 2D spectrum (not shown) also reveals the emission feature in both

noded positions, confirming that it is not a noise spike. This object is a Type 2 AGN with both $L_{0.5-10 \text{ keV}} > 3 \times 10^{42} \text{ erg s}^{-1}$ and $\log f_X/f_O \geq -1$.

8. COSMOS J095806.24+020113.8, $i_{\text{AB}}^+ = 21.26$, $z = 0.62$, $z_{\text{conf}} = 4$: We identify this spectrum as a hybrid “nla” object, since it has both narrow emission lines and the absorption lines of an early-type galaxy. $\text{H}\beta$ is present only in absorption, and while half of the H+K doublet is on a masked-out region, the other line is present.
9. COSMOS J095906.97+021357.8, $i_{\text{AB}}^+ = 21.11$, $z = 0.76$, $z_{\text{conf}} = 4$: This spectrum exhibits only absorption lines and is classified as an early-type galaxy. The continuum shape and H+K doublet make assigning redshifts to these targets straightforward. This object meets both of the X-ray emission criteria of §3.2 and is an optically obscured AGN.
10. COSMOS J095743.85+022239.1, $i_{\text{AB}}^+ = 22.20$, $z = 1.02$, $z_{\text{conf}} = 1$: This spectrum is quite noisy. The single narrow line may be [O II], but it is not strong enough above the noise to reliably classify. Because its entire identification may be a result of noise, we designate this target as $z_{\text{conf}} = 1$.

2.2.3 MMT/Hectospec

We also obtained ancillary spectroscopic data using the Hectospec fiber-fed spectrograph (Fabricant et al., 2005) on the 6.5 m MMT telescope. The field of view for Hectospec is a 1 deg diameter circle, and in March 2007 the COSMOS field was observed with two pointings of 3 hours each, as shown in Figure 2.3. These pointings contained a total of 134 targets to $i_{\text{AB}}^+ < 23.5$ in $2.5''$ fibers. We observed with the 270 l/mm grism over a wavelength coverage of 3800-9200Å, resulting in a resolution of 3Å. Because Hectospec is fiber-fed and the MMT has a brighter sky and generally poorer seeing than Magellan, MMT/Hectospec cannot reach targets as faint as

those reached by Magellan/IMACS. Therefore we use Hectospec observations only as ancillary data on targets which already have IMACS spectra.

The MMT/Hectospec observations were designed primarily to double-check the redshifts derived from IMACS spectra by adding the bluer 3800-5600Å wavelength band. Figure 2.6 shows the observed peak wavelength with redshift for the strong broad emission line in Type 1 AGN. With IMACS, the limited red wavelength range means that broad line AGN at $0.4 < z < 1.9$ and $2.3 < z < 2.9$ will have only one observed broad line, as shaded in the figure. These potentially ambiguous redshifts can be resolved using the Hectospec spectra. Even for targets with non-ambiguous redshifts, the extended wavelength coverage allows for consistency checks and additional line measurements.

In Figure 2.7 we show two objects where a high-confidence redshift could be assigned only after Hectospec spectra were additionally taken. The first of these, 095801.45+014832.9, was assigned $z_{\text{conf}} = 2$ and an incorrect redshift of 1.3 before the Hectospec data allowed us to correctly resolve the degeneracy and assign $z_{\text{conf}} = 4$. The second object, 100149.00+024821.8, had been assigned the correct redshift from its IMACS spectrum but only $z_{\text{conf}} = 2$, and the Hectospec data confirmed the otherwise uncertain solution and allowed us to assign $z_{\text{conf}} = 4$. In general, the additional Hectospec spectra revealed that we were $\sim 75\%$ accurate in assigning redshifts to IMACS spectra with degenerate redshift solutions. (We were better than the 50% chance probability because we were occasionally able to fit to minor features, e.g. FeII/III complexes, weak narrow lines like [O II] and [N IV], or general continuum shape.)

We reduced the Hectospec data into 1D linear spectra with sky subtraction, flux calibration, and cosmic ray rejection using the publicly available HSRED software

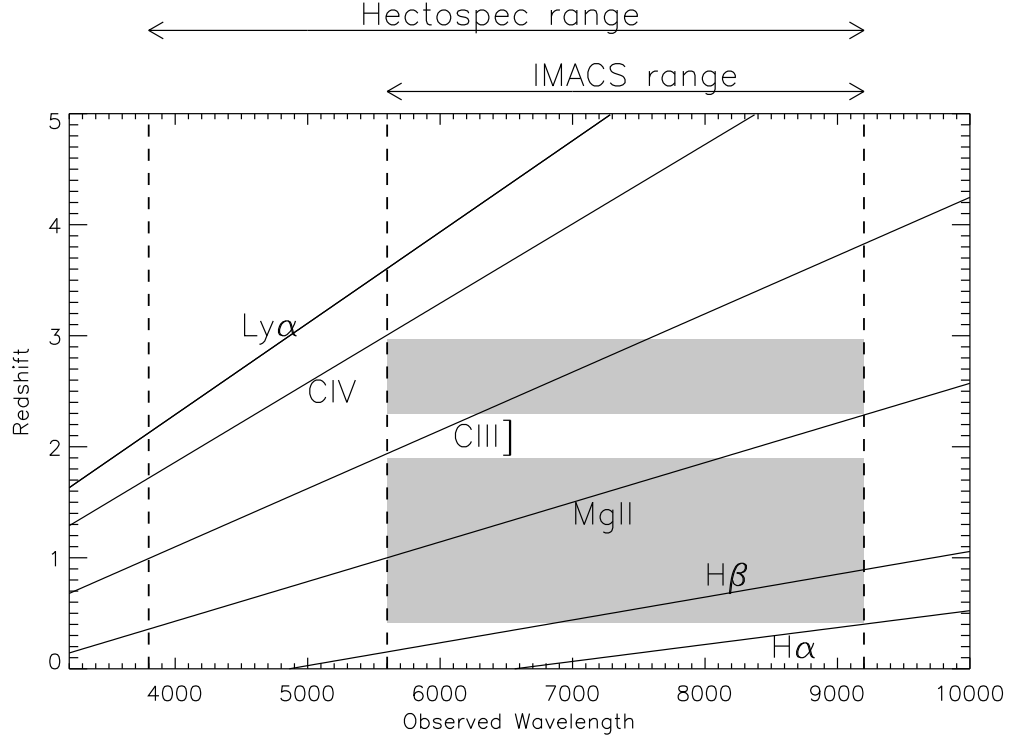


Figure 2.6 The observed wavelengths of prominent broad emission lines with redshift. The spectral ranges of MMT/Hectospec and Magellan/IMACS are shown at the top. The broad emission lines observed at a given redshift can be found by drawing a horizontal line between the wavelength limits: the solid lines of broad emission peak intersecting that redshift line would be present in the spectrum. The narrow wavelength coverage of IMACS means that only one broad line is present in the shaded redshift ranges $0.4 < z < 1.9$ and $2.3 < z < 2.9$, so that spectra with low S/N may be assigned $z_{\text{conf}} = 2$ because they have degenerate redshift solutions. The extended wavelength coverage of Hectospec allows us to resolve the degeneracies and assign $z_{\text{conf}} = 4$.

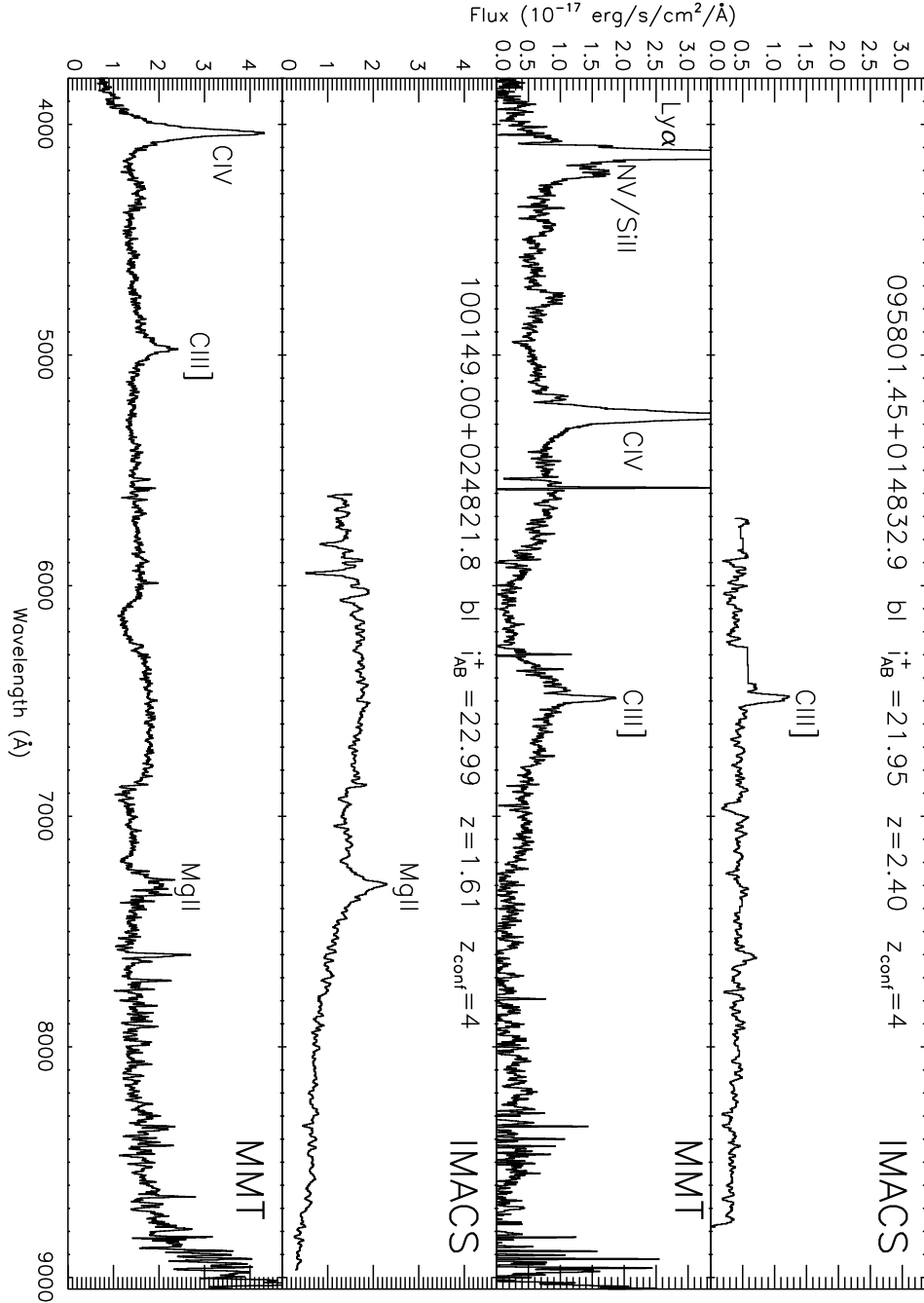


Figure 2.7 Two X-ray targets with both IMACS and Hectospec spectra. In both cases, the IMACS wavelength range only includes one broad emission line and so has a degenerate redshift solution. The additional blue Hectospec coverage resolves the degeneracy and allows us to assign these objects $z_{\text{conf}} = 4$. The fourth panel shows that our Hectospec flux calibration can cause errors in spectral shape at red wavelengths, although this does not affect our redshift solutions.

(written by R. Cool). We also used HSRED to apply an artificial flux calibration to correct the spectral shape, then flux calibrated the spectra using a mean correction from objects with both Hectospec and IMACS data. From the resultant spectral shape we estimate that this technique has flux errors in the blue and red ends of the spectra as large as $\sim 20\%$. Since the analyses are limited to finding redshifts and performing simple line width measurements, errors of this magnitude are acceptable.

2.2.4 SDSS

We include 76 XMM X-ray sources with spectra previously taken as part of the Sloan Digital Sky Survey (SDSS, York et al., 2000). With redshifts already known, these targets were excluded from the main IMACS survey. These objects were selected using the publicly available SDSS Catalog Archive Server (<http://cas.sdss.org/astro/>), which uses the SDSS Data Release 6 (Adelman-McCarthy et al., 2008). Their wavelength coverage is 3800-9200Å and they have a resolution of 3Å. All the SDSS targets are uniformly bright, with $i_{AB}^+ \lesssim 21$, and so they would certainly have been successfully observed with IMACS had their redshifts not been previously known. Including these SDSS targets does not introduce any new incompleteness or complication to the sample.

2.3 Spectral Analysis

Our program as described above is largely motivated as an AGN redshift survey. We especially seek Type 1, Type 2, and optically-obscured (host-dominated AGN), though we also find a small contaminant fraction of local stars and star-forming galaxies. We attempt to separate the population of obscured AGN from star-forming and quiescent galaxies using X-ray and optical color diagnostics. Chapter 3 (see also Trump et al., 2009b) presents basic line measurements and estimates of black hole mass for the Type 1 AGN.

2.3.1 AGN Classification

We used three composite spectra from the Sloan Digital Sky Survey (SDSS, York et al., 2000) as templates for classifying the objects and determining their redshifts: a Type 1 (broad emission line) AGN composite from 2204 sources (Vanden Berk et al., 2001), a Type 2 (narrow emission line) AGN composite from 291 sources (Zakamska et al., 2003), and a red galaxy composite from 965 sources (Eisenstein et al., 2001). The three template spectra are shown in Figure 2.8. We found that the Type 2 AGN composite gave accurate redshifts for both star-forming galaxies and AGN with narrow emission lines. The red galaxy template was likewise accurate for a variety of absorption line galaxies, ranging from old stellar systems with strong 4000Å breaks to post-starburst galaxies. Objects showing a mixture of narrow emission lines and red galaxy continuum shape and absorption features were classified as hybrid objects. We did not use a particular template for local stars, but stars ranging in temperature from O/B to M types were easily visually identified.

To calculate redshifts we used a cross-correlation redshift IDL algorithm in the publicly available `idlspec2d` package written by D. Schlegel². This algorithm used a visually-chosen template to find a best-fit redshift and its associated 1σ error. As discussed in §2.2, all masked-out regions were ignored in the redshift determination. Note that the redshift error returned is probably underestimated for objects with lines shifted from the rest frame with respect to each other, as is often the case between high-ionization (e.g. C IV) and low-ionization (e.g. Mg II) broad emission lines in Type 1 AGN (Sulentic et al., 2000). We manually assigned redshift errors for 6% (41/677) of objects where the cross-correlation algorithm failed but we were able to visually assign a best-fit redshift.

Each object was assigned a redshift confidence according to the ability of the

²publicly available at http://spectro.princeton.edu/idlspec2d_install.html

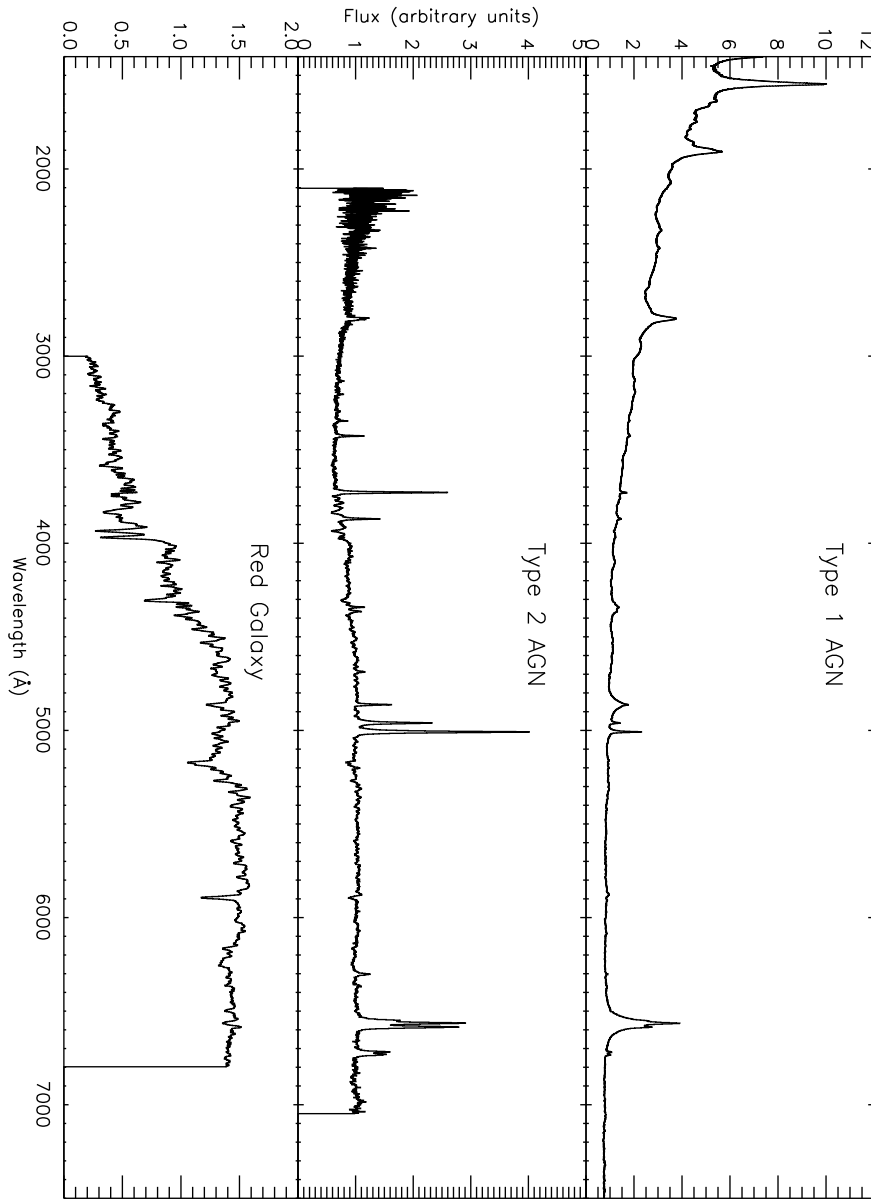


Figure 2.8 The three templates used in the classification and redshift determination scheme. The broad line AGN template is the SDSS quasar composite of Vanden Berk et al. (2001), the narrow emission line template is the SDSS Type II AGN composite of Zakamska et al. (2003), and the absorption line red galaxy template is the composite of the SDSS red galaxy sample (Eisenstein et al., 2001). The wavelength coverages of the templates were sufficient for the entire redshift range (and the corresponding observed wavelength ranges) of the sample.

redshifted template to fit the emission lines, absorption lines, and continuum of the object spectrum. If at least two emission or absorption lines were fit well, or if at least one line and the minor continuum features were fit unambiguously, the redshift was considered at least 90% confident and assigned $z_{\text{conf}} = 4$ (64% of objects). Objects of $z_{\text{conf}} = 3$ (8% of objects) have only one strong line feature with a continuum or second less certain feature that make their assigned redshift likely but not as assured. We assign $z_{\text{conf}} = 2$ (8% of objects) when the spectrum exhibits only one broad or narrow feature and the calculated redshift is degenerate with another solution. Objects of $z_{\text{conf}} = 1$ (5% of objects) are little more than guesses, where a sole feature is present but has little signal over the noise, such that even the spectral type classification is uncertain. (It is notable, however, that the nod and shuffle observations helped to resolve real features from noise, since real features must occupy both noddled positions on the CCD.) If the signal-to-noise of the object spectrum was too low for even a guess at the redshift or spectral type, it was assigned $z_{\text{conf}} = 0$ (13% of objects). We additionally assign $z_{\text{conf}} = -1$ to 13 targets with "broken" slits, severely contaminated by second order lines or mask cutting errors. In total, we were unable to assign redshifts for 15% of targets. Duplicate observations with IMACS and Hectospec indicate that redshift confidences of 4, 3, 2, and 1 correspond to correct redshift likelihoods of 97%, 90%, 75%, and 33%, respectively. These duplicate observations are mainly estimated for brighter targets, however, and so the true likelihoods may be slightly lower. In total, we were able to classify 573 spectra with $z_{\text{conf}} > 0$ and we designate the 485 spectra with $z_{\text{conf}} = 3, 4$ as "high-confidence" objects. We discuss individual targets spanning the classification types and confidence levels in §2.2 and shown in Figures 2.4 and 2.5.

All of the objects observed in the sample are presented in Table 2.2. The classifications are as follows: "bl" for broad emission line objects (Type 1 AGN), "bnl"

for objects with both broad and narrow emission (possibly Type 1.5-1.9 AGN), “nl” for narrow emission line objects (Type 2 AGN and star-forming galaxies), “a” for absorption line galaxies, “nla” for narrow emission and absorption line galaxy hybrids, and “star” for stars (of varied spectral type). We further classify narrow emission and absorption line spectra as AGN or inactive in §3.2 below. In total, 50% (288/573) of the classified targets were designated “bl” or “bnl,” 30% (171/573) were “nl” or “nla,” 16% (92/573) were “a,” and the remaining 4% (22/573) were stars. Objects with a question mark under “Type” in Table 2.2 have too low signal-to-noise to venture a classification, although many of these objects are unlikely to be Type 1 or 2 AGN for reasons we discuss in §4. As mentioned above, objects with $z_{\text{conf}} = 1$ may be incorrectly classified.

Table 2.2. COSMOS XMM Optical Spectroscopy Catalog

Object Name	RA (J2000) ^a	Dec (J2000)	i_{CFHT}^+	S/N	t_{exp}	Type	z	σ_z	z_{conf}^b
	degrees	degrees	AB mag		sec				
SDSS J095728.34+022542.2	149.3680700	2.4283800	19.64	7.00	0	bl	1.5356	0.0015	4
COSMOS J095740.78+020207.9	149.4199229	2.0355304	21.55	17.92	19200	bl	1.4800	0.0028	4
SDSS J095743.33+024823.8	149.4305400	2.8066200	20.43	3.37	0	bl	1.3588	0.0020	4
COSMOS J095743.85+022239.1	149.4327000	2.3775230	23.40	1.33	18000	nl	1.0192	0.0002	1
COSMOS J095743.95+015825.6	149.4331452	1.9737751	21.91	1.54	19200	a	0.4856	0.0030	1
COSMOS J095746.71+020711.8	149.4446179	2.1199407	20.78	11.37	19200	bl	0.9855	0.0002	4
COSMOS J095749.02+015310.1	149.4542638	1.8861407	20.36	13.68	19200	nla	0.3187	0.0002	4
COSMOS J095751.08+022124.6	149.4628491	2.3568402	20.73	9.38	3600	bl	1.1714	0.0004	2
COSMOS J095752.17+015120.1	149.4673623	1.8555716	21.08	7.31	19200	bl	4.1744	0.0005	4
COSMOS J095753.44+024114.2	149.4726733	2.6872864	22.18	0.95	11160	bl	2.3100	0.0169	1
COSMOS J095753.49+024736.1	149.4728835	2.7933716	21.96	4.76	11160	bl	3.6095	0.0128	4
SDSS J095754.11+025508.4	149.4754500	2.9189900	19.45	6.09	0	bl	1.5688	0.0022	4
SDSS J095754.70+023832.9	149.4779200	2.6424700	19.35	8.04	0	bl	1.6004	0.0015	4
SDSS J095755.08+024806.6	149.4795000	2.8018400	19.41	8.66	0	bl	1.1108	0.0017	4
COSMOS J095755.48+022401.1	149.4811514	2.4003076	21.26	19.89	18000	bl	3.1033	0.0003	4

Table 2.2—Continued

Object Name	RA (J2000) ^a	Dec (J2000)	i_{CFHT}^+	S/N	t_{exp}	Type	z	σ_z	z_{conf}^b
	degrees	degrees	AB mag		sec				
COSMOS J095756.77+024840.9	149.4865392	2.8113728	20.81	11.86	11160	bl	1.6133	0.0098	3
COSMOS J095757.50+023920.1	149.4895683	2.6555795	20.30	11.17	11160	nl	0.4674	0.0002	2
SDSS J095759.50+020436.1	149.4979100	2.0766900	18.98	14.57	0	bl	2.0302	0.0016	4
COSMOS J095800.41+022452.5	149.5017000	2.4145710	22.57	3.53	18000	bnl	1.4055	0.0001	4
COSMOS J095801.34+024327.9	149.5055777	2.7244216	20.66	9.67	11160	nla	0.3950	0.0010	1
COSMOS J095801.45+014832.9	149.5060326	1.8091427	21.96	1.79	9600	bl	2.3995	0.0002	4
COSMOS J095801.61+020428.9	149.5067217	2.0746879	22.18	5.46	19200	bl	1.2260	0.0076	1
COSMOS J095801.78+023726.2	149.5074058	2.6239318	17.79	52.98	11160	star	0.0000	0.0000	4
COSMOS J095802.10+021541.0	149.5087524	2.2613900	21.01	3.75	3600	a	0.9431	0.0050	3
COSMOS J095802.88+021106.8	149.5119900	2.1852350	17.54	44.01	18000	star	0.0000	0.0000	4
COSMOS J095804.59+023852.5	149.5191398	2.6479234	22.19	3.44	11160	?	-1.0000	-1.0000	0
COSMOS J095805.10+020445.8	149.5212597	2.0793906	20.75	7.11	19200	nl	0.6741	0.0002	4
COSMOS J095806.24+020113.8	149.5260099	2.0204918	21.26	6.55	19200	nla	0.6218	0.0002	4
COSMOS J095806.99+022248.5	149.5291045	2.3801349	20.89	10.27	3600	bl	3.1042	0.0226	4
COSMOS J095807.16+014708.5	149.5298156	1.7856946	23.26	0.81	9600	nl	1.1135	0.0023	2

Table 2.2—Continued

Object Name	RA (J2000) ^a	Dec (J2000)	i_{CFHT}^+	S/N	t_{exp}	Type	z	σ_z	z_{conf}^b
	degrees	degrees	AB mag		sec				
COSMOS J095807.22+021319.5	149.5300752	2.2220897	22.65	0.80	3600	bl	2.3610	0.0070	2
COSMOS J095808.18+015423.6	149.5340925	1.9065490	22.54	4.60	19200	bl	2.5065	0.0004	4
COSMOS J095808.90+021648.6	149.5370789	2.2801691	23.17	1.72	18000	bl	1.7017	0.0009	3
COSMOS J095808.98+022739.9	149.5374200	2.4610750	21.62	8.16	18000	a	0.8450	-5.0000	3
COSMOS J095809.45+020532.4	149.5393893	2.0923305	20.80	7.73	19200	a	0.6065	0.0008	3
COSMOS J095809.93+021057.7	149.5413655	2.1827083	21.42	6.27	19200	bl	0.8376	0.0003	4
COSMOS J095811.23+024544.0	149.5467786	2.7622244	22.22	0.01	11160	?	-1.0000	-1.0000	0
COSMOS J095812.01+022845.9	149.5500380	2.4794133	23.32	20.85	3600	?	-1.0000	-1.0000	-1
COSMOS J095812.26+021900.8	149.5510731	2.3169025	22.37	4.60	18000	a	1.0984	0.0001	4
COSMOS J095812.58+023526.8	149.5524223	2.5907771	21.49	3.72	11160	nl	1.0052	0.0011	3
COSMOS J095814.71+020033.0	149.5612764	2.0091581	22.70	0.43	19200	?	-1.0000	-1.0000	0
SDSS J095815.50+014923.2	149.5646000	1.8231100	20.25	4.19	0	bl	1.5095	0.0021	4
COSMOS J095815.53+015840.5	149.5647095	1.9779045	21.51	11.48	19200	bl	1.6793	0.0003	4
COSMOS J095815.93+022703.5	149.5663700	2.4509590	17.59	39.24	18000	star	0.0000	0.0000	4
COSMOS J095817.26+023316.2	149.5719000	2.5545040	22.80	3.09	18000	bl	1.5737	0.0005	3

Table 2.2—Continued

Object Name	RA (J2000) ^a	Dec (J2000)	i_{CFHT}^+	S/N	t_{exp}	Type	z	σ_z	z_{conf}^b
	degrees	degrees	AB mag		sec				
COSMOS J095817.86+025258.7	149.5744287	2.8829696	23.44	0.01	11160	?	-1.0000	-1.0000	0
COSMOS J095818.15+023432.4	149.5756384	2.5756578	21.94	8.01	18000	bl	1.1640	0.0003	4
SDSS J095819.88+022903.6	149.5828300	2.4843300	18.19	8.84	11160	bl	0.3448	0.0001	4
COSMOS J095820.44+015931.0	149.5851825	1.9919575	23.09	0.14	19200	nl	0.9829	0.0011	3
COSMOS J095820.57+023330.1	149.5857040	2.5583491	21.51	1.18	18000	a	0.9606	0.0002	4
COSMOS J095820.74+014609.5	149.5864100	1.7693190	21.77	3.21	9600	nl	0.7847	0.0006	4
COSMOS J095821.23+022036.6	149.5884400	2.3434930	23.19	0.89	18000	?	-1.0000	-1.0000	0
COSMOS J095821.38+013322.8	149.5890800	1.5563250	19.16	15.89	9600	nl	0.4379	0.0001	4
SDSS J095821.65+024628.2	149.5901900	2.7744900	19.25	7.22	11160	bl	1.4031	0.0020	4
SDSS J095822.19+014524.3	149.5924500	1.7567600	17.78	24.64	9600	bl	1.9612	0.0001	4
COSMOS J095822.60+023650.6	149.5941837	2.6140550	23.24	0.01	11160	?	-1.0000	-1.0000	0
COSMOS J095823.56+024106.1	149.5981640	2.6850163	23.09	0.27	11160	?	-1.0000	-1.0000	0
COSMOS J095824.50+022333.6	149.6020634	2.3926747	20.00	31.86	3600	bl	1.8540	0.0108	4
COSMOS J095825.18+023511.8	149.6049200	2.5866010	20.87	2.33	11160	?	-1.0000	-1.0000	0
COSMOS J095826.68+022818.0	149.6111763	2.4716724	21.35	7.25	3600	nl	0.6910	0.0038	4

Table 2.2—Continued

Object Name	RA (J2000) ^a degrees	Dec (J2000) degrees	i_{CFHT}^+ AB mag	S/N	t_{exp} sec	Type	z	σ_z	z_{conf}^b
COSMOS J095827.05+021618.3	149.6127100	2.2717390	20.78	11.20	18000	?	-1.0000	-1.0000	-1
COSMOS J095827.71+025605.5	149.6154525	2.9348540	19.72	6.74	11160	nla	0.4890	0.0004	4
COSMOS J095828.77+023805.4	149.6198659	2.6348327	16.05	111.82	11160	?	-1.0000	-1.0000	0
COSMOS J095829.06+024651.3	149.6210999	2.7809181	21.50	1.01	11160	?	-1.0000	-1.0000	0
COSMOS J095829.21+021542.8	149.6217107	2.2618797	20.68	10.36	3600	nl	0.5368	0.0032	1
COSMOS J095829.83+021050.4	149.6242820	2.1806560	20.66	14.76	18000	bl	1.1856	0.0001	4
COSMOS J095830.25+022400.8	149.6260400	2.4002240	21.57	5.51	18000	a	0.8451	0.0001	4
COSMOS J095830.62+022951.7	149.6275951	2.4976827	17.40	63.99	11160	star	0.0000	0.0000	4
COSMOS J095831.63+022218.2	149.6317739	2.3717233	22.98	13.20	18000	bl	0.9297	0.0002	4
COSMOS J095833.17+020858.5	149.6382184	2.1495852	22.58	1.68	19200	nl	0.9521	0.0005	4
SDSS J095834.04+024427.2	149.6418500	2.7408800	18.96	9.20	0	bl	1.8883	0.0013	4
COSMOS J095834.20+022457.3	149.6425100	2.4159300	23.04	1.32	18000	nl	0.9559	0.0001	4
COSMOS J095834.23+024332.5	149.6426043	2.7257013	19.86	14.33	11160	a	0.3919	0.0007	3
COSMOS J095834.40+022054.8	149.6433428	2.3485657	22.13	0.01	3600	?	-1.0000	-1.0000	-1
SDSS J095834.75+014502.4	149.6447800	1.7506600	19.44	7.22	0	bl	1.8987	0.0019	4

Table 2.2—Continued

Object Name	RA (J2000) ^a degrees	Dec (J2000) degrees	i_{CFHT}^+ AB mag	S/N	t_{exp} sec	Type	z	σ_z	z_{conf}^b
COSMOS J095835.06+022316.9	149.6460741	2.3880193	22.28	34.35	18000	bl	1.8452	0.0108	4
COSMOS J095835.28+013609.2	149.6469900	1.6025510	23.37	2.90	9600	bnl	2.8414	0.0094	4
COSMOS J095835.47+023036.1	149.6477800	2.5100380	20.84	0.35	18000	?	-1.0000	-1.0000	0
SDSS J095835.61+024907.5	149.6483600	2.8187400	18.10	3.59	0	a	0.3447	0.0002	4
SDSS J095835.98+015157.1	149.6499300	1.8658700	19.66	36.34	19200	bl	2.9393	0.0006	4
COSMOS J095836.69+022049.0	149.6528600	2.3469350	23.04	2.94	18000	bnl	1.1876	0.0003	4
COSMOS J095837.23+025407.5	149.6551195	2.9020803	18.20	29.01	11160	a	0.3052	0.0003	4
COSMOS J095837.37+023602.9	149.6557119	2.6008110	20.69	3.86	11160	nl	0.7330	0.0002	4
COSMOS J095837.52+020304.0	149.6563258	2.0511127	22.24	1.44	19200	bl	1.8542	0.0087	4
COSMOS J095838.15+025254.9	149.6589379	2.8819095	23.32	1.11	11160	?	-1.0000	-1.0000	0
COSMOS J095838.47+022439.3	149.6602763	2.4109151	21.49	4.08	3600	bl	1.1610	0.0072	3
COSMOS J095838.84+022348.8	149.6618325	2.3968769	18.50	44.81	18000	nl	0.3522	0.0001	4
COSMOS J095839.01+021610.6	149.6625233	2.2696101	20.08	10.42	3600	a	0.6757	0.0037	4
COSMOS J095839.09+022724.1	149.6628800	2.4566890	14.06	182.04	18000	star	0.0000	0.0000	4
COSMOS J095839.27+020506.7	149.6636059	2.0852046	20.65	28.76	19200	bl	1.2200	0.0007	4

Table 2.2—Continued

Object Name	RA (J2000) ^a degrees	Dec (J2000) degrees	i_{CFHT}^+ AB mag	S/N	t_{exp} sec	Type	z	σ_z	z_{conf}^b
COSMOS J095839.55+021837.2	149.6647900	2.3103220	18.70	0.37	18000	?	-1.0000	-1.0000	0
COSMOS J095840.02+021711.1	149.6667503	2.2864257	21.45	9.41	18000	bl	1.0266	0.0001	4
COSMOS J095840.32+020807.2	149.6680167	2.1353271	19.04	25.57	19200	nl	0.3386	0.0001	4
COSMOS J095840.61+020426.6	149.6692072	2.0740582	19.08	30.29	19200	bnl	0.3395	0.0001	4
COSMOS J095840.71+021003.7	149.6696400	2.1676990	23.30	0.21	18000	?	-1.0000	-1.0000	0
COSMOS J095842.01+015442.4	149.6750413	1.9117859	22.11	2.14	19200	nl	0.3147	0.0015	2
COSMOS J095843.39+024057.4	149.6807827	2.6826204	23.41	0.26	11160	?	-1.0000	-1.0000	0
SDSS J095844.72+020249.5	149.6863400	2.0470900	16.35	21.87	19200	nl	0.0926	0.0001	4
SDSS J095844.94+014309.0	149.6872600	1.7191700	20.17	4.35	0	bl	1.3366	0.0017	4
COSMOS J095845.00+014845.5	149.6874968	1.8126486	22.55	3.08	19200	bnl	1.2138	0.0010	4
COSMOS J095845.22+022840.2	149.6884257	2.4778349	23.07	0.01	3600	?	-1.0000	-1.0000	-1
COSMOS J095845.28+022442.6	149.6886600	2.4118460	23.42	1.89	18000	nl	1.1219	0.0001	3
COSMOS J095845.86+022008.0	149.6910981	2.3355421	21.71	8.92	18000	nla	0.8639	0.0001	4
COSMOS J095846.02+014905.6	149.6917600	1.8182200	20.24	5.75	9600	a	0.7379	0.0026	4
COSMOS J095846.75+023910.8	149.6947969	2.6530100	20.35	5.36	11160	nl	0.3159	0.0006	4

Table 2.2—Continued

Object Name	RA (J2000) ^a degrees	Dec (J2000) degrees	i_{CFHT}^+ AB mag	S/N	t_{exp} sec	Type	z	σ_z	z_{conf}^b
COSMOS J095847.00+023256.5	149.6958414	2.5490348	22.17	6.06	18000	bl	1.7715	0.0103	2
COSMOS J095847.01+021552.2	149.6958651	2.2645046	20.47	12.61	18000	nla	0.5500	0.0001	4
COSMOS J095847.17+023619.7	149.6965515	2.6054840	23.28	1.32	11160	nl	1.0406	0.0064	2
COSMOS J095847.33+015418.8	149.6971900	1.9052160	20.36	11.96	19200	nla	0.6603	0.0001	4
COSMOS J095847.71+022628.4	149.6987835	2.4412317	20.98	9.04	3600	bl	1.5174	0.0001	4
COSMOS J095848.30+023320.8	149.7012600	2.5557740	20.80	0.26	18000	?	-1.0000	-1.0000	0
SDSS J095848.67+025243.2	149.7027800	2.8786800	16.44	19.79	0	nla	0.0790	0.0002	4
COSMOS J095848.79+013632.2	149.7032923	1.6089330	22.99	4.11	9600	nl	1.1298	0.0018	3
SDSS J095848.86+023441.1	149.7035800	2.5780800	20.37	2.91	0	bl	1.5512	0.0021	4
SDSS J095849.02+013219.8	149.7042500	1.5388200	18.94	3.55	0	a	0.3639	0.0003	4
COSMOS J095849.41+022511.1	149.7058664	2.4197517	20.48	41.18	18000	bl	1.1221	0.0010	4
COSMOS J095849.52+021640.6	149.7063156	2.2779414	20.85	6.93	3600	nl	0.7300	0.0046	2
COSMOS J095850.60+024621.0	149.7108400	2.7724920	17.70	37.46	11160	nl	0.0789	0.0001	4
COSMOS J095851.03+024436.9	149.7126112	2.7435841	15.40	134.99	11160	a	-0.0003	0.0001	3
COSMOS J095851.40+024118.8	149.7141645	2.6885595	22.52	0.96	11160	?	-1.0000	-1.0000	0

Table 2.2—Continued

Object Name	RA (J2000) ^a	Dec (J2000)	i_{CFHT}^+	S/N	t_{exp}	Type	z	σ_z	z_{conf}^b
	degrees	degrees	AB mag		sec				
COSMOS J095851.66+021758.0	149.7152400	2.2994310	22.93	1.94	18000	?	-1.0000	-1.0000	0
SDSS J095852.14+025156.3	149.7172700	2.8656500	19.18	8.08	0	bl	1.4072	0.0016	4
SDSS J095852.38+025124.2	149.7182600	2.8567300	15.99	27.61	0	a	0.0724	0.0002	4
COSMOS J095852.98+022056.4	149.7207371	2.3489920	22.69	2.32	3600	?	-1.0000	-1.0000	-1
COSMOS J095853.12+023223.9	149.7213297	2.5399843	21.69	9.03	18000	bl	1.7295	0.0006	1
COSMOS J095855.26+022713.7	149.7302531	2.4537989	21.97	1.13	18000	nl	1.1269	0.0001	4
COSMOS J095856.19+024127.9	149.7341412	2.6910704	20.73	7.34	11160	nl	0.9100	0.0056	4
COSMOS J095856.62+020139.3	149.7359255	2.0275941	22.80	2.74	19200	?	-1.0000	-1.0000	0
COSMOS J095856.70+021047.8	149.7362300	2.1799310	22.70	1.08	18000	bl	4.2511	0.0009	4
COSMOS J095857.20+015843.7	149.7383500	1.9788050	21.30	6.02	19200	a	0.5254	0.0007	3
COSMOS J095857.31+022158.8	149.7387930	2.3663370	22.95	7.26	18000	bl	1.6560	0.0004	3
SDSS J095857.35+021314.4	149.7389600	2.2206700	19.96	3.59	0	bl	1.0243	0.0013	4
COSMOS J095857.38+024002.4	149.7390725	2.6673260	22.24	1.23	11160	bnl	0.2730	0.0025	3
SDSS J095858.53+021459.1	149.7438900	2.2497500	16.90	16.67	0	bl	0.1324	0.0010	4
SDSS J095858.68+020139.2	149.7444900	2.0275600	18.87	12.57	0	bl	2.4536	0.0008	4

Table 2.2—Continued

Object Name	RA (J2000) ^a degrees	Dec (J2000) degrees	i_{CFHT}^+ AB mag	S/N	t_{exp} sec	Type	z	σ_z	z_{conf}^b
COSMOS J095859.71+024355.3	149.7487723	2.7320252	22.84	1.09	11160	?	-1.0000	-1.0000	0
COSMOS J095900.22+022811.6	149.7509291	2.4698986	20.75	7.63	3600	nl	0.6554	0.0037	4
COSMOS J095900.99+020830.5	149.7541195	2.1418126	17.20	79.42	19200	star	0.0000	0.0000	4
COSMOS J095901.31+024418.8	149.7554386	2.7385443	22.93	1.18	11160	bl	3.5351	0.0128	4
COSMOS J095901.71+025022.9	149.7571100	2.8397010	22.58	1.38	14400	nl	0.8673	0.0006	2
COSMOS J095902.56+022511.8	149.7606354	2.4199319	21.69	4.88	24840	bl	1.1049	0.0059	4
SDSS J095902.76+021906.5	149.7614800	2.3184600	18.67	7.29	0	bl	0.3454	0.0010	4
COSMOS J095903.84+023858.1	149.7660177	2.6494727	22.01	0.01	11160	?	-1.0000	-1.0000	0
COSMOS J095904.35+022552.8	149.7681074	2.4313312	21.04	2.94	3600	nl	0.9431	0.0050	4
COSMOS J095905.12+021530.1	149.7713205	2.2583523	20.97	14.72	18000	bl	2.2217	0.0004	2
SDSS J095905.51+023810.1	149.7729400	2.6361500	14.97	37.76	11160	a	0.0792	0.0002	4
COSMOS J095905.80+024027.0	149.7741701	2.6741534	21.48	3.67	11160	bl	2.0760	0.0127	2
COSMOS J095906.46+022639.4	149.7769253	2.4442858	22.79	1.36	3600	bl	4.1700	0.0415	4
COSMOS J095906.97+021357.8	149.7790222	2.2327120	21.30	5.11	24840	a	0.7620	0.0005	4
COSMOS J095907.40+023945.9	149.7808186	2.6627545	18.62	120.11	14400	star	0.0000	0.0000	4

Table 2.2—Continued

Object Name	RA (J2000) ^a degrees	Dec (J2000) degrees	i_{CFHT}^+ AB mag	S/N	t_{exp} sec	Type	z	σ_z	z_{conf}^b
COSMOS J095907.65+020820.9	149.7818756	2.1391280	18.97	15.14	13200	nla	0.3542	0.0001	4
COSMOS J095907.70+022816.8	149.7820800	2.4713410	18.60	1.62	18000	nl	0.7996	0.0001	2
SDSS J095908.32+024309.6	149.7846600	2.7193300	19.11	12.13	0	bl	1.3174	0.0015	4
COSMOS J095908.56+023317.2	149.7856682	2.5547738	22.57	4.49	14400	bl	1.7977	0.0016	3
COSMOS J095909.53+021916.5	149.7897339	2.3212631	20.09	9.89	24840	bl	0.3775	0.0009	4
COSMOS J095909.97+022017.7	149.7915649	2.3382571	21.35	7.81	24840	a	0.4319	0.0016	2
COSMOS J095910.03+015222.3	149.7917977	1.8728493	22.19	2.52	19200	a	0.4586	0.0018	1
COSMOS J095910.31+020732.3	149.7929535	2.1256490	18.55	24.11	13200	nl	0.3527	0.0001	4
COSMOS J095910.67+020423.1	149.7944538	2.0730738	22.98	0.30	19200	bl	2.6681	0.0054	4
COSMOS J095911.11+023333.9	149.7962800	2.5594290	22.41	4.26	14400	bl	1.5390	0.0013	3
COSMOS J095914.37+023624.2	149.8098800	2.6067150	21.00	12.32	14400	nl	0.5069	0.0001	4
COSMOS J095914.69+024550.0	149.8112000	2.7638920	14.35	68.55	14400	star	0.0000	0.0000	4
COSMOS J095914.90+014245.6	149.8120900	1.7126760	22.18	0.90	19200	nl	0.7450	0.0047	3
COSMOS J095915.06+014926.3	149.8127375	1.8239699	20.82	7.35	19200	nla	0.5278	0.0003	4
COSMOS J095915.40+020059.0	149.8141632	2.0163829	22.45	3.16	13200	bl	1.3600	0.0026	4

Table 2.2—Continued

Object Name	RA (J2000) ^a	Dec (J2000)	i_{CFHT}^+	S/N	t_{exp}	Type	z	σ_z	z_{conf}^b
	degrees	degrees	AB mag		sec				
COSMOS J095916.36+020311.0	149.8181610	2.0530651	23.40	1.18	13200	a	0.7080	0.0045	2
COSMOS J095917.26+021516.9	149.8219147	2.2546821	20.85	7.88	24840	a	0.9350	0.0005	4
COSMOS J095917.44+020522.9	149.8226776	2.0896831	22.13	4.29	13200	bl	2.0500	0.0144	2
COSMOS J095918.36+024304.9	149.8264977	2.7180262	16.21	79.28	14400	star	0.0000	0.0000	4
SDSS J095918.70+020951.7	149.8279300	2.1643600	19.47	5.46	13200	nl	1.1544	0.0001	4
COSMOS J095920.14+021831.7	149.8339081	2.3087990	22.05	2.88	24840	nla	1.1623	0.0004	4
COSMOS J095920.33+014903.5	149.8347285	1.8176318	21.91	3.31	19200	a	0.3236	0.0023	2
COSMOS J095920.89+020032.0	149.8370209	2.0088961	20.92	8.10	13200	bl	1.4845	0.0004	4
COSMOS J095920.90+023902.9	149.8370900	2.6507920	17.60	0.66	14400	nl	0.4682	0.0004	1
SDSS J095921.30+024030.4	149.8387300	2.6751000	17.45	10.60	0	bl	0.2597	0.0010	4
COSMOS J095921.31+024412.4	149.8388000	2.7367700	20.29	24.29	14400	bnl	1.0037	0.0054	4
COSMOS J095921.54+023215.5	149.8397400	2.5376310	23.20	0.30	14400	nl	0.9388	0.0020	1
COSMOS J095921.62+024119.0	149.8401000	2.6886230	22.30	0.78	14400	?	-1.0000	-1.0000	0
COSMOS J095922.12+013618.5	149.8421542	1.6051421	22.65	0.93	19200	nl	1.2846	0.0016	3
COSMOS J095923.55+022227.5	149.8481140	2.3742981	21.00	19.95	24840	bl	2.6961	0.0010	4

Table 2.2—Continued

Object Name	RA (J2000) ^a degrees	Dec (J2000) degrees	i_{CFHT}^+ AB mag	S/N	t_{exp} sec	Type	z	σ_z	z_{conf}^b
COSMOS J095923.72+022522.6	149.8488464	2.4229479	19.73	15.91	24840	nla	0.3625	0.0003	4
SDSS J095924.47+015954.4	149.8519400	1.9984500	18.40	12.49	0	bl	1.2360	0.0028	4
COSMOS J095925.34+024602.5	149.8556000	2.7673520	23.30	0.51	14400	?	-1.0000	-1.0000	0
COSMOS J095925.68+024646.7	149.8570200	2.7796400	21.80	1.29	14400	?	-1.0000	-1.0000	0
COSMOS J095926.01+014444.3	149.8583687	1.7456456	20.72	6.03	19200	a	0.6673	0.0012	4
COSMOS J095926.16+021529.8	149.8590088	2.2582779	22.97	2.64	24840	?	-1.0000	-1.0000	0
COSMOS J095926.47+023241.1	149.8603068	2.5447605	22.77	3.56	14400	nl	0.4311	0.0002	3
COSMOS J095926.88+015341.5	149.8620148	1.8948630	19.01	14.71	13200	nl	0.4437	0.0001	4
COSMOS J095928.31+022106.9	149.8679810	2.3519061	19.23	15.48	24840	bl	0.3458	0.0001	4
COSMOS J095928.32+021950.7	149.8680115	2.3307400	20.75	19.90	24840	bl	1.4879	0.0005	4
COSMOS J095928.35+021817.6	149.8681030	2.3048899	22.69	2.59	24840	a	0.8115	0.0010	1
COSMOS J095928.46+015934.8	149.8685608	1.9930037	21.41	4.03	13200	bl	1.1834	0.0011	4
COSMOS J095928.99+024435.6	149.8707900	2.7432170	21.57	7.20	14400	nl	1.0248	0.0001	4
COSMOS J095929.23+022034.5	149.8717957	2.3429201	21.87	5.07	24840	bl	1.7434	0.0006	4
COSMOS J095929.86+020151.8	149.8744049	2.0310609	23.34	1.33	13200	?	-1.0000	-1.0000	0

Table 2.2—Continued

Object Name	RA (J2000) ^a	Dec (J2000)	i_{CFHT}^+	S/N	t_{exp}	Type	z	σ_z	$z_{\text{conf}}^{\text{b}}$
	degrees	degrees	AB mag		sec				
COSMOS J095930.36+023407.4	149.8764900	2.5687140	17.73	0.48	14400	?	-1.0000	-1.0000	0
COSMOS J095932.52+023038.2	149.8855000	2.5106070	23.37	0.77	14400	?	-1.0000	-1.0000	0
COSMOS J095932.69+025020.9	149.8862284	2.8391517	17.60	0.01	14400	?	-1.0000	-1.0000	0
COSMOS J095932.91+020702.0	149.8871307	2.1172111	22.50	2.91	13200	?	-1.0000	-1.0000	-1
COSMOS J095933.73+024056.5	149.8905422	2.6823654	20.24	20.96	14400	nl	0.2698	0.0001	4
COSMOS J095934.31+023606.4	149.8929500	2.6017780	20.70	0.75	14400	?	-1.0000	-1.0000	0
COSMOS J095934.35+012849.4	149.8931176	1.4803918	21.17	11.16	19200	bl	1.1598	0.0003	4
COSMOS J095934.44+020627.8	149.8935089	2.1077230	21.27	4.16	13200	nl	0.6862	0.0001	4
COSMOS J095934.76+021028.1	149.8948212	2.1744831	22.04	5.52	24840	bl	1.3800	0.0041	3
COSMOS J095935.43+013060.0	149.8976298	1.5166645	20.58	20.46	19200	bl	1.6630	0.0110	2
COSMOS J095935.50+020538.2	149.8979034	2.0939519	21.90	9.26	13200	bl	1.9208	0.0003	4
COSMOS J095936.53+021937.8	149.9022064	2.3271670	23.37	2.39	24840	?	-1.0000	-1.0000	0
COSMOS J095937.39+025230.8	149.9057900	2.8752260	23.06	1.00	14400	a	1.0538	0.0008	1
COSMOS J095937.42+022347.4	149.9058990	2.3964889	21.15	5.90	24840	a	0.7417	0.0006	4
COSMOS J095937.46+015502.1	149.9060669	1.9172440	22.36	1.98	13200	?	-1.0000	-1.0000	0

Table 2.2—Continued

Object Name	RA (J2000) ^a degrees	Dec (J2000) degrees	i_{CFHT}^+ AB mag	S/N	t_{exp} sec	Type	z	σ_z	z_{conf}^b
COSMOS J095937.95+023950.0	149.9081300	2.6638840	23.28	0.29	14400	?	-1.0000	-1.0000	0
COSMOS J095938.25+013015.8	149.9093812	1.5043868	21.78	2.71	19200	bl	1.4703	0.0006	4
COSMOS J095938.28+020450.2	149.9095001	2.0806060	20.22	22.40	13200	bl	2.8036	0.0010	4
COSMOS J095938.52+020404.8	149.9104919	2.0680020	22.51	1.45	13200	?	-1.0000	-1.0000	0
COSMOS J095938.56+023316.8	149.9106538	2.5546701	19.92	27.31	14400	a	0.7517	0.0001	4
COSMOS J095940.06+022306.8	149.9169006	2.3852229	20.11	27.38	24840	bl	1.1317	0.0001	4
COSMOS J095940.86+023051.2	149.9202422	2.5142265	21.74	7.16	14400	a	0.6981	0.0002	4
COSMOS J095942.25+023134.6	149.9260458	2.5262709	20.91	4.85	14400	nla	0.7272	0.0002	4
COSMOS J095942.74+013240.7	149.9280631	1.5446275	21.47	8.97	19200	bl	2.5898	0.0173	2
COSMOS J095942.94+021753.1	149.9289093	2.2980869	23.05	2.42	24840	?	-1.0000	-1.0000	0
COSMOS J095943.35+013544.1	149.9306200	1.5955780	18.34	23.34	19200	nl	0.2217	0.0001	4
COSMOS J095943.76+022008.0	149.9323425	2.3355429	20.27	13.70	24840	nla	0.9300	0.0050	2
COSMOS J095944.14+025037.7	149.9339200	2.8438060	21.24	14.24	14400	bl	1.9833	0.0004	4
COSMOS J095944.60+022626.2	149.9358368	2.4406121	21.43	10.76	24840	nl	0.9920	0.0001	4
COSMOS J095944.83+020857.6	149.9367828	2.1493390	20.78	1.89	13200	a	0.9525	0.0013	2

Table 2.2—Continued

Object Name	RA (J2000) ^a degrees	Dec (J2000) degrees	i_{CFHT}^+ AB mag	S/N	t_{exp} sec	Type	z	σ_z	z_{conf}^b
COSMOS J095945.18+023439.4	149.9382629	2.5776041	16.78	43.00	24840	nla	0.1240	0.0069	4
COSMOS J095945.21+023021.5	149.9383800	2.5059710	20.76	5.56	14400	a	0.8922	0.0003	4
SDSS J095946.01+024743.6	149.9417100	2.7954500	18.90	12.88	0	bl	1.0670	0.0022	4
COSMOS J095946.92+022209.5	149.9454956	2.3693130	21.08	18.13	24840	bl	0.9087	0.0003	4
COSMOS J095946.95+013450.5	149.9456216	1.5807029	16.69	42.91	19200	star	0.0000	0.0000	4
COSMOS J095947.97+024140.9	149.9498800	2.6946830	23.41	1.10	14400	?	-1.0000	-1.0000	0
COSMOS J095948.72+024309.0	149.9530100	2.7191540	23.05	0.01	14400	?	-1.0000	-1.0000	0
COSMOS J095949.35+023007.3	149.9556168	2.5020209	21.86	3.97	14400	bl	1.4797	0.0019	1
SDSS J095949.40+020141.0	149.9558300	2.0280600	19.03	37.62	13200	bl	1.7533	0.0022	4
COSMOS J095949.84+020011.3	149.9576874	2.0031309	21.05	9.05	13200	bl	1.8108	0.0002	4
COSMOS J095950.05+023310.1	149.9585571	2.5528071	23.39	1.34	24840	?	-1.0000	-1.0000	0
COSMOS J095950.20+022123.1	149.9591675	2.3564100	22.05	0.77	24840	?	-1.0000	-1.0000	-1
COSMOS J095952.75+021100.6	149.9697876	2.1835001	22.95	6.26	13200	?	-1.0000	-1.0000	-1
COSMOS J095953.79+013836.6	149.9741190	1.6434904	20.81	3.37	19200	bl	1.0398	0.0002	4
COSMOS J095954.78+013206.5	149.9782602	1.5351502	19.93	14.32	19200	bl	0.4810	0.0001	4

Table 2.2—Continued

Object Name	RA (J2000) ^a degrees	Dec (J2000) degrees	i_{CFHT}^+ AB mag	S/N	t_{exp} sec	Type	z	σ_z	z_{conf}^b
COSMOS J095955.16+015737.5	149.9798126	1.9604070	22.81	1.90	13200	nl	1.1691	0.0005	3
COSMOS J095956.04+014727.9	149.9835052	1.7910750	20.61	4.73	13200	nl	0.3369	0.0001	4
COSMOS J095956.64+013702.2	149.9859845	1.6172839	22.22	5.41	19200	bl	1.1496	0.0062	4
COSMOS J095957.29+015556.8	149.9887238	1.9324400	22.25	2.35	13200	bl	2.3870	0.0093	2
COSMOS J095957.31+015430.8	149.9888000	1.9085660	22.02	3.46	13200	?	-1.0000	-1.0000	0
SDSS J095957.98+014327.4	149.9915800	1.7242700	20.12	4.34	0	bl	1.6181	0.0016	4
COSMOS J095958.02+020755.2	149.9917450	2.1319909	22.79	2.17	13200	bl	2.1290	0.0151	1
COSMOS J095958.19+024057.3	149.9924600	2.6825900	23.29	2.12	14400	nl	0.6312	0.0003	2
COSMOS J095958.29+015128.4	149.9928700	1.8578760	21.38	2.56	19200	a	0.6881	0.0063	2
COSMOS J095958.41+022238.2	149.9933929	2.3772640	22.41	3.46	24840	nl	0.9310	0.0003	4
COSMOS J095958.46+021530.8	149.9935913	2.2585559	20.12	15.13	24840	a	0.6585	0.0002	4
COSMOS J095958.53+021805.3	149.9938660	2.3014779	20.13	12.46	24840	bl	1.7924	0.0002	4
COSMOS J095959.36+022458.4	149.9973297	2.4162140	20.42	13.67	24840	a	0.5694	0.0002	4
COSMOS J095959.50+024646.6	149.9979300	2.7796030	17.29	44.89	14400	star	0.0000	0.0000	4
SDSS J095959.63+024608.7	149.9984600	2.7690800	16.24	20.89	0	a	0.1656	0.0002	4

Table 2.2—Continued

Object Name	RA (J2000) ^a degrees	Dec (J2000) degrees	i_{CFHT}^+ AB mag	S/N	t_{exp} sec	Type	z	σ_z	z_{conf}^b
COSMOS J100000.82+024444.9	150.0034300	2.7458120	23.03	2.05	14400	a	0.4161	0.0009	1
COSMOS J100001.00+022321.1	150.0041656	2.3891830	22.57	1.98	24840	bl	1.8456	0.0141	4
COSMOS J100001.06+021413.6	150.0044403	2.2371240	21.59	4.13	24840	bl	1.4068	0.0077	4
SDSS J100001.44+024844.7	150.0060000	2.8124300	19.28	10.61	0	bl	0.7659	0.0011	4
COSMOS J100002.21+021631.8	150.0092163	2.2755051	20.05	7.44	24840	bl	0.8500	0.0016	4
COSMOS J100002.89+023131.9	150.0120300	2.5255200	21.77	1.16	14400	nl	1.0280	0.0002	4
COSMOS J100004.99+020334.3	150.0207977	2.0595219	19.39	15.29	13200	?	-1.0000	-1.0000	0
COSMOS J100005.36+023059.6	150.0223236	2.5165470	20.90	6.42	24840	a	0.6773	0.0004	4
COSMOS J100005.98+015453.3	150.0249329	1.9148060	20.79	6.05	13200	nl	0.9689	0.0002	4
COSMOS J100006.11+015239.6	150.0254760	1.8776576	22.57	1.41	19200	?	-1.0000	-1.0000	0
COSMOS J100006.42+023343.4	150.0267487	2.5620470	20.96	8.91	24840	a	0.7450	0.0003	4
COSMOS J100006.50+015528.5	150.0270844	1.9245870	24.06	1.35	13200	?	-1.0000	-1.0000	0
COSMOS J100006.85+021235.7	150.0285339	2.2099271	21.55	8.28	24840	bl	1.2580	0.0005	4
COSMOS J100007.35+024043.5	150.0306367	2.6787539	21.65	15.88	14400	bl	1.9350	0.0011	4
SDSS J100008.10+024554.6	150.0337500	2.7651700	15.14	41.40	0	a	0.0289	0.0001	4

Table 2.2—Continued

Object Name	RA (J2000) ^a degrees	Dec (J2000) degrees	i_{CFHT}^+ AB mag	S/N	t_{exp} sec	Type	z	σ_z	z_{conf}^b
SDSS J100008.14+013306.6	150.0339200	1.5518200	20.71	3.06	0	bl	1.1706	0.0019	4
COSMOS J100010.04+023746.1	150.0418400	2.6294840	21.40	8.24	14400	bl	0.4704	0.0002	2
COSMOS J100010.15+024141.6	150.0422800	2.6948890	17.57	84.74	14400	nla	0.2205	0.0020	4
COSMOS J100010.22+020347.9	150.0425873	2.0633099	22.69	1.95	13200	bl	2.0031	0.0139	1
COSMOS J100010.85+024118.6	150.0452289	2.6885087	22.69	9.45	14400	bl	1.4362	0.0004	4
COSMOS J100011.19+020629.4	150.0466003	2.1081700	20.32	9.31	13200	nla	0.4785	0.0001	4
COSMOS J100011.23+015200.3	150.0467834	1.8667510	23.03	1.52	13200	?	-1.0000	-1.0000	0
COSMOS J100011.68+021919.8	150.0486755	2.3221660	21.35	6.63	24840	nla	0.6246	0.0003	4
COSMOS J100012.10+014439.9	150.0504028	1.7444271	21.56	1.80	19200	bl	1.1477	0.0002	4
COSMOS J100012.44+014057.8	150.0518531	1.6827341	19.95	16.79	19200	bl	2.2767	0.0002	4
COSMOS J100012.48+024459.0	150.0520200	2.7497120	20.86	8.06	14400	nla	0.8232	0.0001	4
SDSS J100012.91+023522.8	150.0537800	2.5896700	18.79	14.00	0	bl	0.6986	0.0013	4
COSMOS J100013.33+022657.2	150.0555573	2.4492121	20.71	7.83	24840	a	0.7317	0.0004	4
COSMOS J100013.41+021400.6	150.0558929	2.2334869	20.76	4.24	24840	a	0.9362	0.0007	4
COSMOS J100013.57+022225.5	150.0565338	2.3737540	23.18	2.46	24840	?	-1.0000	-1.0000	0

Table 2.2—Continued

Object Name	RA (J2000) ^a degrees	Dec (J2000) degrees	i_{CFHT}^+ AB mag	S/N	t_{exp} sec	Type	z	σ_z	z_{conf}^b
COSMOS J100013.70+013034.7	150.0570767	1.5096288	20.24	16.87	19200	bl	0.8512	0.0001	4
COSMOS J100013.73+021221.3	150.0571899	2.2059300	18.30	32.78	24840	nl	0.1865	0.0001	4
COSMOS J100013.79+024344.2	150.0574700	2.7289560	18.57	17.94	14400	a	0.1660	0.0006	4
COSMOS J100013.93+022249.8	150.0580292	2.3804941	18.57	26.71	24840	a	0.3474	0.0002	4
COSMOS J100014.08+022838.8	150.0586700	2.4774370	20.48	27.71	24840	bl	1.2562	0.0003	4
SDSS J100014.14+020054.6	150.0589200	2.0151800	19.91	6.82	0	bl	2.4971	0.0014	4
COSMOS J100014.19+021311.9	150.0591278	2.2199690	21.53	3.02	24840	nl	1.1405	0.0001	4
COSMOS J100015.37+013146.8	150.0640418	1.5296627	22.00	6.82	19200	nl	1.0310	0.0007	3
COSMOS J100015.48+021944.7	150.0645142	2.3290811	21.69	4.35	24840	bla	0.3400	0.0008	3
SDSS J100015.77+025545.4	150.0656900	2.9292900	16.85	17.01	0	a	0.1027	0.0013	4
COSMOS J100016.05+021237.5	150.0668793	2.2104130	18.21	19.86	13200	nl	0.1867	0.0001	4
COSMOS J100016.29+015104.8	150.0678864	1.8513410	20.83	6.21	13200	bnl	1.1347	0.0003	4
COSMOS J100016.42+023725.0	150.0684152	2.6236168	21.99	8.25	14400	a	0.3392	0.0003	2
COSMOS J100016.74+013457.6	150.0697357	1.5826646	21.45	1.82	19200	nl	0.9717	0.0017	3
COSMOS J100016.77+020605.9	150.0698853	2.1016359	22.95	1.82	13200	?	-1.0000	-1.0000	0

Table 2.2—Continued

Object Name	RA (J2000) ^a degrees	Dec (J2000) degrees	i_{CFHT}^+ AB mag	S/N	t_{exp} sec	Type	z	σ_z	z_{conf}^b
COSMOS J100017.52+020012.8	150.0730133	2.0035551	20.68	12.35	13200	nla	0.3500	0.0008	4
COSMOS J100020.98+014431.8	150.0874002	1.7421627	16.56	44.35	19200	star	0.0000	0.0000	4
COSMOS J100021.48+024600.2	150.0894900	2.7667280	17.84	46.66	14400	star	0.0000	0.0000	4
COSMOS J100021.55+024714.1	150.0897900	2.7872570	18.69	56.09	14400	star	0.0000	0.0000	4
COSMOS J100021.96+022356.7	150.0915070	2.3990791	22.06	16.62	9000	bl	2.4800	0.0056	4
COSMOS J100022.70+024210.4	150.0945833	2.7028806	22.28	3.89	21600	nla	0.8495	0.0003	4
COSMOS J100022.71+024956.3	150.0946148	2.8323054	22.03	6.13	14400	bl	1.5580	0.0012	4
COSMOS J100022.80+024830.5	150.0949900	2.8084650	22.20	3.14	14400	bnl	1.3256	0.0003	4
COSMOS J100023.00+020842.7	150.0958405	2.1451831	22.74	1.98	13200	?	-1.0000	-1.0000	-1
COSMOS J100023.62+024807.7	150.0984100	2.8021260	20.60	0.44	18000	?	-1.0000	-1.0000	0
COSMOS J100024.00+024539.8	150.1000100	2.7610560	21.30	1.03	18000	?	-1.0000	-1.0000	0
COSMOS J100024.09+014005.4	150.1003627	1.6681653	19.74	13.96	19200	a	0.6226	0.0009	4
SDSS J100024.39+015054.1	150.1016400	1.8483600	19.44	4.69	0	bl	1.6637	0.0015	4
COSMOS J100024.47+024422.8	150.1019400	2.7396580	13.28	0.76	14400	star	0.0000	0.0003	4
COSMOS J100024.47+020619.9	150.1019745	2.1055181	19.97	22.68	16800	bl	2.2900	0.0001	4

Table 2.2—Continued

Object Name	RA (J2000) ^a degrees	Dec (J2000) degrees	i_{CFHT}^+ AB mag	S/N	t_{exp} sec	Type	z	σ_z	z_{conf}^b
SDSS J100024.64+023149.0	150.1026700	2.5302900	18.71	14.53	0	bl	1.3177	0.0013	4
COSMOS J100024.67+023749.0	150.1027808	2.6302654	22.31	1.28	21600	?	-1.0000	-1.0000	0
COSMOS J100024.86+023302.7	150.1035924	2.5507621	21.05	8.73	21600	a	0.4967	0.0008	4
COSMOS J100024.89+023956.6	150.1037218	2.6657123	21.27	10.45	21600	bl	2.9525	0.0001	4
COSMOS J100025.07+024128.5	150.1044604	2.6912392	21.24	2.25	21600	bl	1.8806	0.0003	4
SDSS J100025.25+015852.2	150.1052100	1.9811800	19.12	13.76	0	bl	0.3728	0.0016	4
COSMOS J100026.08+020925.3	150.1086426	2.1570210	22.74	1.81	16800	bl	1.8141	0.0210	2
COSMOS J100026.91+015414.8	150.1121216	1.9041200	22.83	1.72	16800	?	-1.0000	-1.0000	0
COSMOS J100027.10+020953.7	150.1129150	2.1649120	23.09	1.27	16800	?	-1.0000	-1.0000	0
COSMOS J100028.06+015547.6	150.1169281	1.9298919	22.59	3.52	16800	bl	1.5191	0.0010	4
COSMOS J100028.23+013508.7	150.1176147	1.5857590	22.07	2.22	13080	nla	0.8393	0.0006	4
SDSS J100028.28+024103.5	150.1178500	2.6843100	17.44	7.33	0	a	0.3493	0.0002	4
COSMOS J100028.63+025112.7	150.1193000	2.8535240	20.10	29.46	18000	bl	0.7659	0.0001	4
COSMOS J100028.69+021745.3	150.1195526	2.2959149	23.08	1.41	9000	nl	1.0391	0.0020	1
COSMOS J100030.02+025142.3	150.1250827	2.8617479	19.77	20.62	21600	bl	1.5794	0.0002	4

Table 2.2—Continued

Object Name	RA (J2000) ^a	Dec (J2000)	i_{CFHT}^+	S/N	t_{exp}	Type	z	σ_z	z_{conf}^b
	degrees	degrees	AB mag		sec				
COSMOS J100030.45+023735.6	150.1268716	2.6265438	22.50	0.74	21600	bnl	1.8412	0.0002	4
COSMOS J100030.72+014711.5	150.1280060	1.7865170	22.74	1.37	13080	nla	1.2164	0.0066	2
COSMOS J100031.27+022819.9	150.1303101	2.4721999	21.56	2.69	9000	a	0.9256	0.0008	4
COSMOS J100031.61+014758.1	150.1317139	1.7994590	20.91	10.00	13080	bl	1.6789	0.0002	4
COSMOS J100031.63+025047.4	150.1317800	2.8465090	19.17	32.82	18000	star	0.0000	0.0000	4
COSMOS J100031.76+023123.9	150.1323200	2.5233010	23.48	1.06	18000	?	-1.0000	-1.0000	0
COSMOS J100031.91+021811.9	150.1329651	2.3032980	22.96	1.36	9000	?	-1.0000	-1.0000	0
COSMOS J100033.12+021730.1	150.1379852	2.2916961	18.01	23.65	9000	nl	0.1853	0.0001	4
COSMOS J100033.38+015237.2	150.1390991	1.8770070	20.52	10.96	16800	bl	0.8306	0.0003	4
COSMOS J100033.49+013811.6	150.1395264	1.6365690	21.16	8.70	13080	bl	0.5198	0.0003	4
COSMOS J100033.52+020543.1	150.1396484	2.0953109	16.74	62.01	16800	star	0.0000	0.0000	4
COSMOS J100034.04+024225.3	150.1418500	2.7070330	20.64	7.21	18000	a	0.8489	0.0001	4
COSMOS J100034.21+025420.1	150.1425400	2.9055940	23.18	1.87	18000	nl	1.0114	0.0001	4
COSMOS J100034.55+025358.0	150.1439500	2.8994410	22.55	3.54	18000	nl	0.8964	0.0001	4
COSMOS J100034.93+020235.2	150.1455536	2.0431020	20.63	9.46	16800	bl	1.1767	0.0005	4

Table 2.2—Continued

Object Name	RA (J2000) ^a	Dec (J2000)	i_{CFHT}^+	S/N	t_{exp}	Type	z	σ_z	z_{conf}^b
	degrees	degrees	AB mag		sec				
COSMOS J100035.30+024302.9	150.1470754	2.7174788	21.47	0.89	21600	bl	1.1776	0.0010	4
COSMOS J100036.05+022830.9	150.1502075	2.4752500	20.50	8.96	9000	nl	0.6879	0.0002	4
COSMOS J100036.21+024928.9	150.1508800	2.8246870	18.77	5.69	21600	a	0.4716	0.0009	3
COSMOS J100036.25+023111.7	150.1510300	2.5199140	20.69	13.43	18000	a	0.6564	0.0001	4
COSMOS J100037.29+024950.6	150.1553800	2.8307130	21.36	13.53	18000	bl	0.7284	0.0001	4
COSMOS J100037.99+014248.6	150.1583099	1.7134939	20.39	8.77	13080	a	0.6229	0.0004	4
COSMOS J100038.00+022455.6	150.1583405	2.4154539	23.05	1.64	9000	a	0.7100	0.0039	2
COSMOS J100038.01+020822.6	150.1583557	2.1396151	20.32	14.21	16800	bl	1.8347	0.0005	4
COSMOS J100038.11+024830.6	150.1588000	2.8085130	23.07	1.71	18000	bl	1.5383	0.0008	2
COSMOS J100038.30+013708.4	150.1596069	1.6190100	21.72	1.77	13080	bl	1.2477	0.0002	4
COSMOS J100038.81+021956.7	150.1617279	2.3324161	23.36	1.64	9000	?	-1.0000	-1.0000	0
COSMOS J100039.67+014821.9	150.1653137	1.8060700	21.98	3.36	16800	?	-1.0000	-1.0000	0
COSMOS J100040.08+024608.1	150.1670200	2.7689230	22.36	1.61	18000	bl	2.3873	0.0004	4
COSMOS J100040.15+024751.6	150.1672969	2.7976532	20.69	7.91	21600	bl	1.0411	0.0013	4
COSMOS J100040.36+023656.4	150.1681685	2.6156568	16.91	50.45	21600	star	0.0000	0.0000	4

Table 2.2—Continued

Object Name	RA (J2000) ^a	Dec (J2000)	i_{CFHT}^+	S/N	t_{exp}	Type	z	σ_z	z_{conf}^b
	degrees	degrees	AB mag		sec				
COSMOS J100040.41+024106.0	150.1683700	2.6850120	22.20	14.98	18000	?	-1.0000	-1.0000	-1
COSMOS J100041.13+023350.5	150.1713727	2.5640251	20.94	7.67	21600	nla	0.5012	0.0003	4
COSMOS J100041.56+013658.9	150.1731567	1.6163640	19.46	2.36	13200	nl	0.9946	0.0003	4
COSMOS J100041.62+013052.6	150.1734467	1.5146250	22.28	3.87	13080	bl	1.4327	0.0019	4
COSMOS J100041.75+022410.8	150.1739807	2.4030118	22.39	2.60	9000	nl	0.9793	0.0004	4
COSMOS J100042.07+013207.2	150.1752930	1.5353340	23.37	1.68	13080	bl	1.5682	0.0088	1
COSMOS J100042.37+014534.1	150.1765442	1.7594850	21.63	7.12	13080	bl	1.1610	0.0032	4
COSMOS J100042.67+015323.8	150.1777954	1.8899490	21.89	3.63	16800	nla	0.8645	0.0004	4
COSMOS J100043.15+020637.2	150.1797800	2.1103800	18.34	33.97	16800	bl	0.3596	0.0009	4
COSMOS J100043.53+022524.4	150.1813812	2.4234550	21.36	4.28	12720	nla	0.7274	0.0003	4
COSMOS J100043.64+014009.4	150.1818390	1.6692770	20.17	17.84	13080	?	-1.0000	-1.0000	0
COSMOS J100043.91+021452.6	150.1829376	2.2479520	23.16	0.01	9000	bl	2.4850	0.0063	4
COSMOS J100044.40+025324.6	150.1850100	2.8901550	21.88	5.59	18000	nla	0.8123	0.0001	4
COSMOS J100046.08+013440.0	150.1919861	1.5777650	21.47	4.39	13080	nl	0.5176	0.0004	4
COSMOS J100046.55+024412.0	150.1939500	2.7366800	20.42	28.43	18000	a	0.2199	0.0020	4

Table 2.2—Continued

Object Name	RA (J2000) ^a degrees	Dec (J2000) degrees	i_{CFHT}^+ AB mag	S/N	t_{exp} sec	Type	z	σ_z	z_{conf}^b
COSMOS J100046.72+020404.5	150.1946869	2.0679300	19.58	19.57	16800	bl	0.5524	0.0001	4
COSMOS J100046.81+014737.8	150.1950531	1.7938280	21.90	5.09	16800	bl	1.8669	0.0053	3
COSMOS J100047.07+020709.1	150.1961060	2.1191990	23.27	1.47	16800	?	-1.0000	-1.0000	0
COSMOS J100047.75+020757.2	150.1989441	2.1325560	19.60	24.55	16800	bl	2.1623	0.0001	4
COSMOS J100047.77+023551.5	150.1990400	2.5976380	21.63	5.64	18000	nla	0.9009	0.0001	4
COSMOS J100047.93+014935.8	150.1997070	1.8266160	21.26	5.21	16800	a	0.8935	0.0006	4
COSMOS J100047.94+021127.2	150.1997375	2.1908791	21.01	11.00	9000	bl	1.5145	0.0024	4
COSMOS J100049.28+023010.4	150.2053263	2.5028960	23.17	0.55	21600	?	-1.0000	-1.0000	0
COSMOS J100049.50+021708.9	150.2062683	2.2857921	22.13	2.32	9000	nl	0.8736	0.0003	4
COSMOS J100049.65+014049.2	150.2068634	1.6803390	22.97	1.64	13080	a	0.7134	0.0035	2
COSMOS J100049.91+020500.1	150.2079468	2.0833671	19.36	27.11	16800	bl	1.2373	0.0001	4
COSMOS J100049.97+015231.3	150.2081909	1.8753690	20.63	14.51	13080	bl	1.1563	0.0009	4
COSMOS J100050.57+022329.3	150.2107391	2.3914850	22.58	4.21	9000	bl	3.1019	0.0034	4
COSMOS J100051.51+021215.5	150.2146454	2.2042990	21.04	12.81	16800	bl	1.8291	0.0018	4
COSMOS J100051.63+021922.1	150.2151031	2.3228109	23.40	1.81	9000	?	-1.0000	-1.0000	0

Table 2.2—Continued

Object Name	RA (J2000) ^a	Dec (J2000)	i_{CFHT}^+	S/N	t_{exp}	Type	z	σ_z	$z_{\text{conf}}^{\text{b}}$
	degrees	degrees	AB mag		sec				
COSMOS J100052.99+014123.8	150.2208099	1.6899410	21.84	3.95	13080	a	0.6787	0.0009	4
COSMOS J100053.76+023302.7	150.2239916	2.5507577	22.26	2.91	21600	bl	0.9420	0.0058	2
COSMOS J100054.79+014602.3	150.2282867	1.7673190	20.10	14.06	13080	nl	0.3486	0.0001	4
SDSS J100055.21+022343.9	150.2300600	2.3955200	15.27	28.52	0	a	0.0446	0.0002	4
COSMOS J100055.28+023330.3	150.2303467	2.5584190	17.83	35.45	12720	star	0.0000	0.0000	1
SDSS J100055.39+023441.4	150.2307900	2.5781800	20.12	4.61	0	bl	1.4031	0.0024	4
COSMOS J100055.45+013416.6	150.2310638	1.5712640	20.70	4.11	13080	nla	0.8257	0.0004	4
COSMOS J100055.71+023110.2	150.2321472	2.5195060	20.36	9.44	9000	nl	0.5114	0.0001	4
COSMOS J100056.14+023510.0	150.2339172	2.5861239	22.85	2.74	9000	nl	1.0830	0.0067	1
COSMOS J100056.75+024849.2	150.2364700	2.8136740	22.21	2.79	18000	bl	1.5696	0.0004	2
COSMOS J100057.79+023932.5	150.2407995	2.6590209	22.36	3.50	21600	bl	3.3608	0.0044	3
COSMOS J100058.33+015208.8	150.2430573	1.8691080	21.00	13.00	16800	bl	2.0283	0.0002	4
COSMOS J100058.58+014656.0	150.2440948	1.7822130	22.81	1.80	13080	nl	1.1195	0.0005	4
COSMOS J100058.70+022556.3	150.2445831	2.4322970	20.83	10.81	9000	nl	0.6933	0.0001	4
SDSS J100058.84+015400.3	150.2451700	1.9000900	19.94	3.88	0	bl	1.5591	0.0022	4

Table 2.2—Continued

Object Name	RA (J2000) ^a	Dec (J2000)	i_{CFHT}^+	S/N	t_{exp}	Type	z	σ_z	z_{conf}^b
	degrees	degrees	AB mag		sec				
COSMOS J100059.45+013232.8	150.2476959	1.5424470	22.58	1.46	13080	a	0.8860	0.0024	4
COSMOS J100100.53+021542.9	150.2521973	2.2619259	23.09	1.81	12720	?	-1.0000	-1.0000	0
COSMOS J100100.64+022911.1	150.2526855	2.4864256	20.83	10.71	9000	bl	2.0413	0.0017	4
COSMOS J100100.67+021641.4	150.2527618	2.2781711	17.60	33.94	12720	nl	0.1656	0.0001	4
COSMOS J100100.81+015947.9	150.2533722	1.9966490	21.42	5.48	16800	bl	1.1645	0.0027	4
COSMOS J100101.53+023848.3	150.2563882	2.6467620	23.23	2.60	21600	bl	3.0758	0.0034	3
COSMOS J100101.94+014800.6	150.2580872	1.8001540	20.49	7.78	16800	nla	0.9074	0.0002	4
COSMOS J100103.02+024015.0	150.2625757	2.6708395	19.37	20.64	21600	nl	0.2693	0.0001	4
COSMOS J100103.76+024527.6	150.2656700	2.7576780	22.69	4.61	18000	?	-1.0000	-1.0000	0
COSMOS J100104.89+024913.5	150.2703656	2.8204085	20.14	11.09	21600	nl	0.3453	0.0001	4
COSMOS J100105.31+021348.5	150.2721100	2.2301271	20.75	5.56	9000	bl	2.6145	0.0007	4
COSMOS J100105.60+015603.3	150.2733459	1.9342400	21.94	3.10	16800	nla	0.9148	0.0005	2
COSMOS J100105.84+023041.0	150.2743264	2.5113929	20.64	10.16	21600	a	0.7030	0.0013	4
COSMOS J100105.90+015919.9	150.2745819	1.9888610	22.01	3.36	16800	a	0.8712	0.0001	2
COSMOS J100106.30+023134.9	150.2762604	2.5263672	22.29	8.00	9000	bl	1.4500	0.0093	1

Table 2.2—Continued

Object Name	RA (J2000) ^a	Dec (J2000)	i_{CFHT}^+	S/N	t_{exp}	Type	z	σ_z	z_{conf}^b
	degrees	degrees	AB mag		sec				
COSMOS J100106.52+023839.5	150.2771800	2.6443170	15.58	134.25	18000	star	0.0000	0.0000	4
COSMOS J100107.19+014437.9	150.2799530	1.7438610	22.19	5.17	13080	?	-1.0000	-1.0000	0
COSMOS J100107.32+021100.7	150.2804871	2.1835389	23.29	1.32	9000	nla	1.2409	0.0015	4
SDSS J100108.30+021643.6	150.2845800	2.2787800	16.49	20.17	0	a	0.1216	0.0001	4
COSMOS J100108.36+022342.2	150.2848053	2.3950591	21.53	4.77	9000	bl	1.9317	0.0003	4
COSMOS J100108.55+020052.7	150.2856140	2.0146270	21.11	11.96	16800	bl	2.6807	0.0012	4
COSMOS J100110.20+023242.3	150.2924959	2.5450836	21.45	10.24	21600	bl	2.6534	0.0002	4
COSMOS J100110.25+023127.2	150.2926900	2.5242330	23.13	0.14	21600	?	-1.0000	-1.0000	0
COSMOS J100110.80+024552.7	150.2950100	2.7646330	23.49	2.32	18000	nl	0.8507	0.0001	1
COSMOS J100111.69+021250.8	150.2987061	2.2141030	23.02	1.76	9000	nl	1.1474	0.0005	4
COSMOS J100111.81+023800.3	150.2992028	2.6334287	23.12	0.96	21600	?	-1.0000	-1.0000	0
COSMOS J100111.94+023024.9	150.2997479	2.5069028	21.08	7.91	21600	bl	1.4999	0.0004	4
COSMOS J100112.01+024233.7	150.3000459	2.7093661	21.97	8.64	18000	bl	0.7284	0.0001	4
COSMOS J100112.62+020940.1	150.3025665	2.1611459	20.11	18.88	9000	bl	1.8221	0.0013	4
COSMOS J100113.34+023608.0	150.3055882	2.6022323	21.31	4.94	21600	bl	1.3388	0.0003	4

Table 2.2—Continued

Object Name	RA (J2000) ^a	Dec (J2000)	i_{CFHT}^+	S/N	t_{exp}	Type	z	σ_z	z_{conf}^b
	degrees	degrees	AB mag		sec				
COSMOS J100113.83+014000.9	150.3076172	1.6669101	20.56	12.54	13080	bl	1.5619	0.0009	2
COSMOS J100113.91+022204.9	150.3079376	2.3680179	22.32	2.20	12720	nla	0.8792	0.0005	4
COSMOS J100114.08+024748.1	150.3086500	2.7966860	23.18	0.17	18000	?	-1.0000	-1.0000	0
SDSS J100114.29+022356.9	150.3095600	2.3991500	19.22	8.44	0	bl	1.7988	0.0019	4
COSMOS J100114.35+022800.1	150.3097992	2.4667070	22.80	4.39	9000	bl	1.1655	0.0033	4
COSMOS J100114.64+012959.0	150.3109894	1.4997160	21.78	6.92	13080	bl	1.7786	0.0039	4
COSMOS J100114.68+022449.4	150.3111572	2.4137199	22.72	2.72	9000	nla	1.0698	0.0007	2
COSMOS J100114.86+020208.8	150.3119049	2.0357709	20.79	8.92	16800	bl	0.9690	0.0020	4
COSMOS J100114.95+014348.6	150.3122864	1.7301580	20.06	10.20	13080	nl	0.5799	0.0002	4
COSMOS J100115.28+024813.0	150.3136600	2.8036180	20.80	12.00	18000	bl	1.4594	0.0004	4
COSMOS J100115.41+022253.9	150.3142090	2.3816359	22.15	2.61	12720	a	0.6099	0.0013	2
COSMOS J100115.55+023743.5	150.3147900	2.6287540	20.00	1.98	18000	bl	2.3350	0.0172	3
COSMOS J100116.31+021402.8	150.3179474	2.2341149	20.71	8.08	12720	nl	0.3730	0.0002	4
SDSS J100116.79+014053.8	150.3199400	1.6816000	19.51	5.89	0	bl	2.0551	0.0021	4
COSMOS J100117.14+025255.7	150.3213959	2.8821256	20.24	7.56	18000	nl	0.4535	0.0001	2

Table 2.2—Continued

Object Name	RA (J2000) ^a	Dec (J2000)	i_{CFHT}^+	S/N	t_{exp}	Type	z	σ_z	$z_{\text{conf}}^{\text{b}}$
	degrees	degrees	AB mag		sec				
COSMOS J100117.70+023309.5	150.3237457	2.5526330	22.41	2.50	9000	nl	1.0013	0.0004	4
COSMOS J100117.72+023309.4	150.3238525	2.5526006	22.41	20.18	18000	nl	0.6950	0.0038	4
COSMOS J100117.97+022902.7	150.3248631	2.4840723	18.15	26.41	21600	a	0.3484	0.0006	4
COSMOS J100118.52+015543.0	150.3271942	1.9286160	20.14	16.53	16800	bl	0.5277	0.0001	4
COSMOS J100118.57+022739.4	150.3273926	2.4609561	20.06	14.85	9000	bl	1.0502	0.0003	4
COSMOS J100118.62+023616.7	150.3276000	2.6046400	22.98	3.57	18000	nl	1.0800	0.0001	2
COSMOS J100118.78+020730.0	150.3282471	2.1249931	22.06	3.22	16800	bl	1.7741	0.0116	4
COSMOS J100119.58+013834.0	150.3315735	1.6427770	19.23	43.05	13080	nla	0.3645	0.0001	4
SDSS J100120.26+023341.4	150.3344100	2.5615000	20.26	4.46	0	bl	1.8344	0.0015	4
SDSS J100120.52+021817.8	150.3355000	2.3049500	16.66	15.29	0	a	0.1229	0.0002	4
COSMOS J100121.25+024636.4	150.3385244	2.7767858	22.63	3.03	21600	bl	2.1300	0.0151	2
COSMOS J100122.17+021334.6	150.3423767	2.2262819	21.73	4.14	9000	nl	0.8913	0.0003	4
SDSS J100122.75+021658.8	150.3447800	2.2829900	17.85	26.08	9000	a	0.3738	0.0001	4
COSMOS J100123.97+021446.1	150.3498840	2.2461319	21.82	7.03	9000	nl	0.8936	0.0002	4
COSMOS J100124.06+024936.7	150.3502400	2.8268730	20.54	10.06	18000	a	0.8251	0.0001	4

Table 2.2—Continued

Object Name	RA (J2000) ^a	Dec (J2000)	i_{CFHT}^+	S/N	t_{exp}	Type	z	σ_z	$z_{\text{conf}}^{\text{b}}$
	degrees	degrees	AB mag		sec				
COSMOS J100124.34+024041.7	150.3513975	2.6782375	21.21	8.59	21600	bl	2.7592	0.0002	4
COSMOS J100124.85+022032.0	150.3535614	2.3422120	20.83	8.95	9000	bl	1.7076	0.0008	4
COSMOS J100124.92+025145.3	150.3538400	2.8625860	18.15	59.27	18000	a	0.3330	0.0024	4
COSMOS J100127.53+020837.7	150.3647003	2.1438129	23.16	1.67	16800	bl	3.3500	0.0293	1
COSMOS J100127.86+022358.4	150.3660736	2.3995640	21.84	4.51	9000	nla	0.9856	0.0003	4
COSMOS J100128.00+021819.4	150.3666534	2.3054020	22.66	0.01	9000	bl	1.1874	0.0025	4
SDSS J100129.42+013633.8	150.3725900	1.6093800	16.43	22.57	0	a	0.1042	0.0001	4
COSMOS J100129.83+023239.0	150.3742828	2.5441644	20.55	10.36	9000	bl	0.8255	0.0004	4
SDSS J100130.37+014304.4	150.3765600	1.7178800	20.16	3.53	0	bl	1.5705	0.0013	4
COSMOS J100130.78+021147.1	150.3782349	2.1964140	21.99	3.80	9000	bl	1.5101	0.0044	3
COSMOS J100130.86+024406.3	150.3786000	2.7350780	22.99	1.47	18000	nl	0.9222	0.0001	4
SDSS J100131.15+022924.8	150.3797800	2.4902200	18.26	4.95	0	a	0.3495	0.0002	4
COSMOS J100131.67+024530.3	150.3819700	2.7584060	21.23	17.46	18000	bl	1.2281	0.0001	2
COSMOS J100131.87+023335.4	150.3827667	2.5598259	22.37	4.20	9000	bl	2.0654	0.0126	4
COSMOS J100131.88+024325.2	150.3828200	2.7236600	22.28	7.48	18000	bl	2.0518	0.0005	4

Table 2.2—Continued

Object Name	RA (J2000) ^a degrees	Dec (J2000) degrees	i_{CFHT}^+ AB mag	S/N	t_{exp} sec	Type	z	σ_z	z_{conf}^b
COSMOS J100132.10+023513.7	150.3837401	2.5871496	21.74	1.97	21600	nl	0.7460	0.0047	1
SDSS J100132.16+013420.9	150.3840100	1.5724600	20.04	4.35	0	bl	1.3605	0.0014	4
COSMOS J100132.86+013847.3	150.3869171	1.6464590	20.99	11.60	13080	nla	0.7359	0.0002	4
COSMOS J100135.46+025406.0	150.3977429	2.9016620	20.62	8.46	21600	bl	1.6409	0.0030	4
COSMOS J100135.92+024116.6	150.3996564	2.6879556	18.25	8.46	21600	nl	0.2161	0.0001	4
COSMOS J100136.23+015443.1	150.4009552	1.9119680	21.18	13.60	16800	bl	2.2806	0.0022	2
COSMOS J100136.37+024727.0	150.4015449	2.7908195	21.09	8.81	21600	bl	0.9200	0.0057	4
SDSS J100136.50+025303.7	150.4020900	2.8843500	19.21	7.69	0	bl	2.1172	0.0017	4
COSMOS J100136.59+014251.0	150.4024506	1.7141711	23.41	2.13	13080	nla	0.8696	0.0007	4
COSMOS J100136.71+022323.7	150.4029694	2.3899240	23.40	2.79	9000	?	-1.0000	-1.0000	0
COSMOS J100137.35+024323.9	150.4056109	2.7233062	22.41	0.45	21600	bl	1.2660	0.0079	1
COSMOS J100137.38+023105.2	150.4057300	2.5181020	21.44	6.25	18000	nl	0.8777	0.0001	4
COSMOS J100137.51+020432.5	150.4062805	2.0757051	23.02	1.99	16800	bl	1.2570	0.0094	4
COSMOS J100137.60+022155.9	150.4066467	2.3655140	22.06	4.90	9000	bl	2.0416	0.0058	4
COSMOS J100137.84+015203.7	150.4076843	1.8677000	22.38	3.51	16800	a	0.3356	0.0014	2

Table 2.2—Continued

Object Name	RA (J2000) ^a degrees	Dec (J2000) degrees	i_{CFHT}^+ AB mag	S/N	t_{exp} sec	Type	z	σ_z	z_{conf}^b
COSMOS J100139.10+023824.2	150.4129000	2.6400470	22.60	5.44	18000	a	0.4888	0.0002	4
SDSS J100139.76+022548.7	150.4156700	2.4302000	15.21	26.05	12720	a	0.1241	0.0002	4
COSMOS J100139.82+023132.9	150.4159241	2.5258100	22.81	0.01	9000	bl	1.4436	0.0080	4
COSMOS J100140.36+015836.1	150.4181671	1.9767011	20.81	5.80	16800	nl	0.8634	0.0002	4
COSMOS J100140.96+015643.3	150.4206848	1.9453551	18.84	32.23	16800	bl	2.1811	0.0006	4
COSMOS J100141.01+020644.8	150.4208832	2.1124411	23.15	2.80	16800	bl	1.2629	0.0102	1
COSMOS J100141.09+021300.0	150.4212036	2.2166679	21.43	7.60	9000	bl	0.6212	0.0003	4
COSMOS J100141.26+022308.0	150.4219360	2.3855500	23.42	0.21	9000	bl	1.5142	0.0045	4
COSMOS J100141.33+021031.5	150.4222107	2.1754150	20.75	0.01	16800	bl	0.9820	0.0007	4
COSMOS J100141.41+020051.1	150.4225464	2.0141990	21.77	5.94	16800	bl	2.2699	0.0049	3
COSMOS J100141.88+024927.7	150.4245130	2.8243716	21.52	7.32	21600	nl	0.7373	0.0002	4
SDSS J100141.99+020358.4	150.4249500	2.0662200	16.10	21.33	0	a	0.1248	0.0002	4
COSMOS J100142.23+023633.5	150.4259400	2.6093190	22.98	2.41	18000	?	-1.0000	-1.0000	0
SDSS J100142.35+014058.1	150.4264700	1.6828000	17.30	8.18	13080	a	0.2179	0.0001	4
COSMOS J100142.51+020459.1	150.4271240	2.0830841	21.51	6.10	16800	?	-1.0000	-1.0000	0

Table 2.2—Continued

Object Name	RA (J2000) ^a degrees	Dec (J2000) degrees	i_{CFHT}^+ AB mag	S/N	t_{exp} sec	Type	z	σ_z	z_{conf}^b
COSMOS J100143.03+014932.2	150.4293060	1.8256110	21.89	5.61	16800	bl	2.0763	0.0050	4
COSMOS J100143.21+023252.2	150.4300600	2.5478460	15.12	89.06	18000	star	0.0000	0.0000	4
COSMOS J100143.44+015607.0	150.4310150	1.9352640	21.18	9.71	16800	bl	2.1809	0.0081	4
SDSS J100145.16+022456.9	150.4381500	2.4158100	20.55	3.59	0	bl	2.0318	0.0008	4
COSMOS J100145.58+024212.6	150.4399200	2.7034960	23.08	2.15	18000	bl	3.4650	0.0005	4
COSMOS J100146.15+024549.8	150.4422900	2.7638260	23.37	1.43	18000	nl	0.5047	0.0001	3
COSMOS J100147.25+024458.4	150.4468800	2.7495650	21.83	1.72	21600	?	-1.0000	-1.0000	0
COSMOS J100147.26+024729.4	150.4469100	2.7914950	21.84	5.94	18000	bl	1.5289	0.0002	4
COSMOS J100148.31+014519.3	150.4512939	1.7553630	16.11	110.45	14160	star	0.0000	0.0000	4
COSMOS J100148.33+012956.1	150.4513702	1.4989164	21.85	3.51	14160	bl	1.4819	0.0039	4
COSMOS J100149.00+024821.8	150.4541507	2.8060473	21.20	9.94	21600	bl	1.6081	0.0005	4
COSMOS J100149.60+023853.3	150.4566486	2.6481437	20.51	8.57	21600	bl	2.0566	0.0009	4
COSMOS J100149.84+020345.0	150.4576569	2.0624869	21.69	10.45	17160	bl	2.3337	0.0038	2
COSMOS J100150.53+015836.5	150.4605255	1.9768170	23.37	1.36	17160	?	-1.0000	-1.0000	0
COSMOS J100151.11+020032.7	150.4629669	2.0090771	20.07	30.68	17160	bl	0.9644	0.0052	4

Table 2.2—Continued

Object Name	RA (J2000) ^a	Dec (J2000)	i_{CFHT}^+	S/N	t_{exp}	Type	z	σ_z	z_{conf}^b
	degrees	degrees	AB mag		sec				
COSMOS J100152.23+015608.7	150.4676056	1.9357440	21.86	3.65	17160	nl	0.9693	0.0006	4
COSMOS J100153.29+022436.7	150.4720595	2.4102081	19.99	21.93	18360	nla	0.6667	0.0002	4
COSMOS J100153.45+021152.8	150.4727100	2.1979920	19.31	7.97	18360	a	0.4773	0.0009	3
COSMOS J100153.91+020538.8	150.4746246	2.0941191	23.01	1.91	17160	?	-1.0000	-1.0000	0
COSMOS J100155.61+021623.4	150.4816995	2.2731785	20.94	19.66	18360	?	-1.0000	-1.0000	0
COSMOS J100156.24+020943.4	150.4843445	2.1620519	21.99	22.42	17160	bl	1.6411	0.0049	4
COSMOS J100156.44+014811.3	150.4851837	1.8031430	21.88	5.41	14160	nl	0.9573	0.0003	4
COSMOS J100156.79+025312.3	150.4866168	2.8867513	19.97	16.52	19200	nla	0.6229	0.0003	4
COSMOS J100157.57+015205.1	150.4898834	1.8680919	21.46	1.10	17160	?	-1.0000	-1.0000	0
COSMOS J100157.76+023804.9	150.4906716	2.6346936	19.21	22.60	19200	nla	0.3452	0.0024	4
COSMOS J100158.00+014621.4	150.4916840	1.7726210	20.69	6.42	14160	nl	0.8314	0.0002	4
COSMOS J100158.96+022445.2	150.4956590	2.4125469	21.38	0.64	18360	bl	1.3686	0.0012	4
COSMOS J100159.16+020521.5	150.4964905	2.0893090	22.00	2.71	17160	a	-1.0000	-1.0000	0
COSMOS J100159.43+023935.6	150.4976059	2.6598934	20.60	7.06	19200	bl	0.8535	0.0006	4
COSMOS J100159.44+015140.2	150.4976807	1.8611670	21.40	1.05	17160	?	-1.0000	-1.0000	0

Table 2.2—Continued

Object Name	RA (J2000) ^a degrees	Dec (J2000) degrees	i_{CFHT}^+ AB mag	S/N	t_{exp} sec	Type	z	σ_z	z_{conf}^b
COSMOS J100159.79+022641.6	150.4991297	2.4449014	19.38	25.11	18360	bl	2.0313	0.0002	4
COSMOS J100159.80+013431.8	150.4991455	1.5755020	20.28	19.06	14160	nl	0.5176	0.0001	4
COSMOS J100159.86+013135.3	150.4994202	1.5264790	21.48	7.63	14160	bl	0.9774	0.0014	3
COSMOS J100200.34+022115.0	150.5014003	2.3541762	22.97	1.01	18360	nl	0.2367	0.0002	2
COSMOS J100201.20+023151.6	150.5049800	2.5309940	21.08	15.02	19200	nla	0.6435	0.0001	4
COSMOS J100201.31+024029.6	150.5054736	2.6748943	22.57	3.93	19200	bl	1.2900	0.0154	2
COSMOS J100201.32+013232.8	150.5054932	1.5424560	22.55	2.07	14160	bl	2.0602	0.0144	1
SDSS J100201.51+020329.4	150.5063100	2.0581700	18.34	15.01	0	bl	2.0077	0.0017	4
COSMOS J100202.22+024157.8	150.5092612	2.6993800	21.15	6.17	19200	bl	0.7935	0.0043	4
COSMOS J100202.55+020145.3	150.5106354	2.0292540	20.94	7.12	17160	nl	0.8977	0.0001	4
COSMOS J100202.77+025102.6	150.5115263	2.8507211	22.03	5.03	19200	?	-1.0000	-1.0000	0
SDSS J100202.78+022434.6	150.5115700	2.4096100	20.50	4.89	0	bl	0.9877	0.0015	4
COSMOS J100204.36+023118.1	150.5181826	2.5216848	22.50	0.01	18360	bl	2.7785	0.0014	4
COSMOS J100204.58+021915.5	150.5190755	2.3209692	22.48	2.97	18360	bl	1.8281	0.0024	1
COSMOS J100205.03+023731.5	150.5209760	2.6254150	18.94	7.83	19200	bnl	0.5189	0.0001	4

Table 2.2—Continued

Object Name	RA (J2000) ^a	Dec (J2000)	i_{CFHT}^+	S/N	t_{exp}	Type	z	σ_z	z_{conf}^b
	degrees	degrees	AB mag		sec				
COSMOS J100205.34+024045.1	150.5222600	2.6791960	23.05	1.62	19200	a	0.7464	0.0001	1
COSMOS J100206.29+021441.8	150.5261989	2.2449394	21.53	12.41	18360	bl	1.2711	0.0012	3
COSMOS J100206.43+022304.8	150.5267724	2.3846758	22.50	0.01	18360	bl	1.2995	0.0017	3
COSMOS J100206.49+020218.3	150.5270386	2.0384042	23.41	0.01	17160	?	-1.0000	-1.0000	-1
COSMOS J100207.65+021120.2	150.5318604	2.1889460	21.77	9.42	17160	nl	0.8300	0.0052	4
COSMOS J100208.54+014553.7	150.5355988	1.7649230	21.52	10.20	14160	bl	2.2152	0.0030	4
COSMOS J100208.75+024103.1	150.5364649	2.6841924	23.23	1.70	19200	?	-1.0000	-1.0000	0
COSMOS J100209.09+021837.8	150.5378872	2.3104911	21.37	4.36	18360	nla	0.8379	0.0002	4
COSMOS J100209.27+025119.7	150.5386416	2.8554680	21.57	0.32	19200	?	-1.0000	-1.0000	0
COSMOS J100209.67+021004.1	150.5402985	2.1678157	22.54	1.85	17160	nla	1.2550	0.0078	2
COSMOS J100209.70+023432.3	150.5404193	2.5756293	21.09	14.44	18360	a	0.6076	0.0003	4
COSMOS J100210.25+023621.2	150.5427227	2.6058927	22.12	6.67	19200	bl	0.9800	0.0060	1
COSMOS J100210.44+025557.0	150.5434998	2.9324866	21.51	1.16	19200	?	-1.0000	-1.0000	0
COSMOS J100210.56+022523.0	150.5439926	2.4230538	22.10	5.00	18360	nla	0.9575	0.0003	4
SDSS J100210.73+023026.1	150.5446900	2.5072400	19.48	6.01	0	bl	1.1607	0.0012	4

Table 2.2—Continued

Object Name	RA (J2000) ^a degrees	Dec (J2000) degrees	i_{CFHT}^+ AB mag	S/N	t_{exp} sec	Type	z	σ_z	z_{conf}^b
COSMOS J100211.27+013706.7	150.5469666	1.6185180	22.39	2.02	14160	a	0.7844	0.0019	2
COSMOS J100212.11+014232.4	150.5504456	1.7089911	20.32	17.03	14160	bl	0.3687	0.0001	4
COSMOS J100212.26+022614.1	150.5511021	2.4372460	22.53	2.36	18360	nl	0.8929	0.0002	3
COSMOS J100213.17+023827.6	150.5548748	2.6410093	21.14	0.01	19200	bl	1.1417	0.0061	3
COSMOS J100213.34+022208.9	150.5555645	2.3691440	23.04	1.29	18360	nl	0.9736	0.0002	2
COSMOS J100213.42+023351.7	150.5559085	2.5643538	21.87	9.49	19200	bl	1.1433	0.0011	3
COSMOS J100214.17+020620.8	150.5590363	2.1057889	22.33	15.81	17160	bl	1.2651	0.0013	2
COSMOS J100215.35+015405.2	150.5639648	1.9014330	23.17	1.77	17160	?	-1.0000	-1.0000	0
COSMOS J100216.15+023012.8	150.5672900	2.5035650	21.07	1.23	18360	bl	1.1461	0.0022	4
COSMOS J100216.37+015008.2	150.5682220	1.8356010	21.04	10.32	17160	a	0.6740	0.0003	4
COSMOS J100216.76+013725.2	150.5698395	1.6236540	20.44	8.67	14160	nl	0.6212	0.0001	4
COSMOS J100217.43+022959.7	150.5726228	2.4999089	20.62	27.33	18360	bl	1.1022	0.0016	4
COSMOS J100217.54+021212.5	150.5730734	2.2034584	20.65	7.66	18360	nla	0.8187	0.0004	4
COSMOS J100218.32+021053.1	150.5763245	2.1814060	19.40	6.35	17160	bl	0.5545	0.0011	4
COSMOS J100218.71+024139.0	150.5779395	2.6941632	22.58	2.36	19200	?	-1.0000	-1.0000	0

Table 2.2—Continued

Object Name	RA (J2000) ^a degrees	Dec (J2000) degrees	i_{CFHT}^+ AB mag	S/N	t_{exp} sec	Type	z	σ_z	z_{conf}^b
COSMOS J100218.84+024604.7	150.5784877	2.7679616	21.98	0.01	19200	?	-1.0000	-1.0000	0
COSMOS J100219.48+021315.7	150.5811500	2.2210311	22.24	6.82	18360	bl	2.0302	0.0093	4
SDSS J100219.51+015537.1	150.5812800	1.9269600	20.46	4.44	0	bl	1.5091	0.0029	4
COSMOS J100219.65+021715.7	150.5818667	2.2876972	21.41	2.87	18360	bl	1.3393	0.0020	4
COSMOS J100221.92+021035.1	150.5913367	2.1764069	22.15	3.62	18360	a	1.2640	0.0079	1
COSMOS J100222.99+020639.9	150.5957947	2.1110830	21.44	9.52	17160	nl	0.8992	0.0002	4
COSMOS J100223.02+022009.7	150.5959370	2.3360358	22.74	4.77	18360	?	-1.0000	-1.0000	-1
COSMOS J100223.05+014714.9	150.5960236	1.7874740	21.05	6.66	14160	bnl	1.2426	0.0003	4
COSMOS J100223.36+023704.5	150.5973533	2.6179241	21.74	10.48	19200	bl	1.4429	0.0018	3
COSMOS J100224.16+023107.7	150.6006608	2.5187968	21.68	6.09	19200	a	0.6689	0.0002	4
COSMOS J100225.19+014516.4	150.6049500	1.7545470	18.90	37.37	14160	a	0.2667	0.0001	4
COSMOS J100225.70+015606.5	150.6070709	1.9351300	21.35	3.25	17160	?	-1.0000	-1.0000	0
SDSS J100226.33+021923.2	150.6096900	2.3231100	20.15	4.08	0	bl	1.2945	0.0013	4
COSMOS J100226.74+014052.0	150.6114349	1.6811010	18.67	31.23	14160	nl	0.2468	0.0001	4
COSMOS J100226.93+015940.1	150.6122131	1.9944770	21.54	8.41	17160	bl	1.6092	0.0036	4

Table 2.2—Continued

Object Name	RA (J2000) ^a degrees	Dec (J2000) degrees	i_{CFHT}^+ AB mag	S/N	t_{exp} sec	Type	z	σ_z	z_{conf}^b
COSMOS J100228.15+022857.9	150.6173077	2.4827498	23.11	0.01	19200	bl	2.7456	0.0004	4
COSMOS J100228.68+024901.8	150.6194900	2.8171620	17.84	24.85	19200	nl	0.2127	0.0001	4
COSMOS J100228.82+023732.0	150.6200640	2.6255647	22.07	10.99	19200	nl	0.7252	0.0002	3
COSMOS J100228.82+024016.9	150.6200645	2.6713620	22.07	4.40	19200	bl	3.1440	0.0014	4
COSMOS J100228.95+013544.5	150.6206207	1.5956990	20.45	13.32	14160	nl	0.5846	0.0001	4
COSMOS J100229.22+020931.5	150.6217499	2.1587389	20.30	7.73	17160	bl	1.5228	0.0009	4
COSMOS J100229.33+014528.1	150.6222076	1.7578099	20.17	27.07	14160	bl	0.8761	0.0006	4
COSMOS J100230.06+014810.4	150.6252441	1.8028811	19.61	16.61	14160	bl	0.6263	0.0001	4
COSMOS J100230.65+024427.6	150.6276900	2.7409880	20.25	8.07	19200	bnl	0.8212	0.0003	4
COSMOS J100230.84+022453.0	150.6284924	2.4147256	19.43	27.68	18360	nl	0.1957	0.0001	4
COSMOS J100230.94+015520.7	150.6289062	1.9224130	16.29	48.07	17160	?	-1.0000	-1.0000	0
COSMOS J100231.26+022716.4	150.6302412	2.4545462	20.22	20.00	18360	a	0.8152	0.0003	4
COSMOS J100231.52+014257.2	150.6313171	1.7158900	23.08	1.97	14160	bl	2.2429	0.0253	1
COSMOS J100231.54+020009.7	150.6314240	2.0027039	23.18	2.35	17160	?	-1.0000	-1.0000	0
COSMOS J100231.91+023507.5	150.6329692	2.5854031	22.12	8.34	19200	nl	0.8781	0.0004	3

Table 2.2—Continued

Object Name	RA (J2000) ^a	Dec (J2000)	i_{CFHT}^+	S/N	t_{exp}	Type	z	σ_z	z_{conf}^b
	degrees	degrees	AB mag		sec				
SDSS J100232.13+023537.3	150.6338700	2.5937000	18.74	14.38	19200	bl	0.6577	0.0001	4
COSMOS J100232.15+022925.6	150.6339666	2.4904466	20.88	5.89	19200	a	0.7953	0.0003	4
COSMOS J100232.35+020956.2	150.6347943	2.1656175	20.96	6.06	18360	?	-1.0000	-1.0000	-1
COSMOS J100232.52+014009.0	150.6354980	1.6691750	20.87	16.57	14160	bl	1.7900	0.0120	4
COSMOS J100232.91+020027.6	150.6371002	2.0076780	21.76	7.10	17160	nl	1.2679	0.0001	4
COSMOS J100233.37+022751.9	150.6390455	2.4644081	20.93	12.00	18360	nla	0.7999	0.0002	4
COSMOS J100233.64+021541.9	150.6401594	2.2616446	21.35	6.98	18360	bnl	1.4126	0.0003	4
SDSS J100234.33+015011.3	150.6430400	1.8364600	18.63	8.28	0	bl	1.5057	0.0018	4
SDSS J100234.85+024253.3	150.6452100	2.7148000	18.23	7.79	0	bl	0.1960	0.0012	4
COSMOS J100234.99+022058.7	150.6457982	2.3496260	22.82	1.80	18360	?	-1.0000	-1.0000	0
COSMOS J100235.50+022351.3	150.6479007	2.3975739	20.84	14.80	18360	nla	0.6770	0.0002	4
COSMOS J100236.51+020217.6	150.6521149	2.0382121	19.01	25.67	17160	?	-1.0000	-1.0000	0
SDSS J100236.71+015948.8	150.6529500	1.9968900	19.92	3.86	0	bl	1.5157	0.0016	4
COSMOS J100237.04+013207.1	150.6543121	1.5352980	23.47	1.78	14160	?	-1.0000	-1.0000	0
COSMOS J100237.09+014648.0	150.6545410	1.7800003	20.52	11.70	14160	a	0.6682	0.0003	4

Table 2.2—Continued

Object Name	RA (J2000) ^a degrees	Dec (J2000) degrees	i_{CFHT}^+ AB mag	S/N	t_{exp} sec	Type	z	σ_z	$z_{\text{conf}}^{\text{b}}$
COSMOS J100237.92+024700.6	150.6579900	2.7835100	17.86	22.20	19200	bl	0.2116	0.0001	4
SDSS J100238.25+013746.7	150.6593800	1.6296500	19.28	13.89	0	bl	2.5059	0.0011	4
COSMOS J100238.62+015831.5	150.6609344	1.9754250	21.26	10.70	17160	nl	0.9250	0.0002	2
COSMOS J100238.63+024743.1	150.6609520	2.7953133	21.89	1.90	19200	a	0.8220	0.0003	3
COSMOS J100238.70+013936.7	150.6612549	1.6602060	20.57	18.10	14160	bl	1.3152	0.0006	4
COSMOS J100239.48+023201.1	150.6644953	2.5336317	22.87	2.49	19200	nl	1.0575	0.0001	3
COSMOS J100240.30+020147.3	150.6679077	2.0298059	21.87	5.91	17160	a	0.6383	0.0006	4
COSMOS J100240.32+013659.5	150.6679993	1.6165160	19.84	12.82	14160	nla	0.3711	0.0001	4
COSMOS J100240.93+023448.4	150.6705299	2.5801151	22.31	5.30	19200	bl	1.6770	0.0111	4
COSMOS J100241.29+013109.5	150.6720428	1.5193180	22.80	2.12	14160	bl	1.7824	0.0178	2
COSMOS J100241.33+021550.7	150.6721889	2.2640896	21.04	7.86	18360	a	0.5430	0.0037	2
COSMOS J100241.73+021615.2	150.6738735	2.2708985	20.24	7.45	18360	nl	0.3871	0.0002	4
COSMOS J100243.85+020502.7	150.6827240	2.0840709	20.74	20.41	17160	bl	1.2338	0.0005	4
COSMOS J100243.93+022340.7	150.6830585	2.3946347	21.13	3.82	18360	a	0.6606	0.0005	3
COSMOS J100243.96+023428.6	150.6831560	2.5746237	18.86	9.25	19200	bl	0.3757	0.0002	4

Table 2.2—Continued

Object Name	RA (J2000) ^a degrees	Dec (J2000) degrees	i_{CFHT}^+ AB mag	S/N	t_{exp} sec	Type	z	σ_z	z_{conf}^b
COSMOS J100245.95+015458.9	150.6914520	1.9163550	21.58	6.51	17160	nla	0.4470	0.0001	4
COSMOS J100248.87+013855.3	150.7036133	1.6486980	20.87	5.38	14160	nl	0.6938	0.0001	4
COSMOS J100249.33+023746.5	150.7055610	2.6295879	20.23	7.84	19200	bl	2.1236	0.0007	4
COSMOS J100249.56+015532.8	150.7064972	1.9257820	20.26	12.56	17160	nl	0.3090	0.0001	4
COSMOS J100249.92+021732.3	150.7080154	2.2923157	21.17	17.11	18360	bl	1.0984	0.0021	3
COSMOS J100250.22+020850.8	150.7092434	2.1474569	19.79	21.80	18360	nl	0.3256	0.0001	4
COSMOS J100250.86+024203.6	150.7119229	2.7010096	22.59	2.22	19200	nl	0.9818	0.0002	4
COSMOS J100251.42+021849.8	150.7142338	2.3138296	20.18	15.01	18360	nla	0.6065	0.0002	4
SDSS J100251.62+022905.5	150.7151000	2.4848500	19.62	9.35	0	bl	2.0051	0.0014	4
COSMOS J100251.99+021007.4	150.7166443	2.1687319	23.48	1.29	17160	?	-1.0000	-1.0000	0
COSMOS J100252.33+013319.8	150.7180634	1.5555050	21.13	10.71	14160	nl	0.9366	0.0002	4
COSMOS J100252.85+021452.8	150.7202002	2.2480031	21.11	13.02	18360	nl	0.6652	0.0002	4
COSMOS J100252.88+025426.8	150.7203392	2.9074407	19.95	11.25	19200	bl	0.7952	0.0004	3
COSMOS J100253.12+013456.4	150.7213593	1.5823300	22.95	2.13	14160	bl	2.2481	0.0141	1
COSMOS J100255.88+013730.6	150.7328491	1.6251670	20.58	22.51	14160	bl	2.3888	0.0010	2

Table 2.2—Continued

Object Name	RA (J2000) ^a	Dec (J2000)	i_{CFHT}^+	S/N	t_{exp}	Type	z	σ_z	z_{conf}^b
	degrees	degrees	AB mag		sec				
COSMOS J100256.05+020923.2	150.7335312	2.1564556	20.70	8.57	18360	bl	0.9790	0.0011	3
COSMOS J100256.92+024321.2	150.7371773	2.7225519	22.25	1.04	19200	bl	3.3223	0.0017	3
COSMOS J100257.46+015405.7	150.7394257	1.9015880	21.39	8.14	17160	bl	0.9712	0.0012	3
COSMOS J100258.21+015909.3	150.7425537	1.9859101	21.85	7.86	17160	bl	1.5971	0.0027	4
COSMOS J100258.35+024355.7	150.7431290	2.7321252	22.37	3.92	19200	bl	1.5159	0.0005	2
COSMOS J100258.41+021013.9	150.7433847	2.1705212	21.44	4.81	18360	?	-1.0000	-1.0000	-1
SDSS J100302.93+015208.6	150.7622200	1.8690600	19.96	7.25	0	bl	1.8001	0.0014	4
COSMOS J100303.70+021051.7	150.7654100	2.1810220	19.80	7.55	18360	nla	0.5581	0.0001	4
COSMOS J100305.08+015156.6	150.7711639	1.8657269	20.94	11.22	17160	nl	0.9687	0.0001	3
COSMOS J100305.96+022753.2	150.7748449	2.4647771	21.89	4.75	18360	bl	0.9791	0.0009	2
COSMOS J100306.70+021345.0	150.7779369	2.2291529	20.85	9.03	18360	nl	0.1030	0.0001	4
COSMOS J100307.03+023121.0	150.7793119	2.5225074	23.38	0.79	19200	?	-1.0000	-1.0000	0
COSMOS J100307.68+021514.9	150.7819800	2.2541430	20.91	6.78	18360	nl	0.6970	0.0001	4
COSMOS J100307.82+021135.1	150.7825775	2.1930730	20.57	11.12	17160	nl	0.5824	0.0001	4
COSMOS J100308.83+020903.6	150.7867889	2.1509969	21.43	4.72	17160	a	-1.0000	-1.0000	0

We summarize the efficiencies, from X-ray sources to targeting to redshifts, in Table 2.3.

2.3.2 AGN, Starbursts, and Quiescent Galaxies

We use the following X-ray emission diagnostics to classify the 485 high-confidence extragalactic objects as AGN:

$$L_{0.5-10 \text{ keV}} > 3 \times 10^{42} \text{ erg s}^{-1} \quad (2.1)$$

$$\log f_X/f_O \geq -1, \text{ where } \log f_X/f_O = \log(f_X) + i_{\text{AB}}/2.5 + 5.352 \quad (2.2)$$

Each of these criteria have been shown by several authors to reliably (albeit conservatively) select AGN (e.g., Hornschemeier et al., 2001; Alexander et al., 2001; Bauer et al., 2004; Bundy et al., 2008), although it is important to note that bona fide AGN (e.g., LINERs and other low-luminosity AGN) can be much less X-ray bright than these criteria. Equation 1 is derived from the fact that purely star-forming galaxies in the local universe do not exceed $L_{0.5-10\text{keV}} \simeq 3 \times 10^{42} \text{ erg s}^{-1}$ (e.g., Fabbiano, 1989; Colbert et al., 2004). The X-ray luminosities of the sources are shown in Figure 2.9 along with the X-ray flux limit. Nearly all of the Type 1 AGN (marked as crosses) lie above the AGN luminosity threshold. Equation 2 is the traditional “AGN locus” defined by Maccacaro et al. (1988), shown for the sample in Figure 2.10. Objects marked with x’s have $L_{0.5-10\text{keV}} > 3 \times 10^{42} \text{ erg s}^{-1}$, revealing that the two methods heavily overlap, with 94% (405/432) of the objects that satisfy one of the criteria additionally meeting both. Only 53 “nl” and “a” objects do not meet either of the X-ray criteria, leaving us with 432 X-ray AGN that meet either Eq. 1 or Eq. 2 and have high-confidence redshifts.

Using either Equations 1 or 2 selects all of the spectroscopically identified Type 1 AGN, but it still may exclude some obscured AGN. The source classification diagnostic diagrams, based on the optical emission line measurements Baldwin, Philips,

Table 2.2—Continued

Object Name	RA (J2000) ^a degrees	Dec (J2000) degrees	i_{CFHT}^+ AB mag	S/N	t_{exp} sec	Type	z	σ_z	z_{conf}^b
SDSS J100309.21+022038.4	150.7883700	2.3440100	20.06	5.28	0	bl	1.9555	0.0014	4
COSMOS J100312.45+020002.2	150.8018646	2.0006139	21.49	6.88	17160	bl	1.7843	0.0068	4

^aThe RA and Dec refer to the optical counterpart of the X-ray source, which is where the slit was centered.

^bFrom empirical measurements, the redshift confidence was found to correspond to correct redshift likelihoods of 97%, 90%, 75%, and 33% for $z_{\text{conf}} = 4, 3, 2, 1$, respectively. The redshift confidences are fully explained in §3.1.

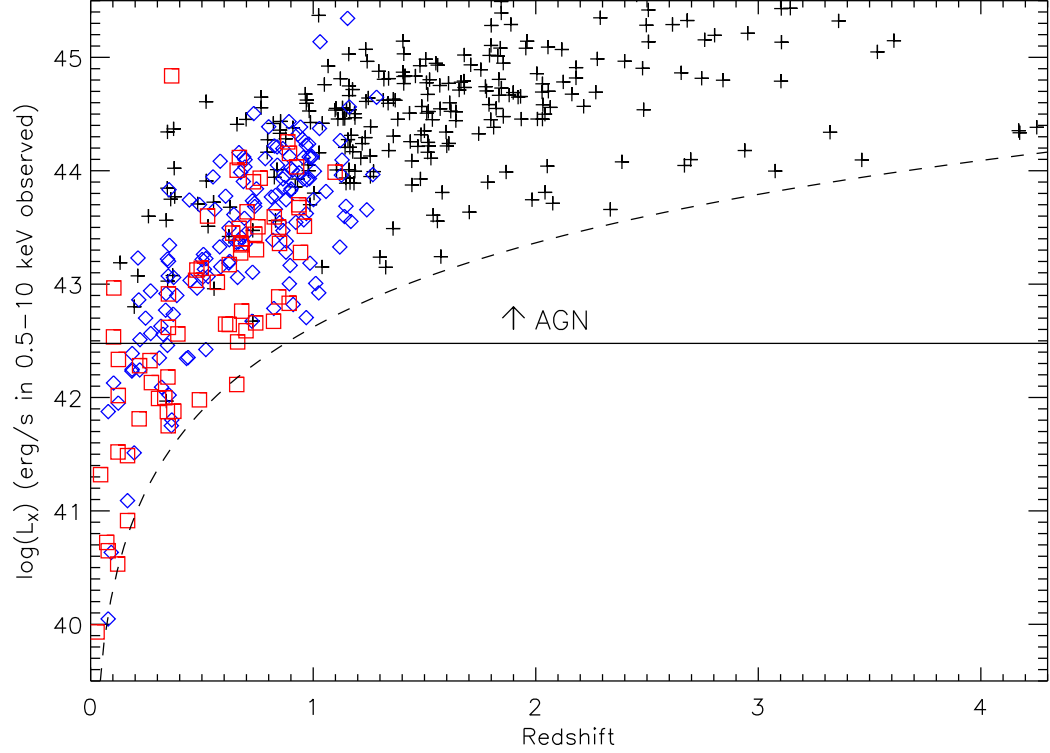


Figure 2.9 The observed 0.5–10 keV X-ray luminosities for $z_{\text{conf}} \geq 3$ objects with redshift. We label objects classified as “bl” (Type 1 AGN) with black crosses, “nl” with blue diamonds, and “a” with red squares. The dashed line shows the survey’s limiting luminosity from the XMM flux limit. The AGN luminosity cut of $L_{0.5-10\text{keV}} = 3 \times 10^{42}$ is drawn as a solid line: all “nl” and “a” above this line are AGN. Objects below this line, however, are not necessarily inactive: two Type 1 AGN are less luminous, and the luminosity limit is conservative.

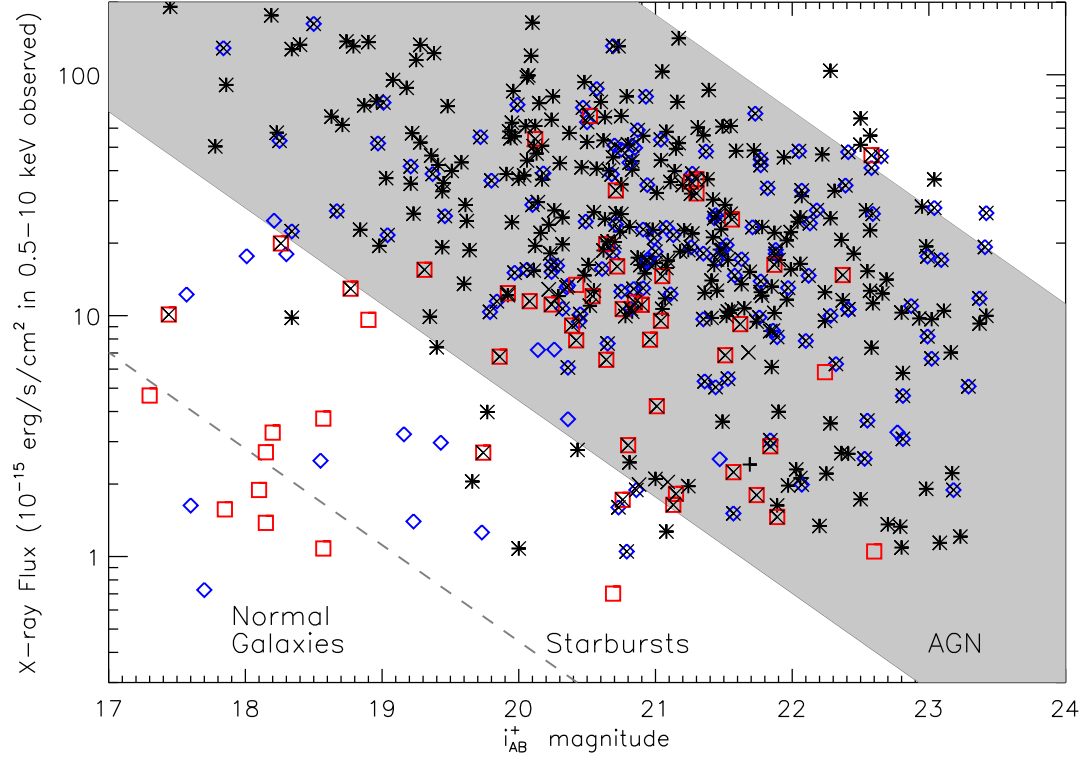


Figure 2.10 The X-ray flux vs. the i_{AB}^+ magnitude for the $z_{\text{conf}} \geq 3$ objects. The AGN locus of $-1 \leq \log f_X/f_O \leq 1$ (Maccacaro et al., 1988, , see also Equation 2) is shown by the gray shaded region, along with approximate boundary between quiescent and star-forming galaxies at $\log f_X/f_O = -2$ (Bauer et al., 2004). Black crosses are targets classified “bl” (Type 1 AGN), blue diamonds are “nl,” and red squares are “a” objects. We additionally mark all targets of $L_{0.5-10\text{keV}} > 3 \times 10^{42}$ with black x’s. We consider targets either in the AGN locus or with $L_X > 3 \times 10^{42}$ to be AGN: this includes all of the “bl” spectra and all but 53 of the “nl” and “a” spectra.

Table 2.3. Targeting and Redshift Yields

X-ray Sources	16-Field	Per Field		
	Total	Minimum	Maximum	Median
All Sources	1640	68	145	105
$i_{\text{AB}}^+ < 23.5$	1310	55	110	86
Targeted	677	9	74	38
Classified ($z_{\text{conf}} > 0$)	573	9	63	30
$z_{\text{conf}} = 3, 4$ Redshifts	485	8	53	26
$z_{\text{conf}} = 3, 4$ with Hectospec	117	1	27	6
$z_{\text{conf}} = 3, 4$ with SDSS	76	2	12	4

& Terlevich (1981, BPT), are usually quite effective in classifying narrow emission line spectra as star forming galaxies or Type 2 AGN, with a sound theoretical basis (Kewley et al., 2001) and use in many surveys (e.g., Kauffmann et al., 2003; Tremonti et al., 2004). The BPT diagnostic uses ratios of nebular emission lines ($[\text{OIII}]\lambda 5007/\text{H}\beta$ and $[\text{NII}]\lambda 6583/\text{H}\alpha$) to distinguish between thermal emission from star formation and nonthermal AGN emission. However, there are two limitations to the BPT diagnostic that make it inapplicable to our sample. First, most of the object do not have the appropriate lines in their observed wavelength range: most of the “nl” objects are at higher redshift and we are limited by the spectral range of IMACS. In addition, accurately measuring the line ratios requires correcting for absorption in $\text{H}\alpha$ and $\text{H}\beta$ from old stellar populations. Because the spectra have low resolution and limited wavelength range, we are unable to accurately fit and

account for stellar absorption.

The color-based diagnostic of Smolčić et al. (2008) can be used to further classify the narrow emission and absorption line spectra which do not satisfy Equations 1 and 2 but are nonetheless AGN. This selection technique is based on the a tight correlation in the local universe between the emission line flux ratios utilized for the spectroscopic BPT selection and the galaxies’ rest-frame optical colors (Smolčić et al., 2008). The method has been well calibrated on the local SDSS/NVSS sample in Smolčić et al. (2008) and successfully applied to the radio VLA-COSMOS data (Smolčić et al., 2009). Following Smolčić et al. (2009) the rest-frame color for the narrow line AGN was computed by fitting each galaxy’s observed optical-to-NIR SED (Capak et al., 2007), de-redshifted using its spectroscopic redshift, with a library of 100,000 model spectra (Bruzual & Charlot, 2003). Smolčić et al. (2008) show that the color diagnostic is a good statistical measure, but may not be accurate for individual objects. So while it further indicates that 17/53 objects are obscured AGN outside the X-ray criteria, we do not include these objects as AGN and note only that the sample of 432 high-confidence X-ray AGN as defined by Equations 1 and 2 probably misses at least ~ 17 additional objects.

2.4 Completeness

Our targeting was based solely on the available X-ray data and the optical flux constraint of $i_{\text{AB}}^+ < 23.5$. While we were only able to target 52% (677/1310) of the available X-ray sources, the spectra obtained were constrained only by slit placement and so represent a random subset of the total X-ray population. Therefore our completeness limits can be determined from the success rate for the spectroscopy, which is dependent on optical magnitude, object type, and redshift. We characterize and justify the flux limits in §4.1 and 4.2, as well as the more detailed redshift

completeness in §4.3. Our goal is a purely X-ray and optical flux-limited sample of AGN, and so in §4.4 we account for the spectroscopic incompleteness to infer the AGN population to $f_{0.5-10\text{keV}} < 1 \times 10^{-15} \text{ erg cm}^{-2} \text{ s}^{-1}$ and $i_{\text{AB}}^+ \leq 23$.

2.4.1 X-ray Flux Limit

The first limit on the completeness is the target selection, which is limited in both X-ray and optical fluxes. The initial selection includes all XMM targets with X-ray flux limits of $1 \times 10^{-15} \text{ erg cm}^{-2} \text{ s}^{-1}$ in 0.5-2 keV or $6 \times 10^{-15} \text{ erg cm}^{-2} \text{ s}^{-1}$ in the hard 2-10 keV band with optical counterparts of $i_{\text{AB}}^+ \leq 23.5$. The X-ray flux limit means that we are complete in X-rays to all AGN with $L_{0.5-10 \text{ keV}} > 3 \times 10^{42} \text{ erg s}^{-1}$ (a classic AGN definition discussed in §3.2) at $z \lesssim 1$.

2.4.2 Optical Flux Limit

Our initial magnitude cut was $i_{\text{AB}}^+ \leq 23.5$, but this was designed to be more ambitious than the capabilities of Magellan/IMACS in 5-hour exposures. In Figure 2.11 we show the spectral signal-to-noise (S/N) with optical i_{AB}^+ magnitude for the targets from all IMACS exposures. The S/N was calculated by empirically measuring the noise in the central 6600-8200Å region of each spectrum. The S/N generally correlates with the optical brightness, with some scatter attributable to varied conditions over the three years of observations. The outliers with high S/N and faint magnitude are all emission line sources where a strong emission line lies in the spectrum but outside the observed i_{AB}^+ filter range. The low-S/N and bright magnitude objects of the lower left may be highly variable sources or targets with photometry contaminated by blending or nearby bright stars. The increasing number of unclassified targets (filled green circles) in Figure 2.11 shows that we do not identify all objects to $i_{\text{AB}}^+ \leq 23.5$.

In Figure 2.12 we show the completeness with i_{AB}^+ magnitude for the various

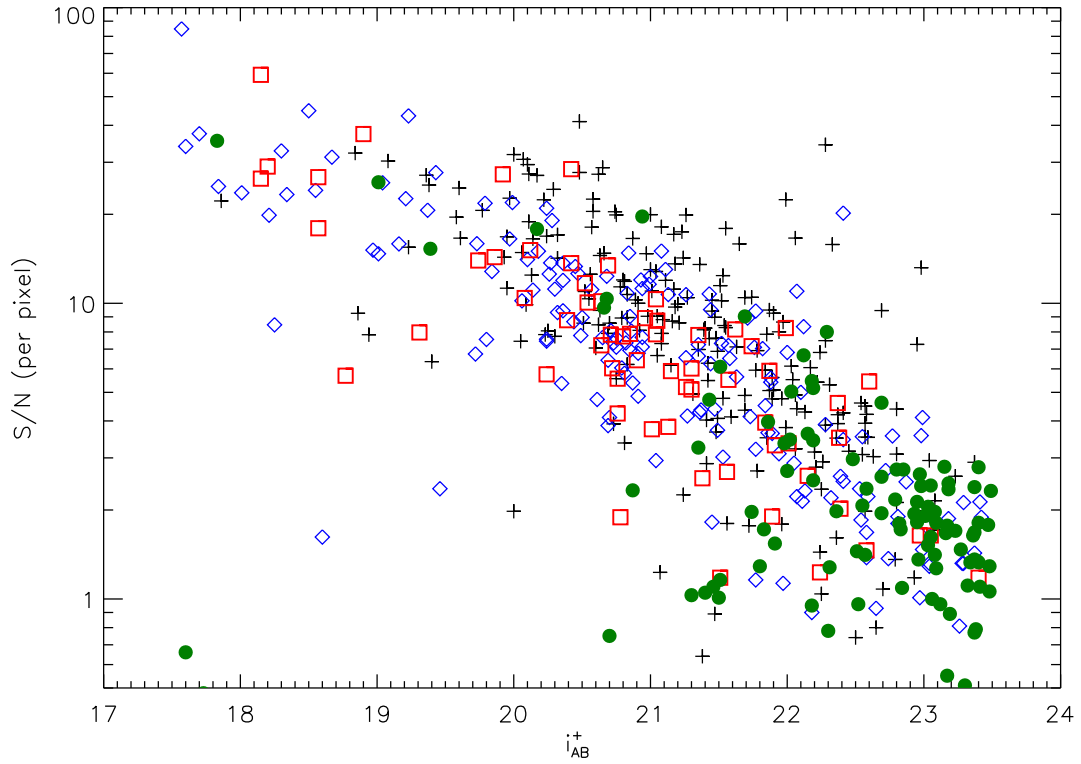


Figure 2.11 The signal-to-noise (S/N) and optical i_{AB}^+ magnitudes for the X-ray targets. Crosses indicate broad emission line spectra, diamonds are narrow emission line spectra, squares are absorption line spectra, and filled circles are unclassified objects. The S/N and optical magnitude are correlated, with scatter from varying conditions over three years of observing. The number of unidentified objects increases greatly at $i_{AB}^+ > 22$, although we still identify emission line spectra at the faintest magnitudes.

classifications. We assume that the identified fractions have Poisson counting errors from the number of the given type and the total number of targets in each magnitude bin. The survey completeness to all targets remains at $\sim 90\%$ to $i_{\text{AB}}^+ < 22$. The identification fractions of emission line targets remains nearly flat a magnitude deeper than the absorption line galaxies, although the fractions of “bl” and “nl” objects decrease slightly from $22 < i_{\text{AB}}^+ < 23$, within the noise.

The completeness is not uniform for all types of objects: the fraction of identified broad and narrow emission line targets remains statistically constant until $i_{\text{AB}}^+ \sim 22.5$, while the fraction of absorption line targets appears complete only to $i_{\text{AB}}^+ \sim 22$. Both narrow and broad emission lines generally exhibit two or more times the signal of their continuum, allowing for identification even when the objects’ broad-band magnitude and average S/N are low. Since different emission lines vary in strength, this also suggests that the identification of “bl” and “nl” may suffer from a redshift dependence (for instance, some redshifts may have only weak emission lines in their wavelength range, while others include several strong lines).

2.4.3 Redshift-Dependent Completeness

The strongest redshift dependence in the spectra come from targets with only one strong emission line in their observed IMACS spectra. The “a” type objects are well-populated with absorption lines and have redshift-independent classifications, but emission line spectra may have only one line in the observed 5600-9200 Å window (see Figure 2.6). The presence of only one emission line causes two problems: the redshift solution will be degenerate, and the line may be confused with noise if it is either narrow or broad but weak. The first problem means that we can only assign $z_{\text{conf}} = 2$ and we may also assign the wrong redshift (bright targets are an exception, since a redshift can be assigned based on strong continuum features). The second problem means that we might completely miss the AGN designation and assign it

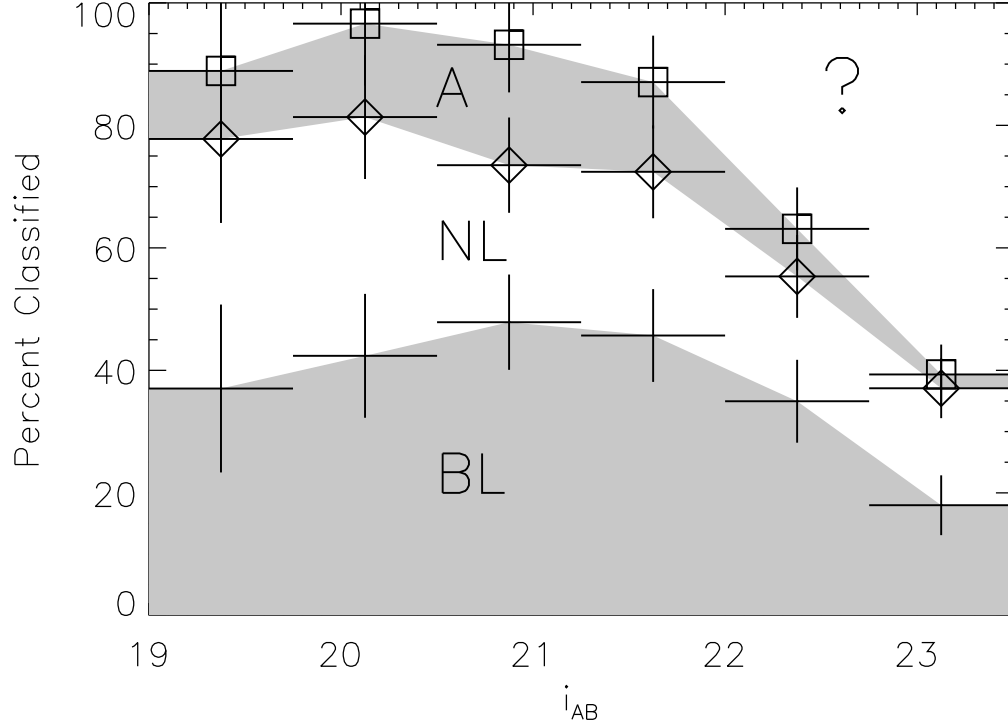


Figure 2.12 Cumulative completeness by classification type versus optical i_{AB}^+ magnitude. Each region (shaded or unshaded) indicates the relative fraction of broad emission line objects (“bl”), narrow emission line objects (“nl”), and absorption line (“a”) spectra. Targets with too low S/N to venture a classification are represented in the upper “?” region. Error bars on the points above each region are calculated assuming that, in each magnitude bin, both the number of each class and the total number have associated Poisson counting errors. The total completeness for each classification is $\sim 90\%$ to $i_{AB}^+ \leq 22$, although we can correct for the incompleteness of each spectral type to $i_{AB}^+ \leq 23$.

a “?” classification. At faint S/N levels, the pattern of two emission lines is much easier to identify over the noise, and so the lower completeness to single-line objects may mean both lower redshift confidence and a lower identification threshold.

We used Monte Carlo simulations to test the redshift and magnitude dependence of the survey’s completeness for emission line spectra. We assume that the SDSS Type 1 composite spectrum (Vanden Berk et al., 2001) and Type 2 composite spectrum (Zakamska et al., 2003) each have infinite signal-to-noise, and degrade these spectra with Gaussian-distributed random noise to represent broad and narrow emission line spectra of varying i_{AB}^+ magnitude. For each bin in magnitude, we calculate the median signal-to-noise of the observed spectra at that brightness, measured at both $\lambda < 8000\text{\AA}$ and in the noisier region with sky lines at $\lambda > 8000\text{\AA}$ (our spectra typically have S/N about 16% worse at $\lambda > 8000\text{\AA}$). Each artificial noise-added spectrum was then redshifted over several values and realized in the IMACS wavelength range (5600 \AA -9200 \AA). We then used the same `idlspec2d` redshift algorithm used on the data described in §3.1 to determine whether or not we would be able to assign the correct redshift with high-confidence ($z_{\text{conf}} = 3, 4$) for these artificial redshifted spectra (a redshift could not be determined if the emission lines were smeared out or if the spectrum could not be distinguished from noise or a different line at another redshift). We used 20 realizations for each redshift and signal-to-noise bin. The fraction of artificial spectra with determined redshifts at a given redshift and signal-to-noise, with different seeds of randomly-added noise, forms an estimate of the completeness.

We found that the simulated completeness for narrow emission line spectra was 90% to $i_{\text{AB}}^+ \sim 23$ ($S/N \approx 1.76$ per pixel) for $z \leq 1.3$, with strong unambiguous lines (e.g., $\text{H}\alpha\lambda 6563$, $\text{H}\beta\lambda 4861$, $[\text{O III}]\lambda 5007$, $[\text{O II}]\lambda 3727$). This is a magnitude fainter than the level of the average redshift completeness of the survey. At $0.9 \leq z \leq 1.4$,

[OII] λ 3727 is the only strong line, but it is bright enough that the redshift solution remains unambiguous even to $i_{\text{AB}}^+ < 23$. At $z > 1.4$ the [OII] line shifts completely out of the wavelength range and no good emission lines remain. The additional blue Hectospec coverage is also useless at $z > 1.4$, since [OII] remains redward of the upper 9200Å wavelength limit. We cannot identify narrow emission line (“nl”) spectra at $z > 1.4$.

The Type 1 AGN completeness has a more complex redshift dependence. As shown in Figure 2.6, in the redshift ranges $0.4 \lesssim z \lesssim 1.9$ and $2.3 \lesssim z \lesssim 2.9$ only one line is present and the redshift solution may be degenerate. This is ameliorated by the ancillary MMT/Hectospec spectra which have broader wavelength coverage. Examples of two objects with only one emission line in their IMACS spectra, but two emission lines in their Hectospec spectra, are shown in Figure 2.7 with accompanying discussion in §3.3. Only 36% (104/288) of the broad emission (“bl”) spectra benefit from MMT/Hectospec coverage. We add this MMT/Hectospec corroboration to the unidentified targets in the simulations, and estimate the redshift completeness as shown in Figure 2.13. We have lower redshift completeness in the redshift ranges $0.5 \lesssim z \lesssim 1.5$, and $2.3 \lesssim z \lesssim 2.6$, where only one line is present (H β , MgII, or CIII]) and although we can reliably classify as a broad line AGN (“bl”) it is difficult to distinguish between the two redshift ranges. Without the degeneracies between redshift, the redshifts would be $> 90\%$ complete to $S/N \approx 1.75$ (per pixel) or $i_{\text{AB}}^+ \sim 23$).

We do not test redshift dependence in identifying absorption line (“a”) spectral types because these spectra are well-populated with absorption lines. At $z > 1.3$ the 4000Å break leaves the wavelength range, but otherwise each absorption line galaxy has the same aptitude for $z_{\text{conf}} \geq 3$ classification at $z < 1.3$. However, because the absorption line (“a”) spectra lack features which are of higher signal

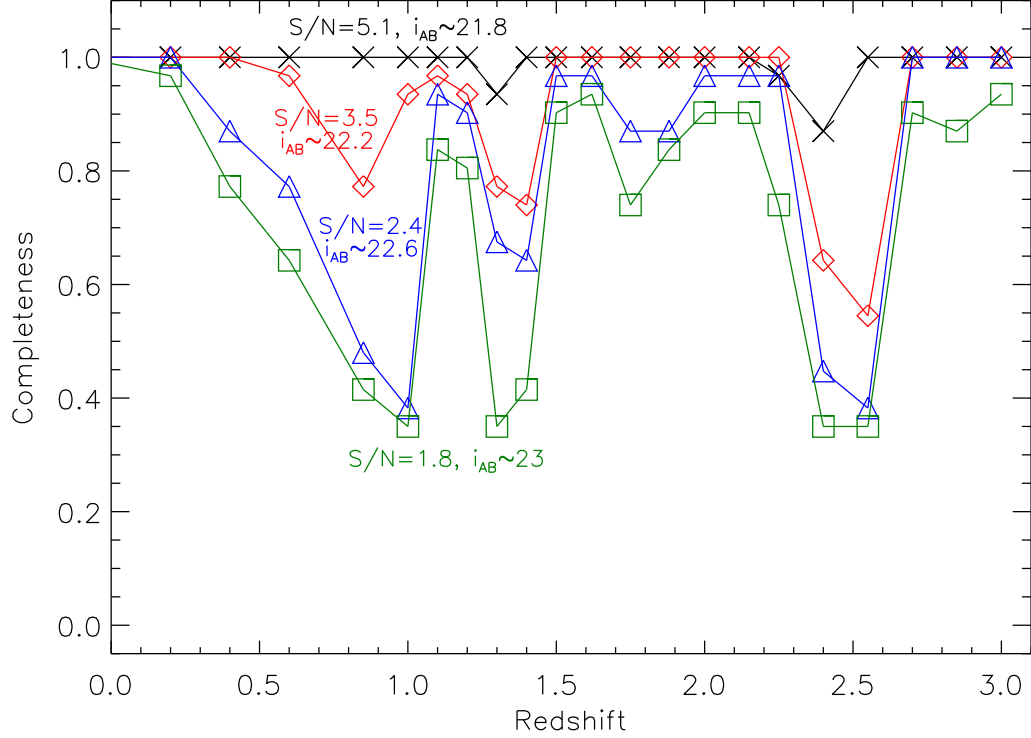


Figure 2.13 Our estimated completeness to assigning $z_{\text{conf}} \geq 3$ redshifts for broad emission line spectra (Type 1 AGN). We used Monte Carlo simulations with 20 different spectra with Gaussian-distributed noise for each of 4 values of S/N and 20 redshift bins. Each point represents the number of simulated spectra assigned $z_{\text{conf}} \geq 3$, with an additional 36% of the bad $z_{\text{conf}} < 3$ simulated spectra based on the partial MMT/Hectospec coverage (since 104/288 observed Type 1 AGN had supplemental Hectospec spectra). Each signal-to-noise is associated with an i_{AB}^+ magnitude according to the median values in Figure 2.11. The redshift ranges of lowest completeness correspond to observed wavelength ranges with only one emission line, as detailed in §4.3. Almost all of the simulated spectra to which we are not complete are identified as “bl” objects but with degenerate spectra.

than their continua, we cannot identify them to the same low S/N levels as emission line spectra. So the incompleteness to absorption line (“a”) spectra at $z < 1.3$ with $22 < i_{\text{AB}}^+ < 23$ is not redshift dependent. Because we have high completeness to broad line AGN (“bl”) and narrow emission line spectra (“nl”) at this magnitude (excepting the redshift ranges described above), most of the unidentified targets at $22 < i_{\text{AB}}^+ < 23$ are probably absorption line galaxies.

In summary, the sample has the following incompleteness outside of the flux limits:

1. Type 1 AGN of $22 < i_{\text{AB}}^+ < 23$ at $z \sim 0.8$, $z \sim 1.3$, and $z \sim 2.4$ (completeness in these regions shown in Figure 2.13).
2. Type 2 AGN of all magnitudes at $z > 1.4$
3. Absorption line galaxies of $22 < i_{\text{AB}}^+ < 23$ at $z < 1.3$ (from §4.2), and absorption line galaxies of all magnitudes at $z > 1.3$

We show the redshift distribution of all AGN (meeting one of the X-ray criteria in §3.2) in Figure 2.14. The uncorrected redshift distribution is shown by the square symbols. We next attempt to describe the complete $i_{\text{AB}}^+ < 23$ flux-limited sample, correcting for the incompleteness of the four points above.

2.4.4 Characterizing the Low-Confidence Targets

We can only assign high-confidence ($z_{\text{conf}} = 3, 4$) redshifts for 72% (485/677) of the targets, leaving 88 spectra with low-confidence ($z_{\text{conf}} = 1, 2$ redshifts and 104 targets of unknown spectral type ($z_{\text{conf}} = -1, 0$)). We characterize these 192 low-confidence and unclassified spectra using the photometric classifications and redshifts of Salvato et al. (2009), which take advantage of the extensive photometry of COSMOS (Capak et al., 2007). The photometric redshift algorithm finds a best-fit redshift and

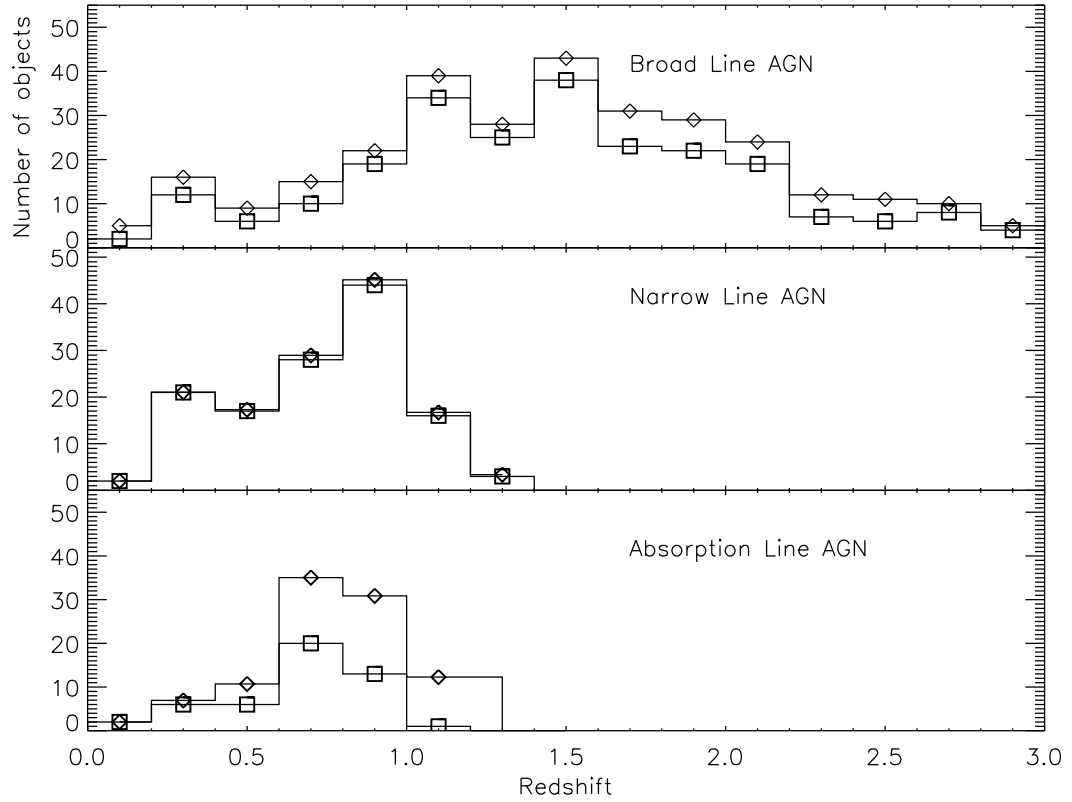


Figure 2.14 The redshift distributions of broad line (“bl”) AGN, narrow emission line (“nl”) spectra, and absorption line (“a”) galaxies. The raw distributions are shown with squares, while the distributions adjusted for the incompleteness (see §4.3 & 4.4 and Figure 2.15) are shown with diamonds. We do not correct the “nl” and “a” types where there is no spectroscopic data at $z > 1.4$.

classification by matching a set of 30 templates to the IR (IRAC), optical (Subaru), and UV (GALEX) photometric data of each object. The templates are described in full detail in Salvato et al. (2009) and are available upon request³. The photometric redshift technique was calibrated upon the spectroscopic redshifts we present for the 485 spectra of high redshift confidence, and has a precision of $\sigma_{\Delta z}/(1+z) < 0.02$ with $< 5\%$ of targets as significant outliers at $z < 4.5$.

The photometric redshift templates rely on multiwavelength fitting from IR to UV wavelengths, and so the photometric classifications can separate AGN-dominated (which we designated “unobscured”) and host-dominated (which we designate “obscured”) AGN types. However, the photometric classifications do not distinguish well between our absorption line spectra (“a” types) and narrow emission line spectra (“nl” types), although they can separate unobscured broad line AGN (“bl” types) from obscured AGN (“a” and “nl” types). We must assume population fractions of absorption line and narrow emission line spectra from the photometrically classified obscured objects using the known fractions from the high-confidence spectroscopy. In Figure 2.12, the fraction of narrow emission (“nl”) spectra does not decrease appreciably to $i_{\text{AB}}^+ \sim 22.5$ and almost all of the unknown objects can be assumed to be absorption line (“a”) types. We also know from §4.3 above that we are incomplete to “nl” spectra at $z > 1.4$, and the spectroscopically unclassified targets at $z > 1.4$ probably follow the $\sim 2:1$ ratio of narrow emission (“nl”) to absorption (“a”) types we find at lower redshifts in §3.1. So we assume that all photometrically classified unobscured AGN correspond to our broad emission (“bl”) type, and assume fractions of absorption (“a”) and narrow emission spectra (“nl”) as follows: (1) for $z < 1.4$, all are “a” types, and (2) for $z > 1.4$, $2/3$ are “nl” types and the remainder are “a” types.

³Mara Salvato, ms@astro.caltech.edu

Figure 2.15 shows the photometric redshift distribution for the 192 low confidence and unclassified spectra. Most of the photometric redshifts fall into one of the three incompleteness categories shown above in §4.3. We will use this redshift distribution to characterize the demographics of the complete flux-limited sample in §5.

We can also use the absolute magnitude distribution of the targets with secure spectroscopic redshifts in Figure 2.16 to make a qualitative assessment of the unidentified targets. The dashed lines mark $i_{\text{AB}}^+ = 22$ and $i_{\text{AB}}^+ = 23$. We will assume that the absolute magnitude distribution for narrow emission (“nl”) and absorption (“a”) objects, which peaks at $M_i \sim -22$, does not change with redshift. Objects of this absolute magnitude distribution should be detected to $z \sim 2$, but there are no narrow emission (“nl”) spectra detected at $z > 1.4$, and no absorption (“a”) spectra detected at $z > 1.3$. So many of the unidentified targets are probably $z > 1.4$ “nl” and $z > 1.3$ “a” type objects. The bright tail of the M_i distribution for “a” and “nl” types at $z > 1.3/z > 1.4$ also has $i_{\text{AB}}^+ < 22$, and so these missing $z > 1.3/z > 1.4$ targets may account for the unidentified targets at $i_{\text{AB}}^+ < 22$. In addition, most obscured AGN have $M_i \sim -22$, which lies within $22 < i_{\text{AB}}^+ < 23$ at $z > 1.3/z > 1.4$, suggesting that these objects may be most of the unidentified $22 < i_{\text{AB}}^+ < 23$ targets. This qualitative assessment confirms the characterization of the unknown spectral types using photometric redshifts.

2.5 Discussion

2.5.1 Demographics

Figure 2.9 indicates that the X-ray flux limit includes all $L_{0.5-10\text{keV}} > 3 \times 10^{42} \text{ erg s}^{-1}$ AGN at $z < 1$. This means we are nearly complete to all X-ray AGN (as defined in §3.2) at $z < 1$, since almost all objects that meet one of the X-ray criteria also meet both. We can additionally see in Figure 2.16 that we observe all but the faint

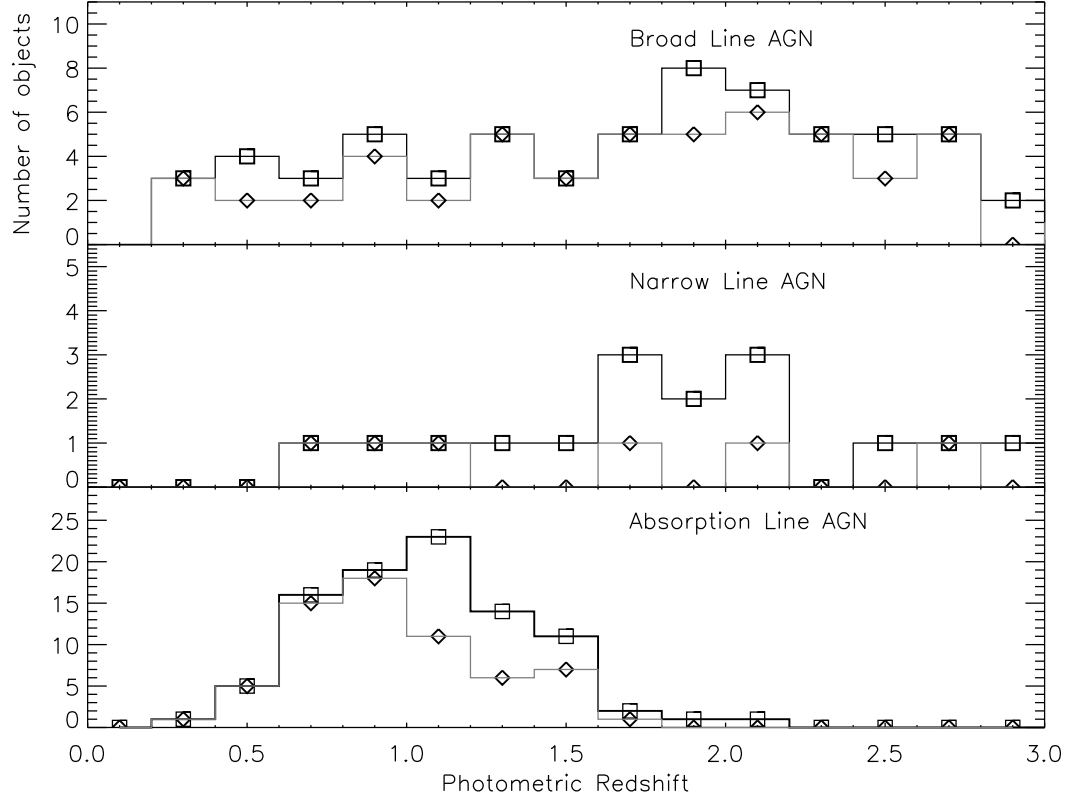


Figure 2.15 The photometric redshifts for the spectra without high-confidence redshifts. Square symbols show all 192 objects, and diamonds show the 146 $i_{AB}^+ < 23$ objects. The spectral type for these objects comes from the template used for the photometric redshift, with “a” and “nl” fractions estimated as described in §4.4. We use the photometric redshifts and classifications to characterize the complete $i_{AB}^+ < 23$ X-ray AGN sample.

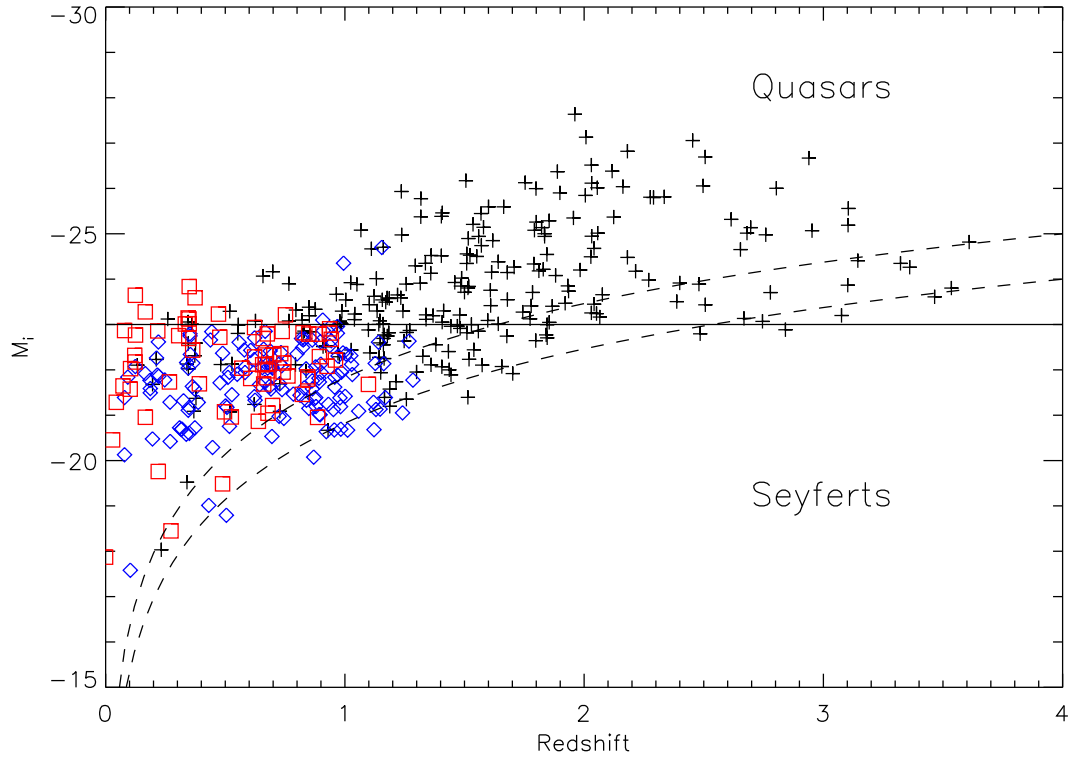


Figure 2.16 The absolute magnitude of the AGN (meeting the X-ray criteria of $\log f_X/f_O \geq -1$ or $L_{0.5-10\text{keV}} > 3 \times 10^{42}$) with redshift. The solid line indicates an arbitrary quasar/Seyfert boundary at $M_i = -23$, and the dashed lines indicate fluxes of $i_{\text{AB}}^+ = 22$ and $i_{\text{AB}}^+ = 23$. Symbols for object types are as in Figures 2.11 and 2.12, with crosses for “bl” or “bnl” objects (Type 1 AGN), diamonds for “nl” and “nla” objects (Type 2 AGN), and squares for “a” objects (optically obscured AGN).

tail of the M_i distributions of obscured and unobscured AGN types to $z < 1$, so long as we use the simple corrections of §4.4 to characterize the sample to $i_{AB}^+ < 23$. This allows us to characterize the complete $z < 1$ X-ray AGN population.

In Figure 2.14 we show the number of each AGN type with redshift. This includes only the 432 high-confidence X-ray AGN as defined by the X-ray criteria. We find raw fractions of broad emission line (56%), narrow emission line (32%), and absorption line (12%) over all redshifts, which roughly agree with other wide-area X-ray surveys (Fiore et al., 2003; Silverman et al., 2005; Eckart et al., 2006; Trump et al., 2007). To characterize the complete $i_{AB}^+ < 23$ and $f_{0.5-10\text{keV}} > 1 \times 10^{-15} \text{ erg s}^{-1} \text{ cm}^{-2}$ sample, we include the 106 $i_{AB}^+ < 23$ targets with bad spectroscopy and photometric redshifts that satisfy the X-ray AGN criteria. The corrected fractions of $i_{AB}^+ < 23$ targets at all redshifts include 57% broad emission line, 25% narrow emission line, and 18% absorption line AGN.

2.5.2 Obscured to Unobscured AGN Ratio

The ratio of obscured to unobscured AGN can help determine the properties of the obscuration which hides nuclear activity. In the simplest unification models (Antonucci, 1993; Urry & Padovani, 1995), obscuration depends only on the orientation and should remain independent of luminosity and redshift. However, since we know that galaxies at higher redshifts have more dust than local galaxies, then one might expect the ratio of obscured to unobscured AGN to depend on redshift if AGN host galaxy dust plays a role in obscuration (e.g., Ballantyne, Everett, & Murray, 2006). And if the obscuring dust (or its sublimation radius) is blown out further by more luminous accretion disks (Lawrence & Elvis, 1982; Lawrence, 1991; Simpson, 2005), then one might expect the ratio to decrease with increasing luminosity. Some models of the X-ray background prefer ratios which suit these physical descriptions, predicting an increasing ratio of obscured to unobscured with increasing redshift

and decreasing luminosity (Ballantyne, Everett, & Murray, 2006; Treister & Urry, 2006). Deep X-ray observations confirm that the ratio depends on luminosity (Steffen et al., 2004; Barger et al., 2005; Treister, Krolik & Dullemond, 2008). Some observations additionally suggest redshift evolution (La Franca et al., 2005; Treister & Urry, 2006; Hasinger, 2008), but other authors claim that redshift evolution is neither necessary in the models nor significant in the observations (Ueda et al., 2003; Akylas et al., 2006; Gilli et al., 2007).

We derive the obscured to unobscured AGN ratio with redshift in Figure 2.17. Here “obscured AGN” refers to both narrow emission line (“nl”) and absorption line (“a”) AGN meeting the X-ray criteria of §3.2, and “unobscured AGN” includes all broad-line (“bl”) AGN. To the limit of the survey at $z < 1$, our average ratio is 3:1 obscured to unobscured AGN. We additionally separate the AGN into X-ray luminous and X-ray faint (in relation to the median X-ray luminosity, $L_{\text{med}} = 1.32 \times 10^{44}$ cgs) in the bottom panel of Figure 2.17. The ratio of obscured to unobscured X-ray faint AGN appears to be much higher than the ratio for X-ray bright AGN, and additionally seems to increase with redshift.

We test the ratio for dependence on redshift and luminosity using logistic regression a useful method for determining how classification depends upon a set of variables. It is commonly used in biostatistical applications, where one expects a binary response (for instance, a patient might live or die) based on a set of variables. Logistic regression considers each data element independently, and is therefore more effective than significance tests which bin the data. An excellent review of logistic regression is found in Fox (1997). We use the method here to learn if the likelihood for an AGN to be classified as obscured or unobscured (a binary response) depends on observed X-ray luminosity and/or redshift. Logistic regression solves for the “logit” (the natural logarithm of the odds ratio) in terms of the variables as follows:

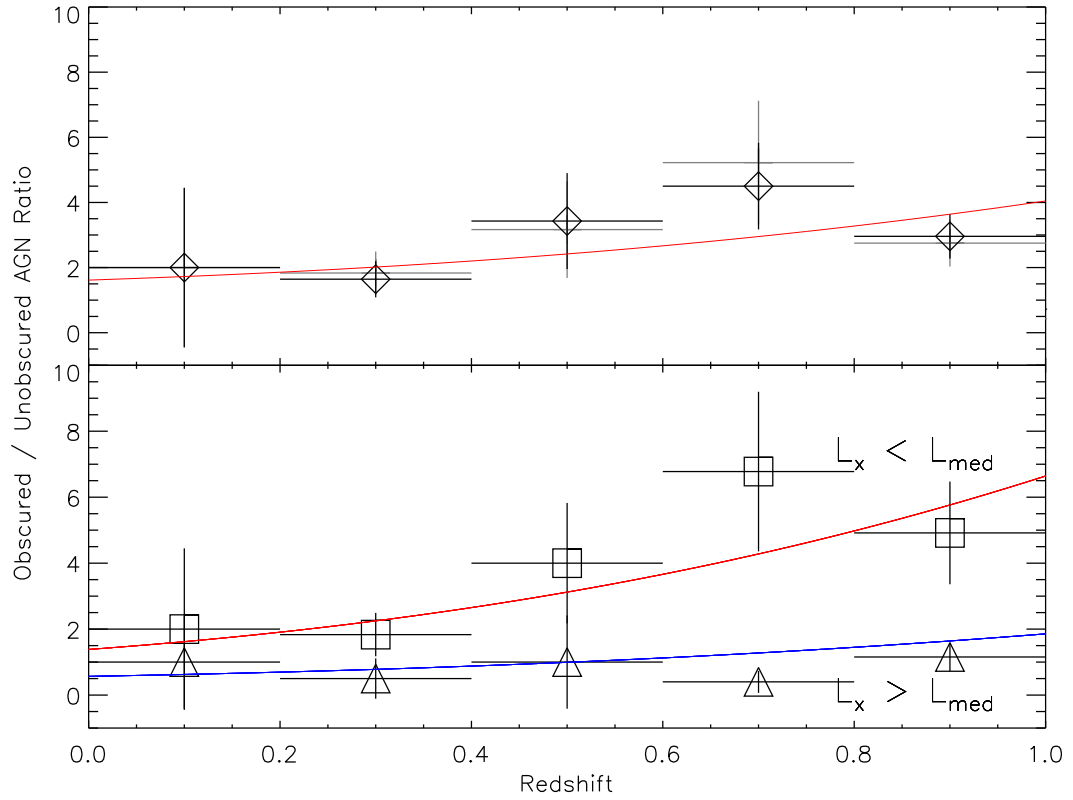


Figure 2.17 The ratio of obscured to unobscured AGN with redshift. We define obscured AGN as spectra with narrow emission or absorption lines (“nl,” “a,” and “nla”) that meet the X-ray AGN criteria of §3.2, while unobscured AGN are all broad-line (“bl” and “bnl”) spectra. In the top panel the raw fractions are shown in gray, while the corrected fractions based on the incompleteness (characterized in §4.3 & 4.4) are shown by the black diamonds. The bottom panel shows the ratios for AGN fainter and brighter than the median luminosity $L_{\text{med}} = 1.32 \times 10^{44}$ cgs, with the $L_{0.5-10 \text{ keV}} < L_{\text{med}}$ ratio as squares, and the $L_{0.5-10 \text{ keV}} > L_{\text{med}}$ ratio as triangles. The errors associated with each point assume that the numbers of objects observed in each redshift bin are Poissonian. Logistic regression analysis shows that the ratio of obscured to unobscured increases with redshift and decreases with luminosity, as shown by the best-fit power-laws.

$$\ln \frac{Pr(G=1|L, z)}{Pr(G=2|L, z)} = \beta_0 + \beta_1 \ln(1+z) + \beta_2 \ln(L_X/10^{42}) \quad (2.3)$$

Here $G = 1$ means an AGN is classified obscured, and $G = 2$ means an AGN is classified unobscured. We use $\log(1+z)$ and $\log(L_X/10^{42})$ as the dependent variables instead of z and L_X for numerical stability. Then the logit, as the logarithm of the ratio of the probabilities, is just the logarithm of the obscured to unobscured ratio. We solve for the coefficients using the Newton-Raphson method and estimate errors by bootstrapping, calculating the standard deviation on the coefficients with 1000 random subsets of the true data. We find the coefficients to be

$$\beta_0 = 1.73 \pm 0.67; \beta_1 = 3.83 \pm 1.57; \beta_2 = -0.69 \pm 0.19 \quad (2.4)$$

In other words, the obscured/unobscured AGN ratio increases with redshift at 2.4σ significance and decreases with observed X-ray luminosity at 3.6σ significance. We can write the power-law equation of the expected ratio for a given luminosity and redshift as:

$$\frac{Pr(\text{obscured})}{Pr(\text{unobscured})} \propto 5.6(1+z)^{3.8}(L_X/10^{42})^{-0.7} \quad (2.5)$$

The curves from this logistic regression model are shown in Figure 2.17. In the bottom panel, the red line shows the power-law relation (Equation 5) computed using $L_X = L_{\text{low}}$, where L_{low} is the median luminosity from only those AGN with $L_{0.5-10 \text{ keV}} < L_{\text{med}}$. Similarly the blue line represents the relation for higher-luminosity AGN of $L_{0.5-10 \text{ keV}} > L_{\text{med}}$. Note that the data as binned in Figure 2.17 shows less signal than the independent data used in the logistic regression fit, and so the fit of the power-laws shown should not be judged by the basis of their by-eye match to the binned data. It is worth noting, however, that high-luminosity sources seem to evolve much more weakly with redshift. This is a natural consequence of the

power-law nature of Equation 5: when L_X is large, the obscured/unobscured ratio becomes small, and so it appears only to weakly evolve with redshift on a linear scale. Our dependence of obscuration on redshift and luminosity are both consistent with recent work by both Treister & Urry (2006) and Hasinger (2008), with the obscured fraction about 4 times higher at low luminosity than at high luminosity and about 2 times higher at $z \sim 1$ than at $z \sim 0$.

The trend with observed X-ray luminosity can be explained in several ways. It may be that obscured AGN are simply more absorbed in the X-rays, such that their intrinsic X-ray luminosities are significantly higher than their observed. Then the apparent lack of obscured AGN at higher X-ray luminosities might be only an observed effect, and not an intrinsic physical effect. But if the intrinsic and observed X-ray luminosities are not significantly different in these obscured AGN, then the luminosity dependence indicates that more luminous AGN have less obscuring material. The luminosity may decrease the opening angle of obscuration by causing dust sublimation to occur at larger radii.

The presence of more obscured AGN at $z \sim 1$ is not likely to indicate physical evolution in AGN, since AGN at similar luminosities at $z \sim 1$ and $z \sim 0$ are not observed to have different physical properties like black hole mass and accretion rate (Kelly et al., 2008) or spectral energy distribution (Vignali et al., 2003; Richards et al., 2006; Hopkins, Richards, & Hernquist, 2007). However, galaxies at $z \sim 1$ show significantly more star formation, gas, and dust than galaxies at $z \sim 0$, and so the increase of obscuration with redshift may be explained by host gas/dust obscuration of the AGN central engine. Indeed, models by Ballantyne (2008) show that star formation can effectively obscure AGN while producing both the observed luminosity and redshift dependence of the obscured/unobscured ratio. Ballantyne (2008) additionally show that starburst-driven obscuration should be easily distinguished from

AGN-heated dust by future Herschel 100 μm surveys.

It is important to note that our definition of “obscured” includes only moderately X-ray obscured AGN. We are not sensitive to Compton-thick and other heavily X-ray obscured AGN, and so may be significantly underestimating the obscured AGN population (Daddi et al., 2007; Fiore et al., 2009). Logistic regression reveals statistically significant evidence for redshift evolution and dependence on X-ray luminosity in the optically obscured/unobscured ratio, but mid-IR surveys may reveal different dependencies by including heavily obscured AGN missed in X-rays.

2.6 Conclusions and Future Projects

We present optical spectroscopy for 677 X-ray targets from COSMOS, with spectra from Magellan/IMACS, MMT/Hectospec, and archival SDSS data. The spectroscopy is uniformly complete to $i_{AB}^+ < 22$. By using photometric redshifts for the bad spectra, we additionally characterize the sample to $i_{AB}^+ < 23$, and we show that this optical limit, along with our X-ray flux limit, allows us to characterize a solely volume-limited sample of all (obscured and unobscured) X-ray AGN at $z < 1$. We provide evidence that at $z < 1$, the ratio of obscured to unobscured AGN increases with redshift and decreases with luminosity, where the redshift dependence is of moderate statistical significance (2.4σ) and the luminosity dependence is of higher statistical significance (3.6σ).

Despite such leverage in the sample presented here, the observations of AGN in COSMOS are by no means complete. We were only able to target 52% of the available $i_{AB}^+ < 23.5$ XMM targets, and we hope to include the remainder of targets in future spectroscopic observations. Some of these targets were observed on Magellan/IMACS and MMT/Hectospec in March 2008, and many of the other XMM targets without spectra will be observed with VLT/VIMOS (at 5600-9400 Å) as

part of the zCOSMOS galaxy redshift survey (Lilly et al., 2007). The zCOSMOS survey will additionally target $i_{AB}^+ > 23.5$ XMM targets which are too faint for Magellan/IMACS. It is also possible to study fainter X-ray sources, since the 0.5-2 keV *Chandra* observations in COSMOS go to 2×10^{-16} erg cm $^{-2}$ s $^{-1}$ in the central 0.8 deg 2 , five times fainter than the XMM observations used here. Optical identification of these sources are still ongoing, but the Chandra data are expected to reveal twice as many X-ray targets as the XMM-selected targets presented here. We will additionally use the previously observed spectra of radio and infrared selected AGN candidates to study Compton-thick and other X-ray faint AGN,

Future work will also use the bolometric studies made possible by the deep multiwavelength coverage of COSMOS. We plan to further study the evolution of obscuration with more fundamental physical quantities like bolometric luminosity. Chapter 3 (see also Trump et al., 2009b) presents virial black hole mass estimates for the Type 1 AGN presented here and suggests that it is difficult to form a broad line region below a critical accretion rate, as suggested previously by Nicastro (2000) and Kollmeier et al. (2006). This concept, combined with the luminosity evolution of the obscuration presented here, suggests that models of the AGN central engine must include a prescription where the amount of obscuring material decreases with increasing luminosity, accretion rate, or both.

CHAPTER 3

OBSERVATIONAL LIMITS ON TYPE 1 AGN ACCRETION RATE IN COSMOS

We present black hole masses and accretion rates for 182 Type 1 AGN in COSMOS. We estimate masses using the scaling relations for the broad $H\beta$, $MgII$, and CIV emission lines in the redshift ranges $0.16 < z < 0.88$, $1 < z < 2.4$, and $2.7 < z < 4.9$. We estimate the accretion rate using an Eddington ratio L_{int}/L_{Edd} estimated from optical and X-ray data. We find that very few Type 1 AGN accrete below $L_{int}/L_{Edd} \sim 0.01$, despite simulations of synthetic spectra which show that the survey is sensitive to such Type 1 AGN. At lower accretion rates the BLR may become obscured, diluted or nonexistent. We find evidence that Type 1 AGN at higher accretion rates have higher optical luminosities, as more of their emission comes from the cool (optical) accretion disk with respect to shorter wavelengths. We measure a larger range in accretion rate than previous works, suggesting that COSMOS is more efficient at finding low accretion rate Type 1 AGN. However the measured range in accretion rate is still comparable to the intrinsic scatter from the scaling relations, suggesting that Type 1 AGN accrete at a narrow range of Eddington ratio, with $L_{int}/L_{Edd} \sim 0.1$.

3.1 Chapter Introduction

Supermassive black holes (SMBHs) reside in almost all local galaxies (Kormendy & Richstone, 1995; Richstone et al., 1998). The mass of the SMBH is observed to be tightly correlated with the mass, luminosity, and velocity dispersion of the host galaxy bulge (e.g., Magorrian et al., 1998; Gebhardt et al., 2000; Ferrarese & Merritt, 2000). SMBHs grow by accretion as active galactic nuclei (AGN), and all massive galaxies have one or more of these active phases (Soltan, 1982; Magorrian et al., 1998;

Marconi et al., 2004). More luminous AGN are observed to peak at higher redshift (Ueda et al., 2003; Brandt & Hasinger, 2005; Bongiorno et al., 2007), exhibiting “downsizing” by analogy to the preference of luminous and massive galaxies to form at high redshifts. Both downsizing and the correlations between SMBH and the host bulge suggest that the growth of AGN and the formation of galaxies are directly connected through feedback (Silva et al., 1998; Di Matteo, Springel, & Hernquist, 2005).

Understanding the role of AGN in galaxy evolution requires measurements of SMBH mass and accretion over the cosmic time. The SMBH mass can be directly estimated by modeling the dynamics of nearby gas or stars, but this requires high spatial resolution and is limited to HST observations of nearby galaxies. Reverberation mapping of Type 1 AGN (with broad emission lines) uses the time lag between variability in the continuum and the broad line region (BLR) to estimate the radius of the broad line region, $R_{BLR} = ct_{lag}$ (for a review, see Peterson & Bentz, 2006). Then, if the broad line region virially orbits the source of the continuum emission, the SMBH mass is $M_{BH} = fR_{BLR}v_{fwhm}^2$, where f represents the unknown BLR geometry and v_{fwhm} is the velocity width of the broad emission line. This technique has many potential systematic errors (Krolik, 2001; Marconi et al., 2008), but its mass estimates agree with those from dynamical estimators (Davies et al., 2006; Onken et al., 2007) and those from the M_{BH} - σ_* correlation (Onken et al., 2004; Greene & Ho, 2006). In principle, reverberation mapping can be applied to AGN at any redshift, but in practice, the need for many periodic observations has limited reverberation mapping mass estimates to only ~ 35 local AGN.

Instead, the vast majority of AGN mass estimates have come from a set of scaling relations. Reverberation mapping data led to the discovery that R_{BLR} correlates with the continuum luminosity (Kaspi et al., 2000), with $R_{BLR} \sim L^\alpha$, where $\alpha \sim 0.5$

(Bentz et al., 2006; Kaspi et al., 2007). This allows for estimates of M_{BH} from single epoch spectra with scaling relations:

$$\log\left(\frac{M_{BH}}{M_{\odot}}\right) = A + B \log(\lambda L_{\lambda}) + 2 \log(v_{FWHM}) \quad (3.1)$$

Some authors replace the continuum luminosity with the recombination line luminosity (Wu et al., 2004) or the FWHM with the second moment σ (Collin et al., 2006), yielding minor systematic differences in estimated M_{BH} (Shen et al., 2008). While these scaling relations are based upon reverberation mapping of only local AGN, the method is based upon the ability of the central engine to ionize the broad line region (Kaspi et al., 2000), and there is no physical reason to suggest that the ionization of AGN should evolve with redshift (Dietrich & Hamann, 2004; Vestergaard, 2004). Thus the scaling relations can be used to study the distribution and evolution of Type 1 AGN masses. Kollmeier et al. (2006) showed that Type 1 AGN tend to accrete at a narrow range of Eddington ratio, typically $0.01 L_{Edd} < L < L_{Edd}$. Kollmeier et al. (2006) suggest a minimum accretion rate for Type 1 AGN, with AGN of lower accretion rate observed as “naked” Type 2 AGN without a broad line region (Hopkins et al., 2009). Gavignaud et al. (2008) additionally suggest that lower luminosity Type 1 AGN accrete less efficiently than brighter quasars.

In this work we report black hole masses and study the demographics of 182 Type 1 AGN in the Cosmic Evolution Survey (COSMOS, Scoville et al., 2007). We introduce the data and outline our spectral fitting in §2, and discuss the black hole masses, their associated errors, and our completeness in §3. We close with discussion of Type 1 AGN accretion rates in §4. All luminosities are calculated using $h = 0.70$, $\Omega_M = 0.3$, $\Omega_{\Lambda} = 0.7$.

3.2 Observational Data

3.2.1 Sample

The Cosmic Evolution Survey (COSMOS, Scoville et al., 2007) is a 2 deg^2 HST/ACS survey (Koekemoer et al., 2007) with ancillary deep multiwavelength observations. The depth of COSMOS over such a large area is particularly suited to the study of low-density, rare targets like active galactic nuclei (AGN). The most efficient way to select AGN is by their X-ray emission, and XMM-*Newton* observations of COSMOS (?) reach fluxes of $1 \times 10^{-15} \text{ cgs}$ and $6 \times 10^{-15} \text{ cgs}$ in the 0.5-2 keV and 2-10 keV bands, respectively. The matching of X-ray point sources to optical counterparts is described by Brusa et al. (2007) and Brusa et al. (2010). Chapter 2 (see also Trump et al., 2009a) described a spectroscopic survey of XMM-selected AGN in COSMOS, revealing 288 Type 1 AGN with X-ray emission and broad emission lines in their spectra. Here we investigate a chief physical property, the black hole mass, for the Type 1 AGN in this survey.

From the Chapter 2 sample, we choose the 182 Type 1 AGN with high-confidence redshifts and with $\text{H}\beta$, MgII , or CIV present in the observed wavelength range. That is, we select only $z_{\text{conf}} \geq 3$ AGN, empirically determined in Chapter 2 to be at least 90% likely to have the correct classification and redshift. All of the Type 1 AGN spectra are dominated by blue power-law continua, with no obvious (beyond the noise) absorption line signature from the host galaxy. The broad emission line requirement restricts us to the redshift ranges $0.16 < z < 0.88$, $1 < z < 2.4$, and $2.7 < z < 4.9$. At these redshifts the AGN spectroscopy is $> 90\%$ complete to $i_{\text{AB}}^+ < 22$ (see Figure 2.13), where i_{AB}^+ is the AB magnitude from the COSMOS CFHT observations. Our ability to measure a broad line width, however, is a slightly more complicated function of the spectral signal to noise. We characterize our completeness as a function of broad line width and S/N in §3.2.

The majority (133) of the 182 AGN have spectra from Magellan/IMACS (Bigelow et al., 1998), with wavelength coverage from 5600-9200Å and $\sim 10\text{\AA}$ resolution. The remaining bright 49 quasars have publicly available spectra from the Sloan Digital Sky Survey quasar catalog (SDSS, Schneider et al., 2007), with 3800-9200Å wavelength coverage and $\sim 3\text{\AA}$ resolution. The resolution of both surveys is more than sufficient for measuring broad emission line widths; our narrowest broad emission line is 1300 km/s wide, compared to the resolution limits of IMACS (~ 600 km/s) and the SDSS (~ 200 km/s).

3.2.2 Spectral Fitting

The optical/UV spectrum of a Type 1 AGN can be roughly characterized as a power-law continuum, $f_\nu \propto \nu^{-\alpha}$, with additional widespread broad iron emission and broad emission lines (Vanden Berk et al., 2001). We followed Kelly et al. (2008) to model the spectra, using an optical Fe template from Veron-Cetty, Joly, & Veron (2004) and a UV Fe template from Vestergaard & Wilkes (2001). Each spectrum was simultaneously fit with a power-law continuum and an iron template using the Levenberg-Marquardt method for nonlinear χ^2 minimization. We calculated the continuum luminosity from the power-law fit parameters. Light from the host galaxy can artificially inflate the estimated AGN continuum luminosity, as shown by Bentz et al. (2008) for the 35 AGN with reverberation mapping data. In particular, Bentz et al. (2008) find that at 5100Å, host galaxies contribute $\sim 20\%$ of the measured flux for AGN with $\lambda L_{5100} > 10^{44}$ erg/s, and $\sim 45\%$ of the flux for AGN of $\lambda L_{5100} < 10^{44}$ erg/s. We note that the expected host contamination at L_{3000} or L_{1350} is much smaller, since most host galaxies (excepting very active star-forming hosts) have much less flux blueward of the 4000Å break. So for the majority of our sample, the 150 AGN with masses measured from MgII or CIV, we do not expect host contamination to be significant. However, the 15 AGN with $\lambda L_{3000} < 10^{44}$ erg/s and

$H\beta$ -derived masses may have luminosity estimates overestimated by a factor of two, leading to black hole masses and Eddington ratios systematically overestimated by ~ 0.15 dex. Future work in COSMOS will use host decompositions from HST/ACS images of $z < 1$ AGN to better characterize host contamination, but in this work we make no corrections for host galaxy flux.

To fit the broad emission lines we subtracted the continuum and Fe emission fits. Narrow absorption lines and narrow emission lines near the broad line (e.g., $[O\text{III}]\lambda 4959$ and $[O\text{III}]\lambda 5007$ near $H\beta$) were fit by the sum of 1-2 Gaussian functions and removed. Again following Kelly et al. (2008), each remaining broad emission line profile was fit by the sum of 1-3 Gaussian functions, minimizing the Bayesian information criterion (BIC, Schwartz, 1979). Roughly, 2 Gaussians provided the best fit for $\sim 40\%$ of line profiles, while 1 or 3 Gaussians each provided the best fit for $\sim 30\%$ of line profiles. All fitting was interactive and inspected visually, and if the multiple-Gaussian fit revealed a narrow (< 600 km/s) line in an $H\beta$ emission line, the component was attributed to non-BLR origins and was removed. The FWHM was calculated directly from the multiple-Gaussian fit in order to minimize the effects of noise in the original spectra. The multiple-Gaussian fit was robust to a variety of line profiles, and simulated spectra (see §3.2) revealed measured FWHM errors of only $\sigma_{FWHM}/FWHM \sim 10\%$.

Three examples of spectra with fitted continua and continuum-subtracted line profiles are shown in Figure 3.1. The spectra are representative of typical fits for each of the C IV, Mg II, and $H\beta$ emission lines. At left the power-law and iron emission fits are shown by the dashed blue lines. The right panel shows the multiple-Gaussian line profile fits as dashed blue lines, with the continuum-subtracted line profile shifted above by an arbitrary amount for clarity. The fit to the $H\beta$ line profile in the bottom right panel includes a narrow ($\sigma = 433$ km/s) Gaussian which is not associated with

the BLR and was removed. Even for noisy spectra like the middle panel, the spectral fitting provides a robust continuum and isolates the emission line.

3.3 Estimated Black Hole Masses

We estimate black hole masses using our measured broad line velocity widths and the scaling relations of Vestergaard & Osmer (2009) for MgII and Vestergaard & Peterson (2006) for H β and C IV. These relations all take the form of Equation 1, with λL_λ in units of 10^{44} erg/s and v_{FWHM} in units of 1000 km/s; $A = 6.91$, $B = 0.50$, and $\lambda = 5100\text{\AA}$ for H β ; $A = 6.86$, $B = 0.50$, and $\lambda = 3000\text{\AA}$ for MgII; $A = 6.66$, $B = 0.53$, and $\lambda = 1350\text{\AA}$ for C IV. The MgII relation was derived from SDSS quasars with both C IV and MgII in the spectrum, and it is designed to produce black hole masses consistent with those measured from C IV. In our sample, we measure H β for 32 AGN, MgII for 134 AGN, and C IV for 38 AGN (19 SDSS AGN have both MgII and C IV, and 3 have both H β and MgII). AGN with estimates of M_{BH} from two different emission lines are treated as two separate objects in our subsequent analyses.

Table 3.1 presents the catalog of black hole masses and line measurements. AGN with both MgII and C IV or both H β and MgII present have two entries in Table 3.1, one for each emission line. The full catalog then contains 204 entries: 182 Type 1 AGN with M_{BH} estimates, 22 of which have two sets of broad emission line measurements. The black hole masses are shown with continuum luminosity (calculated from the power-law fit) and redshift in Figure 3.2. The diagonal tracks in the figure represent Eddington ratios using a bolometric correction of 5 for λL_{3000} (Richards et al., 2006). We also show a comparison sample of brighter SDSS quasars (Kelly et al., 2008) in order to highlight the lower black hole masses probed by COSMOS.

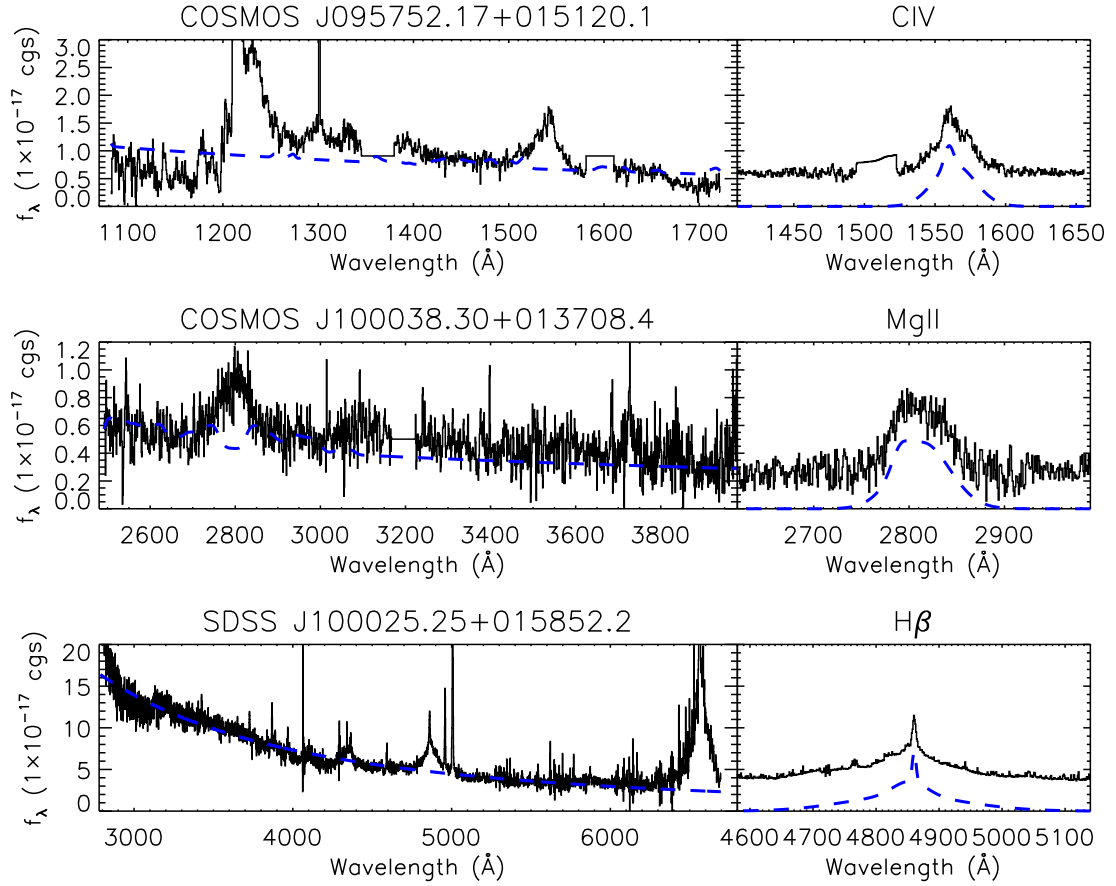


Figure 3.1 Three spectra, representing fits and line profiles for Type 1 AGN with CIV (top), MgII (middle), and H β (bottom). In the left panels, the spectra are shown by black histograms, and the dashed blue lines are the power-law plus iron emission continuum fits. At right, the blue dashed line shows the multiple-Gaussian fit to the continuum-subtracted line profiles, which are shown in black and shifted above for clarity. The fit to the H β line profile in the lower right panel includes a narrow ($\sigma = 433$ km/s) Gaussian which was removed before calculating the broad emission line width. The top two spectra were observed with Magellan/IMACS and have $\sim 10\text{\AA}$ resolution, while the bottom spectrum comes from the SDSS and has $\sim 3\text{\AA}$ resolution.

Table 3.1. COSMOS Type 1 AGN Black Hole Mass Catalog

Object (J2000)	Redshift	S/N (per pixel) ^a	$\log(\lambda L_{3000\text{\AA}})$ [erg/s]	$\log(L_{0.5-2\text{keV}})$ [erg/s] ^b	Line	FWHM (km/s)	$\log(M_{BH})$ [M_{\odot}]
SDSS J095728.34+022542.2	1.54	7.0	45.00	44.47	MgII	4491	8.665
SDSS J095728.34+022542.2	1.54	7.0	45.00	44.47	CIV	2776	8.135
COSMOS J095740.78+020207.9	1.48	17.9	43.46	44.41	MgII	6701	8.244
SDSS J095743.33+024823.8	1.36	3.4	44.60	43.50	MgII	3472	8.243
COSMOS J095752.17+015120.1	4.17	7.3	45.19	44.36	CIV	4603	8.656
COSMOS J095753.49+024736.1	3.61	4.8	44.14	44.53	CIV	2629	7.997
SDSS J095754.11+025508.4	1.57	6.1	45.07	44.45	MgII	4500	8.701
SDSS J095754.70+023832.9	1.60	8.0	45.17	43.69	MgII	3361	8.498
SDSS J095754.70+023832.9	1.60	8.0	45.17	43.69	CIV	6384	8.946
SDSS J095755.08+024806.6	1.11	8.7	44.92	44.08	MgII	3574	8.426
COSMOS J095755.34+022510.9	2.74	3.2	44.38	-1.00	CIV	3879	8.074
COSMOS J095755.48+022401.1	3.10	19.9	45.28	45.00	CIV	3527	8.436
SDSS J095759.50+020436.1	2.03	14.6	45.35	44.35	MgII	4056	8.751
SDSS J095759.50+020436.1	2.03	14.6	45.35	44.35	CIV	6096	9.120
COSMOS J095759.91+021634.5	1.54	3.6	44.00	-1.00	MgII	5032	8.264

Table 3.1—Continued

Object (J2000)	Redshift	S/N (per pixel) ^a	$\log(\lambda L_{3000\text{\AA}})$ [erg/s]	$\log(L_{0.5-2\text{keV}})$ [erg/s] ^b	Line	FWHM (km/s)	$\log(M_{BH})$ [M_{\odot}]
COSMOS J095806.99+022248.5	3.10	10.3	44.87	44.67	CIV	8752	9.336
SDSS J095815.50+014923.2	1.51	4.2	44.74	44.98	MgII	4827	8.599
COSMOS J095815.53+015840.5	1.68	11.5	43.56	44.13	MgII	4392	7.927
COSMOS J095817.26+023316.2	1.57	3.1	43.99	43.26	MgII	5222	8.292
SDSS J095819.88+022903.6	0.34	8.8	43.84	43.27	Hb	5050	8.287
SDSS J095821.65+024628.2	1.40	7.2	45.04	44.64	MgII	6932	9.059
COSMOS J095821.84+020834.0	1.87	2.0	43.92	-1.00	MgII	3009	7.775
SDSS J095822.19+014524.3	1.96	24.6	45.91	44.73	MgII	3453	8.890
SDSS J095822.19+014524.3	1.96	24.6	45.91	44.73	CIV	5130	9.160
COSMOS J095824.50+022333.6	1.85	31.9	45.31	44.37	MgII	2399	8.276
COSMOS J095829.83+021050.4	1.19	14.8	44.48	44.08	MgII	4168	8.339
SDSS J095834.04+024427.2	1.89	9.2	45.18	44.78	MgII	3672	8.582
SDSS J095834.04+024427.2	1.89	9.2	45.18	44.78	CIV	5652	8.916
SDSS J095834.75+014502.4	1.90	7.2	45.28	44.13	MgII	7619	9.264
SDSS J095834.75+014502.4	1.90	7.2	45.28	44.13	CIV	4804	8.743

Table 3.1—Continued

Object (J2000)	Redshift	S/N (per pixel) ^a	$\log(\lambda L_{3000\text{\AA}})$ [erg/s]	$\log(L_{0.5-2\text{keV}})$ [erg/s] ^b	Line	FWHM (km/s)	$\log(M_{BH})$ [M_{\odot}]
COSMOS J095835.28+013609.2	2.84	2.9	43.47	-1.00	CIV	1353	7.196
SDSS J095835.98+015157.1	2.94	36.3	45.55	44.20	CIV	2236	8.114
COSMOS J095836.69+022049.0	1.19	2.9	43.18	43.88	MgII	2610	7.286
COSMOS J095839.27+020506.7	1.22	28.8	45.01	43.86	MgII	2753	8.245
COSMOS J095840.61+020426.6	0.34	30.3	44.08	42.80	Hb	5709	8.388
SDSS J095844.94+014309.0	1.34	4.3	44.68	43.90	MgII	9859	9.189
COSMOS J095847.71+022628.4	1.52	9.0	44.71	44.15	MgII	5573	8.706
SDSS J095848.86+023441.1	1.55	2.9	44.61	44.42	MgII	4967	8.556
SDSS J095848.86+023441.1	1.55	2.9	44.61	44.42	CIV	5208	8.430
COSMOS J095849.41+022511.1	1.12	41.2	44.86	44.36	MgII	5840	8.824
SDSS J095852.14+025156.3	1.41	8.1	45.04	44.59	MgII	4761	8.737
COSMOS J095856.70+021047.8	4.25	1.1	43.95	44.41	CIV	4590	8.162
SDSS J095857.35+021314.4	1.02	3.6	44.41	44.77	MgII	8895	8.964
SDSS J095858.53+021459.1	0.13	16.7	42.99	42.55	Hb	2337	7.310
COSMOS J095901.31+024418.8	3.54	1.2	43.99	44.37	CIV	1346	7.102

Table 3.1—Continued

Object (J2000)	Redshift	S/N (per pixel) ^a	$\log(\lambda L_{3000\text{\AA}})$ [erg/s]	$\log(L_{0.5-2\text{keV}})$ [erg/s] ^b	Line	FWHM (km/s)	$\log(M_{BH})$ [M_{\odot}]
COSMOS J095902.56+022511.8	1.10	4.9	43.91	43.60	MgII	3937	8.008
SDSS J095902.76+021906.5	0.35	7.3	43.60	43.77	Hb	8121	8.657
COSMOS J095903.80+020316.7	1.25	2.3	43.56	-1.00	MgII	1518	7.001
COSMOS J095906.46+022639.4	4.17	1.4	44.43	44.38	CIV	3139	8.014
SDSS J095908.32+024309.6	1.32	12.1	45.19	45.04	MgII	2404	8.215
COSMOS J095908.56+023317.2	1.80	4.5	44.00	44.09	MgII	5620	8.357
COSMOS J095909.53+021916.5	0.38	9.9	43.17	43.26	Hb	3004	7.771
COSMOS J095911.11+023333.9	1.54	4.3	44.01	43.62	MgII	2485	7.656
COSMOS J095915.40+020059.0	1.36	3.2	44.18	43.88	MgII	8394	8.797
COSMOS J095920.89+020032.0	1.48	8.1	45.01	43.88	MgII	3676	8.494
SDSS J095921.30+024030.4	0.26	10.6	43.51	43.10	Hb	2623	7.639
SDSS J095924.47+015954.4	1.24	12.5	45.17	44.60	MgII	5650	8.948
COSMOS J095928.31+022106.9	0.35	15.5	43.52	42.70	Hb	1836	7.243
COSMOS J095928.32+021950.7	1.49	19.9	44.96	44.19	MgII	4268	8.598
COSMOS J095928.46+015934.8	1.18	4.0	44.41	43.52	MgII	2801	7.958

Table 3.1—Continued

Object (J2000)	Redshift	S/N (per pixel) ^a	$\log(\lambda L_{3000\text{\AA}})$ [erg/s]	$\log(L_{0.5-2\text{keV}})$ [erg/s] ^b	Line	FWHM (km/s)	$\log(M_{BH})$ [M_{\odot}]
COSMOS J095934.35+012849.4	1.16	11.2	44.76	44.53	MgII	6977	8.926
COSMOS J095935.50+020538.2	1.92	9.3	44.80	44.18	MgII	4959	8.653
COSMOS J095938.25+013015.8	1.47	2.7	44.39	44.23	MgII	6611	8.695
COSMOS J095940.06+022306.8	1.13	27.4	44.96	44.02	MgII	3668	8.471
SDSS J095946.01+024743.6	1.07	12.9	44.99	44.43	MgII	3796	8.512
SDSS J095949.40+020141.0	1.75	37.6	45.18	44.50	MgII	2683	8.306
SDSS J095949.40+020141.0	1.75	37.6	45.18	44.50	CIV	2463	8.143
COSMOS J095954.78+013206.5	0.48	14.3	44.29	43.41	Hb	3187	7.903
COSMOS J095956.64+013702.2	1.15	5.4	44.29	44.14	MgII	6688	8.657
SDSS J095957.98+014327.4	1.62	4.3	44.82	44.09	MgII	5569	8.761
SDSS J095957.98+014327.4	1.62	4.3	44.82	44.09	CIV	6624	8.825
COSMOS J095958.53+021805.3	1.79	12.5	45.27	44.45	MgII	4766	8.853
COSMOS J100001.00+022321.1	1.85	2.0	44.23	43.94	MgII	2523	7.781
COSMOS J100001.06+021413.6	1.41	4.1	44.32	44.17	MgII	3685	8.153
SDSS J100001.44+024844.7	0.77	10.6	44.68	44.04	Hb	3088	8.159

Table 3.1—Continued

Object (J2000)	Redshift	S/N (per pixel) ^a	$\log(\lambda L_{3000\text{\AA}})$ [erg/s]	$\log(L_{0.5-2\text{keV}})$ [erg/s] ^b	Line	FWHM (km/s)	$\log(M_{BH})$ [M_{\odot}]
SDSS J100001.44+024844.7	0.77	10.6	44.68	44.04	MgII	1863	7.744
COSMOS J100002.21+021631.8	0.85	7.4	44.27	43.87	Hb	5057	8.292
COSMOS J100006.85+021235.7	1.26	8.3	44.29	43.85	MgII	3406	8.071
COSMOS J100007.35+024043.5	1.94	15.9	44.78	43.99	MgII	5250	8.688
SDSS J100008.14+013306.6	1.17	3.1	44.45	43.92	MgII	4640	8.418
COSMOS J100010.85+024118.6	1.44	9.4	44.36	43.90	MgII	3287	8.072
SDSS J100012.91+023522.8	0.70	14.0	44.74	44.10	Hb	2994	8.150
SDSS J100012.91+023522.8	0.70	14.0	44.74	44.10	MgII	2336	7.965
COSMOS J100013.54+013739.1	1.62	19.1	44.76	-1.00	MgII	2910	8.168
COSMOS J100014.08+022838.8	1.26	27.7	44.87	43.55	MgII	4622	8.625
COSMOS J100022.71+024956.3	1.56	6.1	44.13	43.57	MgII	4866	8.299
SDSS J100024.39+015054.1	1.66	4.7	45.10	44.21	MgII	2572	8.229
SDSS J100024.39+015054.1	1.66	4.7	45.10	44.21	CIV	9962	9.079
SDSS J100024.64+023149.0	1.32	14.5	45.12	44.41	MgII	3716	8.560
COSMOS J100024.89+023956.6	2.95	10.4	44.68	44.81	CIV	3334	8.227

Table 3.1—Continued

Object (J2000)	Redshift	S/N (per pixel) ^a	$\log(\lambda L_{3000\text{\AA}})$ [erg/s]	$\log(L_{0.5-2\text{keV}})$ [erg/s] ^b	Line	FWHM (km/s)	$\log(M_{BH})$ [M_{\odot}]
COSMOS J100025.07+024128.5	1.88	2.2	44.39	44.18	MgII	3499	8.144
SDSS J100025.25+015852.2	0.37	13.8	44.30	43.82	Hb	6746	8.576
COSMOS J100028.63+025112.7	0.77	29.5	44.08	44.05	Hb	5104	8.494
COSMOS J100030.02+025142.3	1.58	20.6	45.03	43.82	MgII	2085	8.011
COSMOS J100030.45+023735.6	1.84	0.7	44.23	44.47	MgII	2765	7.859
COSMOS J100031.61+014758.1	1.68	10.0	44.69	44.45	MgII	6253	8.796
COSMOS J100033.38+015237.2	0.83	11.0	44.28	42.88	Hb	2849	8.075
COSMOS J100033.49+013811.6	0.52	8.7	43.57	43.37	Hb	4260	8.006
COSMOS J100034.93+020235.2	1.18	9.5	44.58	44.21	MgII	4140	8.386
COSMOS J100035.30+024302.9	1.18	0.9	43.56	43.71	MgII	5621	8.141
COSMOS J100037.29+024950.6	0.73	13.5	43.82	43.13	Hb	2006	7.405
COSMOS J100038.01+020822.6	1.83	14.2	45.11	43.76	MgII	7190	9.127
COSMOS J100038.30+013708.4	1.25	1.8	44.05	43.98	MgII	7219	8.600
COSMOS J100040.15+024751.6	1.04	7.9	44.75	44.02	MgII	3239	8.255
COSMOS J100042.37+014534.1	1.16	7.1	44.01	43.69	MgII	2482	7.655

Table 3.1—Continued

Object (J2000)	Redshift	S/N (per pixel) ^a	$\log(\lambda L_{3000\text{\AA}})$ [erg/s]	$\log(L_{0.5-2\text{keV}})$ [erg/s] ^b	Line	FWHM (km/s)	$\log(M_{BH})$ [M_{\odot}]
COSMOS J100043.15+020637.2	0.36	34.0	44.24	-1.00	Hb	3727	8.636
COSMOS J100046.72+020404.5	0.55	19.6	43.85	43.33	Hb	2502	7.749
COSMOS J100046.81+014737.8	1.87	5.1	44.53	44.01	MgII	5467	8.602
COSMOS J100047.75+020757.2	2.16	24.5	45.74	44.12	MgII	6216	9.319
COSMOS J100047.94+021127.2	1.51	11.0	44.58	44.06	MgII	7758	8.930
COSMOS J100049.91+020500.1	1.24	27.1	45.14	44.31	MgII	2347	8.171
COSMOS J100049.97+015231.3	1.16	14.5	44.65	43.61	MgII	5706	8.697
COSMOS J100050.57+022329.3	3.10	4.2	44.81	44.19	CIV	4706	8.391
COSMOS J100051.51+021215.5	1.83	12.8	44.88	44.46	MgII	3318	8.341
SDSS J100055.39+023441.4	1.40	4.6	44.77	44.32	MgII	6099	8.814
COSMOS J100057.79+023932.5	3.36	3.5	42.33	44.61	CIV	2034	6.634
COSMOS J100058.33+015208.8	2.03	13.0	45.04	44.25	MgII	3568	8.487
SDSS J100058.84+015400.3	1.56	3.9	44.81	44.44	MgII	4114	8.495
SDSS J100058.84+015400.3	1.56	3.9	44.81	44.44	CIV	5773	8.669
COSMOS J100100.64+022911.1	2.04	10.7	44.97	44.14	MgII	4883	8.725

Table 3.1—Continued

Object (J2000)	Redshift	S/N (per pixel) ^a	$\log(\lambda L_{3000\text{\AA}})$ [erg/s]	$\log(L_{0.5-2\text{keV}})$ [erg/s] ^b	Line	FWHM (km/s)	$\log(M_{BH})$ [M_{\odot}]
COSMOS J100100.81+015947.9	1.16	5.5	43.97	43.83	MgII	7398	8.585
COSMOS J100101.53+023848.3	3.08	2.6	43.84	44.02	CIV	5218	8.378
COSMOS J100108.36+022342.2	1.93	4.8	44.73	44.23	MgII	9319	9.166
COSMOS J100111.94+023024.9	1.50	7.9	44.61	43.95	MgII	3283	8.200
COSMOS J100112.01+024233.7	0.73	8.6	43.27	42.68	Hb	3156	7.771
COSMOS J100112.62+020940.1	1.82	18.9	45.11	44.17	MgII	4035	8.625
COSMOS J100113.34+023608.0	1.34	4.9	44.17	44.18	MgII	6107	8.515
SDSS J100114.29+022356.9	1.80	8.4	45.20	44.56	MgII	4451	8.759
SDSS J100114.29+022356.9	1.80	8.4	45.20	44.56	CIV	5646	8.899
COSMOS J100114.64+012959.0	1.78	6.9	44.45	43.88	MgII	3308	8.126
COSMOS J100115.28+024813.0	1.46	12.0	44.78	44.37	MgII	6588	8.887
SDSS J100116.79+014053.8	2.06	5.9	45.09	44.55	MgII	3848	8.577
SDSS J100116.79+014053.8	2.06	5.9	45.09	44.55	CIV	4428	8.649
COSMOS J100118.52+015543.0	0.53	16.5	43.74	43.13	Hb	4574	8.217
COSMOS J100118.57+022739.4	1.05	14.9	44.54	44.17	MgII	4953	8.519

Table 3.1—Continued

Object (J2000)	Redshift	S/N (per pixel) ^a	$\log(\lambda L_{3000\text{\AA}})$ [erg/s]	$\log(L_{0.5-2\text{keV}})$ [erg/s] ^b	Line	FWHM (km/s)	$\log(M_{BH})$ [M_{\odot}]
COSMOS J100118.78+020730.0	1.77	3.2	44.19	44.06	MgII	7788	8.736
SDSS J100120.26+023341.4	1.83	4.5	44.91	44.28	MgII	4068	8.534
SDSS J100120.26+023341.4	1.83	4.5	44.91	44.28	CIV	5258	8.661
COSMOS J100123.02+020851.3	1.26	13.8	44.63	-1.00	MgII	3751	8.322
COSMOS J100124.34+024041.7	2.76	8.6	44.96	44.70	CIV	8544	9.238
COSMOS J100124.85+022032.0	1.71	8.9	44.99	44.41	MgII	3008	8.314
COSMOS J100128.00+021819.4	1.19	0.0	43.49	43.57	MgII	3378	7.663
SDSS J100130.37+014304.4	1.57	3.5	44.77	43.80	MgII	2448	8.021
SDSS J100130.37+014304.4	1.57	3.5	44.77	43.80	CIV	3752	8.309
COSMOS J100130.78+021147.1	1.51	3.8	44.08	43.97	MgII	5852	8.434
SDSS J100132.16+013420.9	1.36	4.3	44.66	44.08	MgII	2542	8.000
SDSS J100136.50+025303.7	2.12	7.7	45.28	44.80	MgII	5091	8.914
SDSS J100136.50+025303.7	2.12	7.7	45.28	44.80	CIV	3629	8.550
COSMOS J100140.96+015643.3	2.18	32.2	45.72	44.19	MgII	4748	9.075
COSMOS J100141.09+021300.0	0.62	7.6	43.61	43.10	Hb	2030	7.347

Table 3.1—Continued

Object (J2000)	Redshift	S/N (per pixel) ^a	$\log(\lambda L_{3000\text{\AA}})$ [erg/s]	$\log(L_{0.5-2\text{keV}})$ [erg/s] ^b	Line	FWHM (km/s)	$\log(M_{BH})$ [M_{\odot}]
COSMOS J100141.26+022308.0	1.51	0.2	43.76	43.69	MgII	3370	7.794
COSMOS J100143.03+014932.2	2.08	5.6	44.55	43.73	MgII	2211	7.822
COSMOS J100145.58+024212.6	3.46	2.2	43.70	44.12	CIV	3206	7.720
COSMOS J100147.26+024729.4	1.53	5.9	43.96	43.63	MgII	3326	7.883
COSMOS J100148.33+012956.1	1.48	3.5	43.95	43.94	MgII	3395	7.895
COSMOS J100149.00+024821.8	1.61	9.9	44.28	44.02	MgII	2856	7.914
COSMOS J100149.60+023853.3	2.06	8.6	44.81	44.31	MgII	4177	8.507
COSMOS J100156.24+020943.4	1.64	22.4	44.30	43.92	MgII	6478	8.634
COSMOS J100158.96+022445.2	1.37	0.6	44.46	44.09	MgII	5863	8.628
COSMOS J100159.79+022641.6	2.03	25.1	45.45	44.99	MgII	5544	9.072
SDSS J100201.51+020329.4	2.01	15.0	45.65	44.08	MgII	10194	9.702
SDSS J100201.51+020329.4	2.01	15.0	45.65	44.08	CIV	7640	9.219
COSMOS J100202.22+024157.8	0.79	6.2	44.42	43.69	Hb	5316	8.242
SDSS J100202.78+022434.6	0.99	4.9	44.56	43.94	MgII	6609	8.780
COSMOS J100204.36+023118.1	2.78	0.0	43.96	44.99	CIV	6441	8.616

Table 3.1—Continued

Object (J2000)	Redshift	S/N (per pixel) ^a	$\log(\lambda L_{3000\text{\AA}})$ [erg/s]	$\log(L_{0.5-2\text{keV}})$ [erg/s] ^b	Line	FWHM (km/s)	$\log(M_{BH})$ [M_{\odot}]
COSMOS J100205.03+023731.5	0.52	7.8	44.42	44.01	Hb	5134	8.383
COSMOS J100206.29+021441.8	1.27	12.4	44.64	43.64	MgII	2002	7.781
COSMOS J100206.43+022304.8	1.30	0.0	43.98	43.25	MgII	3496	7.938
SDSS J100210.73+023026.1	1.16	6.0	44.82	44.26	MgII	2054	7.897
COSMOS J100212.11+014232.4	0.37	17.0	43.56	42.23	Hb	2944	7.697
COSMOS J100213.17+023827.6	1.14	0.0	44.18	43.91	MgII	4854	8.321
COSMOS J100213.42+023351.7	1.14	9.5	44.34	43.55	MgII	3228	8.049
COSMOS J100217.43+022959.7	1.10	27.3	44.85	44.00	MgII	5564	8.777
COSMOS J100218.32+021053.1	0.55	6.3	44.05	42.47	Hb	6617	8.612
COSMOS J100219.48+021315.7	2.03	6.8	44.35	43.97	MgII	6152	8.614
COSMOS J100223.05+014714.9	1.24	6.7	44.22	44.38	MgII	4702	8.315
COSMOS J100223.36+023704.5	1.44	10.5	44.08	43.59	MgII	4603	8.226
SDSS J100226.33+021923.2	1.29	4.1	44.68	44.39	MgII	2812	8.098
COSMOS J100226.93+015940.1	1.61	8.4	44.51	43.67	MgII	4124	8.346
COSMOS J100228.82+024016.9	3.14	4.4	43.87	44.78	CIV	2612	7.983

Table 3.1—Continued

Object (J2000)	Redshift	S/N (per pixel) ^a	$\log(\lambda L_{3000\text{\AA}})$ [erg/s]	$\log(L_{0.5-2\text{keV}})$ [erg/s] ^b	Line	FWHM (km/s)	$\log(M_{BH})$ [M_{\odot}]
COSMOS J100230.06+014810.4	0.63	16.6	43.98	43.31	Hb	1766	7.497
COSMOS J100230.65+024427.6	0.82	8.1	45.13	43.92	Hb	2570	7.822
SDSS J100232.13+023537.3	0.66	14.4	44.63	43.98	Hb	3234	8.191
SDSS J100232.13+023537.3	0.66	14.4	44.63	43.98	MgII	2791	8.082
COSMOS J100232.52+014009.0	1.79	16.6	44.97	44.24	MgII	5358	8.803
COSMOS J100233.64+021541.9	1.41	7.0	44.13	44.28	MgII	3166	7.927
SDSS J100234.33+015011.3	1.51	8.3	45.20	44.57	MgII	3558	8.561
SDSS J100234.85+024253.3	0.20	7.8	43.08	42.27	Hb	2017	7.179
SDSS J100236.71+015948.8	1.52	3.9	44.80	43.84	MgII	3778	8.416
COSMOS J100237.92+024700.6	0.21	22.2	44.01	41.45	Hb	2108	7.336
COSMOS J100238.70+013936.7	1.32	18.1	44.74	44.12	MgII	4740	8.583
COSMOS J100240.93+023448.4	1.68	5.3	43.88	43.80	MgII	1901	7.356
COSMOS J100243.85+020502.7	1.23	20.4	44.97	43.87	MgII	2254	8.052
COSMOS J100243.96+023428.6	0.38	9.2	44.23	43.51	Hb	4721	8.252
COSMOS J100249.33+023746.5	2.12	7.8	45.18	44.33	MgII	4193	8.695

3.3.1 Error

The scaling relations have uncertainties of ~ 0.4 dex, although there may be larger systematic uncertainties (Krolik, 2001; Collin et al., 2006; Fine et al., 2008; Marconi et al., 2008). Measurement errors in the luminosity and emission line FWHM also contribute, but the uncertainty from the scaling relations dominates. We test the luminosity error in the left panel of Figure 3.3, which compares the luminosity estimates from this work to duplicate estimates from Merloni et al. (2010). The luminosity estimates of Merloni et al. (2010) use independent redshifts from VLT/VIMOS spectra and are calculated from a fit to the IR to X-ray multiwavelength spectral energy distribution, instead of from the optical spectrum itself (as in this work). The scatter between the two luminosity estimates is $\sigma = 0.25$ dex. The Type 1 AGN in COSMOS have an average variability of ~ 0.15 dex (Salvato et al., 2009), the remaining luminosity scatter can be attributed to the different methods of estimates. Since $M_{BH} \sim L^{0.5}$, our luminosity error contributes very little to the overall M_{BH} uncertainty.

Line measurements of synthetic spectra (described in §3.2 below) show that our FWHM error is only $\sigma_{FWHM}/FWHM \sim 10\%$ at $i_{AB}^+ \sim 22$. The right panel of Figure 3.3 compares the duplicate estimates of M_{BH} for spectra with two broad emission lines. Red diamonds indicate spectra with both MgII and H β , while blue crosses indicate both MgII and CIV. The scatter between the different estimates is only $\sigma = 0.36$ dex, nearly the same as the expected intrinsic scatter for M_{BH} . This suggests that the statistical error in the mass estimators is not correlated to the choice of emission line (see also Kelly & Bechtold, 2007). If there were systematic offsets in the mass estimators, they would cause a constant shift in the mass estimate for each line, and therefore would not contribute to the scatter between two lines. The statistical intrinsic scatter, however, would not “cancel” in such a way. Because the

Table 3.1—Continued

Object (J2000)	Redshift	S/N (per pixel) ^a	$\log(\lambda L_{3000\text{\AA}})$ [erg/s]	$\log(L_{0.5-2\text{keV}})$ [erg/s] ^b	Line	FWHM (km/s)	$\log(M_{BH})$ [M_{\odot}]
COSMOS J100249.92+021732.3	1.10	17.1	44.78	44.04	MgII	6334	8.852
SDSS J100251.62+022905.5	2.01	9.4	45.15	44.44	MgII	3391	8.498
SDSS J100251.62+022905.5	2.01	9.4	45.15	44.44	CIV	4556	8.734
COSMOS J100252.88+025426.8	0.80	11.2	44.66	43.98	Hb	3843	7.972
COSMOS J100256.92+024321.2	3.32	1.0	44.04	44.36	CIV	9022	8.997
COSMOS J100258.21+015909.3	1.60	7.9	44.39	43.93	MgII	5764	8.579
SDSS J100309.21+022038.4	1.96	5.3	44.93	44.34	MgII	3580	8.435
SDSS J100309.21+022038.4	1.96	5.3	44.93	44.34	CIV	2621	8.072
COSMOS J100312.45+020002.2	1.78	6.9	44.40	43.92	MgII	10170	9.075

^aThe SDSS spectra have 3 pixels per resolution element, and the Magellan/IMACS spectra have 5 pixels per resolution element.

^bAGN with no soft X-ray detection have an entry of -1.00 for $\log(L_{0.5-2\text{keV}})$.

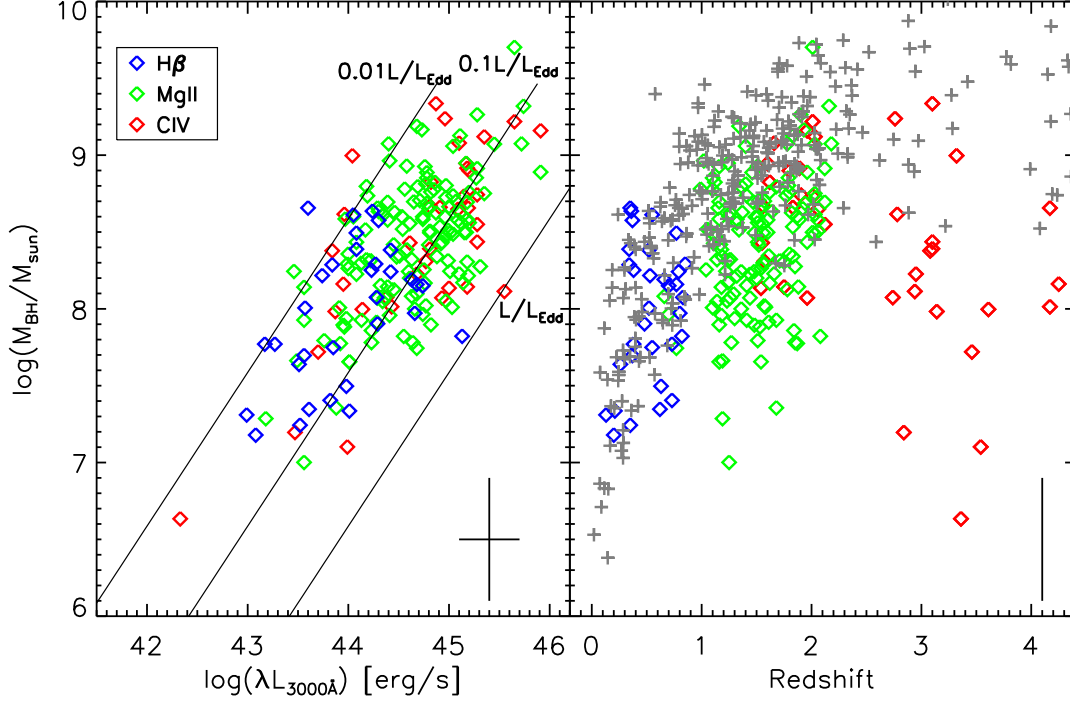


Figure 3.2 Black hole mass versus optical luminosity and redshift for 182 Type 1 AGN in COSMOS. The black hole masses are derived from the broad line velocity widths of $H\beta$ (blue diamonds), $MgII$ (green diamonds), and CIV (red diamonds) depending on the redshift (Vestergaard & Peterson, 2006; Vestergaard & Osmer, 2009). The black hole masses have uncertainties of ~ 0.4 dex from the scaling relations (Krolik, 2001; Shen et al., 2008), as shown by the typical error bars are shown in the lower right of each panel (the redshift error is $\lesssim 1\%$). The diagonal tracks at left represent Eddington ratios, assuming a bolometric correction of $L_{bol} = 5(\lambda L_{3000})$ (Richards et al., 2006). At right the gray crosses show scaling relation masses of SDSS quasars (Kelly et al., 2008). The depth of COSMOS allows us to probe low mass and weakly accreting SMBHs, revealing that $L/L_{Edd} \lesssim 0.01$ Type 1 AGN do not exist.

scatter between lines is comparable to the expected intrinsic scatter, our estimates of M_{BH} probably do not have significant systematic errors.

3.3.2 Completeness

Chapter 2 tested the completeness of the Type 1 AGN sample, with simulated spectra showing that Type 1 AGN are correctly identified (with high confidence redshifts) at 90% completeness to $S/N \gtrsim 2.87$. But even for correctly identified Type 1 AGN, our measurements of M_{BH} are roughly limited by spectral S/N and FWHM, since we cannot identify or measure broad emission lines for spectra that have lines so broad that they become confused with noise or the Fe emission. To test these limits, we create 100 synthetic spectra of Type 1 AGN with MgII in the observed wavelength range. We choose MgII because it is the most common line used for our M_{BH} calculations and also because it is the broad emission line most contaminated by widespread iron emission. These synthetic spectra are formed by making a composite of all $1 < z < 2.4$ observed spectra, then removing the rest-frame $2700\text{\AA} < \lambda < 2900\text{\AA}$ MgII region. To each of the 100 spectra we then re-add a MgII region with random FWHMs and line areas, and then each spectrum has random noise added. We choose the line areas and noise to be normally distributed in the ranges of measured line area and S/N in the original spectra, while the FWHMs are chosen to probe our sensitivity to the broadest line widths, $FWHM \gtrsim 10000 \text{ km/s}$.

We show the FWHM and S/N of both the observed and simulated spectra in Figure 3.4. The blue diamonds and red squares represent the simulated spectra that we successfully measure and those we miss, respectively. The vertical dotted line shows the sample’s 90% completeness limit for correctly identifying high-confidence Type 1 AGN. The dashed line shows the limit to where we can measure broad emission lines, corresponding to $> 95\%$ completeness since only one “missed” synthetic spectrum lies below the line. The observed Type 1 AGN tail off well before the

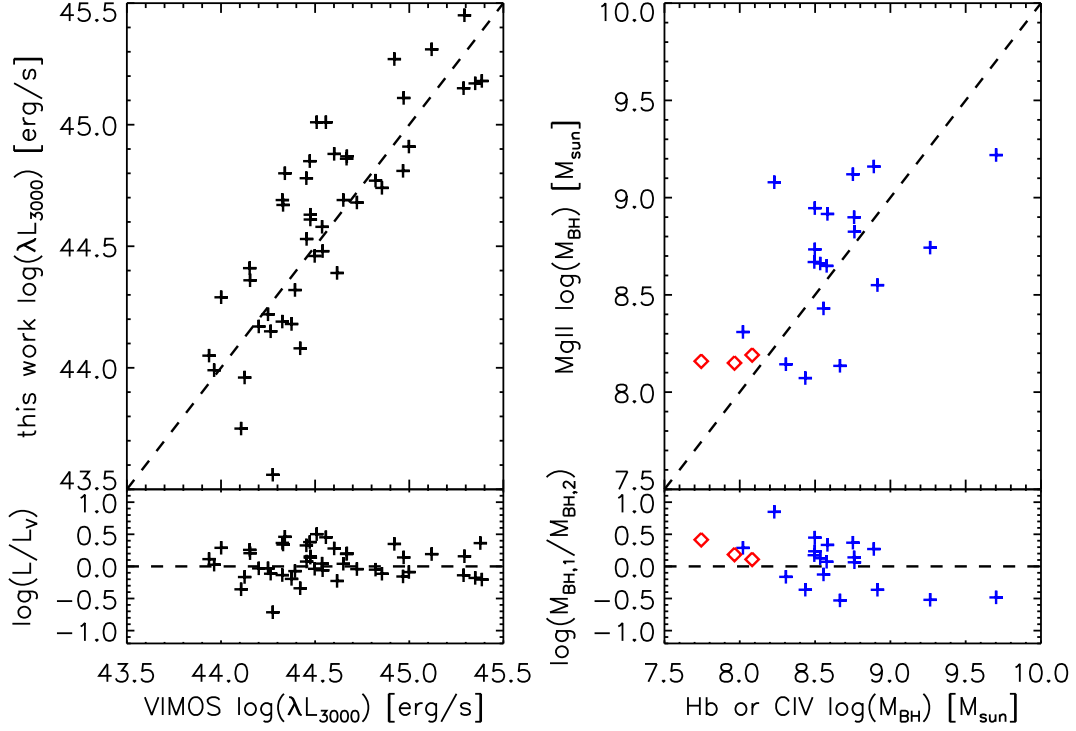


Figure 3.3 At left, the luminosity estimates for 48 AGN in this work are compared to estimates of the same objects from Merloni et al. (2010), which have independent redshifts from VLT/VIMOS spectra and are calculated from a fit to the multiwavelength SED. The scatter between the two luminosity estimates is $\sigma = 0.25$ dex, which contributes very little to the overall scatter in M_{BH} . At right, M_{BH} estimates are compared for the 22 spectra with two emission lines (either MgII and H β , red diamonds, or MgII and CIV, blue crosses). The scatter between separate M_{BH} estimates is only $\sigma = 0.36$ dex, indicative that the intrinsic scatter of ~ 0.4 dex dominates the M_{BH} error.

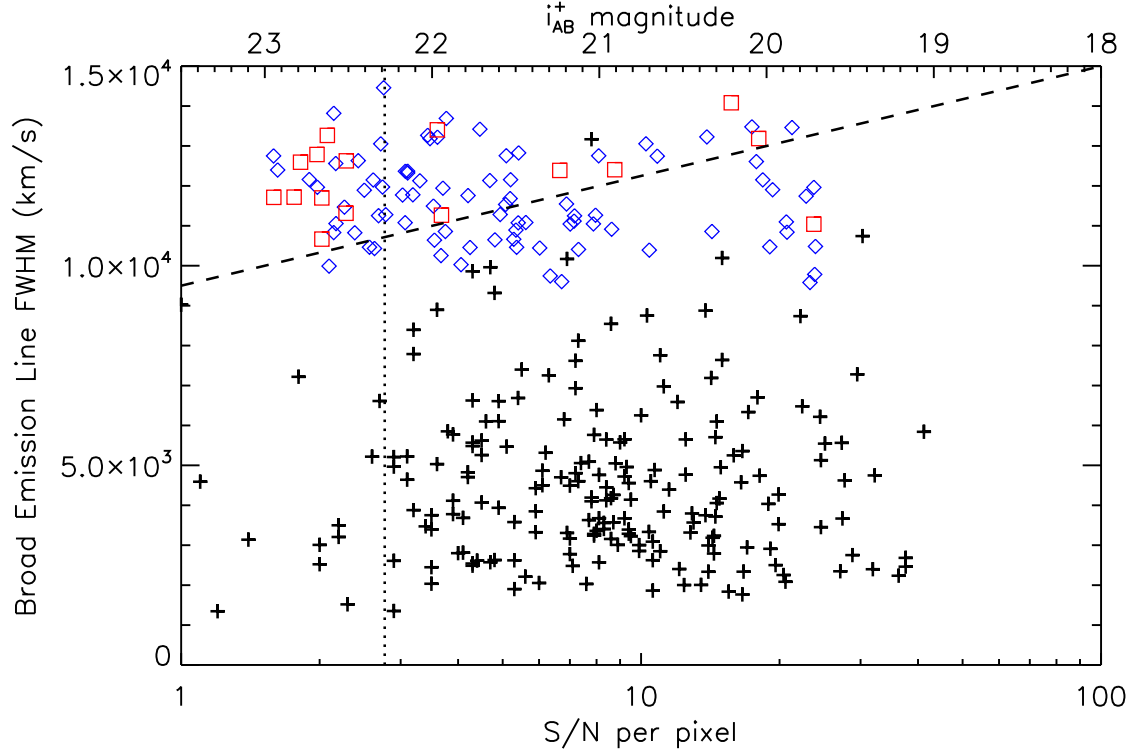


Figure 3.4 The broad emission line FWHM and S/N for our 182 Type 1 AGN are shown as black crosses. The upper axis shows the i_{AB}^+ magnitude scale which roughly corresponds to the S/N (from Figure 2.11). Also shown are the measured FWHM and S/N for 100 simulated Type 1 AGN spectra: blue diamonds represent spectra we can correctly identify and measure, while red squares represent synthetic spectra that we incorrectly identify or cannot properly measure FWHM. The dashed line shows the limit to which we correctly identify and measure $> 95\%$ of synthetic spectra. The dotted vertical line shows the 90% completeness to identifying and assigning high-confidence redshifts to Type 1 AGN, from additional simulations (see Chapter 2). The lack of high-FWHM AGN identified in COSMOS is not from selection effects, since we can correctly identify and measure synthetic Type 1 AGN with much broader lines at $S/N > 3$.

dashed line. Translating FWHM and magnitude into black hole mass, as an example, a Type 1 AGN with $i_{AB}^+ \sim 22$ at $z \sim 1.7$ with a MgII profile of FWHM= 10000 km/s would have $\log(M_{BH}/M_\odot) \sim 10.6$ and $L/L_{Edd} \sim 0.0002$. We do not detect such objects in our sample, yet our simulations show that they do not lie beyond our detection limits.

3.4 Discussion

In Figure 3.2 all Type 1 AGN lie within the region of $0.01 \lesssim L/L_{Edd} \lesssim 1$, a result supported by Kollmeier et al. (2006). This implies that the broad emission line region of Type 1 AGN might become undetectable as the accretion drops below $L \sim 0.01L_{Edd}$. Such objects might be observed as unobscured Type 2 AGN, the possible remnants of “dead” Type 1 AGN whose accretion disk geometries changed as their accretion rates fell (e.g., Hopkins et al., 2009). Or these low accretion rate AGN may be diluted, with their emission falling below the light of their host galaxy. The AGN emission may also be unable to blow out local obscuring material, causing their BLR to lie undetected behind obscuration.

To study the accretion rates of our AGN, we calculate the intrinsic luminosity from our measured λL_{3000} and $L_{0.5-2\text{keV}}$, using the relations of Marconi et al. (2004):

$$\log[L_{int}/(\lambda L_{3000})] = 0.65 - 0.067\mathcal{L} + 0.017\mathcal{L}^2 - 0.0023\mathcal{L}^3 \quad (3.2)$$

$$\log(L_{int}/L_{0.5-2}) = 1.65 + 0.22\mathcal{L} + 0.012\mathcal{L}^2 - 0.0015\mathcal{L}^3 \quad (3.3)$$

Here $\mathcal{L} = \log(L_{int}) - 45.58$ and all luminosities are in units of erg/s. The intrinsic luminosity L_{int} is designed to be a bolometric luminosity which excludes reprocessed (IR) emission, so that the Eddington ratio L_{int}/L_{Edd} represents a robust measure of the accretion onto the black hole. We use the Newton method to solve each equation for L_{int} from λL_{3000} and $L_{0.5-2}$. We then average the two values of L_{int} for our final

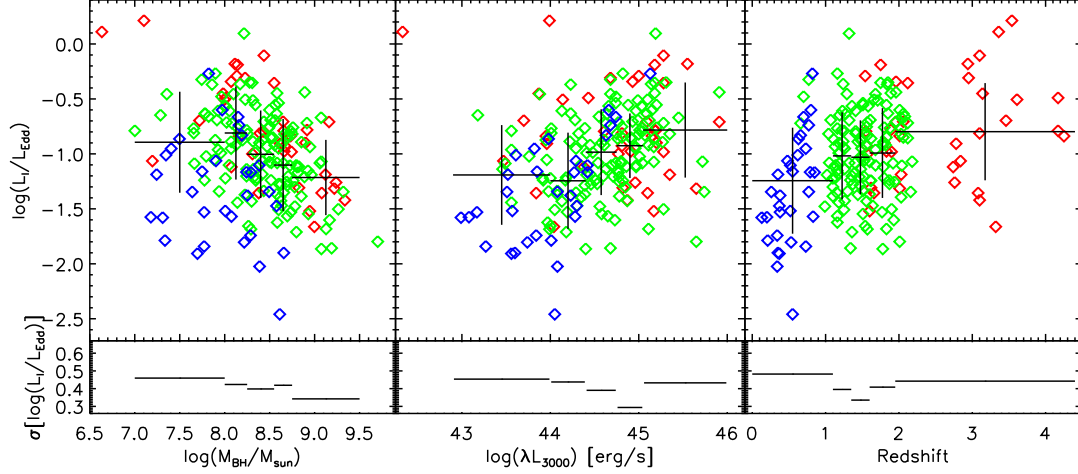


Figure 3.5 The Eddington ratio (accretion rate) with black hole mass, luminosity, and redshift for our Type 1 AGN. Eddington ratio was calculated using an intrinsic luminosity L_{int} estimated from λL_{3000} and $L_{0.5-2\text{keV}}$ using the relations of Marconi et al. (2004). Diamonds represent individual objects with masses estimated from H β (blue), MgII (green), and C IV (red). The large crosses in the top plots show the mean accretion rate in each bin of M_{BH} or redshift, while the gray lines at the bottom show the standard deviation (the square root of the second moment) in each bin. The dispersion deviation is also shown by the vertical error bar in the top plots. Bins were chosen to each have the same number of objects. Selection effects cause the apparent trends of L_{int}/L_{Edd} decreasing with M_{BH} and increasing with redshift, but the increase of L_{int}/L_{Edd} with λL_{3000} is a physical effect caused by changes in the accretion disk. The dispersion is generally ~ 0.4 dex, higher than that of previous, less sensitive surveys.

value (excepting 7 AGN where we estimate L_{int} from λL_{3000} only because they lack soft X-ray detections).

We show the Eddington ratios of our Type 1 AGN with M_{BH} , λL_{3000} , and redshift in Figure 3.5. The diamonds show individual objects, while the solid lines show the means and scatter in equal-sized bins. The scatter (the standard deviation of the mean) is calculated as the square root of the second moment of the data in each bin. Our mean Eddington ratio for all Type 1 AGN is $L_{int}/L_{Edd} \sim 0.1$, lower than the value of $L_{int}/L_{Edd} \sim 0.3$ found in previous surveys (Kollmeier et al., 2006; Gavignaud et al., 2008). This is partly explained by the depth of COSMOS: Kollmeier et al. (2006) noted that their $R \leq 21.5$ AGES sample was only complete to $L_{int}/L_{Edd} \sim 0.1$, while our simulations in §3.2 show that COSMOS can reach much weaker accretors. In addition, the center panel of Figure 3.5 shows that accretion rate may increase with optical/UV luminosity, suggesting an additional reason for our lower mean Eddington ratio: most of the Kollmeier et al. (2006) and Gavignaud et al. (2008) AGN have $\lambda L_{3000} > 10^{45}$ erg/s, where our AGN have $L_{int}/L_{Edd} \sim 0.2$. The majority of our AGN have $\lambda L_{3000} < 10^{45}$ erg/s and so we find a lower mean accretion rate.

The apparent decrease in accretion rate with black hole mass and the apparent increase in accretion rate with redshift can be explained by selection effects: low accretion rate AGN are more difficult to detect if they are also low mass or at higher redshift. The increase in accretion rate with optical luminosity, however, is also observed by Gavignaud et al. (2008) and is probably a physical effect. We performed a linear regression analysis of the correlation between accretion rate and optical luminosity using the publicly available IDL program `linmix_err.pro` (Kelly, 2007). Using errors of 0.25 dex in $\log(\lambda L_{3000})$ and 0.4 dex in $\log(L_{int}/L_{Edd})$, linear regression indicates that $\log(L_{int}/L_{Edd}) \sim (0.28 \pm 0.06) \log(\lambda L_{3000})$. In other words,

accretion rate is correlated with optical luminosity at the 4.8σ level. As a Type 1 AGN increases in accretion rate, its optical emission becomes a larger fraction of its total bolometric output because its cool accretion disk emits more brightly. This is consistent with the results of Kelly et al. (2008), which show that α_{OX} (the ratio between optical/UV and X-ray flux) becomes more X-ray quiet with accretion rate. Thus a more rapidly accreting Type 1 AGN has more of its emission in its cool (optical) disk than in its hot (X-ray) corona, possibly because the disk grows larger or thicker as the accretion rate approaches the Eddington limit.

The scatter (square root of the second moment) in L_{int}/L_{Edd} , shown in the bottom panels of Figure 3.5, is typically only ~ 0.4 dex in each bin. This is greater than previously measured dispersions (Kollmeier et al., 2006; Gavignaud et al., 2008; Fine et al., 2008), and indicates that COSMOS is more sensitive to low accretion rate Type 1 AGN than previous studies. Yet it is remarkable that the dispersion is not larger than the scatter from the scaling relations: the intrinsic dispersion in Eddington ratio might then be ~ 0 , with nearly all Type 1 AGN of a given mass, luminosity, and/or redshift accreting at a very narrow range of accretion rates. Fine et al. (2008) note that at such low measured dispersions, if the intrinsic dispersion in accretion rate is much greater than 0, then the BLR cannot be in a simple virial orbit. Accurate scaling relations would then require a luminosity-dependent ionization parameter (Marconi et al., 2008) or a more complex BLR geometry (Fine et al., 2008). We note, however, that the myriad uncertainties involved in estimating L_{int}/L_{Edd} make concrete conclusions difficult. And although we find significant evidence that $L_{int}/L_{Edd} < 0.01$ Type 1 AGN do not exist (or are very rare), the spectroscopic flux limit may still miss some $L_{int}/L_{Edd} \sim 0.01$ AGN at lower luminosities.

3.5 Summary

The black hole masses of Type 1 AGN in COSMOS indicate that Type 1 AGN accrete at a narrow range of high efficiencies, $L_{int}/L_{Edd} \sim 0.1$. When the accretion rate of an AGN lowers, less of its luminosity is emitted optically. When a Type 1 AGN accretion rate drops below $L_{int}/L_{Edd} \sim 0.01$ the BLR becomes invisible, due to obscuration, dilution, or an altered accretion disk geometry. We additionally measure higher dispersions in accretion rate than previous, less sensitive surveys, although the dispersion is still no larger than the intrinsic uncertainty in the scaling relations. Kelly et al. (2008) find that the bolometric correction depends on black hole mass, and Vasudevan & Fabian (2009) find that it correlates with Eddington ratio. This makes characterizing the distributions of L_{int}/L_{Edd} and its scatter rather difficult. We partially mitigate the systematic uncertainties by using both λL_{3000} and $L_{0.5-2}$ to estimate L_{int} . Future work in COSMOS will use more accurate bolometric luminosities calculated from the full multiwavelength dataset.

CHAPTER 4

THE NATURE OF OPTICALLY DULL ACTIVE GALACTIC NUCLEI IN COSMOS

We present infrared, optical, and X-ray data of 48 X-ray bright, optically dull AGNs in the COSMOS field. These objects exhibit the X-ray luminosity of an active galactic nucleus (AGN) but lack broad and narrow emission lines in their optical spectrum. We show that despite the lack of optical emission lines, most of these optically dull AGNs are not well-described by a typical passive red galaxy spectrum: instead they exhibit weak but significant blue emission like an unobscured AGN. Photometric observations over several years additionally show significant variability in the blue emission of four optically dull AGNs. The nature of the blue and infrared emission suggest that the optically inactive appearance of these AGNs cannot be caused by obscuration intrinsic to the AGNs. Instead, up to $\sim 70\%$ of optically dull AGNs are diluted by their hosts, with bright or simply edge-on hosts lying preferentially within the spectroscopic aperture. The remaining $\sim 30\%$ of optically dull AGNs have anomalously high f_X/f_O ratios and are intrinsically weak, not obscured, in the optical. These optically dull AGNs are best described as a weakly accreting AGN with a truncated accretion disk from a radiatively inefficient accretion flow.

4.1 Chapter Introduction

Deep X-ray surveys have indicated that most X-ray sources in the sky are AGNs with a wide range of luminosities, spectral energy distributions (SEDs), and redshifts (e.g. Brusa et al., 2007; Luo et al., 2008; Ueda et al., 2008). X-ray selection is widely regarded as the most efficient method for finding AGNs (Risaliti & Elvis, 2004; Brandt & Hasinger, 2005) and most of the X-ray background has been resolved into discrete AGN point sources (e.g. Alexander et al., 2003; Bauer et al., 2004;

Ballantyne & Papovich, 2007). Most X-ray selected AGNs are quite similar to bright quasars from optical surveys, but many would not be easily selected as AGNs by their optical emission. The class of “optically dull” AGNs (also called “X-ray bright, optically normal galaxies,” or XBONGs, Comastri et al., 2002) are particularly puzzling because their X-ray emission is bright even while the optical signature of an AGN is completely absent. First pointed out by Elvis et al. (1981), optically dull AGNs lack both the broad emission lines of unobscured Type 1 AGNs and the narrow emission lines of moderately obscured Type 2 AGNs. They are also different from heavily obscured ($N_H \gtrsim 10^{24} \text{ cm}^{-2}$) “Compton-thick” AGNs, which lack both optical and X-ray emission and are frequently missed by X-ray surveys.

What causes an optically dull AGN to have the bright X-ray emission of an AGN while lacking all optical signatures of AGN accretion? The simplest possibility is that optically dull AGNs aren’t special at all, but are normal AGNs diluted by bright hosts. Moran, Filippenko & Chornock (2002) in particular suggest that local Seyfert galaxies would be classified as optically dull if they were observed with large apertures (as is the case at higher redshift, where the host galaxy is an unresolved source fully within the spectroscopic slit or fiber). However, 10-20% of local (undiluted) AGNs are optically dull (La Franca et al., 2002; Hornschemeier et al., 2005), so dilution may not be the cause of all optically dull AGNs.

Another possibility is that the optical emission of optically dull AGNs is absorbed. Narrow emission line (Type 2) AGNs have been long thought to be Type 1 AGNs with an obscured broad line region (e.g., Antonucci, 1993), and optically dull AGNs may similarly have the entire narrow line region obscured. Comastri et al. (2002) and Civano et al. (2007) suggest gas and dust with a large covering fraction a few parsecs from the nuclear source could provide the necessary absorption, blocking the ionizing radiation from exciting the narrow line region. Rigby et al.

(2006) instead suggest that optically dull AGNs are obscured by extranuclear (>100 pc) gas and dust in the host galaxy. No matter the source of the gas and dust, obscuring optically dull AGNs would require material which preferentially absorbs the optical emission, since at least half of optically dull AGNs are relatively unobscured ($N_H < 10^{22} \text{ cm}^{-2}$) in the X-rays (Severgnini et al., 2003; Page et al., 2003).

Optically dull AGNs may instead be exotic AGNs with unusual emission or accretion properties. In particular, Yuan & Narayan (2004) suggest that optically dull AGNs may be radiatively inefficient accretors with truncated accretion disks. In this scenario, gas near the AGN does not form a cool disk, but instead is a very hot, radiatively inefficient, accretion flow (RIAF, also called an advection dominated accretion flow, or ADAF). This gas would then glow brightly in X-rays from inverse Compton emission while lacking the optical/UV blackbody emission from a typical AGN accretion disk. RIAFs have been shown to explain local low-luminosity AGNs (Quataert et al., 1999; Shields et al., 2000; Nagao et al., 2002; Hopkins et al., 2009).

We use a sample of 48 optically dull AGNs from the Cosmic Evolution Survey (COSMOS, Scoville et al., 2007)¹ to test these hypotheses. We describe the selection and multiwavelength observations in §2. In §3 we use a combination of photometry and spectroscopy to fit the optical emission of the optically dull AGNs, revealing that most of our targets show distinct contributions in the optical emission from a weak blue AGN and a dominant red passive galaxy. §3 also shows that at least four of the optically dull AGNs show significant variability. In §4 we summarize our findings and present the case that $\sim 70\%$ of optically dull AGNs are normal AGNs diluted by their host galaxies, while the remaining $\sim 30\%$ are intrinsically weak with radiatively inefficient accretion. We examine the accretion properties of weak AGNs in detail in §5, and summarize our results in §6.

¹The COSMOS website is <http://cosmos.astro.caltech.edu/>.

4.2 Observations

4.2.1 X-ray Selection

We draw the sample of optically dull AGNs from the Cosmic Evolution Survey (COSMOS, Scoville et al., 2007), a survey over 2 deg^2 of sky with deep multiwavelength observations. The XMM-*Newton* observations of COSMOS reach limiting fluxes of $1.7 \times 10^{-15} \text{ erg cm}^{-2} \text{ s}^{-1}$ and $9.3 \times 10^{-15} \text{ erg cm}^{-2} \text{ s}^{-1}$ in the 0.5-2 keV and 2-10 keV energy bands, respectively (Cappelluti et al., 2009). The optical and infrared counterparts to the X-ray sources is presented in Brusa et al. (2010), and all counterpart matches were visually inspected. Spectroscopic follow-up of X-ray targets with $i_{\text{AB}} \leq 23$ is described in Chapter 2 (see also Trump et al., 2009a). In particular, the 48 optically dull AGNs are the objects of Chapter 2 classified as “a” types (absorption line spectra) with 90% redshift confidence. All objects lack strong emission lines (see §2.2 below) in the optical spectra and satisfy one of the two X-ray AGN criteria:

$$L_{0.5-10 \text{ keV}} > 3 \times 10^{42} \text{ erg s}^{-1} \quad (4.1)$$

$$-1 \leq X/O \leq 1 \quad (4.2)$$

In Equation 2, $X/O = \log f_X/f_O = \log(f_{0.5-2 \text{ keV}}) + i_{\text{AB}}/2.5 + 5.352$. These constraints are set by the limit on X-ray luminosity in local star forming galaxies of $L_X \lesssim 10^{42} \text{ erg s}^{-1}$ (e.g., Fabbiano, 1989; Colbert et al., 2004) and the traditional “X-ray AGN locus” of Maccacaro et al. (1988). These equations have been shown to be quite reliable in selecting AGNs, although they are probably overly conservative (e.g., Hornschemeier et al., 2001; Alexander et al., 2001; Bauer et al., 2004; Bundy et al., 2008). Of the 48 optically dull AGNs, 44 meet both criteria, with only 4 meeting one criterion but not the other. The optically dull AGNs are additionally

restricted to $z \leq 1$, since beyond these redshifts the 4000Å break shifts beyond the observed spectral range of (see Chapter 2) and it becomes extremely difficult to measure redshifts from absorption lines. The 48 optically dull AGNs are all of the $z < 1$ AGNs within the 2 deg² of COSMOS that meet either of the X-ray criteria and have Magellan/IMACS or SDSS spectroscopy.

4.2.2 Spectroscopy

Of the optically dull AGNs, 45/48 have optical spectra from observations with the Inamori Magellan Areal Camera and Spectrograph (IMACS, Bigelow et al., 1998) on the 6.5 m Magellan/Baade telescope. These spectra have wavelength ranges of 5600-9200Å, with a resolution element of 10Å (5 pixels). All targets were selected as AGN candidates by their X-ray emission. Details of the observations and reductions are presented in Chapter 2, and all of the spectra are publicly available on the COSMOS IRSA server (<http://irsa.ipac.caltech.edu/data/COSMOS>). The optically dull AGNs in this work all have high-confidence redshifts ($z_{\text{conf}} \geq 3$), which empirically corresponds to a 90% likelihood of the correct redshift measurement (see Chapter 2).

Three of the optically dull AGN spectra come from archival Sloan Digital Sky Survey (SDSS, York et al., 2000) observations. These sources were selected by their X-ray emission, but were excluded from the main Magellan/IMACS survey because their redshifts were already known. Their wavelength coverage is 3800-9200Å and their resolution element is 3Å (3 pixels).

Figure 4.1 shows the measured [OII] ($\lambda 3727\text{\AA}$) and H β ($\lambda 4861\text{\AA}$) narrow emission line luminosities for the optically dull AGNs (black squares), along with a comparison sample of Type 2 AGNs (blue diamonds) from Chapter 2. To compute the line luminosity, we first define a straight-line continuum by averaging the spectral regions 30-40Å redward and blueward of the line region. The line luminosity is then

measured across the continuum-subtracted region 1000 km/s about the line center. The 1000 km/s width is a conservative limit since $< 1\%$ of Type 2 AGNs have narrow emission lines broader than 1000 km/s (Hao et al., 2005). The measured error for each line luminosity is computed using both the spectral error and the error of the continuum fit. When the line luminosity was less than its 5σ error, we used the 5σ error as an upper limit on line luminosity.

All 38 optically dull AGNs with $H\beta$ in the observed wavelength range have $L_{H\beta} < 5\sigma_{L(H\beta)}$ and thus are assigned only upper limits in the bottom panel of figure 4.1. However, 9/40 optically dull AGNs with $[OII]$ in the observed wavelength range have a line luminosity greater than the 5σ threshold, despite the fact that the classification of Chapter 2 identified no emission lines. Still, even when detected, the emission line luminosities of the optically dull AGNs are much lower than those of typical Type 2 AGNs. If the optically dull AGNs were simply Type 2 AGNs observed at low signal-to-noise (S/N), we might expect poorly constrained upper limits on line luminosity. This is not the case, as the upper limits are 10-100 times lower than the line luminosities of typical Type 2 AGNs. Optically dull AGNs are not Type 2 AGNs with low S/N, but have much less luminous emission lines than Type 2 AGNs of similar X-ray luminosities.

4.2.3 Optical and Infrared Photometry

The optical and infrared photometry of the optically dull AGN is drawn from the catalog of Capak et al. (2010). Table 4.1 shows the depths, wavebands, and year of observation for the COSMOS photometry used here.

The optical photometry data are from the Subaru telescope, with observations of the 6 broad, 12 intermediate, and 2 narrow bands described in Taniguchi et al. (2007) and Taniguchi et al. (2010). Fluxes were measured in $3''.0$ diameter apertures, on PSF-matched images with FWHM of $1''.5$, and simulations (Capak et al., 2007)

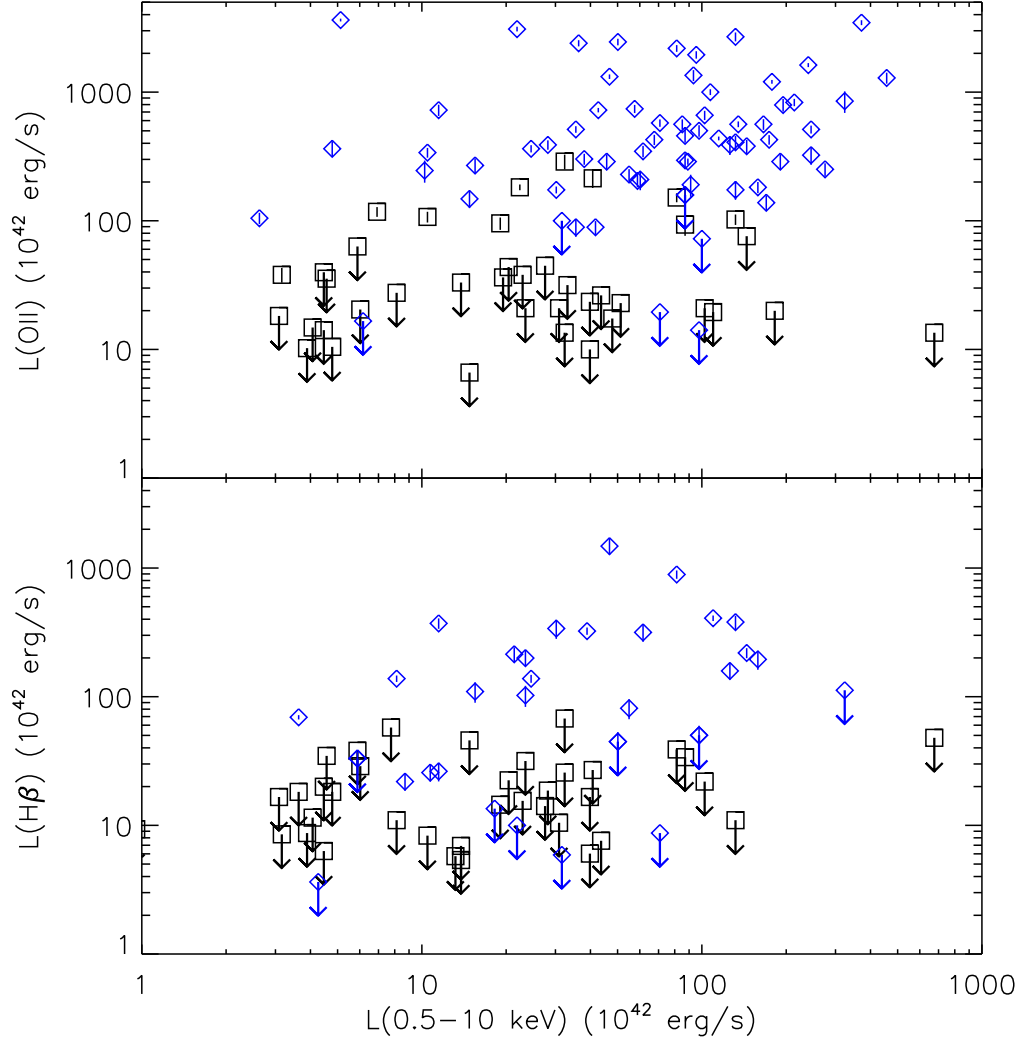


Figure 4.1 Luminosities of the $[\text{OII}]3727\text{\AA}$ and $\text{H}\beta 4861\text{\AA}$ lines with X-ray luminosity for optically dull AGNs (squares) and Type 2 AGNs (blue diamonds, from Chapter 2). For almost all optically dull AGNs, no line is detected above the 5σ threshold, and we assign a 5σ upper limit to the line luminosity. Even when $L > 5\sigma_L$ and the line is positively measured, the $[\text{OII}]$ and $\text{H}\beta$ lines are 10-100 times weaker than those of typical Type 2 AGNs. Optically dull AGNs are not low-S/N Type 2 AGNs, but instead have much less luminous emission lines despite their X-ray brightness.

show that the $3''.0$ diameter aperture contains 76% of the total flux for a point source. We additionally correct each optical magnitude by the zero-point correction from Ilbert et al. (2009).

The infrared photometry is derived from *Spitzer*/IRAC observations. The closest IRAC source within $1''.0$ of the optical counterpart to the XMM source was chosen as the infrared counterpart. IRAC fluxes are given in the COSMOS-IRAC catalog for $3''.8$ diameter apertures, so we translate these into $3''.0$ diameter aperture fluxes as described in Salvato et al. (2009). All of our optically dull AGNs were unambiguously detected in all 4 IRAC bands.

Table 4.1. COSMOS Optical and Infrared Photometry

Filter	Telescope	Center λ \AA	FWHM \AA	Depth ($3''0$) mag_{AB}	Epoch UTC
B_J	Subaru	4460	897	27.7	2004
g^+	Subaru	4750	1265	27.1	2005
V_J	Subaru	5484	946	27.0	2004
r^+	Subaru	6295	1382	27.1	2004
i^+	Subaru	7640	1497	26.7	2004
z^+	Subaru	9037	856	25.7	2004
IA427	Subaru	4271	210	26.5	2006
IA464	Subaru	4636	227	26.0	2006
IA484	Subaru	4842	227	26.5	2007
IA505	Subaru	5063	232	26.2	2006
IA527	Subaru	5272	242	26.5	2007
IA574	Subaru	5743	271	26.2	2007
IA624	Subaru	6226	299	26.3	2006
IA679	Subaru	6788	336	26.1	2006
IA709	Subaru	7082	318	26.3	2007
IA738	Subaru	7373	322	26.1	2007
IA767	Subaru	7690	364	25.9	2007
IA827	Subaru	8275	364	25.8	2006
NB711	Subaru	7126	73	25.4	2006

Table 4.1—Continued

Filter	Telescope	Center λ	FWHM	Depth ($3''0$)	Epoch
		\AA	\AA	mag_{AB}	UTC
NB816	Subaru	8150	119	26.1	2005
IRAC1	Spitzer	35263	7412	23.9	2006
IRAC2	Spitzer	44607	10113	23.3	2006
IRAC3	Spitzer	56764	13499	21.3	2006
IRAC4	Spitzer	77030	28397	21.0	2006

4.2.4 Host Morphologies

We discuss morphological data of the optically dull AGN host galaxies from observations with the Advanced Camera for Surveys (ACS) on the *Hubble Space Telescope* (HST), fully described in Koekemoer et al. (2007). The COSMOS field was imaged in the F814W filter for 583 orbits, reaching a limiting magnitude of $AB(F814W) \leq 27.2$ (5σ). Because the HST/ACS imaging only covers 1.64 deg^2 of the 2 deg^2 COSMOS field, 3/48 optically dull AGNs lack HST/ACS coverage. Gabor et al. (2009) provides morphological data for 37 of the remaining optically dull AGNs, from the point source subtracted host galaxies. (The other 8 optically dull AGNs have HST/ACS imaging, but do not have morphological data because the resultant fit was wildly unphysical or did not converge.)

4.2.5 Completeness

All of the optically dull AGNs are detected in the Subaru and IRAC photometry, and all within the HST areal coverage were detected in ACS, so these do not affect the completeness limits. The soft 0.5-2 keV X-ray limit of $1 \times 10^{-15} \text{ erg cm}^{-2} \text{ s}^{-1}$

means the X-ray AGN sample is complete to all AGNs meeting the luminosity criterion (Equation 1) of $L_{0.5-10 \text{ keV}} > 3 \times 10^{42} \text{ erg s}^{-1}$ at $z \lesssim 1$ (see Figure 2.9). Correct identification of optically dull AGNs is also limited to $z \lesssim 1$, since at higher redshifts the 4000Å break in these objects is redshifted beyond the observed wavelength range, and high-confidence identification becomes difficult. The Magellan/IMACS spectroscopy is uniformly 90% complete to $i_{\text{AB}} \leq 22$ absorption line objects. The optically dull AGN sample is then limited by $z \lesssim 1$ and $i_{\text{AB}} \leq 23$, but is 90% complete to only $i_{\text{AB}} \leq 22$.

4.3 Multiwavelength Properties

Table 4.2 presents the multiwavelength properties of all 48 optically dull AGNs. For each object, we show:

1. The object name, with coordinates given in J2000 hhmmss.ss+ddmmss.s. “COSMOS” or “SDSS” indicates if the spectroscopy is from Magellan/IMACS or the SDSS archives, respectively.
2. The redshift, from Chapter 2.
3. The signal to noise per pixel, averaged over the spectrum in the central wavelength range 6600-8200Å. (The resolution element is 5 pixels for Magellan/IMACS spectra, and 3 pixels for SDSS spectra.)
4. The *i*-band AB magnitude, from Subaru/Suprime-Cam observations.
5. The logarithm of the X-ray luminosity measured in the 0.5-10 keV energy range, in cgs units.
6. The ratio between X-ray and optical flux, X/O , defined in equation 2.

7. The fractional contribution of AGN in the best-fit template (see §3.1). This can be regarded as a rough estimate of the blue AGN contribution to the optical emission.
8. The ratio between X-ray and optical flux, X/O , but where the optical flux includes only the blue AGN contribution (from the template fit in §3.1).
9. The hardness ratio, $HR = (H - S)/(H + S)$. Here S is the flux in the soft 0.5-2 keV band and H is the flux in the hard 2-10 keV band. AGNs undetected in the soft band have $HR = 1$, and those undetected in the hard band have $HR = -1$.
10. The axis ratio b/a , measured using GALFIT after subtracting a point source from the host galaxy (see §3.5).

Table 4.2. Optically Dull AGN Properties

Object Name	z	S/N	i_{AB}	$\log(L_X)$	X/O	f_{AGN}	$X/O(\text{AGN})$	HR^{a}	b/a^{b}
COSMOS J095802.10+021541.0	0.94	3.75	21.01	43.29	-0.6	0.00	1.1	-1.00	-1.00
COSMOS J095808.98+022739.9 ^c	0.85	8.16	21.62	43.51	-0.0	0.21	0.6	-0.27	0.73
COSMOS J095809.45+020532.4	0.61	7.73	20.80	42.65	-0.9	0.12	0.1	-1.00	0.57
COSMOS J095820.57+023330.1 ^c	0.96	1.18	21.51	43.52	-0.2	0.20	0.5	-0.42	0.60
COSMOS J095830.25+022400.8	0.85	5.51	21.57	42.89	-0.7	0.03	0.8	-1.00	-1.00
COSMOS J095834.23+024332.5	0.39	14.33	19.86	42.56	-0.9	0.05	0.4	0.20	0.27
COSMOS J095839.01+021610.6	0.68	10.42	20.08	43.36	-0.6	0.02	1.1	-0.35	0.62
COSMOS J095846.02+014905.6	0.74	5.75	20.24	43.44	-0.5	0.06	0.7	-0.10	0.52
SDSS J095849.02+013219.8	0.36	3.55	18.94	44.83	1.1	0.25	1.7	-0.64	-1.00
COSMOS J095857.20+015843.7	0.52	6.02	21.30	43.60	0.4	0.03	1.9	0.66	0.34
COSMOS J095906.97+021357.8	0.76	5.11	21.30	43.94	0.4	0.02	2.0	0.02	0.42
COSMOS J095917.26+021516.9	0.94	7.88	20.85	43.71	-0.2	0.32	0.2	-0.51	0.76
COSMOS J095926.01+014444.3	0.67	6.03	20.72	43.49	-0.2	0.04	1.3	-0.56	0.83

Table 4.2—Continued

Object Name	z	S/N	i_{AB}	$\log(L_X)$	X/O	f_{AGN}	$X/O(\text{AGN})$	HR^{a}	b/a^{b}
COSMOS J095937.42+022347.4	0.74	5.90	21.15	42.66	-0.9	0.16	-0.1	-1.00	0.82
COSMOS J095938.56+023316.8	0.75	27.31	19.92	43.51	-0.6	0.25	0.0	-0.37	-1.00
COSMOS J095940.86+023051.2	0.70	7.16	21.74	42.59	-0.7	0.12	0.2	-1.00	0.34
COSMOS J095945.21+023021.5	0.89	5.56	20.76	42.84	-1.1	0.26	-0.5	-1.00	0.95
COSMOS J095958.46+021530.8 ^c	0.66	15.13	20.12	44.01	0.1	0.28	0.7	-0.45	0.45
COSMOS J095959.36+022458.4	0.57	13.67	20.42	43.02	-0.6	0.18	0.2	-0.26	0.62
COSMOS J100005.36+023059.6	0.68	6.42	20.90	43.35	-0.2	0.04	1.1	0.02	0.36
COSMOS J100006.42+023343.4	0.75	8.91	20.96	43.31	-0.4	0.11	0.6	-0.52	0.85
COSMOS J100013.33+022657.2	0.73	7.83	20.71	43.91	0.2	0.03	1.6	0.21	-1.00
COSMOS J100013.41+021400.6	0.94	4.24	20.76	43.68	-0.3	0.13	0.6	-0.32	-1.00
COSMOS J100024.09+014005.4	0.62	13.96	19.74	42.65	-1.3	0.03	0.1	-1.00	0.84
COSMOS J100024.86+023302.7	0.50	8.73	21.05	43.14	-0.1	0.28	0.5	-0.45	0.61
SDSS J100028.28+024103.5	0.35	7.33	17.44	42.61	-1.7	0.00	0.0	-0.53	0.72

Table 4.2—Continued

Object Name	z	S/N	i_{AB}	$\log(L_X)$	X/O	f_{AGN}	$X/O(\text{AGN})$	HR^{a}	b/a^{b}
COSMOS J100031.27+022819.9	0.93	2.69	21.56	44.04	0.4	0.07	1.5	-0.18	0.73
COSMOS J100034.04+024225.3	0.85	7.21	20.64	43.37	-0.6	0.22	0.1	-0.30	0.50
COSMOS J100036.21+024928.9	0.47	5.69	18.77	43.03	-1.0	0.25	-0.4	0.20	0.67
COSMOS J100037.99+014248.6	0.62	8.77	20.39	43.17	-0.5	0.20	0.2	-0.30	0.63
COSMOS J100046.55+024412.0	0.22	28.43	20.42	42.27	-0.3	0.00	1.3	1.00	0.33
COSMOS J100047.93+014935.8	0.89	5.21	21.26	44.16	0.4	0.17	1.2	-0.55	0.79
COSMOS J100052.99+014123.8	0.68	3.95	21.84	42.77	-0.4	0.14	0.4	-1.00	0.37
COSMOS J100059.45+013232.8	0.89	1.46	22.58	44.26	1.0	0.00	2.7	0.41	-1.00
COSMOS J100105.84+023041.0	0.70	10.16	20.64	43.64	-0.1	0.13	0.8	0.11	0.39
COSMOS J100124.06+024936.7	0.82	10.06	20.54	43.60	-0.3	0.01	1.5	0.14	-1.00
SDSS J100131.15+022924.8	0.35	4.95	18.26	42.91	-1.0	0.05	0.3	-0.67	0.71
COSMOS J100139.10+023824.2	0.49	5.44	22.60	41.98	-0.6	0.80	-0.5	-1.00	-1.00
COSMOS J100153.45+021152.8	0.48	7.97	19.31	43.12	-0.7	0.16	0.1	1.00	-1.00

4.3.1 Optical Fitting: Host and AGN Components

Each optically dull AGN spectrum lacks strong emission lines and has the red shape and absorption signature (H+K lines, 4000Å break, etc.) of an old, red elliptical galaxy. However, the spectra often have low S/N, and most (45/48) are limited by the 5600-9200Å wavelength range of Magellan/IMACS. The 20 bands of high-S/N optical photometry allow us to take a broader look at the optical SED.

We fit the optical photometry of each optically dull AGN with an “r+q” template that is a mix of a red galaxy component (the SDSS red galaxy composite from Eisenstein et al., 2001) and a blue AGN component (the SDSS quasar composite from Vanden Berk et al., 2001). The scale of each component is an independent free parameter. The two components of the hybrid “r+q” template are well-motivated for two reasons: (a) from the X-ray properties the objects must have an AGN, and (b) the optical spectrum most closely resembles a red galaxy. While both the host and any underlying AGN will not be perfectly described by the “r” and “q” components of the template, we explore the minor systematic deviations below.

We find the red galaxy and AGN components in the best-fitting template by maximizing the Bayesian probability function, $P = \prod \frac{1}{\sqrt{2\pi\sigma_m^2}} \exp\left(\frac{-0.5(m-m_t)^2}{\sigma_m^2}\right)$. Here m is the observed magnitude, σ_m is its error, and m_t is the template magnitude computed by measuring the template flux through the same wavelength response function as the observed magnitude. (The χ_0^2 parameter is the logarithm of this probability function, but we choose the Bayesian approach because it maps out the probability distribution, not just the best-fit values.) In the fits for all objects the best-fit fractions of AGN and red galaxy are tightly constrained: the 99% confidence intervals for the fit contain deviations of $< 3\%$.

Systematic errors will dominate over the fitting errors, however, because the “r+q” template is not likely to be a perfect fit to the observed data. First, the

Table 4.2—Continued

Object Name	z	S/N	i_{AB}	$\log(L_X)$	X/O	f_{AGN}	$X/O(\text{AGN})$	HR^{a}	b/a^{b}
COSMOS J100209.70+023432.3	0.61	14.44	21.09	42.50	-0.9	0.20	-0.2	-1.00	0.18
COSMOS J100216.37+015008.2 ^c	0.67	10.32	21.04	43.28	-0.2	0.02	1.4	1.00	0.46
COSMOS J100224.16+023107.7	0.67	6.09	21.68	43.14	-0.1	0.26	0.5	-0.55	0.85
COSMOS J100231.26+022716.4	0.81	20.00	20.22	43.61	-0.4	0.17	0.3	-0.59	-1.00
COSMOS J100232.15+022925.6	0.80	5.89	20.88	42.78	-1.0	0.28	-0.4	-1.00	0.81
COSMOS J100237.09+014648.0	0.67	11.70	20.52	44.12	0.4	0.03	1.9	-0.13	0.52
COSMOS J100238.63+024743.1	0.82	1.90	21.89	42.68	-0.7	0.00	1.0	-1.00	-1.00
COSMOS J100240.30+020147.3	0.64	5.91	21.87	43.45	0.3	0.04	1.7	-0.15	0.38
COSMOS J100243.93+022340.7	0.66	3.82	21.13	42.49	-1.0	0.16	-0.2	-1.00	0.30

^aAGN undetected in the hard (2-10 keV) X-ray band have $HR = -1$, while those undetected in the soft (0.5-2 keV) X-ray band have $HR = 1$.

^bAGN hosts which lack morphological data are assigned $b/a = -1$.

^cThese optically dull AGN show significant variability in their blue emission.

optically dull AGNs may have active or recent star formation contributing to the blue emission, causing us to overestimate the AGN emission. The contribution from a young stellar population (O/B-star) is likely to be minor, since the emission line luminosities for the optically dull AGNs are very low (see §2.2). A moderate age (A-star) stellar population would not have strong emission lines, but must also be a minor contributor at best because none of the optically dull AGN spectra show a Balmer break. We estimate the effect of any blue star-forming component as $< 20\%$, since any higher contribution would lead to emission lines or a recognizable Balmer break for even the lowest S/N optically dull AGNs. In addition, the AGN template of Vanden Berk et al. (2001) may not well describe the optical shape of the true underlying AGN, since AGNs can be heavily reddened (Hopkins et al., 2004) or obscured (Elitzur, 2008), and even unobscured quasars are known to exhibit a wide variety of optical spectral shapes (Richards et al., 2006). Still, Vanden Berk et al. (2001) notes that the Type 1 AGNs have a variation of only $\sigma < 20\%$ from the mean SED in their blue ($\lambda < 4000\text{\AA}$) continua. So we can assume that our AGN fractions are valid, with the caveat that the true optical AGN emission may differ by up to 20%. While the “r+q” template may not recover the true optical AGN fraction of the optically dull AGNs, our estimated AGN fraction is useful as rough estimate for studying the host-subtracted X/O fraction.

We show examples of our template fits in Figure 4.2. In each panel the black points show the photometry, with the x error bar showing the band width and the y error showing the photometric error. The black histogram is the observed spectrum from Magellan/IMACS or the SDSS, and the blue histogram is the best-fit “r+q” template. Figure 4.2 additionally includes a best-fit red-galaxy-only (“r”) template, shown in red, to illustrate the improvement of including a blue AGN component in the template fit. Reduced chi-square values, and the blue AGN contribution of

the “r+q” template fit, are shown in the upper left of each panel. Note that the χ_0^2 values are quite large because the optical photometry has very small errors and the 14 narrow and intermediate bands are sensitive to details which are not well-described by our templates. But while the fits do not perfectly describe the details of the optically dull AGN SEDs, the templates are useful for studying the shape of the SEDs and providing a rough estimate of the relative blue AGN and red host components.

The top panel represents optically dull AGNs with virtually no quasar contribution in the optical photometry, where the highest probability “r+q” template had zero quasar fraction. Five of the 48 optically dull AGNs had similar fits, with virtually no blue AGN emission. The upper limit on any blue quasar excess in these objects is typically only 2% blue AGN component.

The second panel of Figure 4.2 shows an example of an optically dull AGN with a significant quasar component in the fit. In this example the best-fit “r+q” template is significantly better than the best-fit “r” template, with a much lower reduced chi-square. The majority of the optically dull AGNs, 28/48 objects, exhibited similar fits, with $\chi_0^2(r) \geq 2\chi_0^2(r+q)$. The blue AGN contribution in these objects is typically 15-35%.

The third panel represents optically dull AGNs where the best-fit “r+q” template is only a slight improvement over the plain “r” red galaxy template. These AGNs have only a very weak excess of blue emission, completely invisible in the observed spectrum and only barely detected in the optical photometry. Of the 48 optically dull AGNs, 15 exhibit similar fits, with blue AGN contribution of about 3-7%.

We can additionally compare the predicted line fluxes of the quasar component in the best-fit template to the line flux limits in the optical spectrum. The $H\beta$ and $[OII]$ narrow emission lines (shown in Figure 4.1) do not work well for this comparison

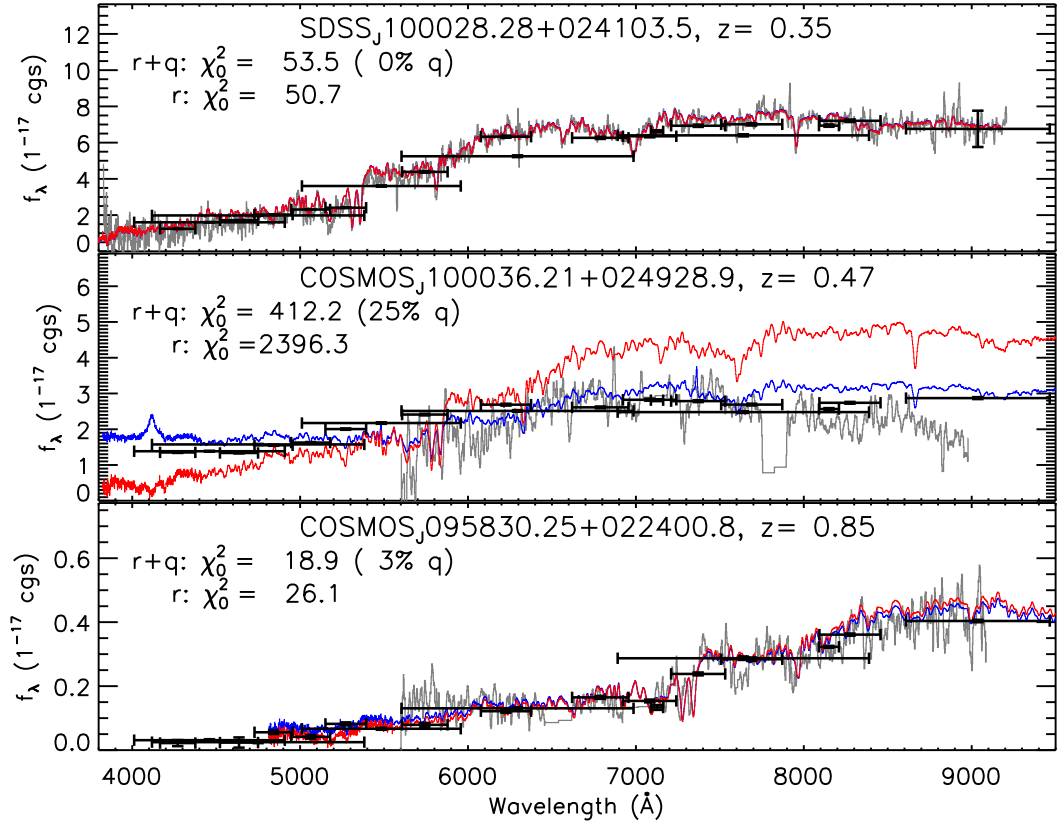


Figure 4.2 Three examples of our fits to the optical photometry of optically dull AGNs. In each panel the gray histogram shows the spectrum, from the SDSS for the first object and from Magellan/IMACS for the other two. The black points with error bars show the measured Subaru optical magnitudes. The red and blue histograms show the best-fit red galaxy (“r”) and quasar/galaxy hybrid (“r+q”) templates, respectively. In the upper left of each panel, we show the reduced chi-square for the best fit, and the fraction of the hybrid template from the quasar component is represented by “(X% q)”. Note that the fitting comes from the photometry and does not use the spectrum. The three panels represent, from top to bottom: optically dull AGNs with virtually no blue quasar emission, objects with significant blue emission above the red galaxy host, and intermediate objects.

because we use a quasar template in our fit, and these narrow lines are often weak or nonexistent in Type 1 AGN. However the [O III] ($\lambda 5007\text{\AA}$) narrow emission line is typically strong in both Type 1 and Type 2 AGN and so is useful for the comparison. Only 30 optically dull AGNs have [O III] in their observed wavelength range, and all of these are upper limits only. Most (19/30) of these AGNs have predicted [O III] fluxes from the best-fit model which lie below the upper limit on [O III] flux from the spectrum. Since these AGNs have low predicted line fluxes and the measured [O III] fluxes are only limits, it is not a strong constraint, but it does suggest that these 19 optically dull AGNs could be diluted Type 1 or Type 2 AGNs.

The optical photometry also reveals significant variability in four optically dull AGNs. When comparing the observations from 2004, 2006, and 2007 (see Table 4.1), these four AGNs exhibited changes in flux 5σ beyond the photometry errors. We show an example of a variable optically dull AGN in Figure 4.3. Magnitudes from each of 2004, 2006, and 2007 are shown in each panel in blue, with the corresponding template fit shown in red in each panel. The template fit to all 20 bands of optical photometry (from all years) is shown in gray, along with the Magellan/IMACS spectrum in black, for comparison in each panel. The optically dull AGN decreases in flux from 2004 to 2007, but almost all of this change is in the blue emission. In the template fit, the red galaxy component remains nearly the same in each year while the AGN component decreases from 43% to 15% contribution.

Old red galaxies do not change in flux over different years of observations. Type 1 AGNs, however, can vary by as much as factors of a few on year timescales (e.g. Morokuma et al., 2008; Kelly et al., 2009). The four variable optically dull AGNs must then have a weak AGN causing the variability. The source of the variability must be ≤ 1 light-year in size, while any obscured gas and dust in an AGN is thought to be on much larger scales [e.g.]nen08. It is then extremely unlikely that the

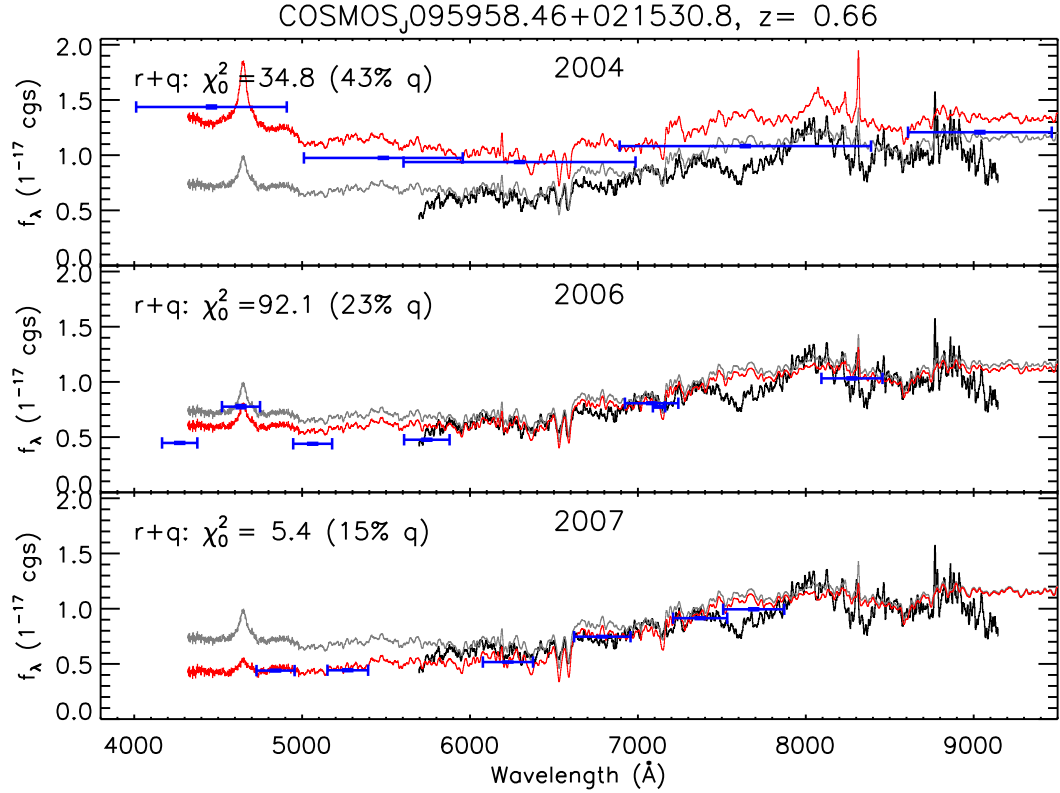


Figure 4.3 An optically dull AGN which exhibits variability in its optical photometry. In all three panels, the black histogram shows the observed Magellan/IMACS spectrum (taken in 2006), and the gray histogram shows the best-fit “r+q” hybrid template to the 20-band photometry from all years. Each panel represents a different year of observations: 2004 at the top, 2006 in the middle, and 2007 at the bottom. The blue points with error bars show the photometry for that year and the red histogram is the best-fit “r+q” template for that year’s data only. The optically dull AGN has a strongly decreasing blue emission component, starting as nearly half of the total emission in 2004 and dropping to less than one-sixth in 2007. Four optically dull AGNs show significant variability.

variability is caused by obscuration or reddening. The variable optically dull AGNs are instead likely to be diluted “normal” AGNs. Indeed, close inspection of Figure 4.3 shows that the optical spectrum may have a weak $H\beta$ broad emission line, although it is difficult to positively identify the line because of low S/N in that part of the spectrum. (§2.2, however, showed that for this and other optically dull AGNs, the narrow [OII] and $H\beta$ lines are not hidden by low S/N, but are instead very weak compared to those of Type 2 AGNs.) So while optically dull AGNs do not have strong emission lines, the four variable objects in particular show evidence for a diluted (not obscured) AGN. These objects are likely to be normal, unobscured Type 1 AGNs diluted by extranuclear light (as we explore in §3.5).

4.3.2 X-ray to Optical Ratio

The defining characteristic of optically dull AGNs is that they are bright in X-rays while their optical spectra have no sign of emission lines. But while optically dull AGNs lack the emission line signature of an AGN, §3.1 showed that they do have excess blue emission which might be attributed to a diluted AGN. But are optically dull AGNs simply diluted by a bright host, or is their optical emission actually depressed when compared to their bright X-rays?

We present the ratio between the X-ray and optical flux in Figure 4.4, where $\log f_X/f_O = \log(f_X) + i_{AB}/2.5 + 5.352$. The optically dull AGNs are shown as squares, and the four variable objects are indicated by filled squares. For comparison the Type 1 (broad line) and Type 2 (narrow line) X-ray AGNs from Chapter 2 are shown in gray. At left, we use the total f_O for the optically dull AGNs, and all but 2 of the optically dull AGNs have f_X/f_O values consistent with typical AGNs. At right, the i_{AB} magnitude includes only the AGN fraction as determined in §3.1. It is important to note that X-ray K-corrections will cause Compton-thick AGNs at higher redshifts to have higher f_X/f_O ratios, (e.g., Comastri et al., 2003), although

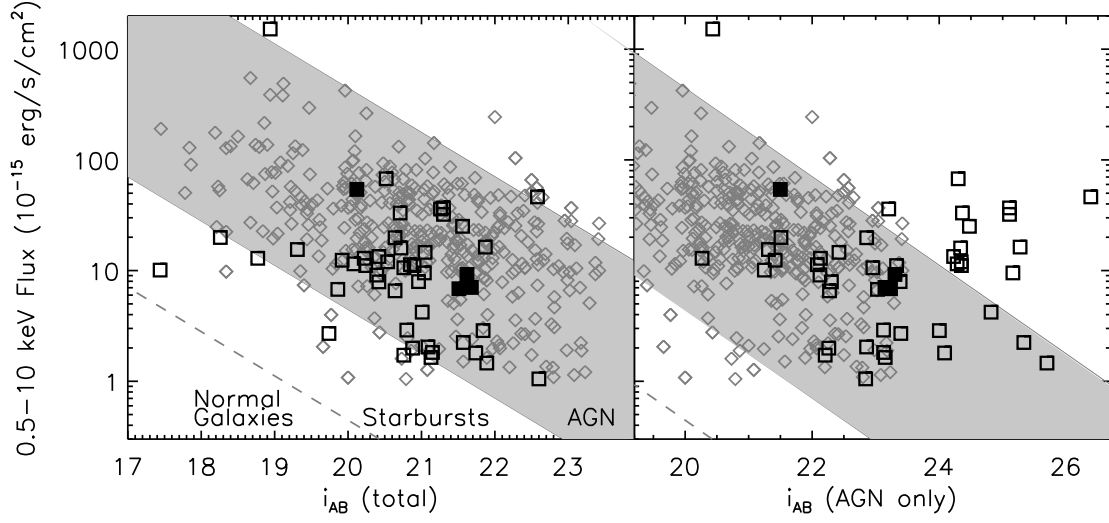


Figure 4.4 The 0.5–2 keV X-ray flux and i_{AB} optical magnitude for the optically dull AGNs, shown by black squares. Filled squares indicate the four optically dull AGNs with significant variability. Also shown by gray diamonds are the Type 1 and Type 2 X-ray AGNs of Chapter 2. In each panel the gray shaded area is the traditional AGN locus (Maccacaro et al., 1988), and the f_X/f_O regions of normal galaxies and starbursts are additionally indicated in the lower left. The left panel uses the full i_{AB} flux from both host and AGN, while the right panel uses only the AGN flux from our photometric fitting. Even with the host contribution removed, 33 of the 48 optically dull AGNs do not lie outside the X-ray AGN f_X/f_O locus.

this effect should be minimal in our sample because very few of the optically dull AGNs are Compton-thick (see §3.4) and all have $z < 1$.

Even after subtracting out the host component, 33/48 optically dull AGNs have f_X/f_O values consistent with typical AGNs. These optically dull AGNs might be normal AGNs diluted by their hosts. However, we note that host dilution should push objects to the left in Figure 4.4, so host dilution may be unlikely for AGNs with $f_X/f_O \sim 1$ and 33/48 may be an upper limit on the true fraction of optically dull AGNs diluted by their hosts. The 15 AGNs with $f_X/f_O > 1$ present the most interesting case, since host dilution is impossible and some physical effect must depress their optical emission while they remain X-ray bright.

4.3.3 Infrared Color: Dust Properties

Bright AGNs are well-known to have redder *Spitzer*/IRAC colors than normal galaxies (Lacy et al., 2004; Stern et al., 2005) as a result of strong mid-IR power-law continua (Sajina et al., 2005; Donley et al., 2007). The IRAC emission is generally associated with the hot, dusty “torus” or outer accretion disk of AGNs. Since optically dull AGNs are optically fainter than normal AGNs, they might also have different mid-IR properties, with the power-law continuum either diluted or absent.

The IRAC colors are shown in Figure 4.5. The optically dull AGNs are marked with red squares, while Type 1 and Type 2 AGNs from Chapter 2 are shown as blue crosses and green diamonds, respectively. Type 1 AGNs generally have the reddest IRAC colors, followed by Type 2 AGNs, while most optically dull AGNs have IRAC colors consistent with normal galaxies. The $[3.6\mu m]_{AB} - [4.5\mu m]_{AB}$ color does a particularly good job of separating the various AGN types. We additionally show the $[3.6\mu m]_{AB} - [4.5\mu m]_{AB}$ color with soft X-ray luminosity in the right panel of Figure 4.5. Donley et al. (2007) suggested that the mid-IR power-law continuum disappears at low X-ray luminosities, but this does not appear to be the case for

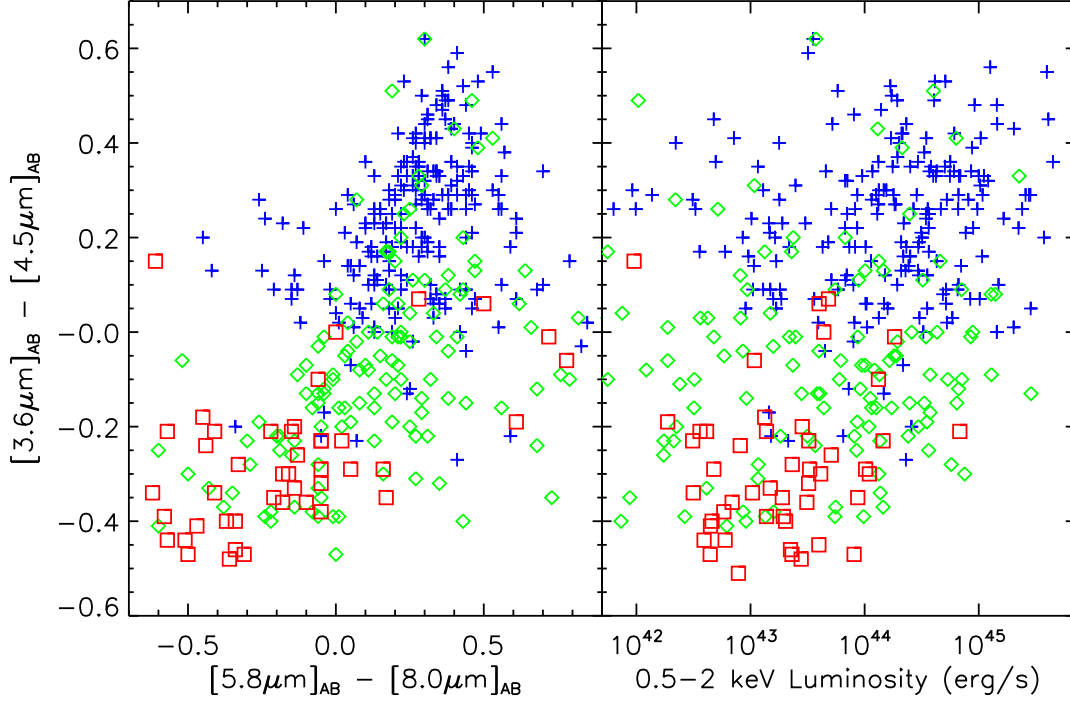


Figure 4.5 At left, *Spitzer*/IRAC colors are shown for the optically dull AGNs (red squares), along with Type 1 (broad-line) AGNs (blue crosses) and Type 2 (narrow-line) AGNs (green diamonds) for comparison (from Chapter 2. Bright Type 1 AGNs are known to have redder IRAC colors due to their strong red continua, indicative of hot dust (Lacy et al., 2004; Stern et al., 2005; Sajina et al., 2005). Most of the optically dull AGNs have IRAC colors consistent with normal galaxies, significantly bluer than Type 1 and Type 2 AGNs. At right, we show the $[3.6\mu\text{m}]_{\text{AB}} - [4.5\mu\text{m}]_{\text{AB}}$ color with the X-ray luminosity. Optically dull AGNs have similar X-ray luminosities to Type 1 and Type 2 AGNs, even as their IRAC colors are markedly different.

our optically dull AGNs. While many Type 1 AGNs are more X-ray luminous than the optically dull AGNs, many have similar luminosities, and there is no apparent correlation between IRAC color and X-ray luminosity in Figure 4.5. The optically dull AGNs have IRAC colors consistent with normal galaxies even though they are as X-ray luminous as some Type 1 AGNs.

4.3.4 X-ray Column Density

Several authors have suggested that the optical emission of optically dull AGNs is obscured, either by material near the central engine (Comastri et al., 2002; Civano et al., 2007) or by gas and dust in the host galaxy (Rigby et al., 2006). But if the optical emission is obscured, then the X-ray emission would probably be obscured as well (so long as the obscuring material for X-ray and optical emission is cospatial). For the 28 optically dull AGNs with >50 full band counts in their XMM or Chandra (Elvis et al., 2009; Lanzuisi et al., in prep.) observations, we estimate N_H from X-ray spectral analysis. We fit each X-ray spectrum as an intrinsically absorbed power-law with Galactic absorption ($N_{H,\text{gal}} = 2.6 \times 10^{20} \text{ cm}^2$ in the direction of the COSMOS field), with the power-law slope and N_H as free parameters. The best-fit N_H value and its 2σ error are found using the Cash (1979) statistic. For the remaining 20 optically dull AGNs, we estimate a less accurate N_H from their hardness ratio, $HR = (H - S)/(H + S)$, following the relation between N_H and HR from Mainieri et al. (2007). Here H is the counts in the hard 2-4.5 keV XMM band and S is the counts in the soft 0.5-2 keV XMM band.

Figure 4.6 shows the column density N_H with the $[3.6\mu\text{m}]_{\text{AB}} - [4.5\mu\text{m}]_{\text{AB}}$ color. Black squares and upper limits show those optically dull AGNs with over 50 counts in their XMM or Chandra observation, while gray diamonds show those objects with N_H estimates from the hardness ratio only. Most (31) optically dull are relatively unobscured in their X-rays, with $N_H < 10^{22} \text{ cm}^{-2}$, and at most only 2-3

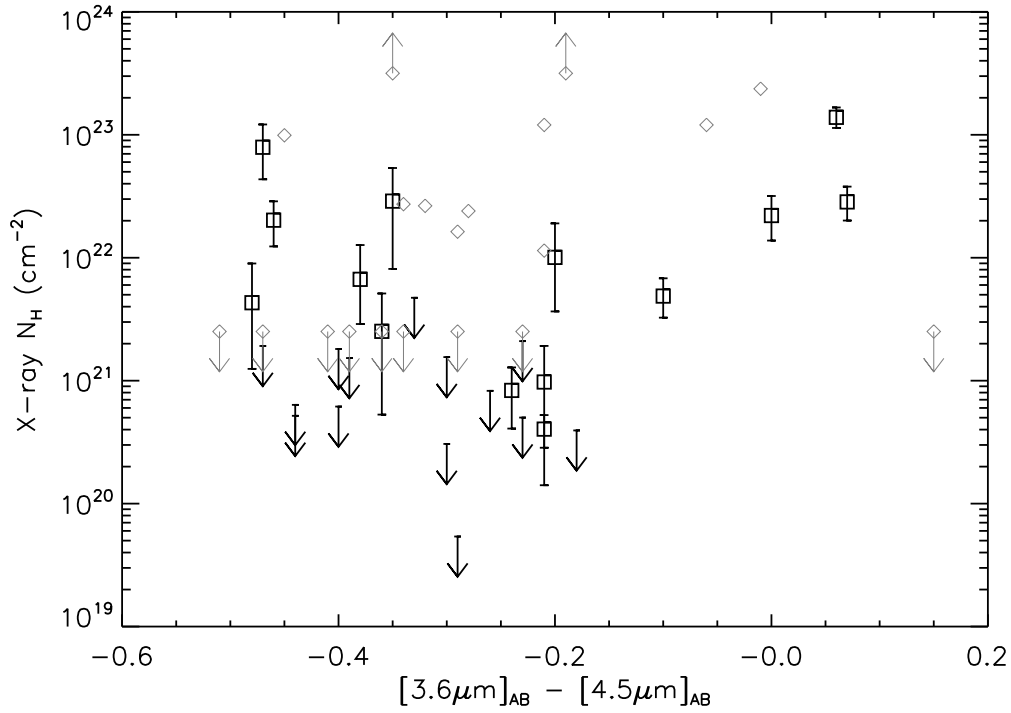


Figure 4.6 The X-ray column density N_H with the $[3.6\mu\text{m}]_{\text{AB}} - [4.5\mu\text{m}]_{\text{AB}}$ *Spitzer*/IRAC color for the optically dull AGNs. For the 28 optically dull AGNs shown as black squares or upper limits, the X-ray or Chandra observation had more than 50 counts and a reliable N_H was calculated directly from the X-ray spectrum. The remaining 20 optically dull AGNs have less reliable column densities inferred from their hardness ratio and are shown in gray. Optically dull are not highly X-ray obscured, and instead have similar N_H to Type 2 AGNs in COSMOS (Mainieri et al., 2007).

are Compton-thick ($N_H > 10^{24} \text{ cm}^{-2}$). The X-ray column densities are similar to those of Type 1 and Type 2 AGNs in COSMOS (Mainieri et al., 2007), so there is no X-ray evidence for additional obscuration in optically dull AGNs.

4.3.5 Host Galaxy Properties

The HST/ACS imaging in COSMOS allows for detailed studies of the host galaxies of the optically dull AGNs. We show postage stamps of the 46 objects with HST/ACS coverage in Figure 4.7. Immediately it is evident that the optically dull AGNs reside in a wide variety of hosts (in contrast with Rigby et al., 2006), despite the fact that they have spectra consistent with old, red elliptical galaxies. A few hosts appear as isolated spheroids or ellipticals, while others have clumpy and dusty disks, and some are disturbed. Type 1 and Type 2 AGNs have similarly been shown to exist in a wide range of host galaxy morphologies (Jahnke et al., 2004; Sánchez et al., 2004; Gabor et al., 2009). Marking the spectroscopic aperture ($1''.0 \times 5''.4$ IMACS slit or $3''.0$ -diameter SDSS fiber) over each of the images, however, reveals a common thread: several of the optically dull AGNs appear to have significant extranuclear light within the aperture. Both of the optically dull AGNs with SDSS spectroscopy in Figure 4.7 have bright elliptical hosts filling the fiber aperture. At least 8 objects with IMACS spectroscopy have a nearby companion falling in the slit, while the hosts of at least 8 others appear to have a bar or disk oriented along the slit. In all of these cases, the AGN optical emission is likely to be diluted by the continuum of one or more normal galaxies. This scenario can explain the optically dull AGNs with normal f_X/f_O ratios, since the extranuclear host galaxy light would increase the total optical brightness.

Rigby et al. (2006) used HST/ACS images in the Chandra Deep Field South (CDF-S) to show that optically dull AGNs have preferentially edge-on hosts compared to other AGNs, further suggesting that optically dull AGNs are optically

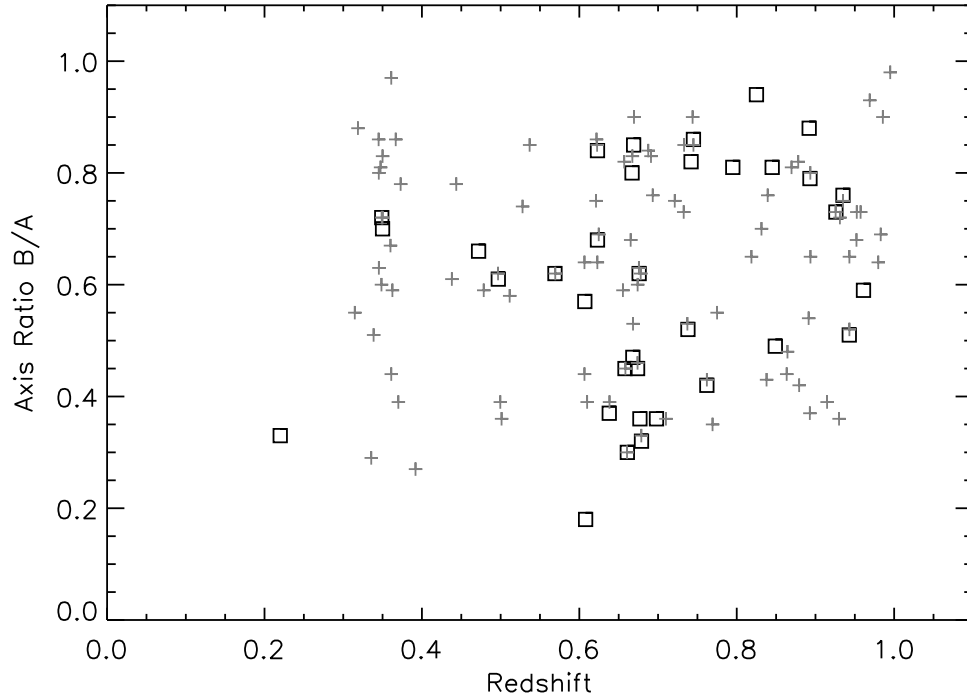


Figure 4.8 The axis ratio b/a with redshift for 37 optically dull AGNs (black squares), with 72 Type 2 AGNs from Gabor et al. (2009) shown by gray crosses. High values of b/a indicate face-on or spheroidal systems, while edge-on disks have low b/a . The axis ratios of optically dull AGNs are quite similar to those of Type 2 AGNs, with no preference for edge-on or face-on systems.

obscured by extranuclear dust in their host galaxies. To test this hypothesis, we present axis ratios with redshift for 37 optically dull AGNs in Figure 4.8, along with a sample of 93 Type 2 AGN from Gabor et al. (2009) in gray. No Type 1 AGN are shown because the point sources are too bright for accurate host galaxy decompositions: in Gabor et al. (2009), 2/3 of Type 1 AGN hosts had unphysical best-fit parameters.

We measure b/a , the ratio of minor to major axis, using the publicly available galaxy fitting software GALFIT (Peng et al., 2002) and following the procedures of Gabor et al. (2009). Sources in the AGN vicinity ($< 35h^{-1}\text{kpc}$ projected on the sky) are identified using Source Extractor (Bertin & Arnouts, 1996) and are either masked out of the image or simultaneously fit by GALFIT (if they are too close to the AGN for masking). We use the Source Extractor outputs based on isophotal profiles to generate initial guesses for the magnitude and shape parameters of the galaxy images in GALFIT. We fit each AGN image two separate times to explore different light distribution models. In one fit, we model the galaxy as a single Sérsic profile, and another uses a Sérsic profile plus a point source representing a nuclear point source (although over half of the optically dull AGNs have no strong nuclear point source; see below). Gabor et al. (2009) explored fits with additional components (e.g. a disk + Sérsic profile), but found that such fits typically give unphysical results because they are unstable for the S/N of the HST/ACS images. By constraining the fits in radius, magnitude, and shape, we prevent GALFIT from exploring wildly unphysical parameter space, but we flag as unacceptable any fits which run into the boundaries or yield strikingly unphysical results (for more details, see Gabor et al., 2009).

The GALFIT analysis yields good fits for 37 of the optically dull AGNs. Most (21) of the optically dull AGNs are best fit with a single Sérsic component and

no nuclear point source. Of the remaining 16 with two-component fits, 13 have only marginal contributions from a point source, and fitting these 13 AGNs with Sérsic-only components does not affect their b/a values. Only 3 optically dull AGNs have significant nuclear point sources which would bias their b/a measurements to high (less elongated) values if not included in the fit. These nuclear point source contributions are consistent with the template fitting in §3.1, which showed that the optically dull AGNs have blue AGN contributions of 35% or less. The GALFIT axis ratios correlate strongly with those measured using Source Extractor, with a mean absolute difference of 0.11 in b/a . This suggests that our axis ratios are robust.

The optically dull AGNs and Type 2 AGNs in COSMOS have nearly identical ranges of axis ratio, with the optically dull AGN mean $b/a = 0.56 \pm 0.20$ and the Type 2 AGN mean $b/a = 0.56 \pm 0.18$. While our optically dull AGNs have consistent axis ratios to those of Rigby et al. (2006), our Type 2 AGNs do not show the face-on preference that Rigby et al. (2006) claim for their “optically active” AGN sample. Part of this difference comes from the differences in sample definitions: the 6 “optically active” AGNs of Rigby et al. (2006) include 4 broad-line Type 1 AGNs, while we compare to only Type 2 AGNs. Rigby et al. (2006) showed that optically dull AGNs are quite different from Type 1 AGNs, while our Figure 4.8 shows that optically dull AGNs have similar hosts to Type 2 AGNs. In Gabor et al. (2009), it was shown that morphological fits to Type 1 AGN hosts suffer from many systematic errors. In particular, a Type 1 host could have an incorrectly high b/a value, since even a slightly incorrect point source removal would leave a symmetric halo and a corresponding round residual. In any case, the fact that Type 2 and optically dull AGNs have similar axis ratios indicates that edge-on hosts are not causing the lack of narrow emission lines in optically dull AGNs.

4.4 Discussion

Combining the optical, X-ray, and infrared data, we have shown that optically dull AGNs exhibit the following properties:

1. Nearly all (43/48) optically dull AGNs have significantly more blue emission than a typical red galaxy.
2. A few (4/48) optically dull AGNs show variability on year timescales, especially in their blue emission.
3. Even when counting only the blue AGN component, $\sim 70\%$ (33/48) of optically dull AGNs have f_X/f_O ratios like typical Type 1 and 2 AGNs.
4. Optically dull AGNs lack the mid-IR power-law signature of Type 1 and Type 2 AGNs, instead exhibiting cool IRAC colors like normal galaxies.
5. The X-ray column densities of optically dull AGNs are similar to those of Type 1 and Type 2 AGN, with no evidence for more absorption.
6. Optically dull AGNs reside in a wide morphological variety of host galaxies, including isolated ellipticals, dusty spirals, and disturbed and potentially merging systems.
7. At least 18/45 optically dull AGNs with HST/ACS imaging are diluted by extranuclear light in the spectroscopic aperture, either by a nearby companion galaxy or host galaxy light.
8. The hosts of optically dull AGNs are not preferentially edge-on compared to Type 2 AGNs, so edge-on host galaxy obscuration cannot explain the lack of narrow emission lines.

While several authors (Comastri et al., 2002; Rigby et al., 2006; Civano et al., 2007) have suggested that optically dull AGNs are optically obscured, we find no evidence for Compton-thick or hot toroidal obscuration. While we can’t rule out weak obscuration (as proposed by Civano et al., 2007), the N_H values for optically dull AGN are fully consistent with those of Type 2 AGNs (Mainieri et al., 2007), and Type 2 AGNs have emission lines while optically dull AGNs do not. Instead, our data support a framework where $\sim 70\%$ (33/48) of optically dull AGNs are normal AGNs diluted by extranuclear galaxy light. The remainder of optically dull AGNs are not diluted or obscured, but have different emission properties for physical reasons: possibly because of a radiatively inefficient accretion flow.

4.4.1 The Case for Dilution

At the redshifts of the optically dull AGNs in the sample, our spectroscopic slit generally includes nearly all of the host galaxy, and occasionally even includes a nearby companion. This is especially evident in Figure 4.7, where at least 10 host galaxies contaminate the spectroscopic aperture and at least 8 others have a companion galaxy in the slit. One can imagine that many “optically normal” local Seyfert AGNs would appear “optically dull” if observed with spectroscopic apertures including extranuclear galaxy emission. Indeed, Moran, Filippenko & Chornock (2002) obtained integrated spectra for 18 local Seyfert 2 galaxies, and found that 11 ($\sim 60\%$) of them would appear optically dull when observed in a $5'' \times 1''$ spectroscopic slit at $z \gtrsim 0.5$. Many of our optically dull AGNs may then be analogs to local Seyfert 2 AGNs. Dilution provides the simplest explanation for the four variable optically dull AGNs, all of which have a clear blue component in their optical photometry and $(f_X/f_O) < 1$ for the AGN fraction of the template fit. Dilution by a host galaxy might explain all 33/48 (70%) of the optically dull AGN with f_X/f_O ratios consistent with Type 1 and Type 2 AGN (that is, $\log(f_X/f_O) < 1$). While only 18 show obvious evidence

for extranuclear galaxy light in the slit, the other $\log(f_X/f_O) < 1$ objects might be weak AGN with the emission lines diluted by a bright host. AGN activity is typically correlated with host luminosity (e.g., Hickox et al., 2009; Silverman et al., 2009), but there is a large scatter in the relation. Under the dilution hypothesis, some optically dull AGNs may represent the weak AGN / bright host tail of the relation.

However, dilution cannot explain all optically dull AGNs. Locally, 10-20% of local AGNs are undiluted and remain optically dull (La Franca et al., 2002; Hornschemeier et al., 2005). And in COSMOS, 15 optically dull AGNs are optically under-luminous compared to their X-ray emission, with $\log(f_X/f_O) > 1$. Dilution by a host galaxy, on the other hand, would cause AGNs to become more optically luminous compared to their X-ray emission. Indeed, optically dull AGNs with $\log(f_X/f_O) \sim 1$ may also not fit the dilution paradigm, since presumably the additional host light would drive the optical flux of “normal” AGNs well below this cutoff. This suggests that 15/48 ($\sim 30\%$) is a lower limit for the optically dull AGNs not explained by dilution.

4.4.2 The Case for Radiatively Inefficient Accretion

The optically dull AGNs in COSMOS do not show signs of strong obscuration, with X-ray column densities similar to Type 2 AGNs and blue IRAC colors. Their host galaxies are not preferentially edge-on compared to the hosts of Type 2 AGNs, suggesting that obscuration by the host is not the cause of their missing narrow emission lines. With no evidence for obscuration, the undiluted optically dull AGNs must be intrinsically weak in their optical emission. AGNs with low accretion rates are expected to be optically underluminous, with very weak or missing emission lines, in just this fashion. In the next section we investigate the properties of the 15/48 (30%) optically dull AGNs which are not explained by obscuration or dilution

to see if they fit the properties expected for low accretion rate AGNs.

4.5 Accretion Properties

Observations have shown that broad lines tend to disappear from AGNs below accretion rates of $L/L_{Edd} \sim 0.01$ (Chapter 3, and also Kollmeier et al., 2006; Trump et al., 2009b). Type 1 AGNs are likely to decay into “naked” Type 2 AGNs (Tran, 2003; Bianchi et al., 2008) which have no evidence for obscuration. The theoretical interpretation (Nenkova et al., 2008; Hopkins et al., 2009; Elitzur & Ho, 2009) is that the broad line region decays as a natural effect of a shrinking accretion disk below $L/L_{Edd} \sim 0.01$, even as the X-ray emission remains bright. The undiluted optically dull AGNs may then be an extension of these ideas, with lower accretion rates driving an altered accretion disk. In the paradigm most suited to explaining optically dull AGNs, the accretion disk is optically thick as normal at higher radii from the black hole, but becomes optically thin below some transition radius (Yuan & Narayan, 2004). Thus the hot optical and UV continuum becomes cooler and redder, and the ionizing continuum becomes much weaker. Without an ionizing continuum, neither the broad nor the narrow line regions are excited, and the spectrum lacks the emission line signature of an AGN. Ho (1999) noted that several local low-luminosity AGNs exhibit this behavior, with a generally redder optical/UV continuum and a lack of the strong UV “big blue bump” found in luminous AGNs. Unfortunately, we cannot measure the accretion rate L/L_{Edd} for these optically dull AGN because we cannot measure the black hole mass: they lack lines for using the scaling relations and they are too distant for dynamical estimates. Future work may leverage the $M_{BH} - M_{bulge}$ relation to estimate L/L_{Edd} , but that is beyond the scope of this work. Instead we will study other properties to see if these optically dull AGN are consistent with predictions of RIAF models.

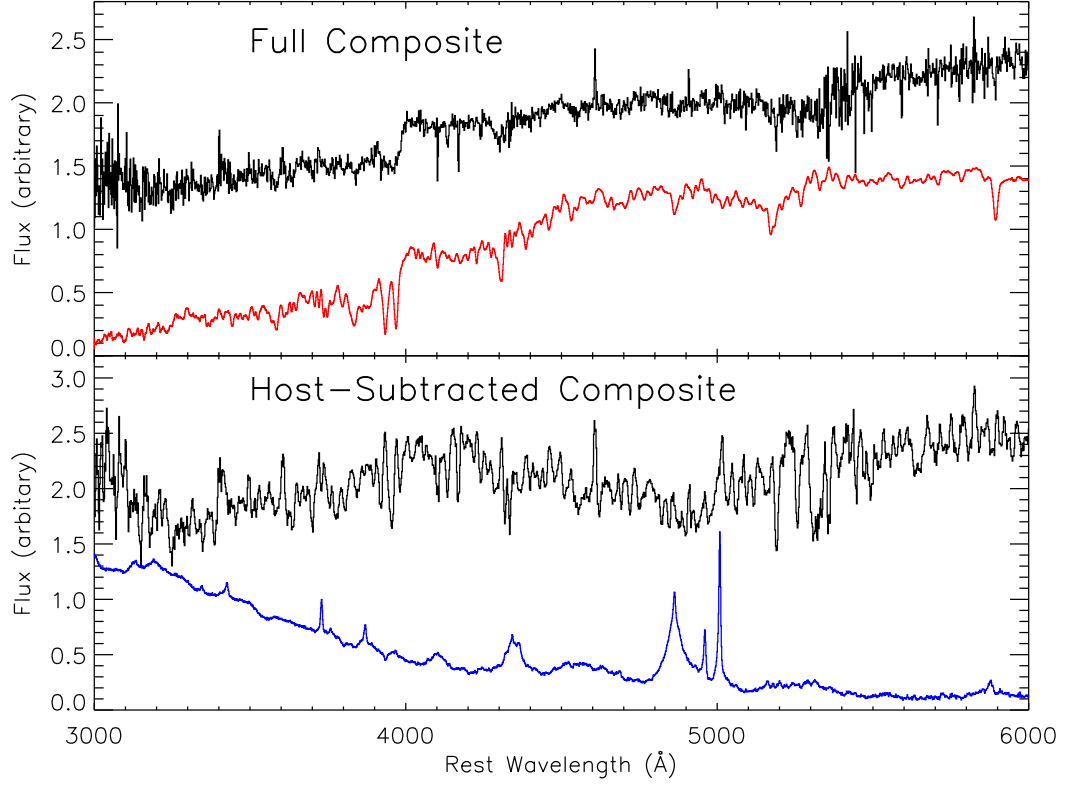


Figure 4.9 The composite spectrum of the 15 optically dull AGNs with $\log(f_X/f_O) > 1$ (those likely to have RIAFs). The top panel shows the full composite, with a red galaxy composite (Eisenstein et al., 2001) shown in red for a comparison. The bottom panel shows the composite of the host-subtracted spectra, with a Type 1 AGN composite (Vanden Berk et al., 2001) shown in blue. The full composite is bluer than a simple red galaxy, and neither composite shows evidence for narrow or broad emission lines. The host-subtracted composite is much redder than a typical Type 1 AGN. This suggests that these optically dull AGNs may have RIAFs, where the optical accretion disk is truncated at lower radii, causing less UV emission and a weaker ionizing continuum.

Figure 4.9 shows the 3000-6000Å optical/UV composite spectrum from the 15 optically dull AGNs likely to have RIAFs. The top panel shows the full composite, while the bottom panel uses only the host-subtracted spectra to compute an AGN-only composite. Each composite spectrum was computed by taking a S/N-weighted mean of the spectra. (The absorption features of the full composite spectrum are artificially broadened by minor redshift errors in some of the optically dull AGN.) Note that the AGN-only composite is not simply the full composite minus a mean host component, but was computed from the individual host-subtracted spectra, using the best-fit “r+q” template from §3.1. For comparison, Figure 4.9 also shows SDSS composites of a red galaxy (Eisenstein et al., 2001) and a Type 1 AGN (Vanden Berk et al., 2001). Neither composite has broad or narrow emission lines, despite having higher S/N than the individual optically dull AGN spectra. While the full composite is bluer than a typical red galaxy, the AGN-only composite is much redder than a typical Type 1 AGN. The optical/UV instead supports a RIAF model with a truncated accretion disk and less hot UV emission.

Another important prediction for low accretion rate AGNs is that the dominant outflow mode switches from disk winds to radio jets (Ho, 2002; Elitzur & Shlosman, 2006). The radio synchrotron emission provides the dominant source of cooling and angular momentum transport for RIAF accretion states as the optically thin inner accretion disk no longer drives strong disk winds. Since the RIAF truncated accretion disk is naturally under-luminous in the optical, low accretion rate AGN should be both radio-bright and optically dim: in other words, their radio-loudness f_R/f_O will be large. The radio properties for the optically dull AGN are shown in Figure 4.10, along a comparison sample of Type 1 AGNs from Chapter 2. Radio data are available from Very Large Array (VLA) observations in COSMOS (Schinnerer et al., 2007), and all optically dull AGN are detected at 1.4 GHz at the $> 5\sigma$ level.

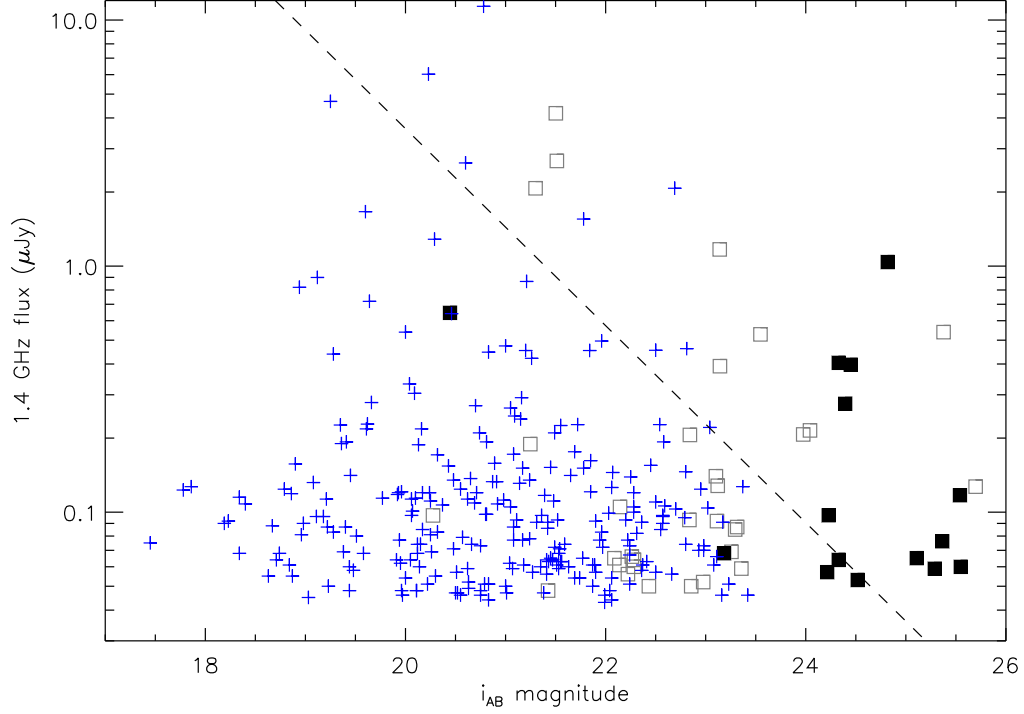


Figure 4.10 The 1.4 GHz radio fluxes and i_{AB} magnitudes for the optically dull AGNs (black squares), along with Type 1 AGNs (blue crosses) from Chapter 2. The optically dull AGN with $\log(f_X/f_O) > 1$ (those likely to have RIAFs) are shown by the filled squares. Optical magnitudes for the optically dull AGNs include only the AGN component, as estimated from the best-fit “r+q” template in §3.1. While the Type 1 AGNs may include some host galaxy light, it is likely minor relative to the AGN contribution. The dashed line represents $f_{1.4\text{ GHz}}/f_i = 10$. Optically dull AGNs, especially those with $\log(f_X/f_O) > 1$, are more likely to be more radio-loud than Type 1 AGNs.

The optically dull AGNs in Figure 4.10 include only the AGN component in the optical emission. The Type 1 AGNs in the figure may also include optical light from the host galaxy, but any host light is likely to be minor compared to the Type 1 AGN optical emission. Nearly all of the optically dull AGN with $\log(f_X/f_O) > 1$ are radio-loud, with $f_{1.4\text{ GHz}}/f_i > 10$, and they are more likely to be radio-loud than Type 1 AGNs. Their radio-loudness suggests that these optically dull AGNs are RIAFs with a strong radio jet.

While a full fit of the optically dull AGN SEDs to low accretion rate models is beyond the scope of this work, we have shown that the RIAF-candidate optically dull AGN have optical/UV and radio properties that differ from those of bright Type 1 and 2 AGNs. We note again that $\log(f_X/f_O) > 1$ is a conservatively low limit for no host galaxy dilution, and so the fraction of optically dull AGNs that are RIAFs is likely to be greater than $\sim 30\%$. Indeed, Figure 4.10 shows that several optically dull AGNs with $\log(f_X/f_O) \leq 1$ are also radio-loud, lending one piece of evidence that even more than 30% of optically dull AGNs are in a weakly accreting RIAF state.

4.6 Chapter Summary

We have presented 48 optically dull AGNs from COSMOS, all of which lack optical emission lines while exhibiting the X-ray brightness typical of an AGNs. Their IR and X-ray emission show no evidence for obscuration in excess of that in Type 1 and 2 AGNs, and their host galaxies are not preferentially edge-on when compared to Type 2 AGNs. We instead propose a framework where up to 70% of optically dull AGNs are diluted by their host galaxies or by nearby companions. The remaining 30% cannot be explained by dilution, and instead have optical/UV and radio properties which are best described by a RIAF state.

CHAPTER 5

ACCRETION RATE AND THE PHYSICAL NATURE OF ACTIVE GALAXIES

We show how accretion rate governs the physical properties of broad-line, narrow-line, and lineless active galactic nuclei (AGNs). We avoid the systematic errors plaguing previous studies of AGN accretion rate by using accurate bolometric luminosities from well-sampled multiwavelength SEDs from the Cosmic Evolution Survey (COSMOS), and accurate black hole masses derived from virial scaling relations (for broad-line AGNs) or host-AGN relations (for narrow-line and lineless AGNs). In general, broad emission lines are present only at the highest accretion rates ($L_{int}/L_{Edd} > 10^{-2}$), and these rapidly accreting AGNs are observed as broad-line AGNs or obscured narrow-line AGNs. Narrow-line and lineless AGNs at lower specific accretion rates ($L_{int}/L_{Edd} < 10^{-2}$) are unobscured and yet lack a broad line region. The disappearance of the broad emission lines is caused by an expanding radiatively inefficient accretion flow (RIAF) at inner radii of the accretion disk. The presence of the RIAF also drives $L_{int}/L_{Edd} < 10^{-2}$ narrow-line and lineless AGNs to be 10-100 times more radio-loud than $L_{int}/L_{Edd} > 10^{-2}$ broad-line AGNs, since the unbound nature of the RIAF means it is easier to form a radio outflow. The IR torus signature also tends to become weaker or disappear from $L_{int}/L_{Edd} < 10^{-2}$ AGNs, although there may be additional mid-IR synchrotron emission associated with the RIAF. Together these results suggest a simple model for AGN unification driven by specific accretion rate.

5.1 Chapter Introduction

Supermassive black holes (SMBHs) are now known to be ubiquitous in the centers of all massive galaxies (Magorrian et al., 1998). SMBHs grow during an “active”

phase of accretion, during which they are observed as active galactic nuclei (AGN). AGN growth is intimately tied to galaxy evolution, as evident in the well-studied correlations between SMBH mass (M_{BH}) and properties of the host galaxy bulge (e.g., Gebhardt et al., 2000; Ferrarese & Merritt, 2000; Marconi & Hunt, 2003). The AGN phase is also hypothesized to regulate star formation in its host galaxy, with the galaxy feeding the black hole in turn (e.g. Di Matteo, Springel, & Hernquist, 2005; Younger et al., 2008). All massive galaxies are thought to experience episodic AGN behavior in their lifetime (Soltan, 1982; Marconi et al., 2004).

AGNs are generally classified by differences in their optical spectra. Type 1 or broad-line AGN have broad ($v_{FWHM} \gtrsim 1000 \text{ km s}^{-1}$) emission lines in their UV/optical continuum and blue unobscured continua (e.g., Vanden Berk et al., 2001), and are the most luminous persistent sources in the sky. Type 2 or narrow-line AGN lack broad emission lines and have weaker continua (frequently dominated by their host galaxies), but have strong narrow emission lines, especially from forbidden transitions. Narrow emission lines associated with nuclear activity can be distinguished from lines caused by star formation by studying the line ratios (Baldwin, Phillips, & Terlevich, 1981). The line ratio diagnostics work because the “harder” emission of an AGN is more efficient at ionizing the surrounding gas and dust than star formation, and thus have stronger lines from high-energy forbidden transitions (e.g., [O III] $\lambda 5007\text{\AA}$ and [N II] $\lambda 6583\text{\AA}$) relative to the lower-energy hydrogen transitions (e.g., H β $\lambda 4861\text{\AA}$ and H α $\lambda 6563\text{\AA}$). The subclass of “low-ionization nuclear emission region” AGNs (LINERs, Heckman, 1980) have narrow emission lines that are probably excited by some combination of ionization from both star formation and an AGN (Eracleous et al., 2010). Deep X-ray surveys have additionally revealed “optically dull” AGN (Comastri et al., 2002), which have bright X-ray emission but none of the broad or narrow emission line signatures of AGN accretion. While many

optically dull AGNs can be explained as Type 2 AGNs diluted by prominent host galaxies (Moran, Filippenko & Chornock, 2002; Caccianiga et al., 2007), at least $\sim 1/3$ are undiluted but intrinsically optically weaker than other AGNs (Chapter 4, see also Trump et al., 2009c). The inferred X-ray column density N_H can also be used to classify AGNs, with Type 2 (narrow-line) AGNs typically more X-ray obscured than Type 1 (broad-line) AGNs. However X-ray and optical classifications differ for $\sim 20\%$ of objects (Trouille et al., 2009).

Historically, Type 2 and optically dull AGNs have been described as obscured versions of Type 1 AGN, with the broad emission line region (BLR) hidden behind a partially opaque “torus” of gas and dust, while the narrow emission lines lie outside the torus (e.g., Krolik & Begelman, 1988). The best evidence for this scenario is the observation that some Type 2 AGNs have a “hidden” BLR, revealed by deep spectropolarimetry (Antonucci, 1993). However, recent observations have revealed several serious limitations of a simple unified model based on geometric obscuration. Even in very deep spectropolarimetric observations, many Type 2 AGNs show no hidden BLR (Barth, Filippenko & Moran, 1999; Tran, 2001; Wang & Zhang, 2007), and observations suggest a lower $L/L_{Edd} \geq 0.01$ limit in accretion rate for broad-line AGNs (Chapter 3, and also Kollmeier et al., 2006; Trump et al., 2009b). The X-ray spectra are unabsorbed ($N_H \lesssim 10^{21} \text{ cm}^{-2}$) for 30-40% of Type 2 AGNs (Mainieri et al., 2007; Trouille et al., 2009), as well as most local LINERs (Ho, 2008, and references therein) and distant optically dull AGNs (Chapter 4). Several well-studied LINERs additionally lack the narrow Fe $K\alpha$ emission signature of a dusty torus (Ptak et al., 2004; Bianchi et al., 2008). Many Type 2 AGNs and most optically dull AGNs have mid-IR colors like normal galaxies (Chapter 4, see also Ho, 2008), in contrast to hot mid-IR colors of Type 1 AGNs described by torus models (Nenkova et al., 2008; Mor, Netzer, & Elitzur, 2009). Toroidal obscuration is additionally ruled

out for some strongly varying Type 2 (Hawkins, 2004) and optically dull AGNs (Chapter 4), since these objects have continua which vary on year timescales, well within the inferred light travel time dimension of any torus.

Several authors have proposed models which use different accretion rates, not geometric obscuration, as the cause of the differences between observed AGNs. Elitzur & Ho (2009) suggest that the BLR and “torus” are inner (ionized) and outer (clumpy and dusty) parts of the same disk-driven wind, and that this wind is no longer supported at low accretion rate (see also Elitzur & Shlosman, 2006; Nenkova et al., 2008). Similarly, Nicastro (2000) suggested that low accretion rates actually drive the disk wind within the last stable orbit of the SMBH, and as a result the BLR never forms. Models for radiatively inefficient accretion (e.g., Yuan, 2007) suggest that at $L/L_{Edd} \lesssim 10^{-2}$, the accretion disk becomes truncated near the SMBH, with a geometrically thick and optically thin disk at low radii, and a normal thin disk (e.g., Shakura & Sunyaev, 1973) at higher radii. Such objects are predicted to lack strong emission lines (both broad and narrow) and have weak UV/optical emission, as observed in many optically weak low-luminosity AGNs (Ho, 2009) and X-ray bright, optically dull AGNs (Chapter 4). Hopkins et al. (2009) additionally show that X-ray hardness, generally attributed to X-ray absorption, may also result from the naturally X-ray hard spectrum expected from radiatively inefficient accretion.

In this work we directly measure specific accretion rates for a large, X-ray selected sample of broad-line, narrow-line, and lineless AGNs. Specific accretion rate is a unitless measure of accretion, defined as $\dot{m} \equiv \dot{M}/\dot{M}_{Edd} = L_{int}/L_{Edd}$. The sample is drawn from the Cosmic Evolution Survey (COSMOS, Scoville et al., 2007) X-ray AGN sample (Chapter 2), as described in Section 5.2. Measurements of specific accretion rates are described in Section 5.3, with specific accretion rates computed directly from fits to the multiwavelength continuum (avoiding uncertain bolomet-

ric corrections) and black hole masses from the broad line scaling relations or the $M_{BH} - M_*$ relations (for narrow-line and lineless AGNs). In Section 5.4 we show that broad emission lines are present at only high accretion rates ($L_{int}/L_{Edd} > 0.01$), while narrow-line and lineless AGNs at lower accretion rates have cooler disks, stronger radio jets, and no torus IR signature. We present a “cartoon” model which summarizes our results in Section 5.5, with predictions for future observations in Section 5.6. We adopt a cosmology with $h = 0.70$, $\Omega_M = 0.3$, $\Omega_\Lambda = 0.7$ throughout.

5.2 Observational Data

Measuring an accurate specific accretion rate requires accurate accretion luminosities and black hole mass estimates. In particular, SED measurements from optical/UV to X-ray are necessary to constrain intrinsic luminosities to within a factor of a few (as we show in §3.2). We select a sample of 348 AGNs from the Cosmic Evolution Survey (COSMOS, Scoville et al., 2007) field. These AGNs have multiwavelength data in the form of Spitzer/IRAC, HST/ACS, Subaru/Suprime-Cam, GALEX, XMM-Newton, and Chandra observations, as described in Table 5.1. Spectroscopic identification and redshifts for these objects comes from archival SDSS data, Magellan/IMACS and MMT/Hectospec (Trump et al., 2009a), and VLT/VIMOS observations (Lilly et al., 2007).

Most (80%) of the AGNs are limited in optical and X-ray flux by $i_{AB} < 22.5$ and $f_{0.5-2\text{keV}} > 2 \times 10^{-16} \text{ erg s}^{-1} \text{ cm}^{-2}$, although there are some subtle dependences on redshift and luminosity fully described by (Trump et al., 2009a) and (Lilly et al., 2007). However we do not seek a complete sample, but rather a representative sample covering a variety of specific accretion rates and AGN spectral types. Beyond the flux selection, the sample is constrained on the basis of our ability to measure accurate black hole masses. For Type 1 AGNs, this means we required the presence

of one of the C IV, Mg II, or H β broad emission lines in the observed spectral range, effectively limiting broad-line AGNs with IMACS or VIMOS spectra to $0.16 < z < 0.88$, $1 < z < 2.4$, and $2.7 < z < 4.9$ and objects with Hectospec or SDSS spectra to $z < 4.9$. For narrow-line and lineless AGNs, we estimate black hole mass from the $M_{BH} \sim L_{bulge}$ relation, and so we require an accurate estimate of L_{bulge} . This restricts our narrow-line and lineless AGNs to the sample of objects in COSMOS with morphological decompositions from HST/ACS images (Gabor et al., 2009). The accurate host measurements from Gabor et al. (2009) additionally allow us to subtract the host component before computing the intrinsic bolometric luminosity. The total sample of 348 AGNs includes 256 broad-line, 65 narrow-line, and 27 lineless AGNs.

Multiwavelength data exists for $> 95\%$ of the AGNs in the sample in every wavelength region except the UV. X-ray data exist from both Chandra and XMM-Newton: we use the deeper Chandra data when available, but the Chandra observations cover only the central 0.8 deg^2 of the COSMOS field. For the IR-UV data, we apply the zero-point offsets derived by Ilbert et al. (2009). All targets, excepting seven broad-line AGNs, are X-ray detected with $L_{0.5-10\text{keV}} > 3 \times 10^{42} \text{ erg s}^{-1}$. This X-ray luminosity requirement confirms that the narrow-line and lineless spectra are bona-fide AGNs. Of the seven broad-line AGNs without X-ray detection, six were selected by their Spitzer/IRAC colors and one was a serendipitous object in the bright zCOSMOS survey (which selected targets based only on $i_{AB} < 22.5$).

Table 5.1. COSMOS Multiwavelength Data

Band	Telescope	Wavelength Å	Energy eV	Limit AB mag ^b	NL/LL AGNs Detected	BL AGNs Detected	Reference ^a
X_{hard}	Chandra	1.24-6.20	2000-10000	7.3×10^{-16}	79/92	228/256	(1)
X_{hard}	XMM	1.24-6.20	2000-10000	9.3×10^{-15}	79/92	228/256	(2)
X_{soft}	Chandra	6.20-24.8	500-2000	1.9×10^{-16}	88/92	249/256	(1)
X_{soft}	XMM	6.20-24.8	500-2000	1.7×10^{-15}	88/92	249/256	(2)
FUV	GALEX	1426-1667	7.44-8.63	25.7	27/92	131/256	(3)
NUV	GALEX	1912-2701	4.59-6.84	26.0	55/92	184/256	(3)
u [*]	CFHT	3642-4180	2.97-3.40	26.4	92/92	254/256	(4)
B _J	Subaru	4036-4843	2.56-3.07	27.7	92/92	256/256	(4)
g ⁺	Subaru	4347-5310	2.33-2.85	27.1	92/92	256/256	(4)
V _J	Subaru	4982-5916	2.10-2.49	27.0	92/92	255/256	(4)
r ⁺	Subaru	5557-6906	1.80-2.23	27.1	92/92	256/256	(4)
i [*]	CFHT	6140-9119	1.36-2.02	26.7	92/92	256/256	(4)
F814W	HST/ACS	7010-8880	1.40-1.77	27.2	92/92	256/256	(5)
z ⁺	Subaru	8544-9499	1.31-1.45	25.7	92/92	254/256	(4)
J	UKIRT	11665-13223	0.94-1.06	23.8	92/92	256/256	(4)

Table 5.1—Continued

Band	Telescope	Wavelength Å	Energy eV	Limit AB mag ^b	NL/LL AGNs Detected	BL AGNs Detected	Reference ^a
Ks	CFHT	19900-23050	0.538-0.623	23.4	92/92	253/256	(6)
IRAC1	Spitzer	31557-38969	0.318-0.383	23.9	91/92	255/256	(4)
IRAC2	Spitzer	39550-49663	0.250-0.313	23.3	91/92	255/256	(4)
IRAC3	Spitzer	50015-63514	0.195-0.248	21.3	91/92	255/256	(4)
IRAC4	Spitzer	62832-91229	0.136-0.197	21.0	91/92	255/256	(4)
1.4 GHz	VLA	2×10^9	6×10^{-9}	$20 \mu\text{Jy}^c$	92/92	256/256	(7)

^aReferences are as follows: (1) Elvis et al. (2009), (2) Cappelluti et al. (2009), (3) Zamojski et al. (2007), (4) Capak et al. (2010), (5) Koekemoer et al. (2007), (6) McCracken et al. (2010), (7) Schinnerer et al. (2007)

^bX-ray flux limits are given in $\text{erg s}^{-1} \text{cm}^{-2}$, and the radio flux limit is given in μJy .

Table 5.2. Catalog of AGN accretion rates

RA+Dec (J2000) hhmmss.ss+ddmmss.s	Type ^a	Redshift	Spec. ^b source	L_{int} $\log(L_{\odot})$	M_{BH} $\log(M_{\odot})$	L_{int}/L_{Edd}
095728.34+022542.2	BL	1.54	S	$46.15^{+0.05}_{-0.16}$	$8.40^{+0.36}_{-0.36}$	$-0.37^{+0.03}_{-0.79}$
095740.78+020207.9	BL	1.48	I	$46.00^{+0.17}_{-0.18}$	$8.24^{+0.35}_{-0.35}$	$-0.36^{+0.65}_{-1.43}$
095743.33+024823.8	BL	1.36	S	$45.87^{+0.06}_{-0.29}$	$8.24^{+0.38}_{-0.38}$	$-0.49^{+0.08}_{-0.83}$
095749.02+015310.1	NL	0.32	I	$44.01^{+0.61}_{-0.07}$	$8.61^{+0.31}_{-0.44}$	$-2.72^{+0.77}_{-0.19}$
095750.20+022548.3	BL	1.24	Z	$44.94^{+0.00}_{-0.27}$	$7.28^{+0.49}_{-0.49}$	$-0.45^{+0.32}_{-0.62}$
095752.17+015120.1	BL	4.16	Z	$46.31^{+0.10}_{-0.12}$	$8.71^{+0.33}_{-0.33}$	$-0.51^{+0.23}_{-0.46}$
095752.17+015120.1	BL	4.17	I	$46.29^{+0.11}_{-0.11}$	$8.66^{+0.40}_{-0.40}$	$-0.48^{+0.31}_{-0.45}$
095753.49+024736.1	BL	3.61	I	$46.34^{+0.30}_{-0.32}$	$8.00^{+0.42}_{-0.42}$	$0.22^{+0.17}_{-1.00}$
095754.11+025508.4	BL	1.57	S	$46.09^{+0.37}_{-0.14}$	$8.70^{+0.40}_{-0.40}$	$-0.73^{+0.25}_{-0.63}$
095754.70+023832.9	BL	1.60	S	$46.16^{+0.27}_{-0.27}$	$8.72^{+0.41}_{-0.41}$	$-0.68^{+0.28}_{-0.59}$
095755.08+024806.6	BL	1.11	S	$45.93^{+0.10}_{-0.19}$	$8.43^{+0.33}_{-0.33}$	$-0.61^{+0.14}_{-0.62}$
095755.34+022510.9	BL	2.74	I	$45.51^{+0.00}_{-0.08}$	$8.07^{+0.42}_{-0.42}$	$-0.67^{+0.34}_{-0.46}$
095755.48+022401.1	BL	3.10	I	$46.61^{+0.13}_{-0.22}$	$8.44^{+0.39}_{-0.39}$	$0.06^{+0.14}_{-0.65}$
095759.50+020436.1	BL	2.03	S	$46.79^{+0.16}_{-0.13}$	$8.94^{+0.37}_{-0.37}$	$-0.26^{+0.00}_{-0.74}$
095759.91+021634.5	BL	1.54	I	$44.69^{+0.00}_{-0.07}$	$8.26^{+0.39}_{-0.39}$	$-1.69^{+0.33}_{-0.49}$
095801.61+020428.9	BL	1.23	Z	$45.29^{+0.14}_{-0.09}$	$8.28^{+0.37}_{-0.37}$	$-1.10^{+0.22}_{-1.10}$
095802.10+021541.0	OD	0.94	I	$45.14^{+0.11}_{-0.08}$	$9.44^{+0.29}_{-0.41}$	$-2.41^{+0.45}_{-0.30}$
095805.10+020445.8	NL	0.67	I	$45.50^{+0.23}_{-0.19}$	$9.33^{+0.34}_{-0.31}$	$-1.94^{+0.39}_{-0.40}$
095806.24+020113.8	NL	0.62	I	$44.44^{+0.43}_{-0.41}$	$9.03^{+0.37}_{-0.36}$	$-2.71^{+0.48}_{-0.37}$
095806.99+022248.5	BL	3.10	I	$46.37^{+0.18}_{-0.19}$	$9.34^{+0.39}_{-0.39}$	$-1.08^{+0.17}_{-0.62}$
095809.45+020532.4	OD	0.61	I	$44.20^{+0.06}_{-0.26}$	$9.26^{+0.34}_{-0.43}$	$-3.18^{+0.42}_{-0.35}$
095810.88+014005.1	BL	2.10	Z	$46.63^{+0.13}_{-0.17}$	$8.37^{+0.41}_{-0.41}$	$0.14^{+0.23}_{-1.02}$
095815.50+014923.2	BL	1.51	S	$46.82^{+0.05}_{-0.20}$	$8.60^{+0.38}_{-0.38}$	$0.11^{+0.85}_{-1.70}$
095815.51+014923.1	BL	1.51	Z	$46.82^{+0.04}_{-0.15}$	$8.66^{+0.47}_{-0.47}$	$0.05^{+0.76}_{-1.62}$

Table 5.2—Continued

RA+Dec (J2000)	Type ^a	Redshift	Spec. ^b	L_{int}	M_{BH}	L_{int}/L_{Edd}
hhmmss.ss+ddmmss.s			source	$\log(L_{\odot})$	$\log(M_{\odot})$	
095815.53+015840.5	BL	1.68	I	$46.15^{+0.34}_{-1.00}$	$7.93^{+0.36}_{-0.36}$	$0.11^{+0.50}_{-1.81}$
095817.26+023316.2	BL	1.57	I	$45.08^{+0.09}_{-0.11}$	$8.29^{+0.39}_{-0.39}$	$-1.33^{+0.18}_{-0.58}$
095817.54+021938.5	BL	0.73	Z	$44.93^{+0.42}_{-1.80}$	$7.72^{+0.37}_{-0.37}$	$-0.90^{+0.08}_{-2.24}$
095818.15+023432.4	BL	1.17	Z	$45.87^{+0.13}_{-0.22}$	$8.45^{+0.51}_{-0.51}$	$-0.69^{+0.40}_{-1.28}$
095819.88+022903.6	BL	0.34	S	$45.38^{+0.07}_{-0.08}$	$8.29^{+0.56}_{-0.56}$	$-1.02^{+0.00}_{-0.94}$
095820.44+015931.0	NL	0.98	I	$44.80^{+0.43}_{-0.27}$	$8.87^{+0.31}_{-0.49}$	$-2.19^{+0.64}_{-0.31}$
095820.45+020304.0	BL	1.35	Z	$46.06^{+0.38}_{-0.43}$	$8.65^{+0.38}_{-0.38}$	$-0.71^{+0.01}_{-0.86}$
095820.74+014609.5	NL	0.78	I	$47.32^{+0.19}_{-0.41}$	$9.28^{+0.34}_{-0.41}$	$-0.07^{+0.42}_{-0.38}$
095821.65+024628.2	BL	1.40	S	$46.33^{+0.05}_{-0.12}$	$9.06^{+0.48}_{-0.48}$	$-0.84^{+0.02}_{-0.90}$
095821.84+020834.0	BL	1.87	I	$45.14^{+0.00}_{-0.41}$	$7.78^{+0.31}_{-0.31}$	$-0.75^{+0.00}_{-0.88}$
095822.19+014524.3	BL	1.96	S	$46.91^{+0.06}_{-0.07}$	$9.03^{+0.37}_{-0.37}$	$-0.23^{+0.28}_{-0.46}$
095824.50+022333.6	BL	1.85	I	$46.31^{+0.16}_{-0.19}$	$8.28^{+0.39}_{-0.39}$	$-0.08^{+0.04}_{-0.89}$
095824.50+022333.6	BL	1.86	Z	$46.31^{+0.16}_{-0.20}$	$8.18^{+0.45}_{-0.45}$	$0.02^{+0.03}_{-0.81}$
095826.68+022818.0	NL	0.69	I	$44.57^{+0.35}_{-0.21}$	$9.15^{+0.35}_{-0.32}$	$-2.69^{+0.42}_{-0.37}$
095829.26+024417.9	BL	1.89	Z	$46.48^{+0.13}_{-0.19}$	$8.29^{+0.41}_{-0.41}$	$0.07^{+0.05}_{-0.98}$
095829.83+021050.4	BL	1.19	I	$45.74^{+0.11}_{-0.15}$	$8.34^{+0.42}_{-0.42}$	$-0.71^{+0.04}_{-0.84}$
095829.83+021050.4	BL	1.19	Z	$45.74^{+0.08}_{-0.12}$	$8.04^{+0.35}_{-0.35}$	$-0.41^{+0.09}_{-0.85}$
095831.65+024901.6	BL	0.34	Z	$44.75^{+0.10}_{-0.09}$	$8.08^{+0.39}_{-0.39}$	$-1.44^{+0.29}_{-1.02}$
095833.17+020858.5	NL	0.95	I	$45.36^{+0.33}_{-0.28}$	$9.14^{+0.32}_{-0.45}$	$-1.89^{+0.51}_{-0.38}$
095834.04+024427.2	BL	1.89	S	$46.61^{+0.06}_{-0.10}$	$8.75^{+0.40}_{-0.40}$	$-0.25^{+0.09}_{-0.67}$
095834.40+022054.8	BL	2.66	Z	$45.89^{+0.06}_{-0.09}$	$8.00^{+0.51}_{-0.51}$	$-0.23^{+0.20}_{-0.70}$
095834.75+014502.4	BL	1.90	S	$46.47^{+0.17}_{-0.25}$	$9.00^{+0.38}_{-0.38}$	$-0.65^{+0.16}_{-0.69}$
095835.28+013609.2	BL	2.84	I	$45.97^{+0.16}_{-0.26}$	$7.20^{+0.50}_{-0.50}$	$0.66^{+0.04}_{-0.82}$
095835.98+015157.1	BL	2.94	S	$46.84^{+0.63}_{-0.43}$	$8.11^{+0.44}_{-0.44}$	$0.62^{+0.21}_{-0.63}$

Table 5.2—Continued

RA+Dec (J2000)	Type ^a	Redshift	Spec. ^b	L_{int}	M_{BH}	L_{int}/L_{Edd}
hhmmss.ss+ddmmss.s			source	$\log(L_{\odot})$	$\log(M_{\odot})$	
095836.69+022049.0	BL	1.19	I	$45.32^{+0.36}_{-0.50}$	$7.29^{+0.53}_{-0.53}$	$-0.08^{+0.47}_{-1.53}$
095837.37+023602.9	NL	0.73	I	$46.18^{+0.05}_{-0.35}$	$9.46^{+0.40}_{-0.31}$	$-1.39^{+0.31}_{-0.42}$
095838.84+022348.8	NL	0.35	I	$45.73^{+0.29}_{-0.08}$	$9.25^{+0.36}_{-0.32}$	$-1.63^{+0.32}_{-0.37}$
095839.27+020506.7	BL	1.22	Z	$45.67^{+0.09}_{-0.14}$	$8.02^{+0.39}_{-0.39}$	$-0.47^{+0.19}_{-0.67}$
095839.27+020506.7	BL	1.22	I	$45.67^{+0.11}_{-0.14}$	$8.24^{+0.54}_{-0.54}$	$-0.69^{+0.35}_{-0.58}$
095840.02+021711.1	BL	1.03	Z	$45.36^{+0.13}_{-0.75}$	$7.84^{+0.41}_{-0.41}$	$-0.60^{+0.07}_{-1.17}$
095840.32+020807.2	NL	0.34	I	$44.41^{+0.14}_{-0.27}$	$9.04^{+0.36}_{-0.39}$	$-2.73^{+0.38}_{-0.44}$
095840.61+020426.6	BL	0.34	I	$44.85^{+0.11}_{-0.08}$	$8.39^{+0.45}_{-0.45}$	$-1.65^{+0.18}_{-1.02}$
095844.94+014309.0	BL	1.34	S	$46.24^{+0.16}_{-0.19}$	$9.19^{+0.37}_{-0.37}$	$-1.07^{+0.28}_{-1.09}$
095845.80+024634.0	BL	0.35	Z	$44.54^{+0.17}_{-0.15}$	$7.39^{+0.39}_{-0.39}$	$-0.97^{+0.27}_{-1.12}$
095846.02+014905.6	OD	0.74	I	$45.40^{+0.69}_{-0.57}$	$9.52^{+0.30}_{-0.37}$	$-2.23^{+0.75}_{-0.48}$
095846.75+023910.8	NL	0.32	I	$44.02^{+0.23}_{-0.29}$	$8.55^{+0.35}_{-0.34}$	$-2.65^{+0.38}_{-0.42}$
095847.71+022628.4	BL	1.52	I	$45.80^{+0.10}_{-0.07}$	$8.71^{+0.44}_{-0.44}$	$-1.01^{+0.11}_{-0.89}$
095848.86+023441.1	BL	1.55	S	$46.13^{+0.08}_{-0.14}$	$8.49^{+0.35}_{-0.35}$	$-0.47^{+0.16}_{-1.03}$
095849.41+022511.1	BL	1.12	I	$46.11^{+0.07}_{-0.18}$	$8.82^{+0.40}_{-0.40}$	$-0.83^{+0.40}_{-1.27}$
095849.44+022510.1	BL	2.09	Z	$46.58^{+0.05}_{-0.14}$	$8.48^{+0.43}_{-0.43}$	$-0.02^{+0.02}_{-0.86}$
095851.75+020059.5	BL	2.69	Z	$45.78^{+0.18}_{-0.14}$	$7.06^{+0.40}_{-0.40}$	$0.60^{+0.04}_{-0.77}$
095852.14+025156.3	BL	1.41	S	$46.32^{+0.08}_{-0.12}$	$8.74^{+0.41}_{-0.41}$	$-0.53^{+0.16}_{-0.66}$
095856.70+021047.8	BL	4.25	I	$45.78^{+0.59}_{-0.62}$	$8.16^{+0.42}_{-0.42}$	$-0.50^{+0.35}_{-1.42}$
095857.20+015843.7	OD	0.52	I	$47.53^{+0.33}_{-0.26}$	$8.75^{+0.30}_{-0.37}$	$0.67^{+0.52}_{-0.38}$
095857.35+021314.4	BL	1.02	S	$46.33^{+0.04}_{-0.05}$	$8.96^{+0.34}_{-0.34}$	$-0.75^{+0.59}_{-1.39}$
095857.35+021314.4	BL	1.02	Z	$46.33^{+0.04}_{-0.06}$	$8.81^{+0.43}_{-0.43}$	$-0.60^{+0.50}_{-1.42}$
095858.53+021459.1	BL	0.13	S	$44.43^{+0.05}_{-0.06}$	$7.31^{+0.37}_{-0.37}$	$-0.99^{+0.12}_{-0.91}$
095900.22+022811.6	NL	0.66	I	$45.93^{+0.16}_{-0.74}$	$9.31^{+0.32}_{-0.29}$	$-1.50^{+0.45}_{-1.33}$

Table 5.2—Continued

RA+Dec (J2000)	Type ^a	Redshift	Spec. ^b	L_{int}	M_{BH}	L_{int}/L_{Edd}
hhmmss.ss+ddmmss.s			source	$\log(L_{\odot})$	$\log(M_{\odot})$	
095901.31+024418.8	BL	3.54	I	$46.26^{+0.21}_{-0.40}$	$7.10^{+0.37}_{-0.37}$	$1.04^{+0.45}_{-1.36}$
095902.56+022511.8	BL	1.10	I	$45.27^{+0.16}_{-0.30}$	$8.01^{+0.35}_{-0.35}$	$-0.85^{+0.09}_{-0.95}$
095902.76+021906.5	BL	0.35	S	$45.41^{+0.06}_{-0.04}$	$8.66^{+0.47}_{-0.47}$	$-1.36^{+0.22}_{-1.05}$
095903.23+022002.8	BL	1.13	Z	$47.02^{+0.54}_{-0.54}$	$8.36^{+0.50}_{-0.50}$	$0.55^{+1.46}_{-2.30}$
095903.80+020316.7	BL	1.25	I	$44.73^{+0.20}_{-0.30}$	$7.00^{+0.39}_{-0.39}$	$-0.38^{+0.30}_{-0.50}$
095904.35+022552.8	NL	0.94	I	$46.05^{+0.12}_{-0.27}$	$9.74^{+0.31}_{-0.40}$	$-1.80^{+0.41}_{-0.37}$
095905.80+024027.0	BL	1.11	Z	$45.64^{+0.26}_{-0.29}$	$8.16^{+0.48}_{-0.48}$	$-0.63^{+0.26}_{-1.15}$
095906.46+022639.4	BL	4.17	I	$45.88^{+0.07}_{-0.10}$	$8.01^{+0.36}_{-0.36}$	$-0.25^{+0.03}_{-0.74}$
095907.65+020820.9	NL	0.35	I	$44.75^{+0.15}_{-0.14}$	$9.17^{+0.37}_{-0.36}$	$-2.53^{+0.36}_{-0.38}$
095908.32+024309.6	BL	1.32	S	$46.76^{+0.04}_{-0.04}$	$8.21^{+0.42}_{-0.42}$	$0.43^{+0.42}_{-1.25}$
095908.56+023317.2	BL	1.80	I	$45.68^{+0.25}_{-0.15}$	$8.36^{+0.34}_{-0.34}$	$-0.79^{+0.23}_{-1.05}$
095909.53+021916.5	BL	0.38	I	$44.65^{+0.10}_{-5.51}$	$7.77^{+0.34}_{-0.34}$	$-1.23^{+0.92}_{-6.42}$
095910.31+020732.3	NL	0.35	I	$44.75^{+0.05}_{-0.24}$	$9.36^{+0.30}_{-0.39}$	$-2.73^{+0.02}_{-0.71}$
095911.11+023333.9	BL	1.54	I	$45.56^{+0.28}_{-0.27}$	$7.66^{+0.42}_{-0.42}$	$-0.21^{+0.41}_{-1.16}$
095913.92+023844.5	BL	2.08	Z	$46.07^{+0.16}_{-0.17}$	$8.20^{+0.41}_{-0.41}$	$-0.25^{+0.15}_{-0.94}$
095915.06+014926.3	NL	0.53	I	$43.98^{+0.20}_{-0.13}$	$9.10^{+0.37}_{-0.34}$	$-3.24^{+0.37}_{-0.37}$
095915.40+020059.0	BL	1.36	I	$45.42^{+0.26}_{-1.31}$	$8.80^{+0.47}_{-0.47}$	$-1.49^{+0.13}_{-1.75}$
095916.05+015048.1	BL	1.03	Z	$45.73^{+0.31}_{-0.37}$	$8.75^{+0.45}_{-0.45}$	$-1.14^{+0.33}_{-1.28}$
095917.26+021516.9	OD	0.94	I	$44.81^{+0.53}_{-0.29}$	$9.72^{+0.30}_{-0.41}$	$-3.03^{+0.66}_{-0.27}$
095917.27+015019.1	BL	1.35	Z	$45.64^{+0.21}_{-0.22}$	$8.56^{+0.48}_{-0.48}$	$-1.03^{+0.20}_{-0.70}$
095920.89+020032.0	BL	1.48	I	$45.56^{+0.14}_{-0.14}$	$8.49^{+0.47}_{-0.47}$	$-1.04^{+0.25}_{-0.66}$
095920.90+020031.8	BL	1.48	Z	$45.56^{+0.11}_{-0.12}$	$8.15^{+0.41}_{-0.41}$	$-0.70^{+0.18}_{-0.59}$
095921.30+024030.4	BL	0.26	S	$44.75^{+0.12}_{-4.83}$	$7.64^{+0.44}_{-5.53}$	$-1.00^{+0.70}_{-5.53}$
095923.56+022227.3	BL	2.73	Z	$46.24^{+0.42}_{-0.28}$	$8.80^{+0.46}_{-0.46}$	$-0.68^{+0.28}_{-0.58}$

Table 5.2—Continued

RA+Dec (J2000)	Type ^a	Redshift	Spec. ^b	L_{int}	M_{BH}	L_{int}/L_{Edd}
hhmmss.ss+ddmmss.s			source	$\log(L_{\odot})$	$\log(M_{\odot})$	
095923.72+022522.6	NL	0.36	I	$43.78^{+0.30}_{-0.07}$	$8.91^{+0.44}_{-0.36}$	$-3.24^{+0.54}_{-0.34}$
095924.47+015954.4	BL	1.24	S	$46.33^{+0.03}_{-0.08}$	$8.95^{+0.42}_{-0.42}$	$-0.74^{+0.22}_{-0.61}$
095924.47+015954.3	BL	1.24	Z	$46.33^{+0.04}_{-0.08}$	$8.36^{+0.36}_{-0.36}$	$-0.15^{+0.16}_{-0.59}$
095926.01+014444.3	OD	0.67	I	$44.55^{+0.27}_{-0.08}$	$9.34^{+0.32}_{-0.35}$	$-2.91^{+0.42}_{-0.25}$
095926.88+015341.5	NL	0.44	I	$45.46^{+0.05}_{-0.25}$	$9.41^{+0.35}_{-0.37}$	$-2.07^{+0.30}_{-0.45}$
095927.74+020011.0	BL	1.25	Z	$45.54^{+0.12}_{-0.21}$	$8.10^{+0.36}_{-0.36}$	$-0.68^{+0.16}_{-0.90}$
095928.31+022106.9	BL	0.35	I	$44.75^{+0.53}_{-0.64}$	$7.24^{+0.41}_{-0.41}$	$-0.60^{+0.22}_{-1.09}$
095928.32+021950.7	BL	1.49	I	$45.72^{+0.10}_{-0.19}$	$8.60^{+0.41}_{-0.41}$	$-0.99^{+0.18}_{-0.62}$
095928.46+015934.8	BL	1.18	I	$45.19^{+0.19}_{-0.16}$	$7.96^{+0.42}_{-0.42}$	$-0.89^{+0.28}_{-0.62}$
095928.73+021738.4	BL	3.35	Z	$46.61^{+0.16}_{-3.74}$	$8.31^{+0.38}_{-0.38}$	$0.18^{+0.77}_{-4.51}$
095931.44+022703.0	BL	1.32	Z	$45.42^{+0.41}_{-1.41}$	$7.96^{+0.42}_{-0.42}$	$-0.65^{+0.49}_{-2.05}$
095934.35+012849.4	BL	1.16	I	$46.05^{+0.25}_{-0.27}$	$8.93^{+0.41}_{-0.41}$	$-0.99^{+0.60}_{-1.47}$
095934.44+020627.8	NL	0.69	I	$45.09^{+0.30}_{-0.09}$	$9.12^{+0.39}_{-0.49}$	$-2.14^{+0.52}_{-0.39}$
095934.76+021028.0	BL	1.32	Z	$45.33^{+0.13}_{-0.12}$	$8.47^{+0.42}_{-0.42}$	$-1.25^{+0.14}_{-0.93}$
095935.50+020538.2	BL	1.92	I	$45.82^{+0.11}_{-0.16}$	$8.65^{+0.39}_{-0.39}$	$-0.94^{+0.16}_{-0.95}$
095935.50+020538.1	BL	1.91	Z	$45.82^{+0.10}_{-0.12}$	$8.09^{+0.51}_{-0.51}$	$-0.39^{+0.02}_{-0.89}$
095937.42+022347.4	OD	0.74	I	$44.17^{+0.51}_{-0.49}$	$9.38^{+0.46}_{-0.26}$	$-3.32^{+0.52}_{-0.56}$
095938.25+013015.8	BL	1.47	I	$45.67^{+0.05}_{-0.08}$	$8.70^{+0.46}_{-0.46}$	$-1.14^{+0.25}_{-1.09}$
095938.29+020450.0	BL	2.79	Z	$46.43^{+0.06}_{-0.07}$	$8.89^{+0.40}_{-0.40}$	$-0.58^{+0.32}_{-0.52}$
095940.06+022306.8	BL	1.13	I	$45.69^{+0.08}_{-0.21}$	$8.47^{+0.45}_{-0.45}$	$-0.90^{+0.15}_{-0.78}$
095944.60+022626.2	NL	0.99	I	$45.88^{+0.21}_{-0.22}$	$9.43^{+0.38}_{-0.39}$	$-1.65^{+0.41}_{-0.44}$
095945.18+023439.4	NL	0.12	I	$44.11^{+0.76}_{-0.46}$	$8.77^{+0.34}_{-0.38}$	$-2.77^{+0.81}_{-0.38}$
095946.01+024743.6	BL	1.07	S	$46.30^{+0.08}_{-0.09}$	$8.51^{+0.40}_{-0.40}$	$-0.33^{+0.13}_{-0.79}$
095949.40+020141.0	BL	1.75	S	$46.45^{+0.81}_{-2.36}$	$8.22^{+0.41}_{-0.41}$	$0.11^{+0.79}_{-2.54}$

Table 5.2—Continued

RA+Dec (J2000)	Type ^a	Redshift	Spec. ^b	L_{int}	M_{BH}	L_{int}/L_{Edd}
hhmmss.ss+ddmmss.s			source	$\log(L_{\odot})$	$\log(M_{\odot})$	
095954.78+013206.5	BL	0.48	I	$44.87^{+0.12}_{-0.14}$	$7.90^{+0.39}_{-0.39}$	$-1.15^{+0.13}_{-0.64}$
095956.04+014727.9	NL	0.34	I	$43.89^{+0.18}_{-0.13}$	$8.58^{+0.33}_{-0.37}$	$-2.80^{+0.41}_{-0.33}$
095956.64+013702.2	BL	1.15	I	$45.46^{+0.12}_{-0.13}$	$8.66^{+0.44}_{-0.44}$	$-1.31^{+0.33}_{-1.11}$
095957.98+014327.4	BL	1.62	S	$46.04^{+1.00}_{-1.80}$	$8.79^{+0.35}_{-0.35}$	$-0.86^{+0.98}_{-1.94}$
095958.41+022238.2	NL	0.93	I	$47.79^{+0.33}_{-0.19}$	$9.13^{+0.27}_{-0.41}$	$0.55^{+0.42}_{-0.33}$
095958.46+021530.8	OD	0.66	I	$45.84^{+0.13}_{-0.93}$	$9.65^{+0.38}_{-0.37}$	$-1.93^{+0.23}_{-0.83}$
095958.53+021805.3	BL	1.79	I	$45.99^{+0.29}_{-0.97}$	$8.85^{+0.42}_{-0.42}$	$-0.98^{+0.25}_{-1.37}$
095959.36+022458.4	OD	0.57	I	$44.33^{+0.42}_{-0.18}$	$9.32^{+0.31}_{-0.37}$	$-3.11^{+0.57}_{-0.20}$
100001.00+022321.1	BL	1.85	I	$45.85^{+0.11}_{-0.18}$	$7.78^{+0.39}_{-0.39}$	$-0.05^{+0.54}_{-1.42}$
100001.06+020220.0	BL	3.50	Z	$46.02^{+0.16}_{-0.12}$	$8.10^{+0.44}_{-0.44}$	$-0.19^{+0.26}_{-0.69}$
100001.06+021413.6	BL	1.41	I	$45.56^{+0.10}_{-0.09}$	$8.15^{+0.45}_{-0.45}$	$-0.71^{+0.07}_{-0.94}$
100001.44+024844.7	BL	0.77	S	$45.88^{+0.09}_{-0.13}$	$7.95^{+0.38}_{-0.38}$	$-0.19^{+0.00}_{-0.82}$
100002.21+021631.8	BL	0.85	I	$45.38^{+0.06}_{-0.06}$	$8.29^{+0.44}_{-0.44}$	$-1.02^{+0.15}_{-0.69}$
100005.36+023059.6	OD	0.68	I	$45.57^{+0.32}_{-0.17}$	$9.26^{+0.39}_{-0.39}$	$-1.81^{+0.40}_{-0.41}$
100005.98+015453.3	NL	0.97	I	$44.98^{+0.60}_{-0.58}$	$9.79^{+0.32}_{-0.29}$	$-2.91^{+0.42}_{-0.48}$
100006.42+023343.4	OD	0.75	I	$44.64^{+0.19}_{-0.25}$	$9.53^{+0.33}_{-0.39}$	$-2.99^{+0.38}_{-0.38}$
100006.85+021235.7	BL	1.26	I	$45.43^{+0.11}_{-0.11}$	$8.07^{+0.41}_{-0.41}$	$-0.76^{+0.03}_{-0.86}$
100007.35+024043.5	BL	1.93	I	$45.80^{+0.23}_{-0.25}$	$8.69^{+0.37}_{-0.37}$	$-1.00^{+0.08}_{-0.70}$
100008.14+013306.6	BL	1.17	S	$45.61^{+0.17}_{-0.14}$	$8.42^{+0.33}_{-0.33}$	$-0.93^{+0.10}_{-0.67}$
100010.20+023745.0	BL	1.57	Z	$46.11^{+0.15}_{-0.16}$	$8.65^{+0.41}_{-0.41}$	$-0.65^{+0.13}_{-0.95}$
100010.85+024118.6	BL	1.44	I	$45.38^{+0.20}_{-0.22}$	$8.07^{+0.39}_{-0.39}$	$-0.81^{+0.36}_{-1.21}$
100011.68+021919.8	NL	0.62	I	$43.99^{+0.54}_{-0.28}$	$9.03^{+0.39}_{-0.34}$	$-3.15^{+0.61}_{-0.46}$
100012.91+023522.8	BL	0.70	S	$45.63^{+0.05}_{-0.12}$	$8.06^{+0.43}_{-0.43}$	$-0.54^{+0.30}_{-0.50}$
100013.33+022657.2	OD	0.73	I	$45.50^{+0.45}_{-0.51}$	$9.49^{+0.44}_{-0.38}$	$-2.11^{+0.55}_{-0.62}$

Table 5.2—Continued

RA+Dec (J2000) hhmmss.ss+ddmmss.s	Type ^a	Redshift	Spec. ^b source	L_{int} $\log(L_{\odot})$	M_{BH} $\log(M_{\odot})$	L_{int}/L_{Edd}
100013.41+021400.6	OD	0.94	I	$45.12^{+0.62}_{-0.40}$	$9.81^{+0.28}_{-0.38}$	$-2.81^{+0.68}_{-0.50}$
100013.54+013739.1	BL	1.62	I	$45.79^{+0.48}_{-0.73}$	$8.17^{+0.27}_{-0.27}$	$-0.49^{+0.49}_{-0.91}$
100014.08+022838.8	BL	1.26	I	$45.84^{+0.12}_{-0.17}$	$8.62^{+0.35}_{-0.35}$	$-0.90^{+0.08}_{-0.75}$
100014.09+022838.6	BL	1.26	Z	$45.84^{+0.11}_{-0.17}$	$8.51^{+0.42}_{-0.42}$	$-0.79^{+0.02}_{-0.83}$
100014.55+023852.7	BL	0.44	Z	$45.80^{+0.58}_{-0.56}$	$7.79^{+0.47}_{-0.47}$	$-0.10^{+1.24}_{-2.11}$
100017.52+020012.8	NL	0.35	I	$44.45^{+0.24}_{-0.22}$	$8.61^{+0.34}_{-0.41}$	$-2.27^{+0.44}_{-0.35}$
100017.54+020012.6	BL	0.35	Z	$44.50^{+25.60}_{-2.69}$	$7.59^{+0.42}_{-0.42}$	$-1.20^{+25.31}_{-3.07}$
100022.71+024956.3	BL	1.56	I	$45.37^{+0.07}_{-0.19}$	$8.30^{+0.43}_{-0.43}$	$-1.05^{+0.00}_{-0.85}$
100024.09+014005.4	OD	0.62	I	$44.49^{+0.16}_{-0.08}$	$9.42^{+0.40}_{-0.39}$	$-3.04^{+0.44}_{-0.40}$
100024.39+015054.1	BL	1.66	S	$46.08^{+0.20}_{-3.25}$	$8.65^{+0.41}_{-0.41}$	$-0.69^{+0.04}_{-3.52}$
100024.64+023149.0	BL	1.32	S	$46.26^{+0.05}_{-0.09}$	$8.56^{+0.46}_{-0.46}$	$-0.41^{+0.31}_{-0.55}$
100024.86+023302.7	OD	0.50	I	$44.67^{+0.28}_{-0.27}$	$8.98^{+0.37}_{-0.31}$	$-2.42^{+0.38}_{-0.43}$
100024.89+023956.6	BL	2.95	I	$46.30^{+0.23}_{-0.18}$	$8.23^{+0.38}_{-0.38}$	$-0.04^{+0.13}_{-0.71}$
100024.89+023956.6	BL	2.95	Z	$46.30^{+0.22}_{-0.17}$	$8.09^{+0.40}_{-0.40}$	$0.10^{+0.16}_{-0.61}$
100025.07+024128.5	BL	1.88	I	$45.88^{+0.11}_{-0.17}$	$8.14^{+0.34}_{-0.34}$	$-0.37^{+0.00}_{-0.79}$
100025.25+015852.2	BL	0.37	S	$45.49^{+0.03}_{-0.16}$	$8.58^{+0.31}_{-0.31}$	$-1.20^{+0.14}_{-0.86}$
100025.25+015852.1	BL	0.37	Z	$45.49^{+0.03}_{-0.14}$	$8.28^{+0.44}_{-0.44}$	$-0.91^{+0.01}_{-0.83}$
100028.23+013508.7	NL	0.84	I	$46.70^{+0.37}_{-0.35}$	$9.20^{+0.38}_{-0.34}$	$-0.62^{+0.46}_{-0.53}$
100028.63+025112.7	BL	0.77	I	$45.96^{+0.07}_{-0.10}$	$8.49^{+0.46}_{-0.46}$	$-0.65^{+0.52}_{-1.32}$
100029.69+022129.7	BL	0.73	Z	$45.15^{+0.06}_{-0.12}$	$8.03^{+0.49}_{-0.49}$	$-1.00^{+0.10}_{-0.70}$
100030.02+025142.3	BL	1.58	I	$46.02^{+0.05}_{-0.16}$	$8.01^{+0.44}_{-0.44}$	$-0.10^{+0.28}_{-0.55}$
100030.45+023735.6	BL	1.84	I	$45.66^{+0.37}_{-2.97}$	$7.86^{+0.43}_{-0.43}$	$-0.31^{+0.09}_{-3.55}$
100031.27+022819.9	OD	0.93	I	$44.42^{+0.31}_{-0.17}$	$9.65^{+0.35}_{-0.27}$	$-3.34^{+0.36}_{-0.30}$
100031.61+014758.1	BL	1.68	I	$46.07^{+0.86}_{-3.64}$	$8.80^{+0.38}_{-0.38}$	$-0.84^{+0.67}_{-3.99}$

Table 5.2—Continued

RA+Dec (J2000)	Type ^a	Redshift	Spec. ^b	L_{int}	M_{BH}	L_{int}/L_{Edd}
hhmmss.ss+ddmmss.s			source	$\log(L_{\odot})$	$\log(M_{\odot})$	
100033.38+015237.2	BL	0.83	I	$45.54^{+0.20}_{-0.19}$	$8.07^{+0.38}_{-0.38}$	$-0.65^{+0.11}_{-0.83}$
100033.49+013811.6	BL	0.52	I	$45.46^{+0.11}_{-0.24}$	$8.01^{+0.45}_{-0.45}$	$-0.66^{+0.63}_{-1.55}$
100033.49+013811.4	BL	0.52	Z	$45.46^{+0.11}_{-0.34}$	$7.73^{+0.42}_{-0.42}$	$-0.39^{+0.66}_{-1.52}$
100034.93+020235.2	BL	1.18	I	$45.69^{+0.07}_{-0.12}$	$8.39^{+0.40}_{-0.40}$	$-0.81^{+0.09}_{-0.74}$
100035.30+024302.9	BL	1.18	I	$45.42^{+0.15}_{-0.15}$	$8.14^{+0.43}_{-0.43}$	$-0.84^{+0.02}_{-0.79}$
100035.30+024302.9	BL	1.18	Z	$45.42^{+0.15}_{-0.15}$	$7.83^{+0.38}_{-0.38}$	$-0.53^{+0.07}_{-0.94}$
100036.05+022830.9	NL	0.69	I	$46.82^{+0.22}_{-0.14}$	$9.48^{+0.33}_{-0.33}$	$-0.78^{+0.35}_{-0.35}$
100036.21+024928.9	OD	0.47	I	$45.27^{+0.52}_{-0.42}$	$9.61^{+0.38}_{-0.36}$	$-2.46^{+0.60}_{-0.46}$
100037.29+024950.6	BL	0.73	I	$44.93^{+0.55}_{-1.28}$	$7.41^{+0.40}_{-0.40}$	$-0.59^{+0.10}_{-1.50}$
100037.99+014248.6	OD	0.62	I	$44.63^{+0.31}_{-0.47}$	$9.45^{+0.39}_{-0.36}$	$-2.93^{+0.42}_{-0.49}$
100038.01+020822.6	BL	1.83	I	$45.98^{+0.66}_{-2.99}$	$9.13^{+0.40}_{-0.40}$	$-1.26^{+0.62}_{-3.12}$
100038.01+020822.4	BL	1.83	Z	$45.98^{+0.59}_{-2.73}$	$8.98^{+0.42}_{-0.42}$	$-1.11^{+0.60}_{-2.98}$
100038.16+024930.4	BL	1.86	Z	$46.19^{+0.13}_{-0.19}$	$8.06^{+0.46}_{-0.46}$	$0.01^{+0.16}_{-1.05}$
100038.30+013708.4	BL	1.25	I	$46.01^{+0.18}_{-0.52}$	$8.60^{+0.48}_{-0.48}$	$-0.70^{+0.71}_{-1.80}$
100040.15+024751.6	BL	1.04	I	$45.71^{+0.10}_{-0.18}$	$8.26^{+0.47}_{-0.47}$	$-0.65^{+0.08}_{-0.81}$
100041.13+023350.5	NL	0.50	I	$44.81^{+0.21}_{-0.29}$	$8.97^{+0.30}_{-0.53}$	$-2.28^{+0.56}_{-0.33}$
100042.37+014534.1	BL	1.16	I	$45.03^{+0.24}_{-0.08}$	$7.66^{+0.39}_{-0.39}$	$-0.74^{+0.14}_{-0.59}$
100042.67+015323.8	NL	0.86	I	$44.86^{+0.26}_{-0.24}$	$9.35^{+0.32}_{-0.39}$	$-2.60^{+0.42}_{-0.38}$
100043.15+020637.2	BL	0.36	S	$44.87^{+0.08}_{-0.07}$	$8.07^{+0.42}_{-0.42}$	$-1.32^{+0.20}_{-0.63}$
100043.53+022524.4	NL	0.73	I	$45.96^{+0.74}_{-0.49}$	$9.29^{+0.36}_{-0.37}$	$-1.45^{+0.79}_{-0.52}$
100046.08+013440.0	NL	0.52	I	$43.99^{+0.24}_{-0.09}$	$8.75^{+0.37}_{-0.29}$	$-2.88^{+0.33}_{-0.36}$
100046.72+020404.5	BL	0.55	I	$44.95^{+0.10}_{-0.16}$	$7.75^{+0.47}_{-0.47}$	$-0.92^{+0.27}_{-0.58}$
100046.81+014737.8	BL	1.87	I	$45.65^{+0.19}_{-2.64}$	$8.60^{+0.41}_{-0.41}$	$-1.06^{+0.30}_{-3.08}$
100046.94+020015.9	BL	1.92	Z	$46.31^{+0.11}_{-0.10}$	$8.39^{+0.34}_{-0.34}$	$-0.20^{+0.02}_{-0.77}$

Table 5.2—Continued

RA+Dec (J2000)	Type ^a	Redshift	Spec. ^b	L_{int}	M_{BH}	L_{int}/L_{Edd}
hhmmss.ss+ddmmss.s			source	$\log(L_{\odot})$	$\log(M_{\odot})$	
100047.75+020757.2	BL	2.16	I	$46.52^{+0.21}_{-0.27}$	$9.32^{+0.31}_{-0.31}$	$-0.91^{+0.07}_{-0.69}$
100047.76+020757.0	BL	2.16	Z	$46.52^{+0.27}_{-0.22}$	$9.19^{+0.46}_{-0.46}$	$-0.78^{+0.21}_{-0.60}$
100047.93+014935.8	OD	0.89	I	$45.27^{+0.25}_{-0.15}$	$9.64^{+0.37}_{-0.44}$	$-2.48^{+0.47}_{-0.38}$
100047.94+021127.2	BL	1.51	I	$45.79^{+0.12}_{-0.23}$	$8.93^{+0.39}_{-0.39}$	$-1.26^{+0.05}_{-0.86}$
100049.50+021708.9	NL	0.87	I	$45.23^{+0.82}_{-0.11}$	$9.17^{+0.24}_{-0.32}$	$-2.05^{+0.50}_{-0.12}$
100049.91+020500.1	BL	1.24	I	$46.00^{+0.03}_{-0.02}$	$8.17^{+0.43}_{-0.43}$	$-0.29^{+0.11}_{-0.71}$
100049.97+015231.3	BL	1.16	I	$45.75^{+0.15}_{-0.21}$	$8.70^{+0.37}_{-0.37}$	$-1.06^{+0.02}_{-0.71}$
100050.13+022854.8	BL	3.33	Z	$46.50^{+0.30}_{-0.15}$	$8.90^{+0.37}_{-0.37}$	$-0.51^{+0.30}_{-0.55}$
100050.16+022618.5	BL	3.71	Z	$46.14^{+0.09}_{-0.08}$	$8.96^{+0.44}_{-0.44}$	$-0.93^{+0.33}_{-0.55}$
100050.57+022329.3	BL	3.10	I	$45.83^{+0.32}_{-0.33}$	$8.39^{+0.42}_{-0.42}$	$-0.67^{+0.10}_{-0.74}$
100051.51+021215.5	BL	1.83	I	$45.93^{+0.10}_{-3.12}$	$8.34^{+0.43}_{-0.43}$	$-0.52^{+0.25}_{-3.51}$
100051.52+021215.3	BL	1.84	Z	$45.94^{+0.23}_{-2.56}$	$8.10^{+0.32}_{-0.32}$	$-0.28^{+0.17}_{-2.92}$
100052.99+014123.8	OD	0.68	I	$44.23^{+0.44}_{-0.27}$	$9.06^{+0.33}_{-0.39}$	$-2.94^{+0.48}_{-0.38}$
100054.79+014602.3	NL	0.35	I	$45.97^{+1.09}_{-0.59}$	$8.91^{+0.25}_{-0.44}$	$-1.06^{+1.25}_{-0.56}$
100055.39+023441.4	BL	1.40	S	$45.94^{+0.10}_{-0.18}$	$8.81^{+0.41}_{-0.41}$	$-0.99^{+0.12}_{-0.78}$
100055.40+023441.4	BL	1.40	Z	$45.94^{+0.12}_{-0.16}$	$8.75^{+0.42}_{-0.42}$	$-0.93^{+0.14}_{-0.71}$
100055.63+022150.3	BL	1.94	Z	$46.01^{+0.12}_{-0.17}$	$8.53^{+0.38}_{-0.38}$	$-0.63^{+0.14}_{-0.61}$
100057.79+023932.5	BL	3.36	I	$46.63^{+0.16}_{-0.42}$	$6.63^{+0.49}_{-0.49}$	$1.88^{+0.22}_{-1.23}$
100058.33+015208.8	BL	2.03	I	$45.90^{+0.13}_{-0.16}$	$8.49^{+0.34}_{-0.34}$	$-0.70^{+0.12}_{-0.62}$
100058.70+022556.3	NL	0.69	I	$44.92^{+0.23}_{-0.07}$	$9.22^{+0.34}_{-0.31}$	$-2.41^{+0.39}_{-0.28}$
100058.71+022556.2	BL	0.69	Z	$44.93^{+0.13}_{-0.38}$	$7.92^{+0.42}_{-0.42}$	$-1.10^{+0.11}_{-0.75}$
100058.84+015400.3	BL	1.56	S	$46.08^{+0.05}_{-0.12}$	$8.58^{+0.35}_{-0.35}$	$-0.61^{+0.04}_{-0.83}$
100100.64+022911.1	BL	2.04	I	$45.94^{+0.88}_{-0.27}$	$8.72^{+0.51}_{-0.51}$	$-0.90^{+0.42}_{-0.56}$
100100.81+015947.9	BL	1.16	I	$45.36^{+0.11}_{-0.58}$	$8.59^{+0.42}_{-0.42}$	$-1.34^{+0.03}_{-1.05}$

Table 5.2—Continued

RA+Dec (J2000)	Type ^a	Redshift	Spec. ^b	L_{int}	M_{BH}	L_{int}/L_{Edd}
hhmmss.ss+ddmmss.s			source	$\log(L_{\odot})$	$\log(M_{\odot})$	
100101.53+023848.3	BL	3.08	I	$45.66^{+0.06}_{-0.16}$	$8.38^{+0.39}_{-0.39}$	$-0.83^{+0.08}_{-0.68}$
100101.94+014800.6	NL	0.91	I	$44.88^{+0.11}_{-0.08}$	$9.69^{+0.40}_{-0.33}$	$-2.93^{+0.35}_{-0.39}$
100104.89+024913.5	NL	0.35	I	$43.94^{+0.43}_{-0.30}$	$7.52^{+0.30}_{-0.39}$	$-1.70^{+0.48}_{-0.26}$
100105.84+023041.0	OD	0.70	I	$45.34^{+0.35}_{-0.26}$	$9.39^{+0.28}_{-0.31}$	$-2.16^{+0.35}_{-0.33}$
100106.95+015734.6	BL	1.55	Z	$45.43^{+0.09}_{-0.20}$	$7.96^{+0.43}_{-0.43}$	$-0.64^{+0.32}_{-0.51}$
100108.36+022342.2	BL	1.93	I	$46.06^{+0.15}_{-1.19}$	$9.17^{+0.41}_{-0.41}$	$-1.22^{+0.09}_{-1.62}$
100108.55+020052.4	BL	2.67	Z	$46.22^{+0.11}_{-0.12}$	$8.57^{+0.35}_{-0.35}$	$-0.47^{+0.09}_{-0.68}$
100110.20+023242.3	BL	2.65	Z	$46.18^{+0.21}_{-0.20}$	$8.21^{+0.39}_{-0.39}$	$-0.15^{+0.02}_{-0.79}$
100111.94+023024.9	BL	1.50	I	$45.60^{+0.20}_{-0.16}$	$8.20^{+0.39}_{-0.39}$	$-0.72^{+0.13}_{-0.67}$
100112.01+024233.7	BL	0.73	I	$44.38^{+0.05}_{-0.06}$	$7.77^{+0.33}_{-0.33}$	$-1.50^{+0.03}_{-0.77}$
100112.62+020940.1	BL	1.82	I	$45.94^{+0.40}_{-5.69}$	$8.62^{+0.38}_{-0.38}$	$-0.80^{+0.37}_{-5.79}$
100113.34+023608.0	BL	1.34	Z	$46.12^{+0.19}_{-0.21}$	$8.38^{+0.49}_{-0.49}$	$-0.38^{+0.78}_{-1.69}$
100113.34+023608.0	BL	1.34	I	$46.12^{+0.17}_{-0.12}$	$8.52^{+0.41}_{-0.41}$	$-0.51^{+0.87}_{-1.63}$
100113.91+022204.9	NL	0.88	I	$46.38^{+1.21}_{-0.52}$	$9.18^{+0.38}_{-0.46}$	$-0.91^{+1.38}_{-0.61}$
100114.29+022356.9	BL	1.80	S	$46.32^{+0.33}_{-1.88}$	$8.83^{+0.33}_{-0.33}$	$-0.62^{+0.22}_{-2.15}$
100114.64+012959.0	BL	1.78	I	$46.39^{+0.46}_{-2.72}$	$8.13^{+0.44}_{-0.44}$	$0.15^{+0.58}_{-3.70}$
100114.95+014348.6	NL	0.58	I	$44.57^{+0.14}_{-0.16}$	$9.30^{+0.30}_{-0.40}$	$-2.85^{+0.40}_{-0.30}$
100115.28+024813.0	BL	1.46	I	$45.89^{+0.12}_{-0.09}$	$8.89^{+0.34}_{-0.34}$	$-1.11^{+0.19}_{-0.99}$
100116.31+021402.8	NL	0.37	I	$43.81^{+0.24}_{-0.26}$	$8.67^{+0.36}_{-0.29}$	$-2.97^{+0.32}_{-0.37}$
100116.79+014053.8	BL	2.06	S	$46.48^{+0.13}_{-0.17}$	$8.61^{+0.43}_{-0.43}$	$-0.24^{+0.26}_{-0.59}$
100118.52+015543.0	BL	0.53	I	$44.76^{+0.12}_{-0.16}$	$8.22^{+0.41}_{-0.41}$	$-1.57^{+0.15}_{-0.63}$
100118.57+022739.4	BL	1.05	I	$45.89^{+0.13}_{-0.18}$	$8.52^{+0.41}_{-0.41}$	$-0.74^{+0.12}_{-0.97}$
100118.78+020730.0	BL	1.77	I	$45.28^{+0.62}_{-2.03}$	$8.74^{+0.45}_{-0.45}$	$-1.57^{+0.44}_{-2.51}$
100119.58+013834.0	NL	0.36	I	$44.00^{+0.11}_{-0.11}$	$9.18^{+0.33}_{-0.40}$	$-3.30^{+0.43}_{-0.31}$

Table 5.2—Continued

RA+Dec (J2000)	Type ^a	Redshift	Spec. ^b	L_{int}	M_{BH}	L_{int}/L_{Edd}
hhmmss.ss+ddmmss.s			source	$\log(L_{\odot})$	$\log(M_{\odot})$	
100120.26+023341.4	BL	1.83	S	$46.16^{+0.55}_{-4.13}$	$8.60^{+0.45}_{-0.45}$	$-0.55^{+0.39}_{-4.15}$
100120.26+023341.3	BL	1.84	Z	$46.04^{+0.60}_{-5.04}$	$8.14^{+0.36}_{-0.36}$	$-0.21^{+0.45}_{-5.17}$
100122.17+021334.6	NL	0.89	I	$45.33^{+0.12}_{-0.08}$	$9.36^{+0.31}_{-0.35}$	$-2.15^{+0.36}_{-0.31}$
100123.02+020851.3	BL	1.26	I	$45.37^{+0.07}_{-0.08}$	$8.32^{+0.40}_{-0.40}$	$-1.06^{+0.28}_{-0.55}$
100123.97+021446.1	NL	0.89	I	$45.16^{+0.12}_{-0.23}$	$9.11^{+0.34}_{-0.39}$	$-2.07^{+0.38}_{-0.37}$
100124.33+024041.7	BL	2.75	Z	$46.37^{+0.11}_{-0.11}$	$8.95^{+0.32}_{-0.32}$	$-0.69^{+0.05}_{-0.86}$
100124.34+024041.7	BL	2.76	I	$46.29^{+0.09}_{-0.11}$	$9.24^{+0.39}_{-0.39}$	$-1.06^{+0.09}_{-0.70}$
100124.85+022032.0	BL	1.71	I	$45.93^{+1.00}_{-3.97}$	$8.31^{+0.36}_{-0.36}$	$-0.50^{+0.72}_{-4.38}$
100127.86+022358.4	NL	0.99	I	$44.76^{+0.39}_{-0.32}$	$9.41^{+0.36}_{-0.38}$	$-2.76^{+0.51}_{-0.39}$
100128.00+021819.4	BL	1.19	I	$44.95^{+0.21}_{-0.16}$	$7.66^{+0.49}_{-0.49}$	$-0.83^{+0.02}_{-0.86}$
100129.67+020643.4	BL	1.91	Z	$46.06^{+0.11}_{-0.14}$	$8.75^{+0.38}_{-0.38}$	$-0.80^{+0.07}_{-0.79}$
100130.37+014304.4	BL	1.57	S	$45.91^{+0.17}_{-0.19}$	$8.16^{+0.34}_{-0.34}$	$-0.37^{+0.12}_{-0.63}$
100130.78+021147.1	BL	1.51	I	$45.51^{+0.12}_{-0.08}$	$8.43^{+0.38}_{-0.38}$	$-1.04^{+0.23}_{-1.14}$
100132.16+013420.9	BL	1.36	S	$46.06^{+0.11}_{-0.12}$	$8.00^{+0.35}_{-0.35}$	$-0.06^{+0.06}_{-0.76}$
100132.82+015759.9	BL	1.54	Z	$45.58^{+0.29}_{-0.22}$	$8.19^{+0.39}_{-0.39}$	$-0.72^{+0.13}_{-0.66}$
100132.86+013847.3	NL	0.74	I	$45.11^{+0.25}_{-0.22}$	$9.30^{+0.39}_{-0.31}$	$-2.30^{+0.35}_{-0.40}$
100136.50+025303.7	BL	2.12	S	$46.54^{+0.23}_{-0.15}$	$8.73^{+0.38}_{-0.38}$	$-0.31^{+0.23}_{-0.61}$
100136.59+014251.0	NL	0.87	I	$46.35^{+0.41}_{-0.24}$	$8.84^{+0.31}_{-0.45}$	$-0.61^{+0.54}_{-0.38}$
100140.36+015836.1	NL	0.86	I	$46.45^{+0.26}_{-0.26}$	$9.57^{+0.36}_{-0.42}$	$-1.24^{+0.50}_{-0.38}$
100140.96+015643.3	BL	2.18	I	$46.81^{+0.12}_{-0.28}$	$9.07^{+0.41}_{-0.41}$	$-0.37^{+0.17}_{-0.72}$
100141.09+021300.0	BL	0.62	I	$44.78^{+0.06}_{-0.28}$	$7.35^{+0.46}_{-0.46}$	$-0.68^{+0.11}_{-0.94}$
100141.26+022308.0	BL	1.51	I	$45.40^{+0.10}_{-0.16}$	$7.79^{+0.37}_{-0.37}$	$-0.51^{+0.60}_{-1.43}$
100141.88+024927.7	NL	0.74	I	$44.63^{+0.23}_{-0.16}$	$9.25^{+0.31}_{-0.38}$	$-2.73^{+0.43}_{-0.30}$
100143.03+014932.2	BL	2.08	I	$45.81^{+0.07}_{-0.08}$	$7.82^{+0.35}_{-0.35}$	$-0.13^{+0.06}_{-0.84}$

Table 5.2—Continued

RA+Dec (J2000)	Type ^a	Redshift	Spec. ^b	L_{int}	M_{BH}	L_{int}/L_{Edd}
hhmmss.ss+ddmmss.s			source	$\log(L_{\odot})$	$\log(M_{\odot})$	
100145.58+024212.6	BL	3.46	I	$45.97^{+0.07}_{-0.64}$	$7.72^{+0.42}_{-0.42}$	$0.13^{+0.01}_{-1.02}$
100146.49+020256.7	BL	0.67	Z	$45.50^{+0.06}_{-0.13}$	$7.73^{+0.45}_{-0.45}$	$-0.34^{+0.02}_{-0.91}$
100147.05+020236.6	BL	1.17	Z	$46.08^{+0.16}_{-0.31}$	$8.38^{+0.41}_{-0.41}$	$-0.41^{+0.58}_{-1.53}$
100147.26+024729.4	BL	1.53	I	$45.34^{+0.36}_{-0.44}$	$7.88^{+0.42}_{-0.42}$	$-0.66^{+0.11}_{-0.83}$
100148.33+012956.1	BL	1.48	I	$45.58^{+0.10}_{-0.49}$	$7.89^{+0.41}_{-0.41}$	$-0.43^{+0.03}_{-0.98}$
100149.00+024821.8	BL	1.61	I	$46.32^{+0.62}_{-1.11}$	$7.91^{+0.46}_{-0.46}$	$0.29^{+0.13}_{-2.11}$
100149.60+023853.3	BL	2.06	I	$46.19^{+0.09}_{-0.08}$	$8.51^{+0.42}_{-0.42}$	$-0.43^{+0.13}_{-0.71}$
100149.60+023853.3	BL	2.05	Z	$46.18^{+0.11}_{-0.10}$	$8.52^{+0.36}_{-0.36}$	$-0.45^{+0.05}_{-0.77}$
100152.23+015608.7	NL	0.97	I	$44.96^{+0.13}_{-0.14}$	$9.48^{+0.28}_{-0.43}$	$-2.64^{+0.43}_{-0.29}$
100153.45+021152.8	OD	0.48	I	$44.27^{+0.26}_{-0.15}$	$9.33^{+0.30}_{-0.42}$	$-3.17^{+0.52}_{-0.29}$
100154.17+024753.9	BL	4.12	Z	$46.06^{+0.00}_{-0.07}$	$8.40^{+0.40}_{-0.40}$	$-0.45^{+0.29}_{-0.60}$
100156.24+020943.4	BL	1.64	I	$45.61^{+0.19}_{-0.60}$	$8.63^{+0.35}_{-0.35}$	$-1.13^{+0.23}_{-1.32}$
100156.44+014811.3	NL	0.96	I	$44.91^{+0.19}_{-0.16}$	$9.14^{+0.32}_{-0.38}$	$-2.34^{+0.43}_{-0.32}$
100157.76+023804.9	NL	0.35	I	$46.09^{+0.21}_{-0.23}$	$9.06^{+0.34}_{-0.33}$	$-1.08^{+0.42}_{-0.39}$
100158.00+014621.4	NL	0.83	I	$45.51^{+0.19}_{-0.24}$	$9.58^{+0.37}_{-0.29}$	$-2.18^{+0.30}_{-0.41}$
100158.96+022445.2	BL	1.37	I	$45.48^{+0.17}_{-0.21}$	$8.63^{+0.41}_{-0.41}$	$-1.26^{+0.06}_{-0.73}$
100158.96+022445.2	BL	1.37	Z	$45.48^{+0.15}_{-0.23}$	$8.35^{+0.40}_{-0.40}$	$-0.98^{+0.05}_{-0.80}$
100159.79+022641.6	BL	2.03	I	$46.85^{+0.07}_{-0.16}$	$9.07^{+0.42}_{-0.42}$	$-0.33^{+0.18}_{-1.03}$
100159.79+022641.6	BL	2.03	Z	$46.85^{+0.06}_{-0.13}$	$9.09^{+0.35}_{-0.35}$	$-0.35^{+0.26}_{-1.00}$
100201.51+020329.4	BL	2.01	S	$46.73^{+0.19}_{-0.16}$	$9.46^{+0.29}_{-0.29}$	$-0.84^{+0.20}_{-0.66}$
100202.22+024157.8	BL	0.79	I	$45.27^{+0.12}_{-0.18}$	$8.24^{+0.39}_{-0.39}$	$-1.08^{+0.20}_{-1.04}$
100202.22+024157.8	BL	0.79	Z	$45.27^{+0.14}_{-0.24}$	$7.96^{+0.46}_{-0.46}$	$-0.80^{+0.15}_{-0.89}$
100202.55+020145.3	NL	0.90	I	$45.55^{+0.14}_{-0.19}$	$9.66^{+0.30}_{-0.39}$	$-2.22^{+0.38}_{-0.31}$
100202.78+022434.6	BL	0.99	S	$45.58^{+0.16}_{-0.20}$	$8.78^{+0.39}_{-0.39}$	$-1.32^{+0.10}_{-0.74}$

Table 5.2—Continued

RA+Dec (J2000)	Type ^a	Redshift	Spec. ^b	L_{int}	M_{BH}	L_{int}/L_{Edd}
hhmmss.ss+ddmmss.s			source	$\log(L_{\odot})$	$\log(M_{\odot})$	
100204.36+023118.1	BL	2.78	I	$46.80^{+0.09}_{-1.01}$	$8.62^{+0.50}_{-0.50}$	$0.07^{+0.49}_{-1.92}$
100205.03+023731.5	BL	0.52	I	$45.94^{+0.04}_{-3.40}$	$8.38^{+0.37}_{-0.37}$	$-0.56^{+1.45}_{-4.88}$
100206.29+021441.8	BL	1.27	I	$45.44^{+0.14}_{-0.19}$	$7.78^{+0.49}_{-0.49}$	$-0.45^{+0.20}_{-0.76}$
100206.43+022304.8	BL	1.30	I	$44.92^{+0.16}_{-0.26}$	$7.94^{+0.34}_{-0.34}$	$-1.13^{+0.17}_{-0.62}$
100209.09+021837.8	NL	0.84	I	$45.88^{+0.22}_{-0.20}$	$9.39^{+0.36}_{-0.35}$	$-1.63^{+0.38}_{-0.39}$
100210.73+023026.1	BL	1.16	S	$46.03^{+0.09}_{-0.16}$	$7.90^{+0.46}_{-0.46}$	$0.02^{+0.12}_{-0.65}$
100212.11+014232.4	BL	0.37	I	$45.15^{+0.21}_{-0.18}$	$7.70^{+0.40}_{-0.40}$	$-0.67^{+0.56}_{-1.41}$
100212.26+022614.1	NL	0.89	I	$44.24^{+0.35}_{-0.22}$	$8.98^{+0.33}_{-0.50}$	$-2.86^{+0.57}_{-0.31}$
100213.17+023827.6	BL	1.14	I	$45.63^{+0.12}_{-0.36}$	$8.32^{+0.47}_{-0.47}$	$-0.81^{+0.31}_{-1.36}$
100213.42+023351.7	BL	1.14	I	$45.60^{+0.19}_{-0.21}$	$8.05^{+0.39}_{-0.39}$	$-0.56^{+0.56}_{-1.36}$
100216.37+015008.2	OD	0.67	I	$44.76^{+0.12}_{-0.11}$	$9.34^{+0.37}_{-0.36}$	$-2.69^{+0.37}_{-0.36}$
100216.76+013725.2	NL	0.62	I	$44.39^{+0.48}_{-0.34}$	$9.32^{+0.27}_{-0.48}$	$-3.05^{+0.69}_{-0.24}$
100217.43+022959.7	BL	1.10	Z	$45.80^{+0.10}_{-0.17}$	$8.45^{+0.42}_{-0.42}$	$-0.77^{+0.13}_{-0.92}$
100217.43+022959.7	BL	1.10	I	$45.80^{+0.11}_{-0.17}$	$8.78^{+0.43}_{-0.43}$	$-1.10^{+0.11}_{-0.94}$
100217.54+021212.5	NL	0.82	I	$45.01^{+0.36}_{-0.38}$	$9.65^{+0.33}_{-0.38}$	$-2.76^{+0.44}_{-0.37}$
100218.32+021053.1	BL	0.55	I	$44.84^{+0.30}_{-0.17}$	$8.61^{+0.40}_{-0.40}$	$-1.88^{+0.16}_{-0.67}$
100219.48+021315.7	BL	2.03	I	$46.24^{+0.27}_{-0.32}$	$8.61^{+0.44}_{-0.44}$	$-0.49^{+0.63}_{-1.44}$
100219.65+021715.7	BL	1.34	Z	$45.46^{+0.19}_{-0.11}$	$7.79^{+0.33}_{-0.33}$	$-0.45^{+0.05}_{-0.90}$
100222.99+020639.9	NL	0.90	I	$44.99^{+0.15}_{-0.09}$	$9.12^{+0.38}_{-0.38}$	$-2.25^{+0.41}_{-0.35}$
100223.05+014714.9	BL	1.24	I	$46.14^{+0.06}_{-0.08}$	$8.31^{+0.38}_{-0.38}$	$-0.29^{+0.80}_{-1.55}$
100223.06+014714.8	BL	1.25	Z	$46.15^{+0.06}_{-0.07}$	$8.21^{+0.43}_{-0.43}$	$-0.18^{+0.75}_{-1.62}$
100223.36+023704.5	BL	1.44	I	$45.45^{+0.26}_{-0.23}$	$8.23^{+0.45}_{-0.45}$	$-0.88^{+0.03}_{-0.79}$
100226.33+021923.2	BL	1.29	S	$46.12^{+0.07}_{-0.15}$	$8.10^{+0.47}_{-0.47}$	$-0.10^{+0.02}_{-0.81}$
100226.93+015940.1	BL	1.61	I	$45.57^{+0.27}_{-0.25}$	$8.35^{+0.40}_{-0.40}$	$-0.89^{+0.01}_{-0.79}$

Table 5.2—Continued

RA+Dec (J2000)	Type ^a	Redshift	Spec. ^b	L_{int}	M_{BH}	L_{int}/L_{Edd}
hhmmss.ss+ddmmss.s			source	$\log(L_{\odot})$	$\log(M_{\odot})$	
100228.82+024016.9	BL	3.14	I	$46.68^{+0.13}_{-1.92}$	$7.98^{+0.45}_{-0.45}$	$0.58^{+1.18}_{-3.34}$
100228.82+024016.9	BL	3.14	Z	$46.68^{+0.12}_{-1.92}$	$8.29^{+0.45}_{-0.45}$	$0.28^{+1.25}_{-3.32}$
100230.06+014810.4	BL	0.63	I	$44.99^{+0.09}_{-0.68}$	$7.50^{+0.40}_{-0.40}$	$-0.62^{+1.10}_{-2.12}$
100230.65+024427.6	BL	0.82	I	$45.59^{+0.08}_{-0.08}$	$7.82^{+0.38}_{-0.38}$	$-0.35^{+0.13}_{-0.91}$
100231.91+023507.5	NL	0.88	I	$44.74^{+0.29}_{-0.12}$	$9.00^{+0.40}_{-0.34}$	$-2.37^{+0.45}_{-0.34}$
100232.13+023537.3	BL	0.66	S	$45.88^{+0.06}_{-0.12}$	$8.14^{+0.35}_{-0.35}$	$-0.37^{+0.06}_{-0.77}$
100232.52+014009.0	BL	1.79	I	$45.78^{+0.66}_{-4.73}$	$8.80^{+0.41}_{-0.41}$	$-1.13^{+0.63}_{-5.01}$
100233.64+021541.9	BL	1.41	I	$45.97^{+0.10}_{-0.19}$	$7.93^{+0.41}_{-0.41}$	$-0.07^{+0.53}_{-1.34}$
100234.33+015011.3	BL	1.51	S	$46.53^{+0.06}_{-0.11}$	$8.56^{+0.37}_{-0.37}$	$-0.14^{+0.22}_{-0.57}$
100234.85+024253.3	BL	0.20	S	$44.53^{+0.14}_{-0.11}$	$7.18^{+0.45}_{-0.45}$	$-0.77^{+0.00}_{-0.85}$
100236.71+015948.8	BL	1.52	S	$45.98^{+0.16}_{-0.16}$	$8.42^{+0.48}_{-0.48}$	$-0.56^{+0.37}_{-0.56}$
100237.09+014648.0	OD	0.67	I	$46.03^{+0.13}_{-0.09}$	$9.30^{+0.31}_{-0.42}$	$-1.38^{+0.47}_{-0.33}$
100237.92+024700.6	BL	0.21	I	$47.27^{+0.21}_{-0.15}$	$7.34^{+0.41}_{-0.41}$	$1.82^{+2.76}_{-3.49}$
100238.63+024743.1	OD	0.82	I	$44.73^{+0.10}_{-0.13}$	$9.11^{+0.36}_{-0.32}$	$-2.49^{+0.33}_{-0.38}$
100238.70+013936.7	BL	1.32	I	$45.82^{+0.12}_{-0.20}$	$8.58^{+0.40}_{-0.40}$	$-0.88^{+0.08}_{-0.87}$
100240.30+020147.3	OD	0.64	I	$44.96^{+0.19}_{-0.29}$	$8.80^{+0.28}_{-0.33}$	$-1.96^{+0.36}_{-0.38}$
100240.32+013659.5	NL	0.37	I	$44.63^{+0.38}_{-0.44}$	$8.89^{+0.37}_{-0.31}$	$-2.37^{+0.46}_{-0.58}$
100240.93+023448.4	BL	1.68	I	$46.80^{+0.30}_{-0.65}$	$7.36^{+0.48}_{-0.48}$	$1.34^{+1.35}_{-2.49}$
100241.73+021615.2	NL	0.39	I	$44.19^{+0.41}_{-0.27}$	$8.78^{+0.24}_{-0.61}$	$-2.71^{+0.79}_{-0.20}$
100243.85+020502.7	BL	1.23	I	$45.79^{+0.12}_{-0.21}$	$8.05^{+0.44}_{-0.44}$	$-0.38^{+0.07}_{-0.79}$
100243.93+022340.7	OD	0.66	I	$44.04^{+0.46}_{-0.12}$	$9.32^{+0.34}_{-0.32}$	$-3.39^{+0.43}_{-0.34}$
100243.96+023428.6	BL	0.38	Z	$45.28^{+0.06}_{-0.08}$	$8.29^{+0.41}_{-0.41}$	$-1.12^{+0.37}_{-1.20}$
100243.96+023428.6	BL	0.38	I	$45.28^{+0.06}_{-0.07}$	$8.25^{+0.46}_{-0.46}$	$-1.08^{+0.32}_{-1.15}$
100248.87+013855.3	NL	0.69	I	$47.49^{+0.23}_{-0.21}$	$9.20^{+0.34}_{-0.32}$	$0.18^{+0.36}_{-0.39}$

5.3 Characterizing AGN Specific Accretion Rate

In this work we describe the specific accretion rate using the observable Eddington ratio parameter, L_{int}/L_{Edd} . Here L_{int} is the intrinsic luminosity, a measure of the total accretion luminosity which includes only light from the accretion disk and X-ray corona and excludes any reprocessed IR emission. In this work when using “intrinsic” luminosity we are always referring to the total of the disk (optical/UV) and corona (X-ray) emission, without the reprocessed (IR) emission. The Eddington luminosity is derived from the black hole mass, with $L_{Edd} = 1.3 \times 10^{38} (M_{BH}/M_{\odot}) \text{ erg s}^{-1}$. AGN luminosity is powered by accretion rate, with $L_{int} = \eta \dot{M} c^2$. Assuming $\eta \sim 0.15$ (Elvis et al., 2002), the Eddington accretion rate can be written $\dot{M}_{Edd} = 3.3 M_8 \text{ M}_{\odot} \text{ yr}^{-1}$ with $M_8 = M/(10^8 M_{\odot})$. We can then define the dimensionless specific accretion rate $\dot{m} \equiv \dot{M}/\dot{M}_{Edd} = L_{int}/L_{Edd}$.

Below we outline our methods for estimating black hole masses and bolometric luminosities from the data for the AGNs in our sample. Table 5.2 presents the full catalog of L_{int} , M_{BH} , and L_{int}/L_{Edd} , and their associated errors, for our AGNs.

5.3.1 Intrinsic Luminosity Estimates

We calculate the intrinsic luminosity from the full near-IR to X-ray multiwavelength data. This avoids monochromatic bolometric corrections which are highly uncertain and probably depend on Eddington ratio (e.g., Kelly et al., 2008; Vasudevan & Fabian, 2009). Instead we measure intrinsic luminosity by integrating the best-fit accretion disk + X-ray power-law SED model. We compile the broad-band near-IR (Ks , J), optical (z^+ , r^+ , i^* , g^+ , V_J , B_J , u^*), UV (GALEX NUV & FUV), and X-ray (0.5-2 keV and 2-10 keV from Chandra when available or XMM-Newton) data, for which the wavebands and limits are described in Table 5.1. We do not include the mid-IR (Spitzer/IRAC) data, since this is reprocessed emission and we seek only the intrinsic AGN luminosity. Likewise the radio emission is negligible in the total

Table 5.2—Continued

RA+Dec (J2000)	Type ^a	Redshift	Spec. ^b	L_{int}	M_{BH}	L_{int}/L_{Edd}
hhmmss.ss+ddmmss.s			source	$\log(L_{\odot})$	$\log(M_{\odot})$	
100249.33+023746.5	BL	2.12	I	$46.30^{+0.17}_{-0.17}$	$8.70^{+0.42}_{-0.42}$	$-0.51^{+0.27}_{-0.57}$
100249.92+021732.3	BL	1.10	Z	$45.65^{+0.09}_{-0.13}$	$8.58^{+0.41}_{-0.41}$	$-1.04^{+0.18}_{-0.95}$
100249.92+021732.3	BL	1.10	I	$45.65^{+0.10}_{-0.12}$	$8.85^{+0.35}_{-0.35}$	$-1.32^{+0.22}_{-1.00}$
100250.86+024203.6	NL	0.98	I	$45.53^{+0.24}_{-0.29}$	$9.12^{+0.35}_{-0.41}$	$-1.71^{+0.44}_{-0.47}$
100251.42+021849.8	NL	0.61	I	$45.28^{+0.31}_{-0.20}$	$9.44^{+0.40}_{-0.37}$	$-2.28^{+0.46}_{-0.43}$
100251.62+022905.5	BL	2.01	S	$46.35^{+0.17}_{-0.16}$	$8.62^{+0.35}_{-0.35}$	$-0.38^{+0.19}_{-0.64}$
100252.85+021452.8	NL	0.67	I	$44.58^{+0.40}_{-0.23}$	$9.10^{+0.37}_{-0.33}$	$-2.63^{+0.47}_{-0.30}$
100252.88+025426.8	BL	0.80	I	$45.64^{+0.23}_{-0.16}$	$7.97^{+0.50}_{-0.50}$	$-0.44^{+0.14}_{-0.71}$
100256.92+024321.2	BL	3.32	I	$46.10^{+0.06}_{-0.21}$	$9.00^{+0.40}_{-0.40}$	$-1.01^{+0.16}_{-0.62}$
100258.21+015909.3	BL	1.60	I	$45.59^{+0.24}_{-0.29}$	$8.58^{+0.39}_{-0.39}$	$-1.10^{+0.05}_{-0.92}$
100309.21+022038.4	BL	1.96	S	$46.62^{+0.26}_{-0.22}$	$8.25^{+0.40}_{-0.40}$	$0.25^{+0.26}_{-1.05}$
100312.45+020002.2	BL	1.78	I	$45.55^{+0.97}_{-2.70}$	$9.07^{+0.46}_{-0.46}$	$-1.64^{+0.78}_{-3.07}$

^a“BL” refers to a broad-line AGN, “NL” is a narrow-line AGN, and “OD” is a lineless or optically dull AGN.

^b“S” means the spectrum and redshift are from the SDSS archive, “I” is from the COSMOS Magellan/IMACS campaign (Trump et al., 2009a), and “Z” is from the zCOSMOS VLT/VIMOS campaign (Lilly et al., 2007).

energy output of our AGNs. While narrow-band optical photometry also exists for our AGNs, we seek the multiwavelength SED, for which the broad-band data is better suited.

The near-IR and optical emission of narrow-line and lineless AGNs is dominated by the emission from the host galaxy. For these objects, accurate intrinsic luminosities require modeling and subtracting the host galaxy light. Gabor et al. (2009) measured the host F814W luminosities from surface brightness fitting to the HST/ACS data of our AGNs. We use this luminosity to scale a galaxy template from Polletta et al. (2007). Lineless AGNs have early-type hosts, since their spectra lack the emission lines associated with a late-type star-forming galaxy, and so we use the “Ell5” early-type template from Polletta et al. (2007). The narrow-line galaxies in our sample typically have intermediate-type (“green valley”) hosts based on their morphologies (Gabor et al., 2009) and star formation rates (Silverman et al., 2009), and so we use the “S0” template of Polletta et al. (2007). We subtract the host contribution in each photometric band before performing our SED fit. The reddest (“Ell2”) and bluest (“Sd”) normal galaxy templates of Polletta et al. (2007) are additionally used as extreme hosts to estimate the possible error contribution from choosing the wrong host template (described in §3.3). While broad-line AGNs are likely to have some host contribution, we cannot use surface brightness fitting to estimate their host luminosity because they are at high redshift and their point source overwhelms their extended emission (Gabor et al., 2009). We do, however, account for the error resulting from not subtracting the host from L_{int} for broad-line AGNs (described in §3.3): in general this error is $< 0.1\text{dex}$.

We shift the observed (and host-subtracted, for narrow-line and lineless AGNs) photometry to the rest-frame from the measured spectroscopic redshift and convert the magnitudes or fluxes to luminosities. We then fit an accretion disk model to

the optical/UV emission within the range $1 < E < 100$ eV ($4.8 \times 10^{14} < \nu < 2.4 \times 10^{16}$ Hz, or $6200 > \lambda > 124$ Å) and a power-law representing the X-ray corona emission to the rest-frame X-ray data. We measure the total bolometric luminosity from the sum of the disk luminosity (given by the analytic solution in Equation 4 below) and the power-law luminosity from $4E_{peak} < E < 250$ keV (where E_{peak} is the peak energy of the best-fit disk model). Measurements of AGN X-ray cutoff energies vary widely and may depend on unknown properties of the AGN in question (Perola et al., 2002; Molina et al., 2006), but for simplicity we choose 250 keV since it lies well within the range of various cutoff energy measurements.

We use the accretion disk model of Gierliński et al. (1999), which improves upon a basic blackbody accretion disk by including a correction for relativistic effects. (The Gierliński et al. (1999) model is the “diskpn” model of the XSpec X-ray fitting software.) This model is based on the pseudo-Newtonian gravitational potential $\Phi = -GM/(R - R_g)$ (Paczynski & Wiita, 1980), where R_g is the Schwarzschild radius $R_g = GM/c^2$. From Gierliński et al. (1999), the model takes the form:

$$L = KE^4 \int_{r_{in}}^{\infty} \frac{r dr}{\exp[E/kT(r)] - 1} \quad (5.1)$$

where $r = R/R_g$ and we assume the innermost stable orbit $r_{in} = 6$. The temperature depends on radius as

$$T(r) = \frac{T_0}{c_0} \left[\frac{r - 2/3}{r(r - 2)^3} \left(1 - \frac{3^{3/2}(r - 2)}{2^{1/2}r^{3/2}} \right) \right]^{1/4}, \quad (5.2)$$

with $c_0 \simeq 0.1067$, and $T_0 \propto \dot{M}^{1/4}$. The coefficient K depends on inclination angle, coronal absorption, and the color to effective temperature ratio. Rather than estimate these values, we assume that K is a constant, computed by simply scaling the model to our data. T_0 is the sole free parameter. In our analyses below we refer to E_{peak} , the peak energy of the disk, rather than T_0 , and in general $kT_0 \simeq E_{peak}/24$. We find the best-fit disk model in terms of T_0 by minimizing the χ^2 function using

the Newton-Raphson method. While most of the best-fit disk models have significant emission at $E < 1$ eV, we restrict the fit to $1 < E < 100$ eV to mitigate the effects of a contaminating torus and/or host galaxy light.

The total disk luminosity is then calculated analytically (see Appendix A of Gierliński et al., 1999):

$$L_{disk} = K \frac{h^3 c^2}{16\pi} \left(\frac{T(r_{in})}{c_0} \right)^4. \quad (5.3)$$

Errors in both E_{peak} and L_{disk} are found by bootstrapping 100 fits to the resampled data.

To characterize the X-ray corona emission, we fit a power-law, $L = L_0 \nu^\alpha$, to the rest-frame equivalent of the observed 0.5-2 keV and 2-10 keV bands. The X-ray slope α_X is related to the photon index Γ_X as $\Gamma_X = 2 - \alpha_X$. We integrate this model over $4E_{peak} < E < 250$ keV (where E_{peak} is the energy peak of the disk model), using the analytic solution:

$$L_X = L_0 / (\alpha + 1) \times [(250 \text{ keV} / h)^{\alpha+1} - (4E_{peak} / h)^{\alpha+1}] \quad (5.4)$$

Figure 5.1 shows a representative sample of broad-line, narrow-line, and lineless SEDs with model fits. The total bolometric luminosity is simply the sum of the integrated accretion disk and X-ray power-law components, $L_{int} = L_{disk} + L_X$.

5.3.2 Black Hole Mass Estimates

For Type 1 AGNs, we estimate black hole masses using the scaling relations of Vestergaard & Osmer (2009) for the MgII broad emission line and Vestergaard & Peterson (2006) for the H β and CIV broad emission lines. These relations estimate black hole mass from single-epoch spectra by employing the correlation between the radius of the broad emission line region and the continuum luminosity, $R_{BLR} \sim L^{0.5}$, observed in local AGN with reverberation mapping (Bentz et al., 2006; Kaspi et al.,

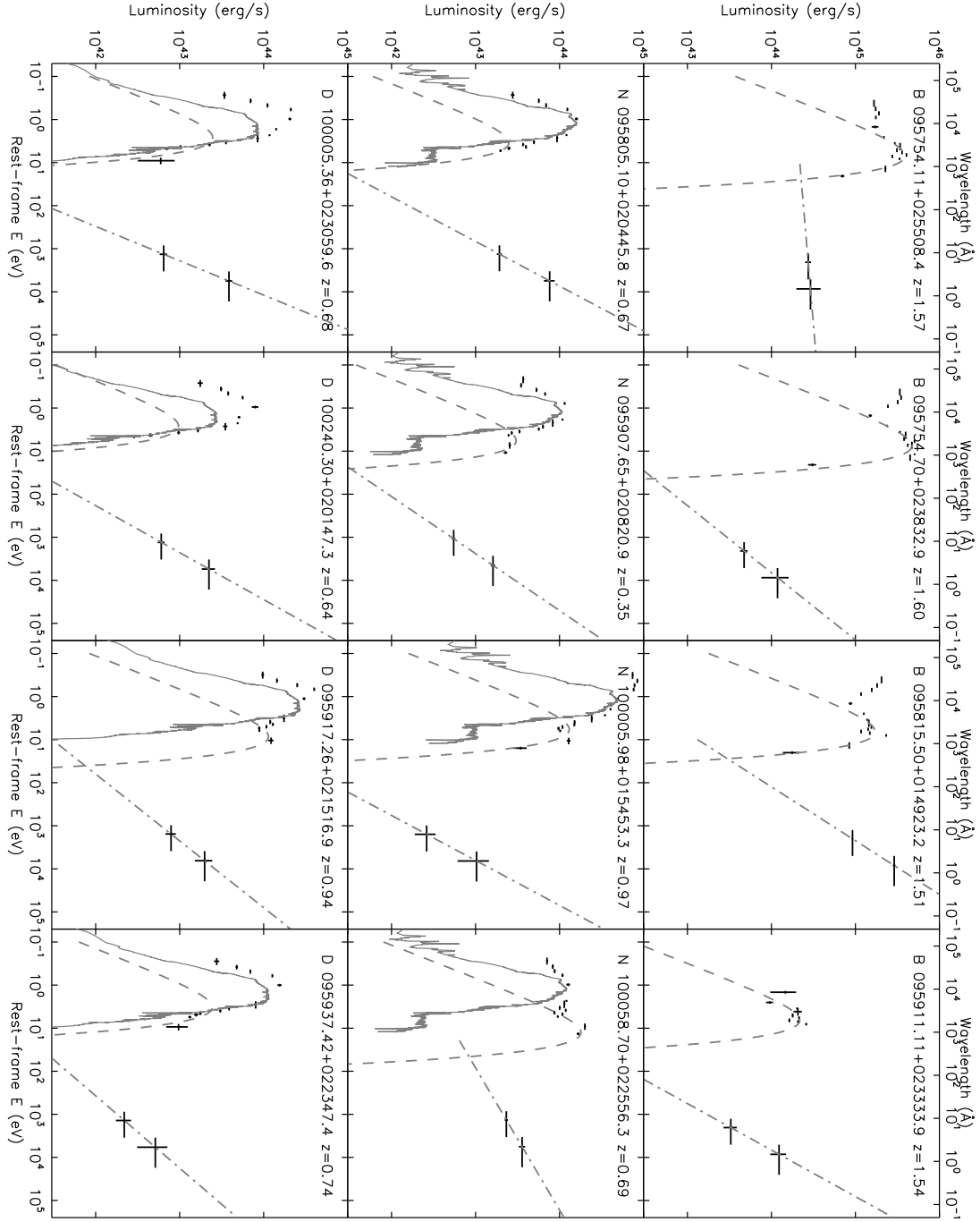


Figure 5.1 Multiwavelength photometry and model fits for 12 example AGNs. The top four panels are broad-line AGNs (represented by 'B'), the middle four are narrow-line AGNs (represented by 'N'), and the bottom four are lineless “optically dull” AGNs (represented by 'D'). In each panel, the dashed line is the best-fit accretion disk model and the dot-dashed line is the X-ray power-law fit. Estimated host SEDs are shown by solid lines for the narrow-line and lineless AGNs.

2007). In general, masses estimated from the scaling relations are accurate to ~ 0.4 dex (Vestergaard & Peterson, 2006; Shen et al., 2008) and agree with local AGN masses from dynamical estimators (Davies et al., 2006; Onken et al., 2007) and the M_{BH} - σ_* correlation (Onken et al., 2004; Greene & Ho, 2006). The scaling relations take the form of Equation 5, with λL_λ in units of 10^{44} erg/s and v_{FWHM} in units of 1000 km/s; $A = 6.91$, $B = 0.50$, and $\lambda = 5100\text{\AA}$ for H β ; $A = 6.86$, $B = 0.50$, and $\lambda = 3000\text{\AA}$ for MgII; $A = 6.66$, $B = 0.53$, and $\lambda = 1350\text{\AA}$ for CIV.

$$\log\left(\frac{M_{BH}}{M_\odot}\right) = A + B \log(\lambda L_\lambda) + 2 \log(v_{FWHM}) \quad (5.5)$$

Black hole masses for the Type 1 AGNs with Magellan/IMACS or SDSS spectra in COSMOS are already published in previous work (Trump et al., 2009b), and we repeat the same techniques for Type 1 AGNs with VLT/VIMOS spectra. Briefly, a power-law fit plus iron emission are fit to each AGN. The continuum luminosity is estimated directly from the continuum fit, while the velocity widths are computed from Gaussian fits to the continuum-subtracted emission lines. Some objects also have black hole masses from Merloni et al. (2010); for these objects, our masses are consistent with a random scatter of only ~ 0.4 dex: equivalent to the intrinsic scatter of the scaling relations (see Figure 3.3).

Estimating black hole masses for AGNs without broad emission lines requires secondary estimators. We employ the relationship between M_{BH} and rest-frame K -band host bulge luminosity (Graham, 2007):

$$\log(M_{BH}/M_\odot) = (0.93 \pm 0.15) \log(L_K) - (30.73 \pm 0.11), \quad (5.6)$$

with L_K in units of erg s^{-1} . The $M_{BH} - L_{K,bulge}$ relation comes from the more fundamental $M_{BH} - M_*$ relation, since rest-frame K bulge luminosity is correlated with M_* (e.g., Ilbert et al., 2010). We measure rest-frame L_K from the host galaxy template from the multiwavelength SED fit (described above in §3.1). The early-type

template for the lineless AGNs is, by definition, bulge-dominated, and so $L_{K,bulge} = L_{K,host}$. The S0 template used for the narrow-line AGNs, however, has a significant bulge component, and so we take $L_{K,bulge} = 0.5L_{K,host}$. The intrinsic error in the $M_{BH} - L_K$ is 0.35 dex (Graham, 2007), and we increase this to 0.5 dex for narrow-line AGNs to reflect our uncertainty in the relationship between $L_{K,bulge}$ and the measured $L_{K,host}$.

5.3.3 Error Budget

We estimate errors for each of our specific accretion rates, propagating the errors from both the intrinsic luminosity estimate and the black hole mass estimate. Our intrinsic luminosity is subject to three major uncertainties:

- Photometry errors, σ_{phot} . We measure the error contribution of the photometry by bootstrapping, fitting our model SED to 1000 realizations of randomly drawn photometry values distributed according to the measurement errors. In general, $\sigma_{phot} \sim 0.1$ dex.
- Errors in the host subtraction, σ_{host} . For broad-line AGN, where we do not subtract any host light, the presence of a host means that L_{int} is overestimated and so its associated error is only negative (because the true L_{int} is less than the measured L_{int} which includes host light). For narrow-line and lineless AGN we estimate σ_{host} from the difference in the resultant L_{int} when using a very red (“Ell2”) and a very blue (“Sd”) template from Polletta et al. (2007). Since the accretion disk is fit only at $E > 1$ eV where there is little host emission (even from the “Sd” galaxy), this error is usually insignificant ($\sigma_{host} \lesssim 0.1$ dex).
- Incorrect L_{int} resulting from obscuration, σ_{obsc} . Obscuration will make the true L_{disk} greater than our estimate because optical/UV light will be missed, but will make the true L_X lower than our estimate because the power-law slope

will be steepened. The N_H can be connected to optical extinction as $N_H/A_V \sim 2 \times 10^{-23} \text{ cm}^2$ (Martinez-Sansigre et al., 2006), such that an object with $N_H = 10^{23} \text{ cm}^{-2}$ is obscured in V by 2 magnitudes (a factor of ~ 6). If we assume that the X-ray overestimation is comparable to the optical underestimation, then we can estimate $\sigma_{obsc}/L_{int} = 10^{(0.8 \times 10^{-23} \text{ cm}^2)N_H}$. We discuss the possible effects of obscuration more rigorously in §4.1.

The black hole estimate is subject to two major uncertainties:

- Intrinsic errors in the M_{BH} relations, σ_{rel} . For broad-line AGN, the intrinsic error in the scaling relations is 0.4 dex (Vestergaard & Peterson, 2006), such that $\sigma_{rel} = 2.5 M_{BH}$. For narrow-line and lineless AGN, we use the $M_{BH} - L_{K,host}$ relation, and its associated intrinsic scatter is 0.35 dex (Graham, 2007), such that $\sigma_{rel}/M_{BH} = 2.2$. These errors dominate the error in L_{int}/L_{Edd} , except for obscured AGNs with $N_H > 10^{22.5} \text{ cm}^{-2}$.
- Measurement error in the luminosity used in the scaling relation, σ_{lum} . For broad-line AGN, this is the measured continuum luminosity associated with the appropriate scaling relation, estimated by Trump et al. (2009b) as $\sigma_{lum} \sim 0.05$ dex. Since $M_{BH} \propto L^{0.5}$, $\sigma_{lum} = 1.3 M_{BH}$ for broad-line AGNs. For other AGNs the σ_{lum} comes from our measured $L_{K,rest}$. We estimate this error for the narrow-line and lineless AGNs from 1000 fits to the randomly subsampled data, and find that the error is generally insignificant compared to the intrinsic error ($\sigma_{lum} \sim 0.05$ dex). Note the contribution from error in v_{FWHM} to M_{BH} in broad-line AGNs is also negligible, since for our AGNs $\sigma(v_{FWHM}) < 0.2 v_{FWHM}$ (Trump et al., 2009b).

The total error in specific accretion rate, $\sigma_{\dot{m}}$, is then given by:

$$\frac{\sigma_{\dot{m}}^2}{\dot{m}^2} = \frac{\sigma_{phot}^2 + \sigma_{host}^2 + \sigma_{obsc}^2}{L_{int}^2} + \frac{\sigma_{rel}^2 + \sigma_{lum}^2}{M_{BH}^2} \quad (5.7)$$

The intrinsic error in the M_{BH} relations (σ_{rel}) dominates the error, except for obscured ($N_H > 10^{22.5} \text{ cm}^{-2}$) AGNs. The average errors are ~ 0.5 dex (compared to the 4 dex range in L_{int}/L_{Edd} for the AGN in the sample).

5.4 The Physical Effects of Specific Accretion Rate

The distribution of specific accretion rates for each AGN type is shown in Figure 5.2. It is immediately evident that narrow-line and lineless AGNs accrete much more weakly than broad-line AGNs, with specific accretion rates differing, on average, by ~ 2 orders of magnitude. This suggests that most narrow-line and lineless AGNs are not simply geometrically obscured versions of broad-line AGNs, but that instead have fundamentally different accretion physics which we examine in more detail below. The few narrow-line and lineless AGNs at $L_{int}/L_{Edd} \gtrsim 0.01$, on the other hand, do fit the geometrical-obscuration model quite well, as we additionally show below.

The large ~ 0.5 dex errors in accretion rate artificially broaden the distributions, such that the intrinsic distributions are likely to be narrower than the histograms in Figure 5.2 appear (although many $L_{int}/L_{Edd} \lesssim 10^{-3}$ narrow-line and lineless AGNs could be too faint for the COSMOS X-ray and spectroscopy limits). The $L_{int}/L_{Edd} \gtrsim 0.01$ limit for broad-line AGNs could be partially explained by selection effects, since low accretion rates AGNs are less luminous at all but the highest black hole masses. However at the highest masses ($M_{BH} \gtrsim 10^9 M_\odot$), broad-line AGNs with $L_{int}/L_{Edd} \lesssim 0.01$ must be very rare (Kollmeier et al., 2006; Trump et al., 2009b). We will show in Section 4.1 below that unobscured narrow-line and lineless AGNs are limited by $L_{int}/L_{Edd} \lesssim 0.01$, even if the true accretion rate limit for broad-line AGNs is uncertain due to selection effects.

We can compare the specific accretion rates and AGN types with the physical

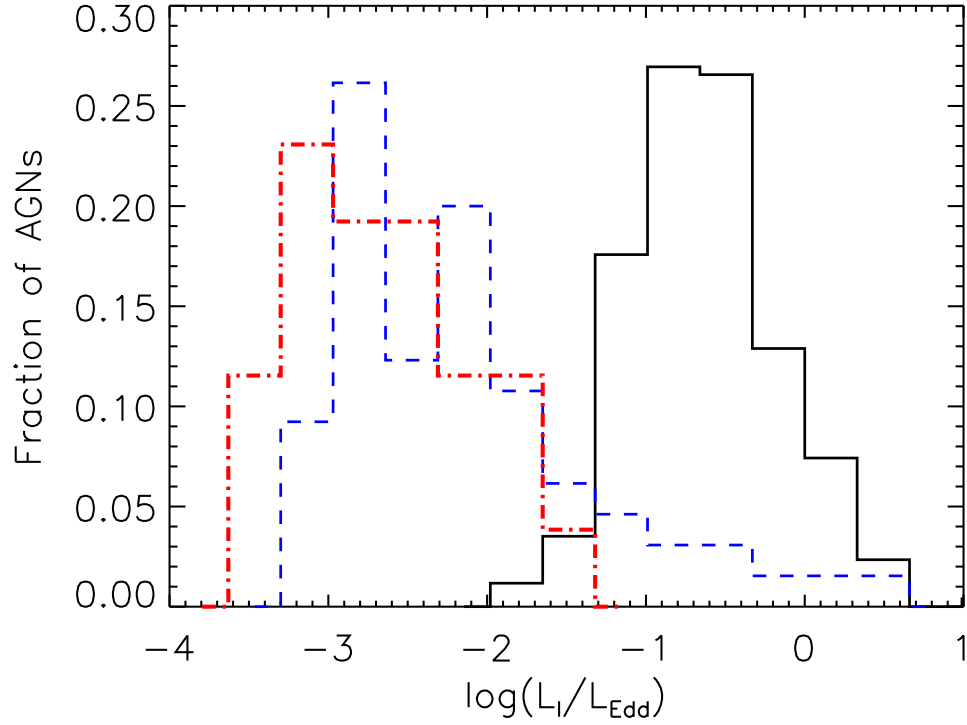


Figure 5.2 The distribution of calculated specific accretion rates (L_{int}/L_{Edd}), for the 256 broad-line AGNs (black histogram), 65 narrow-line AGNs (blue dashed histogram), and 27 lineless AGNs (red dotted histogram). Narrow-line and lineless AGNs have significantly lower accretion rates than broad-line AGNs. The $L_{int}/L_{Edd} \gtrsim 0.01$ limit for broad-line AGNs is not a selection effect (Trump et al., 2009b).

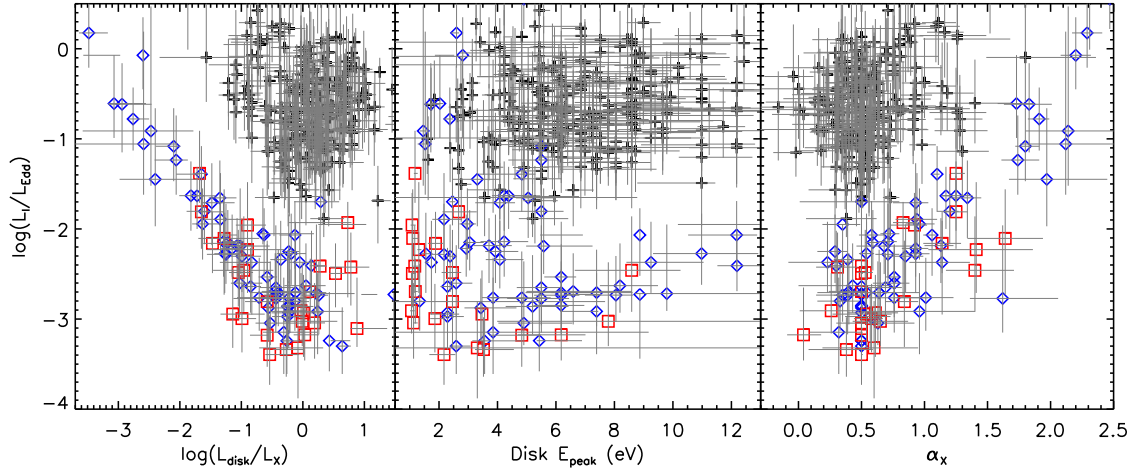


Figure 5.3 Specific accretion rate L_{int}/L_{Edd} and the ratio of disk to corona emission $\log(L_{disk}/L_X)$, disk temperature E_{peak} and X-ray power-law slope α_X for the 348 AGNs. In each panel, black crosses represent broad-line AGNs, blue diamonds are narrow-line AGNs, and red squares are lineless AGNs. The peak energy of the disk increases with accretion rate (and AGN) type, indicating that higher accretion rates are associated with hotter accretion disks. For narrow-line and lineless AGNs, the disk/corona ratio decreases and the X-ray slope increases with increasing accretion rate, probably because more highly accreting narrow-line and lineless AGNs are obscured.

parameters of our model fits, namely the ratio of disk to power-law emission, the peak energy of the accretion disk model, and the X-ray power-law slope. These quantities are particularly useful in unifying AGN in terms of their accretion physics. Figure 5.3 shows the specific accretion rate with these parameters for each AGN type. Once again, narrow-line and lineless AGNs have lower specific accretion rates. Linear regression shows the following correlations associated with the three panels:

$$E_{peak} \sim (L_{int}/L_{Edd})^{0.08 \pm 0.02}, \quad (5.8)$$

$$\log(L_{disk}/L_X) \sim (0.09 \pm 0.06) \log(L_{int}/L_{Edd}), \quad (5.9)$$

$$\alpha_X \sim (0.062 \pm 0.027) \log(L_{int}/L_{Edd}). \quad (5.10)$$

The correlation of E_{peak} with L_{int}/L_{Edd} is the most significant (4.1σ), with an intrinsic scatter of only $0.25\Delta E_{peak}$. The correlation between L_{disk}/L_X and L_{int}/L_{Edd} is only marginally significant (1.5σ) and has a large 0.8 dex scatter, and we show below that this correlation is compromised by a subsample of obscured AGNs. The X-ray power-law slope α_X similarly depends weakly on accretion rate (2.3σ significance) with $0.35\Delta\alpha_X$ scatter, and we show below that this marginal correlation is driven by the fact that higher accretion rate narrow-line and lineless AGNs are obscured (with consequently harder X-ray slopes).

5.4.1 The Role of Obscuration

Obscuration could pose a challenge to our interpretations of accretion rates and other physical properties. The most heavily obscured AGNs (e.g. Compton-thick AGNs with $N_H > 10^{24} \text{ cm}^{-2}$) will be entirely missed by our survey because they would lack detectable X-ray emission. But if an AGN is moderately obscured and still X-ray detected, we might expect its disk to appear cooler because the UV light is preferentially obscured, and its X-ray slope to appear steeper because the soft X-rays are preferentially absorbed. With incorrectly steep X-rays and weak disk

emission, the disk/corona ratio would decrease. The accretion rate, however, might remain accurate since the disk is underestimated and the X-rays are overestimated.

Then the objects most likely to be obscured are those with low disk/corona ratios, low disk temperatures, and high X-ray slopes (in Figure 5.3, at the left, left, and right in panels 1, 2, and 3, respectively). At high accretion rate, we see such a population of narrow-line AGNs. These objects are likely to be obscured Type 1 AGNs, with the broad-line region hidden by obscuring material (as in the model of Antonucci, 1993). We also detect a torus IR signature in most of these obscured candidates, as discussed in Section 5.4.3. The lower accretion rate AGNs, on the other hand, do not have higher X-ray slopes (although they do have lower disk temperatures and slightly lower disk/corona ratios). This suggests that the lower accretion rate AGNs are not obscured, but instead have intrinsically lower disk temperatures.

We estimate N_H for the 153 AGNs (93 broad-line, 38 narrow-line, 22 lineless AGNs) in the sample which have > 40 XMM or Chandra counts. Column density and optical extinction are roughly correlated, with $N_H/A_V \sim 2 \times 10^{-23} \text{ cm}^2$ (Martinez-Sansigre et al., 2006). Then at $N_H < 10^{22} \text{ cm}^{-2}$, optical magnitude should be obscured by $\lesssim 20\%$ ($\lesssim 0.2 \text{ mag}$). Maiolino et al. (2001) shows that the $N_H - A_V$ relation has up to a factor of 30 scatter because of unknown changes in the gas-to-dust ratio, grain size, and/or different physical locations of the optical and X-ray absorbing material. However for all AGNs in the Maiolino et al. (2001) sample with $L_X > 10^{42} \text{ erg s}^{-1}$, $N_H/A_V < 1.8 \times 10^{-22} \text{ cm}^2$, meaning at $N_H \sim 10^{22} \text{ cm}^{-2}$ even the maximum optical extinction is only a factor of 5: much less than the factor of ~ 100 difference we observe in accretion rates. For $N_H \leq 10^{22} \text{ cm}^{-2}$ the simple power-law fit is also typically accurate (e.g. Mainieri et al., 2007)

Figure 5.4 shows the accretion rates with disk/corona ratio, disk temperature,

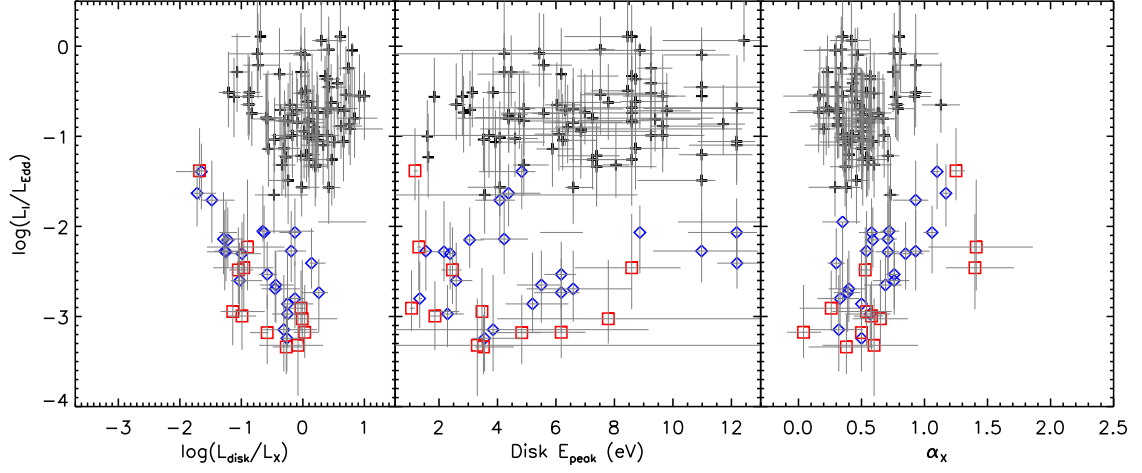


Figure 5.4 Specific accretion rate (L_{int}/L_{Edd}) and the ratio of disk to corona emission ($\log(L_{disk}/L_X)$), disk temperature (E_{peak}), and X-ray power-law slope (α_X) for unobscured AGNs with $N_H < 10^{22} \text{ cm}^{-2}$. This figure is very similar to Figure 5.3, although many obscured AGNs with low L_{disk}/L_X and steep α_X are absent. In each panel, black crosses represent broad-line AGNs, blue diamonds are narrow-line AGNs, and red squares are lineless AGNs. Once again, the disk peak energy and the disk/corona ratio increase with increasing accretion rate.

and X-ray slope for the 118 unobscured AGNs with $N_H < 10^{22} \text{ cm}^{-2}$ (82 broad-line, 24 narrow-line, and 12 lineless AGNs). The plots are quite similar to those of Figure 5.3, minus several of the low L_{disk}/L_X and steep α_X AGNs.

Unobscured narrow-line and lineless AGNs are generally limited by $L_{int}/L_{Edd} \lesssim 0.01$. With low X-ray column densities and low accretion rates, these objects have similar properties to the “naked” Type 2 AGNs of Tran (2003), which additionally lack reflected broad emission lines in spectropolarimetry (see also Gliozzi et al., 2007; Wang & Zhang, 2007). We expect that the X-ray unobscured low accretion rate AGNs would similarly lack reflected broad emission lines. For the set of unobscured

AGNs we find the trends shown in the linear regression fits below:

$$E_{peak} \sim (L_{int}/L_{Edd})^{0.09 \pm 0.01}, \quad (5.11)$$

$$\log(L_{disk}/L_X) \sim (0.30 \pm 0.08) \log(L_{int}/L_{Edd}), \quad (5.12)$$

$$\alpha_X \sim (-0.04 \pm 0.03) \log(L_{int}/L_{Edd}). \quad (5.13)$$

The correlation of E_{peak} with L_{int}/L_{Edd} is very similar to Equation 8, with slightly lower significance (3.4σ) likely due to the fewer objects used in calculating the correlation. For unobscured AGNs, the correlation of L_{disk}/L_X and L_{int}/L_{Edd} is highly significant (3.9σ), with 0.5 dex scatter. Higher accretion rate AGNs tend to have more emission from the accretion disk than the X-ray corona, and the lack of correlation in Equation 9 above was caused by obscured narrow-line AGNs with high accretion rates. The anti-correlation between X-ray power-law slope α_X and accretion rate is not significant for unobscured AGNs.

Hopkins et al. (2009) suggest that steep X-ray slopes may correspond not to increased absorption, but instead to intrinsically different X-ray emission associated with the radiatively inefficient accretion flow (RIAF) at low accretion rates. We present X-ray slopes α_X with column density N_H in Figure 5.5. We do not find evidence for a large population of unabsorbed weakly accreting AGNs with intrinsically steep X-ray slopes: instead the AGNs with steep X-ray slopes seem to be genuinely absorbed. The appearance of a RIAF at inner radii will tend to produce more X-ray emission, as we show in Equation 12 below, but this emission probably has a similar power-law slope as the X-ray corona present in broad-line AGNs with high accretion rates. This is unsurprising, since both the RIAF and the corona are thought to be ionized plasmas with X-ray emission from bremsstrahlung. We can conclude that the onset of a RIAF in unobscured narrow-line and lineless AGNs with accretion rates of $10^{-4} < L_{int}/L_{Edd} < 10^{-2}$ do not cause steeper X-ray power-law slopes.

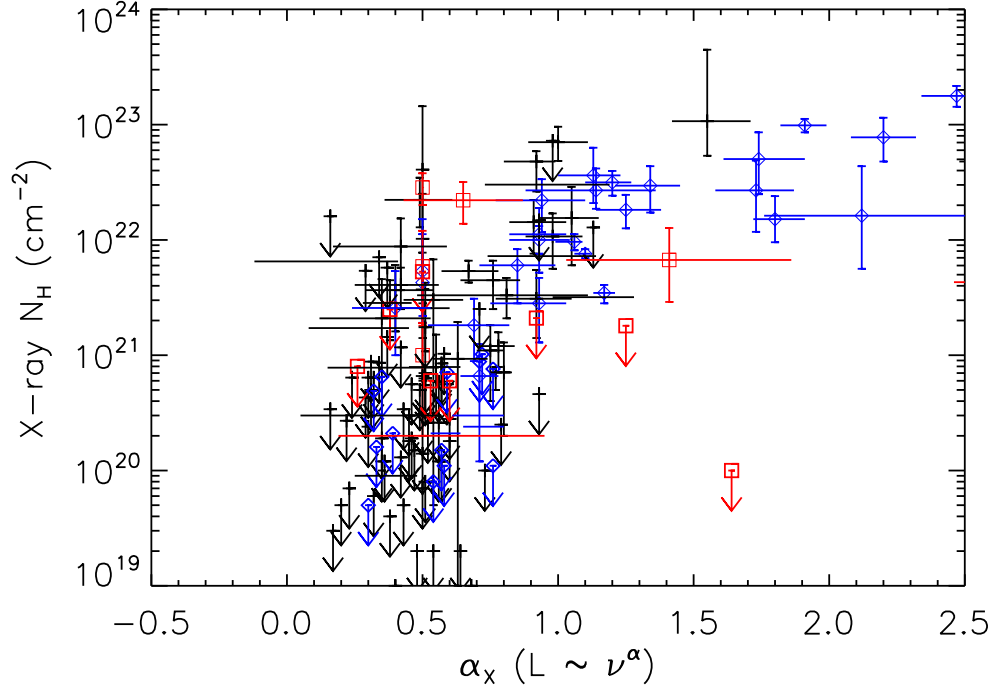


Figure 5.5 The column density N_H with the X-ray slope from our model fits, with α_X defined by $L \propto \nu^{\alpha_X}$ (as typically written, the photon index $\Gamma_X = 2 - \alpha_X$ with $L_\nu \propto \nu^{1-\Gamma_X}$). Black crosses show broad-line AGNs, blue diamonds show narrow-line AGNs, and red squares show lineless (optically dull) AGNs. We do not find evidence for a large population of unobscured AGNs with steep X-ray slopes, as suggested by Hopkins et al. (2009).

5.4.2 Physics of the Accretion Disk

The correlation of peak disk energy and accretion rate means that as accretion rate increases from lineless to narrow-line to broad-line AGNs, the temperature of the disk increases. The Gierliński et al. (1999) disk model predicts that $T_{max} \propto \dot{m}^{1/4}$, while from linear regression we find $E_{peak} \sim (L_{int}/L_{Edd})^{0.09}$ (Equations 8 and 11). While part of the observed correlation probably comes from the physics in the Gierliński et al. (1999) disk model, we discuss below how the onset of a radiatively inefficient accretion flow causes the correlation to flatten further than the expected value. Both the correlation between temperature and accretion rate and the correlation of L_{disk}/L_X with accretion rates (Equation 12) contribute to the observed increase of α_{OX} (the ratio of rest-frame UV to X-ray emission) with accretion rate (Kelly et al., 2008). In Chapter 4, we suggested that the increase of α_{OX} with accretion rate was due only to the disk luminosity decreasing with respect to the corona luminosity. While this is partly correct, the correlation is also caused by increasing disk temperatures at higher accretion rates.

AGNs with $\dot{m} \lesssim 0.01$ are predicted to have radiatively inefficient accretion flows (RIAFs) near the central black hole (Narayan et al., 1995; Yuan, 2007; Narayan & McClintock, 2008). At such accretion rates, we can define a truncation radius R_t where the collisional cooling time is comparable to the accretion time. Beyond R_t , accretion will remain in a standard geometrically thin and optically thick disk with a thermal blackbody spectrum (e.g., Shakura & Sunyaev, 1973). However within R_t , there are too few collisions to couple the ions and electrons and the gas becomes a two-temperature plasma. The electrons are cooled by bremsstrahlung, synchrotron, and Compton up-scattering, while the ions remain at the virial temperature. This means the flow is geometrically thick and optically thin. The introduction of a truncation radius changes the $R_{in} = 6R_g$ assumption for the accretion disk model,

since by definition $R_{in} \geq R_t$. The peak energy of the best-fit accretion disk model is not very sensitive to the choice of R_{in} , although larger inner radii change the shape of the model with additional red emission. At accretion rates $L_{int}/L_{Edd} \gtrsim 10^{-3}$, as in our sample, $R_t \sim 40R_g$ (Yuan & Narayan, 2004). Using $r_{in} = 40$ in the accretion disk model fitting in Section 5.3.1 doesn't change the best-fit values of E_{peak} , although it does result in somewhat better fits.

The correlation of L_{disk}/L_X and L_{int}/L_{Edd} (Equation 12 and the left panel of Figure 5.4) is likely caused by the onset of the RIAF. As R_t expands outwards, the disk emission decreases and the RIAF emission increases. The RIAF hot plasma emission is mostly X-ray bremsstrahlung and Compton up-scattering (like the corona), with an additional IR synchrotron component (which we discuss in Sections 5.4.4). As accretion rate drops and R_t increases, the rise of the RIAF X-ray emission compared to the optical/UV disk emission is seen as a decrease of L_{disk}/L_X . Indeed, local low-luminosity AGNs have even lower accretion rates and larger R_t , with consequently lower L_{disk}/L_X ratios and cooler optical thin-disk emission (Ho, 2008).

The transition to an inner RIAF also causes the disappearance of broad emission lines at $L_{int}/L_{Edd} \lesssim 0.01$. Nicastro (2000) was the first to elegantly show that the broad emission lines are only present above a critical accretion rate. However Nicastro (2000) assumed that the innermost possible orbit was given by the Shakura & Sunyaev (1973) thin-disk model, $r_{crit} \simeq 8.16R_g$. Here we follow their basic derivation, with the key difference that we use the RIAF transition radius as the innermost orbit for the presence of a broad-line region. We use a $R_t \sim 40R_g$ as an approximate RIAF transition radius, a value typical of the best-fit RIAF models for $L_{int}/L_{Edd} \sim 10^{-3} - 10^{-2}$ AGNs (Yuan & Narayan, 2004).

There is evidence that the broad emission line region is part of a disk wind (e.g.

Emmering et al., 1992; Murray & Chiang, 1998; Elvis, 2000; Elitzur & Shlosman, 2006). The positions of individual broad emission lines are stratified and set by the ionizing luminosity of continuum (e.g. Peterson & Bentz, 2006; Denney et al., 2009). The base of the wind itself, however, is set by the radius at which the radiation pressure equals the gas pressure, defined by Shakura & Sunyaev (1973) as:

$$\frac{r_{wind}}{(1 - r_{wind}^{-0.5})^{16/21}} \simeq 15.2(\alpha M)^{2/21} \left(\frac{\dot{m}}{\eta} \right)^{16/21}, \quad (5.14)$$

with r_{wind} is in units of $R/(6R_g) = R/(6GM/c^2)$, M in units of M_{BH}/M_\odot , $\dot{m} = L_{int}/L_{Edd}$, α is the viscosity parameter, and η is the accretion efficiency. While RIAFs are expected to have strong outflows (see Section 5.4.3), the RIAF region is a high-temperature ionized plasma and so any associated disk wind would not emit broad emission lines in the UV/optical. Thus the RIAF truncation radius sets the innermost possible radius for the existence of a broad-line region. Rearranging Equation 8 with $R_t \simeq 40R_g$, $\alpha \simeq 0.1$, and $\eta \simeq 0.15$, this sets the minimum specific accretion rate for a broad line region as:

$$\dot{m} \gtrsim 0.011 M_8^{-1/8}, \quad (5.15)$$

with $M_8 = M_{BH}/(10^8 M_\odot)$. As an AGN drops below this minimum accretion rate, its broad lines disappear and only narrow lines (or no lines) are observed, as seen in the transition at $\log(L_{int}/L_{Edd}) \sim -2$ transition in Figures 5.2, 5.3, and 5.4.

Elitzur & Ho (2009) also predict that the disk wind associated with the BLR will disappear below an accretion rate at which the outflowing velocity drops below the random velocity of the disk. Elitzur & Ho (2009) measure a BLR-disappearance accretion rate of $\log(L/L_{Edd}) < C + \beta \log(L_{bol})$ from the low-luminosity local AGNs of Ho (2009), with $\beta = -0.5$ and $C = 14.4$. In this sample and in Chapter 3 (as well as in work by Kollmeier et al., 2006; Trump et al., 2009b), the BLR disappears at $\log(L/L_{Edd}) < 0.01$. For a typical bolometric luminosity of $L_{int} \sim 10^{44.5} \text{ erg s}^{-1}$

(also appropriate for the Kollmeier et al., 2006, sample), and assuming the same $\beta = -0.5$, this instead corresponds to $C = 20.3$: a remarkable difference of 6 orders of magnitude. It is unlikely that the bolometric corrections of Ho (2009) are incorrect by 6 orders of magnitude, and so we must conclude that the Elitzur & Ho (2009) model does not describe the disappearance of the BLR for high luminosity AGNs. Instead a disk-wind model following Nicastro (2000) best describes the BLR disappearance as the radius of wind generation region moves within the inner RIAF region.

5.4.3 Accretion Rate and Outflows

The gas in a RIAF is not gravitationally bound to the supermassive black hole because the ions are not losing energy through radiation. As a result, AGNs with RIAFs are predicted to have strong radio outflows (Narayan et al., 1995; Meier, 2001). The coupling between a RIAF and a strong radio outflow has been confirmed by observations of black hole binaries (Fender & Belloni, 2004), and it is possible to translate these observations to AGN scales (e.g. Maccarone et al., 2003). In Figure 5.6 we show the AGNs of our sample with the ratio of radio luminosity to disk luminosity. The $L_{int}/L_{Edd} < 10^{-2}$ AGNs which are expected to have RIAFs also tend to be more radio-loud. Linear regression reveals an anti-correlation between L_{disk}/L_{radio} and L_{int}/L_{Edd} , as $\log(L_{disk}/L_{radio}) \sim (-0.54 \pm 0.04) \log(L_{int}/L_{Edd})$ (14σ significance) with 0.5 dex scatter in the relation.

The large scatter in the correlation between accretion rate and radio-loudness is likely because the radio power is additionally dependent on properties like black hole spin and orientation. But the high significance in the correlation confirms that $L_{int}/L_{Edd} < 10^{-2}$ AGNs with RIAFs tend to have stronger radio jets. Melendez et al. (2010) noticed a similar trend of increasing radio luminosity with increasing accretion rate, using [OIV] as a proxy for intrinsic luminosity (e.g., Melendez et al.,

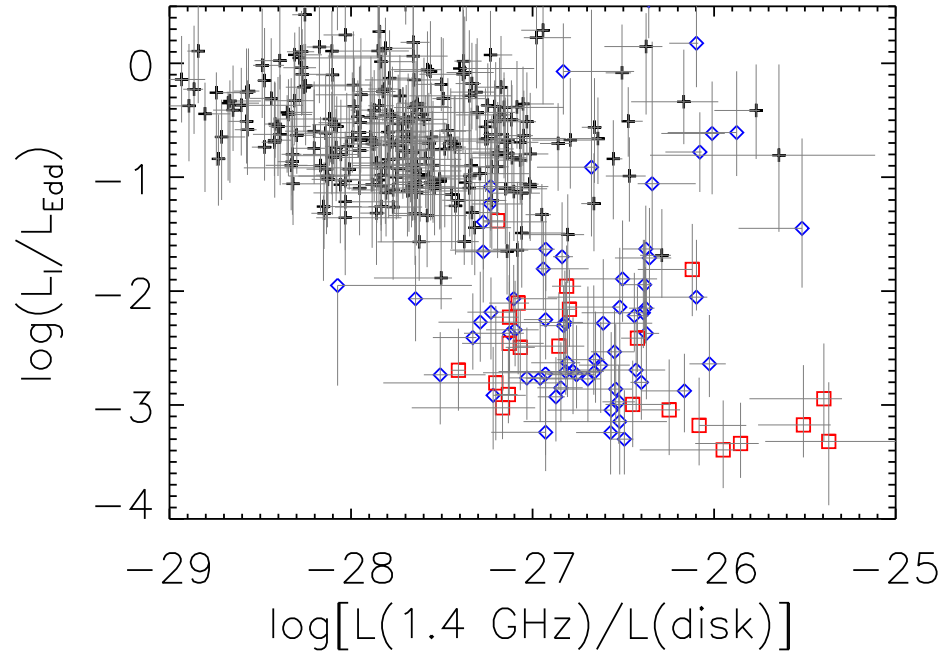


Figure 5.6 Accretion rate with a measure of radio-loudness: the ratio of radio luminosity to disk luminosity for the AGNs in our sample. Broad-line AGNs are shown by black crosses, narrow-line AGNs by blue diamonds, and lineless AGNs by red squares. Narrow-line and lineless AGNs, at lower accretion rates than broad-line AGNs, tend to be more radio-loud.

2008; Diamond-Stanic et al., 2009).

In general, the radiation and disk winds of AGNs are thought to cause feedback on galaxy scales by quenching star formation (e.g., Hopkins et al., 2006; Hopkins & Elvis, 2010), while radio jets are thought to cause larger-scale feedback which can heat the cores of galaxy clusters (e.g., ?) and is observed as extended emission line regions (Fu & Stockton, 2009). The fact that RIAFs tend to have stronger radio outflows suggests that weakly accreting AGNs may actually be more important for this large-scale radio-mode feedback than highly accreting broad-line AGNs. This suggests that heating cluster cores may not require bright quasars, but can be accomplished by faint AGNs, in agreement with ?.

5.4.4 Accretion Rate and the IR “Torus”

A clumpy dust “torus” emits a unique power-law signature in the mid-IR from $\sim 1\text{--}10\mu\text{m}$ (Nenkova et al., 2008). This was first noticed observationally as a distinct AGN locus in Spitzer/IRAC color-color space (Lacy et al., 2004; Stern et al., 2005), although Donley et al. (2007) show that power-law selection is the most effective way to select AGN in the mid-IR. We compute the IR power-law slope in our AGNs from the observed IRAC photometry within the rest-frame wavelength range $1 < \lambda < 10\mu\text{m}$, shown with accretion rate in Figure 5.7. Type 1 AGNs typically have $\alpha_{IR} < 0.5$ ($\beta_{IR} < -0.5$ in terms of the $f_\lambda \sim \lambda^\beta$ form used by Donley et al., 2007), matching the predictions of clumpy dust models (Nenkova et al., 2008). However the torus signature is present in only about half of narrow-line AGNs (2/3 of those with $L_{int}/L_{Edd} > 0.01$) and none of the lineless AGNs. Linear regression analysis reveals that the anti-correlation of specific accretion rate and the IR power-law slope is marginally significant at best, with $\alpha_{IR} \sim (-0.007 \pm 0.006) \log(L_{int}/L_{Edd})$ (1.1σ significant).

A unified model based on geometrical obscuration suggests that narrow-line

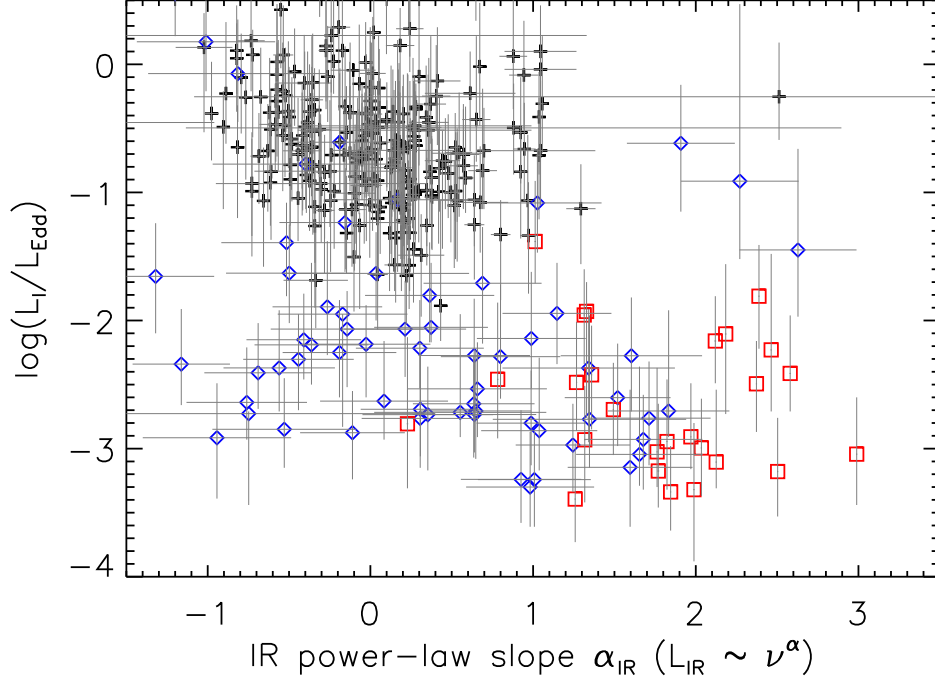


Figure 5.7 Accretion rate with the power-law slope of the $1 < \lambda < 10\mu\text{m}$ IR emission. We measure the slope α_{IR} as $L \sim \lambda^\alpha$, corresponding to the slope β used in the power-law selection of Donley et al. (2007) as $\beta = \alpha_{IR} - 1$. High accretion rate ($L_{int}/L_{Edd} > 0.01$) AGNs, including a 2/3 of narrow-line AGNs, have IR power-law slopes corresponding to a dusty torus ($\alpha_{IR} < 0.5$). Of $L_{int}/L_{Edd} < 0.01$ AGNs, however, half the narrow-line and all but one of the lineless AGNs lack the torus signature.

and lineless AGNs are obscured by the same torus present in broad-line AGNs (e.g., Antonucci, 1993). This describes the majority of the high-accretion rate ($L_{int}/L_{Edd} > 0.01$) AGNs, and so we again conclude that narrow-line AGNs with $L_{int}/L_{Edd} > 0.01$ (which also have high N_H as shown in Section 5.4.1) are likely to be “true” Type 1 AGNs with the broad emission lines obscured along the line of sight. On the other hand the low accretion rate AGNs ($L_{int}/L_{Edd} < 0.01$) tend to lack the torus IR signature. In part, this may be because the torus power-law is simply being overwhelmed by the accretion disk SED at $L_{int}/L_{Edd} < 0.01$. At low accretion rates, the temperature of the disk decreases, and a disk with $E_{peak} = 1$ eV will peak at $1.2 \mu\text{m}$, emitting a power-law of $\alpha \sim 2$ at $1 < \lambda < 10 \mu\text{m}$. In a typical broad-line AGN, the IR torus is roughly the same strength as the accretion disk (Richards et al., 2006, , see also Figure 5.1). However many $L_{int}/L_{Edd} < 0.01$ AGNs in Figure 5.7 have $\alpha \gtrsim 2$, suggesting they are dominated by the accretion disk emission and they have, at best, very little emission from the torus.

The weaker or missing torus in many $L_{int}/L_{Edd} < 0.01$ AGNs can be described in a similar fashion to the vanishing disk-wind BLR in Section 5.4.2. There is good evidence that the outer edge of the BLR coincides with the inner edge of the clumpy dust (Netzer & Laor, 1993; Suganuma et al., 2006). Some authors additionally suggest that the BLR and the clumpy dust “torus” are two components of the same wind driven off the accretion disk (e.g., Elitzur & Shlosman, 2006). If the clumpy dust wind emerges from the disk at a similar radius to that calculated in Section 5.4.2, then we would expect the IR power-law signature to disappear at $L_{int}/L_{Edd} < 0.01$, just as the BLR disappears. However many narrow-line AGNs with $L_{int}/L_{Edd} < 0.01$ still have the negative IR power-law slopes, suggesting that there must be another source of mid-IR emission. Either there is a distant source of clumpy dust beyond the expanding RIAF, or there is mid-IR synchrotron emission

in the RIAF region at the base of the radio jet.

5.5 A Simple Model for Unifying AGNs by Specific Accretion Rate

Figure 5.8 presents a simple schematic outlining the changes in AGNs from high ($L_{int}/L_{Edd} > 0.01$) to low ($L_{int}/L_{Edd} < 0.01$) accretion rate. At the top is a broad-line AGN with high accretion rate ($L_{int}/L_{Edd} \sim 0.1$). At these high accretion rates the gas and dust falling into the black hole forms a thin accretion disk and a disk wind originates at $R_{wind} \sim 250R_g$. The broad emission lines are emitted in stratified regions along this wind based on the radiation pressure (which ionizes and excites the wind material), with $R_{BLR} \sim L^{0.5}$ and high ionization lines (e.g., C IV) emitted from nearer radii than low ionization lines (e.g., H β) (Peterson & Bentz, 2006). At higher radii, the disk wind forms clumpy dust (Nenkova et al., 2008). This dusty “torus” can obscure the AGN along lines of sight near the disk, causing an observer to see an obscured narrow-line AGN (Antonucci, 1993).

The bottom of Figure 5.8 shows an AGN with low accretion rate ($L_{int}/L_{Edd} \sim 0.003$), characteristic of the unobscured narrow-line and lineless AGNs in our sample. The onset of a geometrically thick RIAF changes the picture dramatically. Because the disk wind radius is within the RIAF, there are no broad emission lines. Instead the dominant outflow is a radio jet, and AGNs with low accretion rates and RIAFs are typically more radio-loud than broad-line AGNs. The lack of a disk wind also means that there is not the typical clumpy dust “torus” seen in broad-line AGNs. However we cannot rule out the presence of dust completely, as clumpy dust may come from another source besides the disk wind and some $L_{int}/L_{Edd} \lesssim 0.01$ have the IR signature of hot dust.

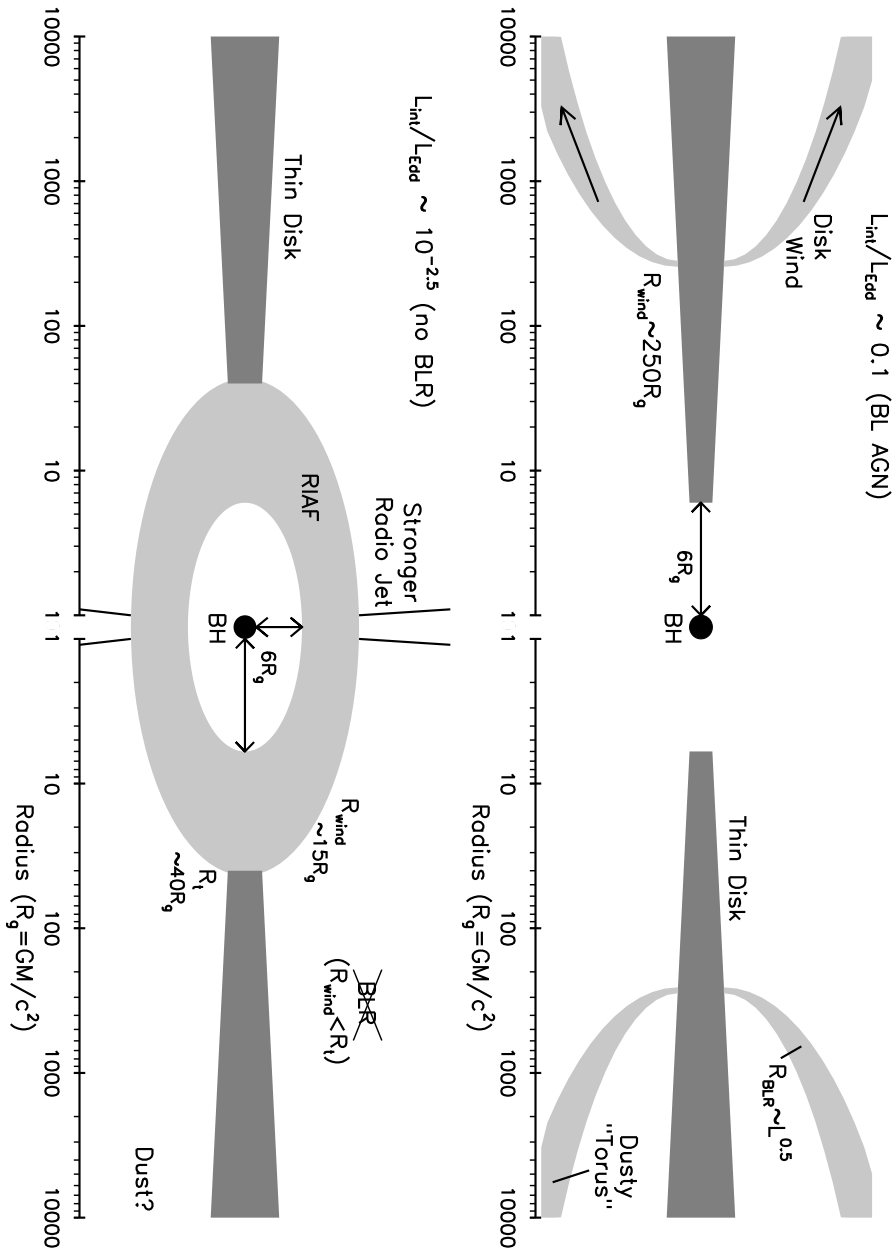


Figure 5.8 A schematic model showing the changes in the accretion disk from a broad-line AGN with high accretion rate ($L_{int}/L_{Edd} \sim 0.1$) to a narrow-line or lineless AGN with low accretion rate ($L_{int}/L_{Edd} \sim 0.003$). The x axis shows the radial distance from the black hole in units of GM/c^2 . The y axis is qualitative only. At $L_{int}/L_{Edd} \lesssim 0.01$, the disk wind falls inside the RIAF. As a result there are no broad emission lines, the hot dust signature becomes very different, and the radio jet becomes stronger.

5.6 Predictions and Future Observational Tests

The multiwavelength data of COSMOS provides many diagnostic capabilities, and we have argued that decreasing accretion rates lead to the onset of a RIAF at $\dot{m} < 0.01$ and subsequently stronger radio jets, a weaker torus, and the disappearance of broad emission lines. The onset of a RIAF also makes several predictions testable by future observations. In addition the simple model in Section 5.5 can be more fully constrained by additional investigations.

If the broad-line region is truly disappearing at $\dot{m} < 0.01$ then we would expect spectropolarimetry to reveal reflected broad emission lines in high accretion rate ($\dot{m} > 0.01$) narrow-line and lineless AGNs. Spectropolarimetry of nearby AGNs shows a dichotomy based on accretion rate, although most authors place the change from hidden broad lines to “true” Type 2 AGN at $\dot{m} \sim 0.001$ (Tran, 2003; Wang & Zhang, 2007). Most likely, the difference results from the uncertain bolometric corrections used in these previous works, compared to the full modeled SEDs used here. In March 2010 we observed a few AGNs from this sample, with results to follow in future work.

Mid-IR broad-band polarimetry could determine the cause of the negative IR power-law slopes in $\dot{m} < 0.01$ AGNs. If the clumpy dust “torus” is associated with the same wind that drives the broad line region, it should disappear in these objects. The mid-IR signature might instead be synchrotron radiation in the RIAF at the base of the jet, which would appear polarized at the $> 3\%$ level (e.g., Jannuzi et al., 1994). If no polarization is detected, then we must conclude that clumpy dust exists at higher radii than the BLR disk-wind, beyond the RIAF region of $\dot{m} < 0.01$ AGNs.

It is very difficult to measure accretion rates of obscured AGNs, and such objects are generally missed by the X-ray and optical limits of this study. However we do

make a few predictions for the accretion rates of various AGNs. If the torus is part of a disk-wind that vanishes at $\dot{m} < 0.01$, then torus-obscured AGNs of the classical Antonucci (1993) unified model will have only high accretion rates ($\dot{m} > 0.01$). Obscuration by cooler dust associated with host galaxy star formation, as predicted by the observed redshift evolution in the narrow-line/broad-line AGN ratio (Chapter 2, and also Treister et al., 2009; Trump et al., 2009a), could conceivably be present at any accretion rate (although it may be limited by the ability of the dusty star formation to feed the black hole, Ballantyne, 2008). We might then expect that obscured AGNs with a strong mid-IR torus signature should have $\dot{m} > 0.01$, while AGNs obscured by the cooler dust associated with host galaxy star formation might have a wider range of accretion rates.

CHAPTER 6

CONCLUSIONS, PREDICTIONS, AND FUTURE OBSERVATIONS

Taken together, my work in the Cosmic Evolution Survey demonstrates that AGNs can be described by a unified model based on accretion rate. The physics driving this model are best summarized by Figure 5.8. At low accretion rates, the standard thin accretion disk becomes a radiatively inefficient accretion flow near the black hole, causing the broad emission lines to disappear, the radio jet to become stronger, and the obscuring “torus” changes or disappears. The lack of broad lines in most narrow-line (Type 2) and lineless (optically dull) AGNs in COSMOS is not caused by obscuration, as historical AGN unification would suggest, but by the different accretion physics at their low accretion rates. Only high accretion rate narrow-line AGNs show evidence of obscuration, and these objects are likely to be “true” Type 1 AGNs with the broad emission lines hidden by obscuring material. We highlight several predictions of this model in Section 5.6, and note a few additional observational tests here.

In Chapter 2 we find tentative evidence that narrow-line and lineless AGNs are preferentially fed by material associated with star formation, in the increase of narrow-line and lineless AGNs with redshift compared to broad-line AGNs. As Chapter 5 showed, nearly all of these narrow-line and lineless AGNs have low accretion rates. Models predict that high accretion rate (Type 1) AGNs require mergers (Hopkins et al., 2006), while low accretion rate (Type 2 and optically dull) AGNs might be fed by star formation in galactic disks or bulges (Ballantyne, 2008; Hopkins & Hernquist, 2006). Our tentative evidence can be easily tested by studying the environments and host morphologies of AGNs at different accretion rate. If low accretion rate AGNs tend to occupy disk galaxies in the field, then our interpretation

(and the model predictions) are correct. Likewise we would expect high accretion rate (both Type 1 and obscured Type 2) AGNs to lie in merger-rich environments and show tidal features in their host morphologies. While there have been studies of AGN environments and searches for host galaxy merger signatures, there have been no studies comparing AGNs across different accretion rates.

The largest error in our accretion rate estimates comes from the intrinsic ~ 0.4 dex error in the black hole mass relations, and so reducing this error significantly refines our analyses based on accretion rate (especially in better constraining the $\dot{m} \equiv \dot{m}_{crit} \sim 0.01$ boundary for the appearance of a RIAF and the disappearance of the broad emission lines). More accurate masses for broad-line AGN can be achieved using reverberation mapping, which directly measures the broad-line region size using the time lag between variability in the continuum and a broad emission line. I'm currently leading a COSMOS AGN reverberation mapping campaign on MMT/Hectospec, and we anticipate masses accurate to ~ 0.2 dex for > 30 Type 1 AGNs. More accurate masses for narrow-line and lineless AGNs are available in local objects, for which dynamical estimators can be used. Because local low-luminosity AGNs also tend to be smaller, they can additionally be used to test the $M_{BH}^{1/8}$ dependence expected in \dot{m}_{crit} .

It is worth highlighting again that X-ray selection, like that used here for our COSMOS AGN sample, is not efficient at selecting obscured AGNs. As mentioned in Section 5.6, the AGN schematic of Figure 5.8 does not include a description for obscured sources. Infrared selection (by Spitzer/IRAC or even future Herschel observations) could build a sample of obscured AGNs, for which we could measure accretion rates using the SED fitting of Chapter 5 along with a treatment for reddening and X-ray absorption. We could then learn where such objects fit in the paradigm of Figure 5.8, and additionally learn if their obscuration comes from local

accretion physics or from a process in the host galaxy.

With these predictions, I conclude the thesis. It is my hope that I've graduated and you've learned something. The model for AGN unification culminating in Figure 5.8 is quite ambitious, but it is well-supported by current observational evidence and makes several testable predictions for future observations. The study of AGN physics remains very young in the long history of astronomy, and no doubt the future will bring refinements and new advances in our understanding of these strange phenomena.

REFERENCES

- Abraham, R. G. et al. 2004, AJ, 127, 2455
- Adelman-McCarthy, J.K. et al. 2008, ApJS, 175, 297-313
- Akylas, A., Georgantopoulos, I., Georgakakis, A., Kitsionas, S., & Hatziminaoglou, E. 2006, A&A, 459, 693
- Alexander, D. M. et al. 2001, AJ, 122, 2156
- Alexander, D. M. et al. 2003, ApJ, 126, 539
- Antonucci, R. 1993, ARA&A, 31, 473
- Babic, A. et al. 2007, A&A, 474, 755
- Baldwin, J. A., Phillips, M. M., & Terlevich, R. 1981, PASP, 93
- Ballantyne, D. R., Everett, J. E., & Murray, N. 2006, ApJ, 639, 740
- Ballantyne, D. R. & Papovich, C. 2007, ApJ, 660, 988
- Ballantyne, D. R. 2008, ApJ, 685, 787
- Barger, A. J. et al. 2003, AJ, 126, 632
- Barger, A. J., Cowie, L. L., Mushotzky, R. F., Yang, Y., Wang, W.-H., Steffen, A. T., Capak, P. et al. 2005, AJ, 129, 578
- Barth, A. J., Filippenko, A. V. & Moran, E. C. 1999, ApJ, 525, 673
- Bauer, F. E. , Alexander, D. M., Brandt, W. N., Schneider, D. P., Treister, E., Hornschemeier, A. E., & Garmire, G. P. 2004, AJ, 128, 2048

- Bentz, M. C., Peterson, B. M., Pogge, R. W., Vestergaard, M., & Onken, 2006, C. A. ApJ, 644, 133
- Bentz, M. C., Peterson, B. M., Pogge, R. W., & Vestergaard, M. 2008, ApJ, 694, 166
- Bertin, E. & Arnouts, S. 1996, A&A, 117, 393
- Bianchi, S. et al. 2008, MNRAS, 385, 195
- Bigelow, B. C., Dressler, A. M., Shectman, S. A., & Epps, H. W. 1998, in Proc. SPIE Vol. 3355, 225, Optical Astronomical Instrumentation, Sandro D’Odorico; Ed.
- Bongiorno, A. et al. 2007, A&A, 472, 443.
- Brand, K. et al. 2006, ApJ, 641, 140
- Brandt, W. N., Laor, A., & Wills, B. J. 2000, ApJ, 528, 637
- Brandt, W. N. & Hasinger, G. 2005, ARA&A, 43, 827
- Brusa, M. et al. 2007, ApJS, 172, 353
- Brusa, M. et al. 2010 in prep.
- Bruzual, G. & Charlot, S. 2003, MNRAS, 344, 1000
- Bundy, K. et al. 2008, ApJ, 681, 931
- Caccianiga, A., Severgnini, P., Della Ceca, R., Maccacaro, T., Carrera, F. J., & Page, M. J. 2007, A&A, 470, 557
- Capak, P. et al. 2007, ApJS, 172, .99

- Capak, P. et al. 2010, in prep.
- Cappelluti, N. et al. 2007, ApJS, 172, 341
- Cappelluti, N. et al. 2009, A&A, 497, 635
- Cash, W. 1979, ApJ 228, 939
- Chartas, G. et al. 2007, AJ, 133, 1849
- Civano, F. et al. 2007, A&A, 476, 1223
- Cocchia, F. et al. 2007, A&A, 466, 31
- Colbert, E. J. M., Heckman, T. M., Ptak, A. F., Strickland, D. K., & Weaver, K. A. 2004, ApJ, 602, 231
- Collin, S., Kawaguchi, T., Peterson, B. M. & Vestergaard, M. 2006, A&A, 456, 75
- Comastri, A. et al. 2002, ApJ, 571, 771
- Comastri, A., Brusa, M., & Mignoli, M. 2003, AN, 324, 28
- Croom, S. M., Smith, R. J., Boyle, B. J., Shanks, T., Loaring, N. S., Miller, L., & Lewis, I. J. 2001, MNRAS, 322, 29
- Croton, D. J. et al. 2006, MNRAS, 365, 11
- Daddi, E. et al. 2007, ApJ, 670, 173
- Davies, R. I. et al. 2006, ApJ, 646, 754
- Davis, M. et al. 2007, ApJ, 660, 1
- Denney, K. D. et al. 2009, ApJ, 704, 80

- Di Matteo, T., Springel, V., & Hernquist, L. 2005, *Nature*, 433, 604
- Diamond-Stanic, A. M., Rieke, G. H. & Rigby, J. R. 2009, *ApJ*, 698, 623
- Dietrich, M. & Hamann, F. 2004, *ApJ*, 611, 761
- Donley, J. L., Rieke, G. H., Prez-Gonzalez, P. G., Rigby, J. R., & Alonso-Herrero, A. 2007, *ApJ*, 660, 167
- Eckart, M. E., Stern, D., Helfand, D. J., Harrison, F. A., Mao, P. H., & Yost, S. A. 2006, *ApJ*, 165, 19
- Eisenstein, D. J. et al. 2001, *AJ*, 122, 2267
- Elitzur, M., & Shlosman, I. 2006, *ApJ*, 648, L101
- Elitzur, M. 2008, *NewAR*, 52, 274
- Elitzur, M. & Ho, L. C. 2009, *ApJL*, 701, 91
- Elvis, M., Schreier, E. J., Tonry, J., Davis, M., & Huchra, J. P. *ApJ*, 246, 20
- Elvis, M. 2000, *ApJ*, 545, 63
- Elvis, M., Risaliti, G. & Zamorani, G. 2002, *ApJ*, 565, 75
- Elvis, M. et al. 2009, *ApJS*, 184, 158
- Emmering, R. T., Blandford, R. D. & Shlosman, I. 1992, *ApJ*, 385, 460
- Eracleous, M., Hwang, J. A. & Flohic, H. M. 2010, *ApJ*, 711, 796
- Fabbiano, G. 1989, *ARA&A*, 27, 87
- Fabricant, D. et al. 2005, *PASP*, 117, 1411

- Fender, R. & Belloni, T. 2004, ARA&A, 42, 317
- Ferrarese, L. & Merritt, D. 2000, ApJ, 593, 9
- Fine, S. et al. 2008, MNRAS, 390, 1413
- Finoguenov, A. et al. 2007, ApJS, 172, 182
- Fiore, F. et al. 2003, A&A, 409, 79
- Fiore, F. et al. 2009, ApJ, 693, 447
- Fox, J. 1997, Applied Regression Analysis, Linear Models, and Related Methods (Thousand Oaks, CA: Sage Publications), 438
- Fu, H. & Stockton, A. 2009, ApJ, 690, 953
- Gabor, J. M. et al. 2009, ApJ, 691, 705
- Gallagher, S. C., Brandt, W. N., Chartas, G., Priddey, R., Garmire, G. P., & Sambruna, R. M. 2006, ApJ, 644, 709
- Gavignaud, I. et al. 2006, A&A, 457, 79
- Gavignaud, I. et al. 2008, A&A, 492, 637
- Gebhardt, K. et al. 2000, ApJ, 539, 13
- Ghez, A. M. et al. 2003, ApJ, 127, 131
- Gierliński, M. Zdziarski, A. A., Poutanen, J. Coppi, P. S., Ebisawa, K. & Johnson, W. N. 1999, MNRAS, 399, 496
- Gilli, R., Salvati, M., & Hasinger, G. 2001, A&A, 366, 407
- Gilli, R., Comastri, A., & Hasinger, G. 2007, A&A, 463, 79

- Glazebrook, K. & Bland-Hawthorn, J. 2001, *PASP*, 113, 197
- Glozzi, M., Sambruna, R. M., & Foschini, L. 2007, *ApJ*, 662, 878
- Graham, A. W. 2007, *MNRAS*, 379, 711
- Green, P. J. et al. 2004, *ApJS*, 150, 43
- Greene, J. E., & Ho, L. C. 2006, *ApJ*, 641, 21
- Hao, L. et al. 2005, *AJ*, 129, 1795
- Häring, N. & Rix, H.-W. 2004, *ApJ*, 604, L89
- Hasinger, G., Miyaji, T., & Schmidt, M. 2005, *A&A*, 441, 417
- Hasinger, G. et al. 2007, *ApJS*, 172, 29
- Hasinger, G. 2008, *A&A*, 490, 905
- Hawkins, M. R. S. 2004, *A&A*, 424, 519
- Heckman, T. M. 1980, *A&A*, 87, 152
- Hewett, P. C., Foltz, C. B., & Chaffee, F. H. 1995, *AJ*, 109, 1498
- Hickox, R. C. et al. 2009, *ApJ*, 696, 891
- Ho, L. C. 1999, *ApJ*, 516, 672
- Ho, L. C. 2002, *ApJ*, 564, 120
- Ho, L. C. 2008, *ARA&A*, 46, 475
- Ho, L. C. 2009, *ApJ*, 699, 626
- Hopkins, P. F. et al. 2004, *AJ*, 128, 1112

- Hopkins, P. F. et al. 2005, *ApJ*, 630, 705
- Hopkins, P. F., Hernquist, L., Cox, T. J., di Matteo, T., Robertson, B., & Springel, V. 2006, *ApJS*, 163, 1
- Hopkins, P. F., & Hernquist, L. 2006, *ApJS*, 166, 1
- Hopkins, P. F., Richards, G. T., Hernquist, L. 2007, *ApJ*, 654, 731
- Hopkins, P. F., Hickox, R., Quataert, E., & Hernquist, L. 2009, *MNRAS*, 398, 333
- Hopkins, P. F. & Elvis, M. 2010, *MNRAS*, 401, 7
- Hornschemeier, A. F. et al. 2001, *ApJ*, 554, 742
- Hornschemeier, A. E., Heckman, T. M., Ptak, A. F., Tremonti, C. A., & Colbert, E. J. M. 2005, *AJ*, 129, 86
- Ilbert, O. et al. 2009, *ApJ*, 690, 1236
- Ilbert, O. et al. 2010, *ApJ*, 709, 644
- Jahnke, K., Kuhlbrodt, B., & Wisotzki, L. 2004, *MNRAS*, 352, 399
- Jahnke, K. et al. 2009, *ApJ*, 706, L215
- Jannuzi, B. T., Smith, P. S. & Elston, R. 1994, *ApJ*, 428, 130
- Kaspi, S., Smith, P. S., Netzer, H., Maoz, D., Jannuzi, B. T. & Giveon, U. 2000, *ApJ*, 533, 631
- Kaspi, S., Brandt, W. N., Maoz, D., Netzer, H., Schneider, D. P. & Shemmer, O. 2007, *ApJ*, 659, 997
- Kauffmann, G. et al. 2003, *MNRAS*, 346, 1055

- Kelly, B.C. 2007, ApJ, 665, 1489
- Kelly, B. C. & Bechtold, J. 2007, ApJS, 168, 1
- Kelly, B. C., Bechtold, J., Trump, J. R., Vestergaard, M., & Siemiginowdka, A. 2008, ApJS, 176, 3557
- Kelly, B. C., Bechtold, J., & Siemiginowska, A. 2009, ApJ, 698, 895
- Kewley, L. J., Dopita, M. A., Sutherland, R. S., Heisler, C. A., & Trevena, J. 2001, ApJ, 556, 121
- Kim, D.-W. et al. 2004, ApJ, 600, 59
- Koekemoer, A. M. et al. 2007, ApJS, 172, 196
- Kollmeier, J. A. et al. 2006, ApJ, 648, 128
- Kormendy, J. & Richstone, D. 1995, ARA&A, 33, 581
- Krolik, J. H., & Begelman, M. C. 1988, ApJ, 329, 702
- Krolik, J. H. 2001, ApJ, 551, 72
- Lacy, M. et al. 2004, ApJS, 154, 166
- La Franca, F. et al. 2002, ApJ, 570, 100
- La Franca, F. et al. 2005, ApJ, 635, 864
- Lanzuisi et al. 2009, in prep.
- Lauer, T. R., Tremaine, S., Richstone, D., & Faber, S. M. 2007, ApJ, 670, 249
- Laor, A. 2003, ApJ, 590, 86

- Lawrence, A. & Elvis, M. 1982, *ApJL*, 256, 410
- Lawrence, A. 1991, *MNRAS*, 252, 586
- Lehmann, I. et al. 2001, *A&A*, 371, 833
- Lilly, S. J. et al. 2007, *ApJS*, 172, 70
- Lonsdale, C. J. et al. 2003, *PASP*, 115, 897
- Luo, B. et al. 2008, *ApJS*, 179, 19
- Lynden-Bell, D. 1969, *Nature*, 223, 690
- Maccacaro, T., Gioia, I. M., Wolter, A., Zamorani, G., & Stocke, J. T. et al. 1988, *ApJ*, 326, 680
- Maccarone, T. J., Gallo, E. & Fender, R. 2003, *MNRAS*, 345, L19
- Magorrian, J. et al. 1998, *AJ*, 115, 2285
- Mainieri, V. et al. 2007, *ApJS*, 172, 368
- Maiolino, R. & Rieke, G. H. 1995, *ApJ*, 454, 95
- Maiolino, R., Marconi, A., & Oliva, E. 2001, *A&A*, 365, 37
- Marconi, A. & Hunt, L. K. 2003, *ApJ*, 589, 21
- Marconi, A., Risaliti, G., Gilli, R., Hunt, L. K., Maiolino, R. & Salvati, M. 2004, *MNRAS*, 351, 169
- Marconi, A. et al. 2008, *ApJ*, 678, 693
- Martinez-Sansigre, A. et al. 2005, *Nature*, 436, 666

- Martinez-Sansigre, A. et al. 2006, MNRAS, 370, 1479
- McCracken, H. J. et al. 2010, ApJ, 708, 202
- McLure, R. J., & Jarvis, M. J. 2002, MNRAS, 337, 109
- Meier, D. L. 2001, ApJ, 548, L9
- Melendez, M. et al. 2008, ApJ, 682, 94
- Melendez, M., Kraemer, S. B. & Schmitt, H. R. 2010, MNRAS in press (astro-ph/1003.2984)
- Merloni, A. et al. 2010, ApJ, 708, 137
- Molina, M. et al. 2006, MNRAS, 371, 821
- Mor, R., Netzer, H., & Elizur, H. 2009, ApJ, 705, 298
- Moran, E. C., Filippenko, A. V., & Chornock, R. 2002, ApJL, 579, 71
- Morokuma et al. 2008, ApJ, 676, 121
- Moustakas, J. & Kennicutt, R. C. 2006, ApJ, 651, 155
- Murray, N. & Chiang, J. 1998, ApJ, 494, 125
- Nagao, T., Murayama, T., Shioya, Y., & Taniguchi, Y. 2002, ApJ, 567, 73
- Narayan, R., Yi, I. & Mahadevan, R. 1995, Nature, 374, 623
- Narayan, R. & McClintock, J. E. 2008, NewAr, 51, 733
- Nenkova, M., Sirocky, M. M., Nikutta, R., Ivezić, Ž. & Elitzur, M. et al. 2008, ApJ, 685, 160

- Netzer, H. & Laor, A. 1993, *ApJ*, 404, 51
- Nicastro, F. 2000, *ApJ*, 530, L65
- Nicastro, F. & Elvis, M. 2000, *NewAR*, 44, 569
- Nicastro, F., Martocchia, A. & Matt, G. 2003, *ApJ*, 589, L13
- Onken, C. A., Ferrarese, L., Merritt, D., Peterson, B. M., Pogge, R. W., Vestergaard, M., & Wandel, A. 2004, *ApJ*, 615, 645
- Onken, C. A. et al. 2007, *ApJ*, 670, 105
- Paczynski, B. & Wiita, P. K. 1980, *A&A*, 88, 23
- Page, M. J. et al. 2003, *AN*, 324, 101
- Peng, C. Y., Ho, L. C., Impey, C. D., & Rix, H.-W. 2002, *AJ*, 124, 266
- Peng, C. Y. et al. 2006, *ApJ*, 649, 616
- Perola, G. C. et al. 2002, 389, 802
- Peterson, B. M. & Bentz, M. C. 2006, *NewAR*, 50, 796
- Polletta, M. et al. 2007, *ApJ*, 663, 81, 102
- Ptak, A., Terashima, Y., Ho, L. C. & Quataert, E. 2004, *ApJ*, 606, 173
- Puccetti, S. et al. 2009, *ApJS*, 185, 586
- Quataert, E., Di Matteo, T., Narayan, R., & Ho, L. C. 1999, *ApJ*, 525, 89
- Richards, G. T. et al. 2006, *ApJ*, 166, 470
- Richstone, D. et al. 1998, *Nature*, 395, 14

- Rigby, J. R., Rieke, G. H., Alonso-Herrero, A., & Perez-Gonzalez, P. G. 2006, *ApJ*, 645, 115
- Risaliti, G. & Elvis, M. 2004, in *Supermassive Black Holes in the Distant Universe*, ed. A. J. Barger (Dordrecht, The Netherlands: Kluwer), 187
- Sajina, A., Lacy, M., & Scott, D. 2005, *ApJ*, 621, 256
- Salpeter, E. E. 1964, *ApJ*, 140, 796
- Salvato, M. 2009, *ApJ*, 690, 1250
- Sánchez, S. F et al. 2004, *ApJ*, 614, 586
- Schinnerer, E. et al. 2007, *ApJS*, 172, 46S
- Schmidt, M. 1963, *Nature*, 197, 1040
- Schmidt, M. & Green, R. F. 1983, *ApJ*, 269, 352
- Schneider, D. P. et al. 2007, *AJ*, 134, 102
- Schodel, R. et al. 2002, *Nature*, 419, 696
- Schwartz, G. 1979, *Ann. Statist.*, 6, 461
- Schwope, A. D. et al. 2000, *AN*, 321, 1
- Scoville, N. et al. 2007, *ApJS*, 172, 38
- Severgnini, P. et al. 2003, *A&A*, 406, 483
- Shakura, N. I., & Sunyaev, R. A. 1973, *A&A*, 24, 337
- Shen, Y., Greene, J. E., Strauss, M. A., Richards, G. T., & Schneider, D. P. 2008, *ApJ*, 680, 169

- Shi, Y. et al. 2009, ApJ, 703, 1107
- Shields, J. C. et al. 2000, ApJ, 534, 27
- Silk, J. & Rees, M. J. 1998, A&A, 331, 1
- Silva, L., Granato, G. L., Bressan, A., & Danese, L. 1998, ApJ, 509, 103
- Silverman, J. D. et al. 2005, ApJ, 618, 123
- Silverman, J. D. et al. 2009, ApJ, 696, 396
- Simpson, C. 2005, MNRAS, 360, 565
- Smolčić, V. et al. 2008, ApJS, 177, 14
- Smolčić, V. et al. 2009, ApJ 696, 24
- Soltan, A. 1982, MNRAS, 200, 115
- Spergel, D. N., et al. 2003, ApJ, 148, 175
- Stern, D. et al. 2005, ApJ, 631, 163
- Steffen, A. T., Barger, A. J., Cowie, L. L., Mushotzky, R. F. & Yang, Y. 2004, ApJL, 596, 23
- Suganuma, M. et al. 2006, ApJ, 639, 46
- Sulentic, J. W., Marziani, P., & Dultzin-Hacyan, D. 2000, ARA&A, 38, 521
- Szokoly, G. P. et al. 2004, ApJS, 155, 271
- Taniguchi, Y. 1999, ApJ, 524, 65
- Taniguchi, Y. et al. 2007, ApJS, 172, 9

- Taniguchi, Y. et al. 2010, in prep.
- Tran, H. D. 2001, ApJ, 554, L19
- Tran, H. D. 2003, ApJ, 583, 632
- Treister, E. & Urry, C. M. 2006, ApJL, 652, 79
- Treister, E., Krolik, J. H. & Dullemond, C. 2008, ApJ, 679, 140
- Treister, E. et al. 2009, ApJ, 693, 1713
- Tremonti, C. A. et al. 2004, 613, 898
- Trouille, L., Barger, A. J., Cowie, L. L., Yang, Y., & Mushotzky, R. F. 2009, ApJ, 703, 2160
- Trump, J. R. et al. 2007, ApJS, 172, 383
- Trump, J. R. et al. 2009a, ApJ, 696, 1195
- Trump, J. R. et al. 2009b, ApJ, 700, 49
- Trump, J. R. et al. 2009c, ApJ, 696, 1195
- Ueda, Y., Akiyama, M., Ohta, K., & Miyaji, T. 2003, ApJ, 598, 886
- Ueda et al. 2008, ApJS 179, 124
- Urry, C. M. & Padovani, P. 1995, PASP, 107, 803
- Vanden Berk, D. E. et al. 2001, AJ, 122, 549
- Vasudevan, R. V. & Fabian, A. C. 2009, MNRAS, 392, 1124
- Veron-Cetty, M.-P., Joly, M., & Veron, P. 2004, A&A, 417, 515

- Vestergaard, M. & Wilkes, B. J. 2001, ApJS, 134, 1
- Vestergaard, M. 2004, ApJ, 601, 676
- Vestergaard, M. & Peterson, B. M. 2006, ApJ, 641, 689
- Vestergaard, M. & Osmer, P. S. 2009, 699, 800
- Vignali, C., Brandt, W. N., Schneider, D. P., Garmire, G. P., & Kaspi, S. 2003, AJ, 125, 2876
- Wang, J.-M. & Zhang, E.-P. 2007, ApJ, 660, 1072
- Wang, J. X. et al. 2004, AJ, 127, 213
- Wisotzki, L., Christlieb, N., Bade, N., Beckmann, V., Köhler, T., Vanelle, C., & Reimers, D. 2000, A&A, 358, 77
- Woo, J.-H., Treu, T., Malkan, M. A., & Blandford, R. D. 2008, ApJ, 681, 925
- Wu, X.-B., Wang, R., Kong, M. Z., Liu, F. K., & Han, J. L. 2004, A&A, 424, 793
- Yang, Y. et al. 2004, AJ, 128, 1501
- York, D. et al. 2000, AJ, 120, 1579
- Younger, J. D. et al. 2008, ApJ, 686, 815
- Yuan, F. & Narayan, R. 2004, ApJ, 612, 724
- Yuan, F. 2007, in ASP Conf. Ser. 373, The Central Engine of Active Galactic Nuclei, ed. L. C. Ho & J.-W. Wang (San Francisco, CA: ASP), 95
- Zakamska, N. L. et al. 2003, AJ, 126, 2125
- Zamojski, M. A. 2007, ApJS, 172, 468